JULY-SEPTEMBER 2022 VOL. 14 № 3 (54)

ISSN 2075-8251

ActaNaturae

Human Artificial Chromosomes and Their Transfer to Target Cells

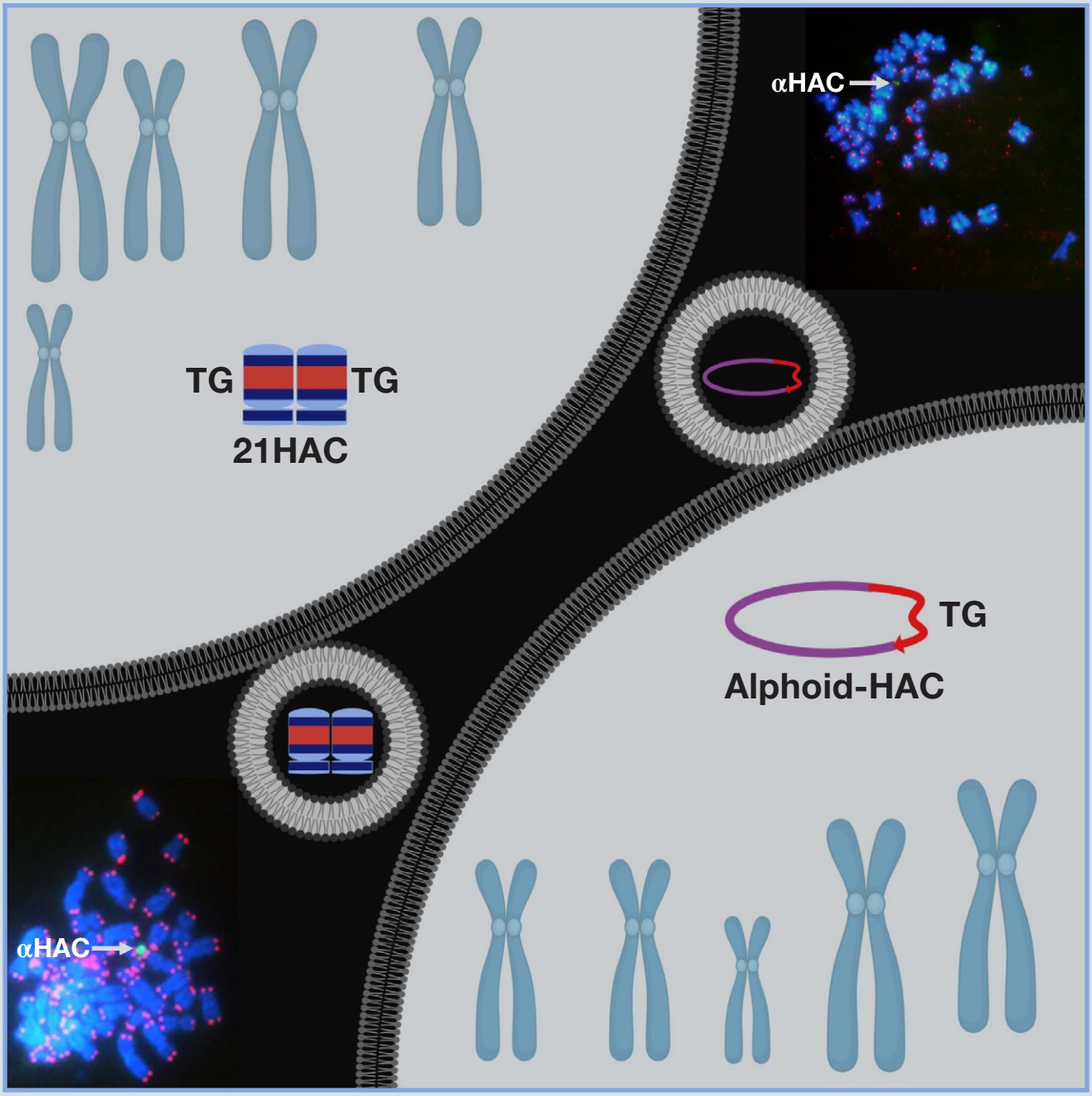

III JOINT LIFE SCIENCES FORUM

VII RUSSIAN CONGRESS ON BIOCHEMISTRY & MOLECULAR BIOLOGY

♦

X RUSSIAN SYMPOSIUM "PROTEINS AND PEPTIDES"

In Memory of Professor Vadim Ivanov

Sochi, Russia ***October 3–7, 2022***

We are happy to announce the Forum new dates and venue.
The Forum will be held on October 3–7 2022
in the Grand Hotel "Zhemchuzhina", one of the best hotels in Sochi.
To learn more, please visit our website at
http://rusbiochem.org/Page224.html

CONGRESS ORGANIZERS

- Russian Academy of Sciences
- Ivan Pavlov Russian Physiological Scoeity
- Russian Biochemical Society (National Committee of Russian Biochemists)
- Russian Science Foundation

with the involvement of

- CIS Union of Physiological Societies

PROGRAM COMMITTEE CO-CHAIRS

Full Members of the Russian Academy of Sciences
Alexander Gabibov, Mikhail Ostrovsky

ADDITIONAL APPLICATION FOR ORAL PRESENTATION ARE ACCEPTED
BEFORE JULY 15, 2022

ADDITIONAL APPLICATIONS FOR POSTER PRESENTATION AND
PARTICIPATION IN THE YOUNG SCIENTISTS' CONTEST ARE ACCEPTED
BEFORE JULY 20, 2022

Any questions? Please contact us by e-mail: info@rusbiochem.org

The preliminary scientific program is already published online at www.rusbiochem.org and www.physiology-cis.org. Upon receipt of additional applications, we will revise the program. The final version will be placed at our web sites before September 1, 2022.

WWW.RUSBIOCHEM.ORG

Suppression of the Testis-Specific Transcription of the *ZBTB32* and *ZNF473* Genes in Germ Cell Tumors

S. S. Bulanenkova, O. B. Filyukova, E. V. Snezhkov, S. B. Akopov, L. G. Nikolaev

The aim of this work was to identify C2H2 family genes with tissue-specific transcription and analyze changes in their activity during tumor progression. To search for these genes, authors used four databases containing data on gene transcription in human tissues obtained by RNA-Seq analysis. A decrease in *ZBTB32* and *ZNF473* transcription levels was demonstrated in germ cell tumors. The studied genes can serve as candidate markers in germ cell tumors.

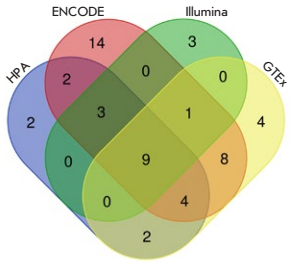

Venn diagram showing preselected genes common to the four databases: Human Protein Atlas, ENCODE, Illumina BodyMap, and GTEx

An ELISA Platform for the Quantitative Analysis of SARS-CoV-2 RBD-neutralizing Antibodies As an Alternative to Monitoring of the Virus-Neutralizing Activity

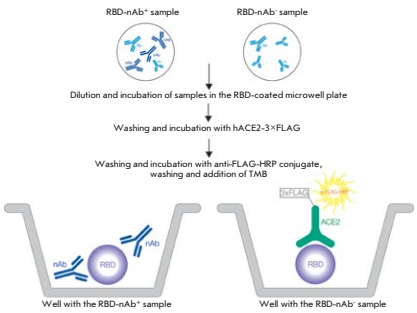

Scheme of the quantitative determination of the activity of SARS-CoV-2 RBD-specific neutralizing antibodies in serum or plasma (sVNT)

N. N. Kostin, T. V. Bobik, G. A. Skryabin, M. A. Simonova, V. D. Knorre, V. A. Abrikosova, Y. A. Mokrushina, I. V. Smirnov, N. L. Aleshenko, N. A. Kruglova, D. V. Mazurov, A. E. Nikitin, A. G. Gabibov

Authors are proposing an ELISA platform for performing a quantitative analysis of SARS-CoV-2 RBD-neutralizing antibodies, as an alternative to the monitoring of the virus-neutralizing activity using pseudovirus or “live” virus assays. The advantage of the developed platform is that it can be adapted to newly emerging virus variants in a very short time (1–2 weeks) and, thereby, provide quantitative data on the activity of SARS-CoV-2 RBD-neutralizing antibodies. The developed platform can be used to study herd immunity to SARS-CoV-2, monitor the effectiveness of the vaccination drive (re-vaccination) in a population, and select potential donors of immune plasma.

The Role of a Pathological Interaction between β-amyloid and Mitochondria in the Occurrence and Development of Alzheimer’s Disease

N. S. Nikolaeva, E. Yu. Yandulova, Yu. R. Aleksandrova, A. S. Starikov, M. E. Neganova

Alzheimer’s disease is one of the most common neurodegenerative diseases in existence. It is characterized by an impaired cognitive function that is due to a progressive loss of neurons in the brain. Extracellular β-amyloid (Ab) plaques are the main pathological features of the disease. In addition to abnormal protein aggregation, increased mitochondrial fragmentation, altered the expression of the genes involved in mitochondrial biogenesis, disturbances in the ER–mitochondria interaction, and mitophagy are observed. In this review, the authors summarize available knowledge about the pathological effects of Aβ on mitochondria and the potential molecular targets associated with proteinopathy and mitochondrial dysfunction for the pharmacological treatment of Alzheimer’s disease.

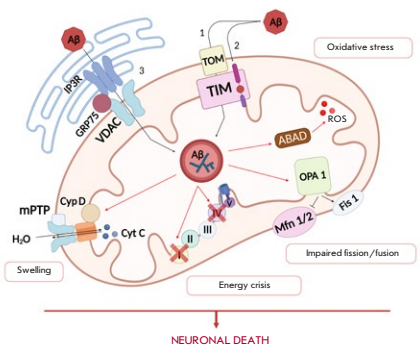

Schematic representation of the pathways of β-amyloid (Aβ) entry into mitochondria and its pathological effects on these organelles

ActaNaturae
JULY-SEPTEMBER 2022 VOL. 14 № 3 (54)
since april 2009, 4 times a year

Adress: 101000, Moscow, Myasnitskaya Ulitsa, 13, str. 4
Phone/Fax: +7 (495) 727 38 60
E-mail: actanaturae@gmail.com

Номер подписан в печать 30 сентября 2022 г.
Тираж 15 экз. Цена свободная.
Отпечатано в типографии: НИУ ВШЭ,
г. Москва, Измайловское шоссе, 44, стр. 2

Indexed in Pubmed, Web of Science, Scopus, and RISC

Impact Factor: 2.204

CONTENTS

REVIEWS

RESEARCH ARTICLES

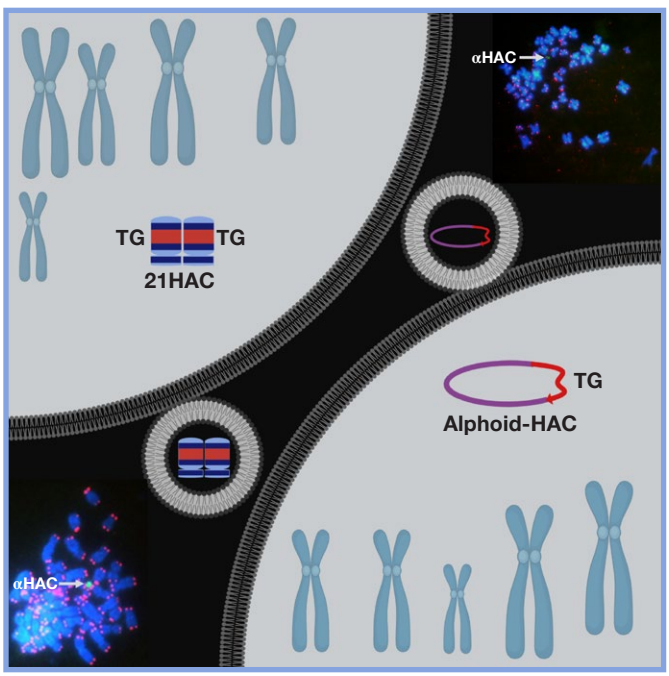

IMAGE ON THE COVER PAGE
(see the article by S. V. Ponomartsev et al.)

Visualization of G-Quadruplexes, i-Motifs and Their Associates

E. V. Dubrovin[1*], N. A. Barinov[1], D. V. Klinov[2,3]
[1]M.V. Lomonosov Moscow State University, Faculty of Physics, Moscow, 119991 Russia
[2]Federal Research and Clinical Center of Physical-Chemical Medicine of Federal Medical Biological Agency, Moscow, 119435 Russia
[3]Peoples' Friendship University of Russia (RUDN University), Moscow, 117198 Russia
*E-mail: dubrovin@polly.phys.msu.ru
Received March 08, 2022; in final form, July 13, 2022
DOI: 10.32607/actanaturae.11705

ABSTRACT **The non-canonical structures formed by G- or C-rich DNA regions, such as quadruplexes and i-motifs, as well as their associates, have recently been attracting increasing attention both because of the arguments in favor of their existence *in vivo* and their potential application in nanobiotechnology. When studying the structure and properties of non-canonical forms of DNA, as well as when controlling the artificially created architectures based on them, visualization plays an important role. This review analyzes the methods used to visualize quadruplexes, i-motifs, and their associates with high spatial resolution: fluorescence microscopy, transmission electron microscopy (TEM), and atomic force microscopy (AFM). The key approaches to preparing specimens for the visualization of this type of structures are presented. Examples of visualization of non-canonical DNA structures having various morphologies, such as G-wires, G-loops, as well as individual quadruplexes, i-motifs and their associates, are considered. The potential for using AFM for visualizing non-canonical DNA structures is demonstrated.**
KEYWORDS **G-quadruplexes, i-motifs, (immuno)fluorescence microscopy, atomic force microscopy, transmission electron microscopy.**
ABBREVIATIONS **TEM – transmission electron microscopy; BMVC – 3,6-*bis*(1-methyl-4-vinylpyridinium)carbazole diiodide; AFM – atomic force microscopy; DAPI – 4',6-diamidino-2-phenylindole; GM – N,N'-(decane-1,10-diyl)*bis*(tetraglycinamide); SPM – scanning probe microscopy; ThT – thioflavin T.**

INTRODUCTION

Hoogsteen binding of nucleotide bases in DNA gives rise to a number of non-canonical structures, including G-quadruplexes and i-motifs [1, 2]. In recent years, evidence has emerged that G-quadruplexes and i-motifs exist in the living cells of various organisms, including humans [3, 4]. These non-canonical DNA structures may be responsible for regulating molecular processes within the cell, including DNA replication, transcription, and genome maintenance [5, 6]. A large number of G-rich sequences in the promoter and telomeric regions of oncogenes (which, therefore, are also C-rich according to the DNA complementarity principle) makes G-quadruplexes (and i-motifs) a potential target for the delivery of antitumor agents into the cell [7–10]. In addition, DNA architectures based on G-quadruplexes and i-motifs are in demand in bionanotechnology: for creating molecular machines, developing biosensors and molecular electronic devices, performing molecular diagnostics, etc. [11–16].

The conventional methods for detecting and analyzing non-canonical DNA structures include circular dichroism, nuclear magnetic resonance spectroscopy, and UV absorption spectrophotometry during melting [17, 18]. These methods provide characteristics averaged over a large ensemble of molecules (e.g., light absorption or molar ellipticity at certain wavelengths), which allow one to assess the structure of G-quadruplexes and i-motifs. A no less important aspect in the study of the structure and properties of non-canonical DNA structures is their visualization. In addition, direct visualization is required in order to be able to control the generated DNA architectures. However, the nanoscale of the guanine quadruplex quartet or the cytosine–cytosine pair in the i-motif significantly limits the number of methods that can cope with this task.

One of the solutions to this problem is to fluorescently label antibodies against non-canonical DNA structures (immunofluorescence microscopy) or non-canonical DNA structures per se (fluorescence microscopy). These labels make it possible to reveal non-canonical DNA structures in the test sample (e.g., inside the cell) and analyze their distribution. Using this method, non-canonical structures are visualized according to a dot label, which precludes any evaluation of the morphology of the DNA structure per se.

Sufficient spatial resolution for visualizing non-canonical DNA structures is provided by electron and scanning probe microscopy. Meanwhile, scanning electron microscopy, where the image is produced by backscattered electrons, is almost never used for visualizing DNA structures due to a number of inherent limitations, such as the need to study conductive samples and lower resolution compared to transmission electron microscopy. On the contrary, transmission electron microscopy (TEM), which is based on the transmission of an electron beam through an ultrathin (~ 0.1 μm thick) sample, is widely used for studying DNA. In TEM, an image produced by the electrons that have passed through a sample is amplified by electromagnetic lenses and focused on a CCD array.

Scanning probe microscopy (SPM) is a class of methods where image production is based on local interaction between a probe and the sample surface in a large number of points. The most common type of SPM is atomic force microscopy (AFM), which is based on the exchange interaction between probe atoms and a sample [19].

SPM significantly differs from TEM not only in terms of its principle of operation, but also in terms of the sample preparation procedure. Thus, a typical procedure for preparing DNA for TEM examination includes fixing the sample using glutaraldehyde or formaldehyde, as well as creating a contrast by sputtering heavy metal ions onto the sample or treating it with a contrast agent. In addition, electron microscopy studies are usually carried out under vacuum (the low-vacuum models of transmission electron microscopes, which allow one to examine samples in an aqueous vapor or solutions, are characterized by a significantly lower spatial resolution and a complicated procedure of sample preparation and selection of working parameters) [20, 21]. The aforelisted conditions of DNA sample preparation and investigation are far from physiological; therefore, DNA structures visualized using electron microscopy can significantly differ from native ones. In addition, contrasting reduces the resolution of the resulting TEM images. Scanning probe microscopy methods are a more flexible tool in the context of sample preparation conditions and scanning environment as they allow DNA to be deposited from aqueous solutions without additional components alien to the native environment and to conduct the study in air and liquid media [22]. An additional distinguishing feature of AFM is that it allows real-time visualization of dynamic processes [23]. Thanks to these factors, AFM is a method widely used for visualizing various DNA structures and their associates at the level of individual molecules.

This review systematizes the key methods and approaches used to visualize G-quadruplexes, i-motifs and their associates, as well as to analyze the main scientific achievements related to the visualization of these non-canonical DNA structures. The methodological aspects of DNA sample preparation for AFM are also discussed.

FLUORESCENCE MICROSCOPY OF NON-CANONICAL DNA STRUCTURES

This line of research has recently been intensively developing thanks to the design of small fluorescent molecules (probes) that specifically bind to G-quadruplexes and i-motifs and allow one to localize the latter through fluorescence. For a G-quadruplex, such specific binding can be performed thanks to the π-stacking interaction between a fluorescent dye and the outer tetrad of the G-quadruplex, the interaction between a probe and the loops or grooves of the G-quadruplex, as well as the intercalation of the dye between two quadruplexes [24]. Such ligands are often used in tandem with DNA-duplex-specific fluorophores (e.g., Hoechst dye or propidium iodide), making it possible to compare the localization of canonical and non-canonical DNA structures in one image. One of the quadruplex ligands is 3,6-*bis*(1-methyl-4-vinylpyridinium)carbazole diiodide (BMVC). For example, it has been used to establish that quadruplexes are formed on the proximal (telomeric) regions of chromosomes [25, 26]. Another fluorescent dye, thiazole orange, is also used to visualize G-quadruplexes [27] and i-motifs [28] thanks to the highly specific binding to them, accompanied by the strong increase in fluorescence. The disadvantage of this dye in the context of the visualization of G-quadruplexes and i-motifs is its low selectivity, as it is able to bind to other nucleic acid structures as well, including double-stranded DNA, three-stranded DNA, and RNA [27, 29, 30]. Another fluorescent dye, thioflavin T (ThT), widely used for specific staining of amyloids, also binds to various DNA structures, while the fluorescence amplification upon binding to G-quadruplexes is especially high (~ 2,100-fold in the visible region) [31, 32]. In recent years, a number of new compounds have been developed and studied in order to be used as fluores-

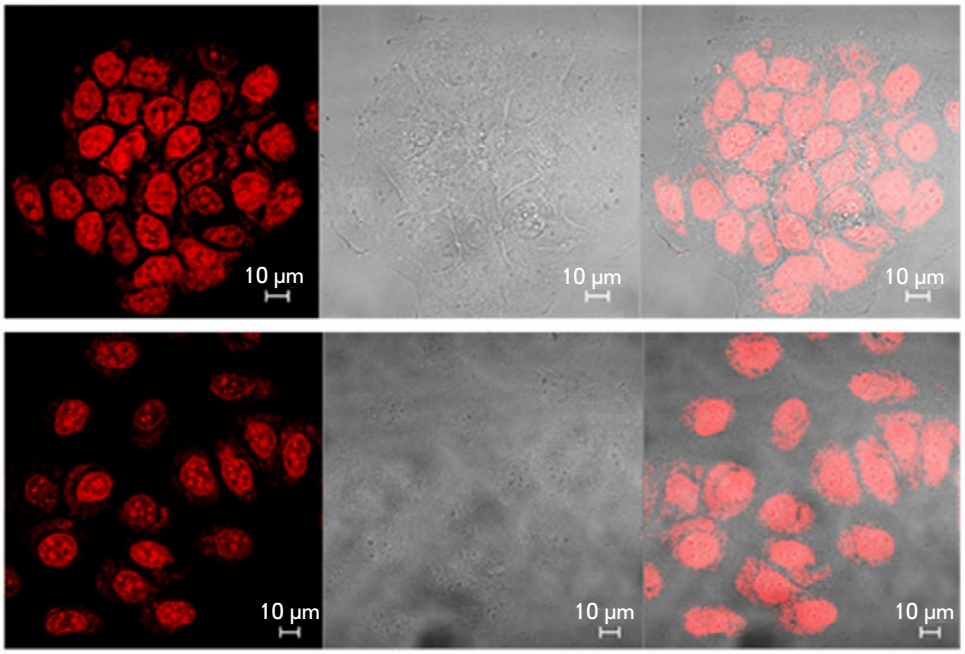

Fig. 1. A confocal laser scanning microscopy image of fixed MCF-7 cancer cells labeled (before fixation) for 6 h using c_{ex}-NDI, demonstrating nuclear localization of G-quadruplexes (left – fluorescence signal; center – bright field observation; right – superposition of two signals). Reproduced from [37] under the CC 4.0 license (http://creativecommons.org/licenses/by/4.0/)

cent probes for G-quadruplexes and i-motifs [33], and benzothiazole derivatives in particular [34, 35].

Because of the supposed participation of G-quadruplexes in gene expression and disease pathogenesis, intracellular visualization of these structures is of particular interest. For a long time, such studies were mainly conducted in fixed cells. Thus, Yan et al. [36] designed a new quadruplex fluorophore, S1, which exhibited high selectivity for binding to G-quadruplexes in i*n vitro* experiments, as well as strong fluorescence in the nucleolus of fixed HeLa cells and weak fluorescence in the remaining portion of the nucleus. The DNA dye 4',6-diamidino-2-phenylindole (DAPI), added simultaneously, stained the nucleus more uniformly. This suggested that G-quadruplexes have a nucleolar localization. The localization of G-quadruplexes in the nuclei of MCF-7 cancer cells was pinpointed using a core-extended naphthalene diimide fluorescent probe (c_{ex}-NDI) (*Fig. 1*) [37].

Probes that allow to visualize quadruplexes in living cells are of the greatest value. Not only should such probes be highly specific to G-quadruplexes, but they also need to have a low ability to bind to proteins and other biological molecules, be capable of passing through the plasma and nuclear membranes, and possess low cytotoxicity [38].

One of the quadruplex probes used in the fluorescence microscopy of living cells is the BMVC isomer, o-BMVC. Experiments using model objects showed different fluorescence decay times for o-BMVC upon their interaction with G-quadruplexes. Using this fluorophore, G-quadruplexes were localized both in the cytoplasm and in the nucleus of living cells of the CL1-0 line (human lung cancer cells) [39]. Fluorescence lifetime imaging microscopy allowed researchers to both differentiate between duplexes and G-quadruplexes and identify G-quadruplexes of different types, which differ in terms of fluorescence decay time of the ligand bound to them. A similar method – but with a different fluorescent probe (DAOTA-M2) – was used to specify the nuclear localization and stability of G-quadruplexes in living U2OS osteosarcoma cells (*Fig. 2*) [40, 41]. Nucleolar localization of G-quadruplexes in live MCF-7 cells has recently been confirmed using ThT as a fluorescent probe [42].

Novel fluorophores have recently been developed: they are characterized by a high selectivity to G-quadruplexes, while being highly stable, and can be used in living cells. Examples include such ligands as N-TASQ [43], 2,6-*bis*((E)-2-(1H-indole-3-yl)vinyl)-1-methylpyridine-1 iodide [44], carbazole derivatives (4a – 4c) [45], etc. [46, 47]. It has been demonstrated

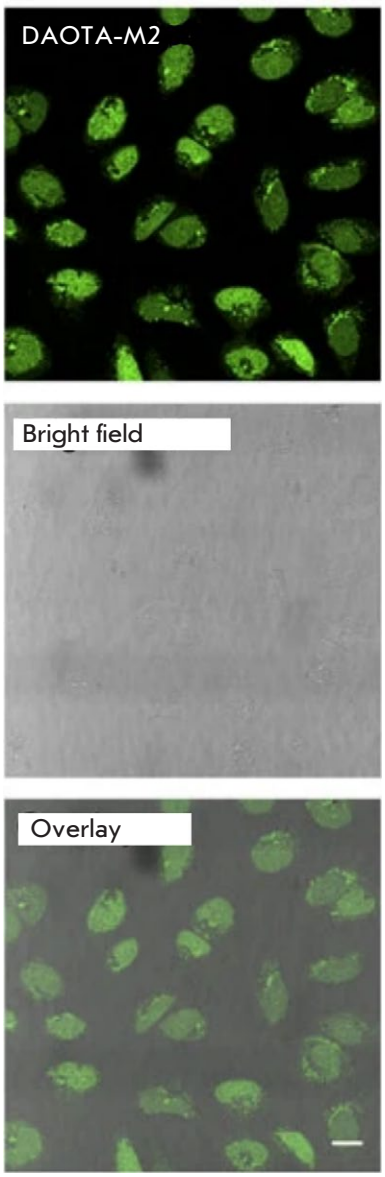

Fig. 2. A confocal microscopy image of living U2OS cells incubated with the DOTA-M2 dye, demonstrating nuclear localization of G-quadruplexes (top – fluorescence signal; center – bright field observation; bottom – superposition of two signals). Reproduced from [40] under the CC 4.0 license (http://creativecommons.org/licenses/by/4.0/)

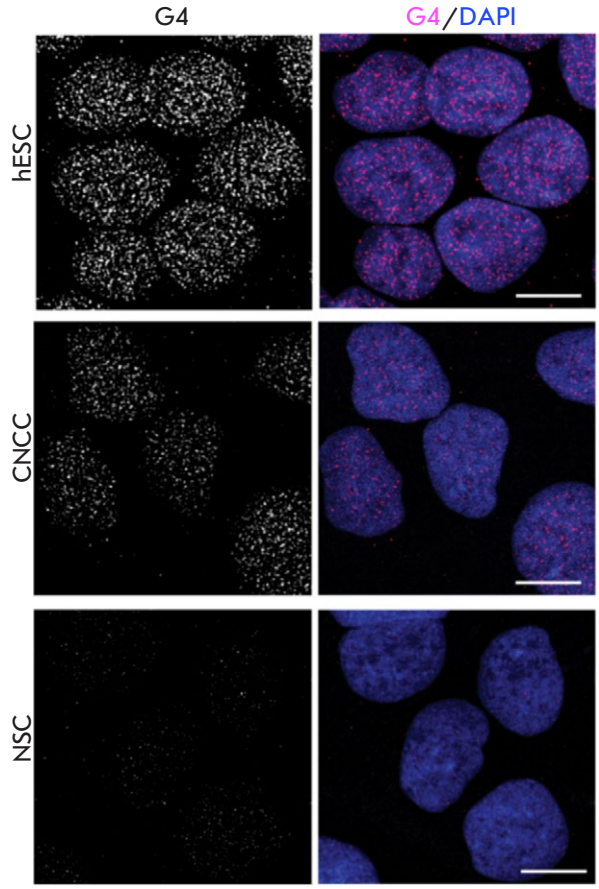

Fig. 3. An immunofluorescence microscopy image of fixed pluripotent embryonic stem cells (hESCs), cranial neural crest cells (CNCCs), and neural stem cells (NSCs) labeled with G-quadruplex-specific antibodies BG4 after treatment with RNase (secondary antibodies labeled with fluorescent dye AlexaFluor 488). On the left-hand side, only the quadruplexes are visualized; while on the right-hand side, the nuclei are stained blue due to the contrast with the DNA dye DAPI. The scale bar is 10 μm. Reproduced from [54] under the CC 4.0 license (http://creativecommons.org/licenses/by/4.0/)

using these probes that G-quadruplexes have nucleolar localization in living cells. N-TASQ has also been used to visualize RNA-based G-quadruplexes in the cytoplasm [48]. Finally, the existence of mitochondrial G-quadruplexes in living cells was shown using fluorescence microscopy [35, 49].

An alternative approach to the visualization of G-quadruplexes and i-motifs by fluorescence microscopy is to use specific antibodies enhanced with secondary antibodies tagged with fluorescent labels (immunofluorescence microscopy). For this purpose, various antibodies specific to DNA and RNA G-quadruplexes (e.g., 1H6 and BG4) were synthesized; they allowed one to visualize G-quadruplexes in various cells and tissues [50–53]. These results are important arguments in favor of the existence of G-quadruplexes in mammalian cells, including the nucleus, cytoplasm, and mitochondria. Thus, immunofluorescence microscopy studies based on BG4 quadruplex antibodies visualized the distribution of G-quadruplexes in the nucleus of hESC pluripotent embryonic stem cells and revealed that the number of G-quadruplexes is significantly reduced during cell differentiation (*Fig. 3*) [54].

Recently, i-motifs were visualized *in vivo* in the nuclei and chromosomes in the *Bombyx mori* testis using immunofluorescence staining with an antibody specifically recognizing the endogenous transcription factor BmILF, which is highly specific to the structure of i-motifs [55].

Meanwhile, the application of immunofluorescence microscopy is hampered by such factors as the relatively high cost of antibodies, as well as their low stability and potential immunogenicity [38]. Therefore, the development and application of G-quadruplex-specific fluorophores remain relevant in our efforts to visualize these structures in living cells.

TEM IMAGING OF NON-CANONICAL DNA STRUCTURES

Although TEM is commonly used to study DNA and DNA-containing structures in general, this method is quite rarely employed for visualizing non-canonical DNA structures. The typical objects of such visualization are DNA molecules with a non-canonically folded fragment. In particular, TEM has helped discern various loops on double-stranded DNA molecules associated with the formation of G-quadruplexes on one of the two DNA strands.

One of the types of such loops arising after the intracellular transcription of G-rich sites are known as G-loops [56]. G-loops are formed on the plasmid genome *in vitro* or in *Escherichia coli*, and they consist of a G-quadruplex on the non–coding DNA chain and a stable RNA/DNA hybrid on the coding DNA chain. In addition, the formation of a specific complex between the G-quadruplex of the G-loop and the mismatch repair factor, the MutSa heterodimer, as well as the formation of a MutSa-mediated synapsis between two DNA strands was observed. The observation of such synapses suggested a mechanism of MutSa operation during class-switch recombination. The so-called R-loops, RNA/DNA hybrids that are formed during the transcription of repetitive motifs $(CTG)_n$, $(CAG)_n$, $(CGG)_n$, $(CCG)_n$ and $(GAA)_n$ and are associated with some human diseases, also have a structure similar to that of G-loops. R-loops were visualized using TEM [57], but there was no evidence of the formation of G-quadruplexes on a non-coding chain of R-loops. The formation of loops on the G-rich regions of the insulin gene after denaturation and renaturation of the DNA molecule, visualized using TEM [58], was attributed to the formation of quadruplexes on one of the DNA chains.

TEM has also been used to visualize quadruplexes formed in a controlled environment by parallel duplexes bearing G-repeats [59]. The TEM images showed a narrow distribution of the lengths of such structures, consistent with the expected size. In addition, one-dimensional quadruplex-containing nanostructures in the form of nanowires of various lengths are visualized.

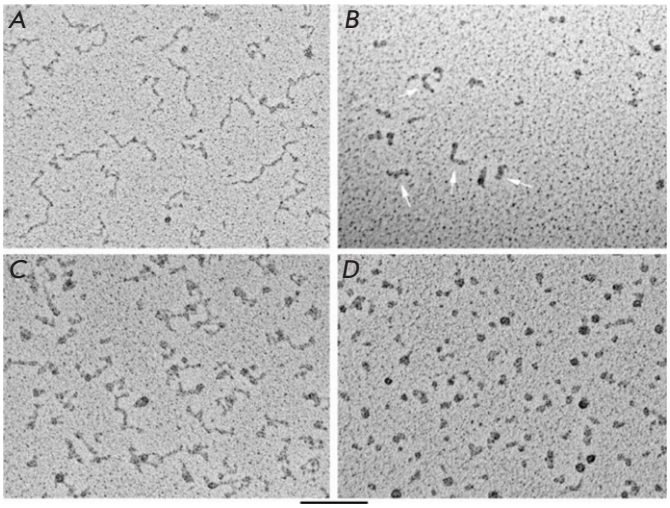

Fig. 4. Visualization of C- and G-rich telomeric transcripts. C-rich (*A*) and G-rich (*B*) RNA molecules in 100 mM KCl were deposited for EM on thin carbon substrates, dehydrated, and shaded with tungsten on a rotating substrate. C-rich RNAs look like elongated strands with nodes. G-rich RNAs look like a mixture of balls and sticks (arrows). The rod thickness is significantly greater than that of C-rich or duplex RNAs. C-rich (*C*) and G-rich (*D*) RNA molecules are deposited from 10 mM KCl in the same way as in (*A*) and (*B*). C-rich RNA looks straightened with nodes, while G-rich RNA is mainly ball-shaped. The scale bar is 100 nm. Reproduced from [60] under the CC 4.0 license (http://creativecommons.org/licenses/by/4.0/)

An analysis of the RNA transcripts of C- and G-rich mammalian telomeric DNA carried out using TEM revealed fundamental differences in their morphologies. C-rich RNA transcripts have a more elongated structure, with a thickness typical of single-stranded RNA, while G-rich transcripts are round particles and short, thick rod-like structures that prevail at elevated salt concentrations (*Fig. 4*). The observed morphology allowed one to propose a model suggesting that G-rich telomeric RNA is assembled into particle chains, each consisting of four UUAGGG repeats stabilized by parallel G-quartets and connected by UUA linkers [60].

With the advent of anti-G-quadruplex antibodies, quadruplexes were also studied using immunoelectron microscopy. In this method, the quadruplexes are detected using TEM imaging of tags (gold nanoparticles) conjugated to secondary anti-G-quadruplex

antibodies. Immunoelectron microscopy does not attain the molecular resolution of the quadruplexes per se, but it allows one to observe the distribution of G-quadruplexes inside the cell, which is important for understanding the role played by quadruplexes in intracellular processes. Thus, the formation of G-quadruplexes in cells infected with the herpes simplex virus type 1 was visualized using this method. The formation of G-quadruplexes depended on the stage of the infection cycle: viral G-quadruplexes whose number reached the maximum during virus replication in the cell nucleus moved to the nuclear membrane at the time of virus exit from the nucleus (*Fig. 5*) [61]. G-quadruplexes in mammalian heterochromatin were detected in a similar way [62]. Therefore, not only do the findings accumulated using immunoelectron microscopy indicate the existence of G-quadruplexes in cells, but they also suggest that G-quadruplexes play a crucial role in biological processes.

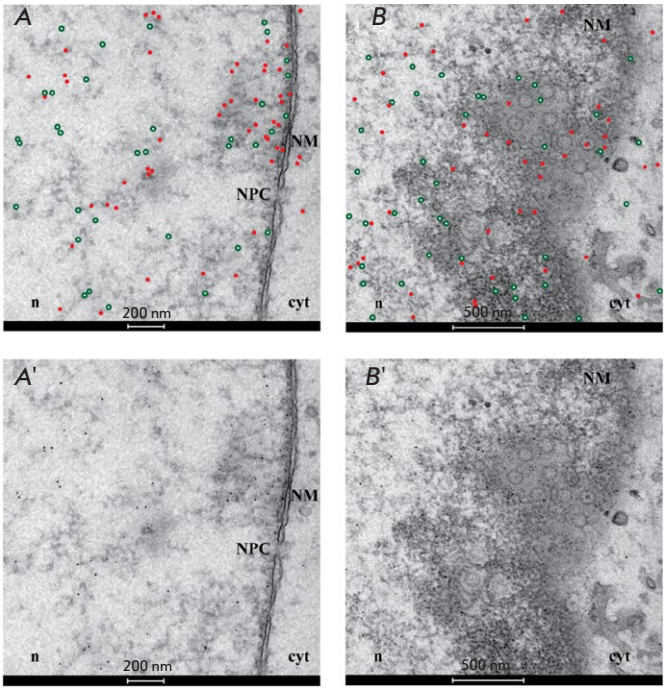

Fig. 5. An immunoelectron microscopy image of cells infected with herpes simplex virus type 1 (HSV-1), fixed for 15 h post-infection, and incubated with the anti-G-quadruplex antibody (1H6) and anti-ICP8 serum. Primary antibodies to 1H6 and to ICP8 were detected using gold particles with a diameter of 5 and 10 nm, respectively. To improve image clarity, the golden particles are highlighted with red dots (showing G-quadruplexes) and green circles (showing ICP8) on *Figs. A* and *B*. The original images are shown in panels *A'* and *B'*. (*A-A'*) G-quadruplexes and ICP8 concentrate in the vicinity of the nuclear membrane (NM), where the nuclear pore complex (NPC) is located. The exit from the nucleus through the nuclear pore complex is one of the pathways used by HSV-1 capsids to leave the nucleus (n) and get into the cytoplasm (cyt). (*B-B'*) G-quadruplexes and the ICP8 cluster near the nuclear membrane, where the newly formed virions bud off. Reproduced from [61] under the CC 4.0 license (http://creativecommons.org/licenses/by/4.0/)

GENERAL APPROACHES TO STUDYING NUCLEIC ACIDS BY AFM

The key component of an atomic force microscope [19] is an elastic plate called a cantilever, with a tip (probe) on it. The interaction between the probe and the surface causes cantilever bending, which is detected by a high-precision optical system consisting of a laser, a photodiode, and the mirror surface of the cantilever. The contact mode of scanning, when cantilever bending serves as a feedback signal and is maintained constant, is rarely used for investigating DNA because of the significant interaction forces between the cantilever and the sample, which cause biomolecule deformation and deteriorate the spatial resolution of the image. AFM studies of biomolecules are typically carried out in the intermittent contact mode [63], when the cantilever oscillates near the resonant frequency, and the interaction between the probe and the sample is determined by the changes in the oscillation amplitude caused by this interaction, which is maintained constant by the feedback. In the intermittent contact mode, the normal forces between the cantilever and the sample are significantly lower than those in the contact mode of scanning and the lateral forces associated with adhesion do not substantially affect the production of the AFM image, since the cantilever periodically "unsticks" from the sample surface, when it moves along the surface during scanning. Over the past decade, the modes based on the periodic approach and withdrawal of the cantilever to/from the surface (the PeakForce mode, "jumping" mode, etc.) have become widely used; these modes can significantly reduce the interaction force between the cantilever and the sample surface [64].

The essential condition for studying DNA using AFM is being able to immobilize a molecule on a substrate. Immobilization of a biomolecule depends on a number of factors such as the composition, pH, concentration of the components of the solution from which the sample is deposited, temperature, the application method, adsorption time, substrate properties, etc. Therefore, sample preparation plays a crucial role in AFM. Smoothness (low roughness) is one of the

requirements imposed on the substrate surface for biopolymer deposition. The two most common AFM substrates having areas with atomic smoothness, mica and highly oriented pyrolytic graphite (HOPG), are of a crystalline nature. However, when DNA is deposited onto these surfaces from aqueous solutions, individual molecules in the straightened state are not adsorbed: so, they cannot be studied by AFM.

The reason hindering DNA adsorption on freshly cleaved mica is the similar negative charge of the phosphate groups in the biopolymer and the mica surface, leading to electrostatic repulsion of DNA from the surface. Several strategies have been developed and successfully applied for many years to overcome this phenomenon. The most common one is to use divalent cations such as Mg^{2+}, Ca^{2+}, Zn^{2+}, etc., which act as electrostatic "bridges" between the mica atomic lattice and DNA phosphate groups [65, 66]. In the real world, freshly cleaved mica is pre-modified in an appropriate saline solution before applying DNA or a small amount of this solution (1–10 mM) is applied to mica simultaneously with DNA. Another method, preliminary modification of the mica surface with aminosilanes (e.g., 3-aminopropyltriethoxysilane), is also used to deposit DNA onto mica [67]. In this case, DNA adsorption on the substrate is caused by its attraction to the positively charged amino groups of the modifier. The two strategies described above (the use of divalent cations and aminosilanes) differ in terms of the strength of DNA adsorption: adsorption of molecules mediated by divalent metal cations is relatively weak, enabling thermal motion of DNA near the surface [68–71]. On the contrary, mica modified with aminosilanes typically serves as a "kinetic trapping" for DNA; i.e., adsorbed DNA molecules remain immobile on the surface, and their conformation represents the conformation in the solution [72].

A large body of evidence has been accumulated, indicative of the formation of potassium carbonate on the mica surface during its cleavage under laboratory conditions [73]. When immersed into an aqueous solution, the resulting salt can ensure high ionic strength near the mica surface (i.e., just within the area where the main interactions between the biopolymer and the surface occur during its adsorption). This effect, in particular, was observed according to the intense dissociation of the DNA–protein complexes deposited onto mica from a solution with low ionic strength [74]. This characteristic of mica significantly complicates the interpretation of the results obtained for this substrate and, in particular, makes it impossible to perform studies on its surface at low ionic strengths.

Unlike mica, HOPG is electrically neutral and does not form any salts on its surface. However, due to the weak interaction between DNA and graphite, adsorption of DNA molecules in the straightened state onto a freshly cleaved graphite surface is also difficult: DNA is usually adsorbed on this substrate only as aggregates or network structures [75, 76]. A number of approaches based on graphite modification have been developed to overcome this difficulty. The use of modified graphite makes it possible to study DNA at low or zero ionic strengths, which is important for studying the patterns of formation of non-canonical DNA structures.

One of such approaches is to preliminarily modify graphite in a glow discharge in the presence of pentylamine vapors: the surface modified in this way, saturated with amino groups, enables the adsorption of individual straightened DNA molecules onto it, and the dimensions of the biopolymer measured from AFM images (height and width at half-height) are much closer to the native DNA dimensions compared to the size of DNA adsorbed on mica [77, 78]. Later, a methodically simpler method was proposed for modifying HOPG: from an aqueous solution of an oligoglycine derivative N,N'-(decane-1,10-diyl)*bis*(tetraglycinamide) ($[Gly_4–NHCH_2]C_8H_{16}[CH_2NH–Gly_4]$) known as a graphite modifier or GM [79]. Modification of the HOPG surface with GM, usually carried out by drop casting, gives rise to a homogeneous, self-ordered layer of these molecules with a thickness of less than 1 nm [80, 81]. As is the case with pentylamine modification, GM amino groups make it possible to adsorb individual DNA molecules onto the surface and further study them by AFM [82].

In addition, a number of other organic nanotemplates self-organizing on the graphite surface have recently been used to deposit DNA onto HOPG. Such nanopatterns are formed on crystal surfaces by many alkane derivatives, including stearic acid, dodecylamine, octadecylamine, stearyl alcohol, etc. [83–86]. DNA molecules are typically aligned along nanopattern-forming lamellae upon adsorption onto such surfaces [87, 88]. In this case, the chemical nature of the modifier molecule can significantly affect the conformation and properties of the adsorbed DNA molecule [89, 90].

The described approaches for preparing and using DNA samples can also be applied to non-canonical DNA structures, including G-quadruplexes and i-motifs.

AFM VISUALIZATION OF NON-CANONICAL DNA STRUCTURES

As noted above, the main factor complicating direct visualization of non-canonical DNA structures without using labels is their small size. The guanine tetrad or double Hoogsteen cytosine dimer has a fixed size,

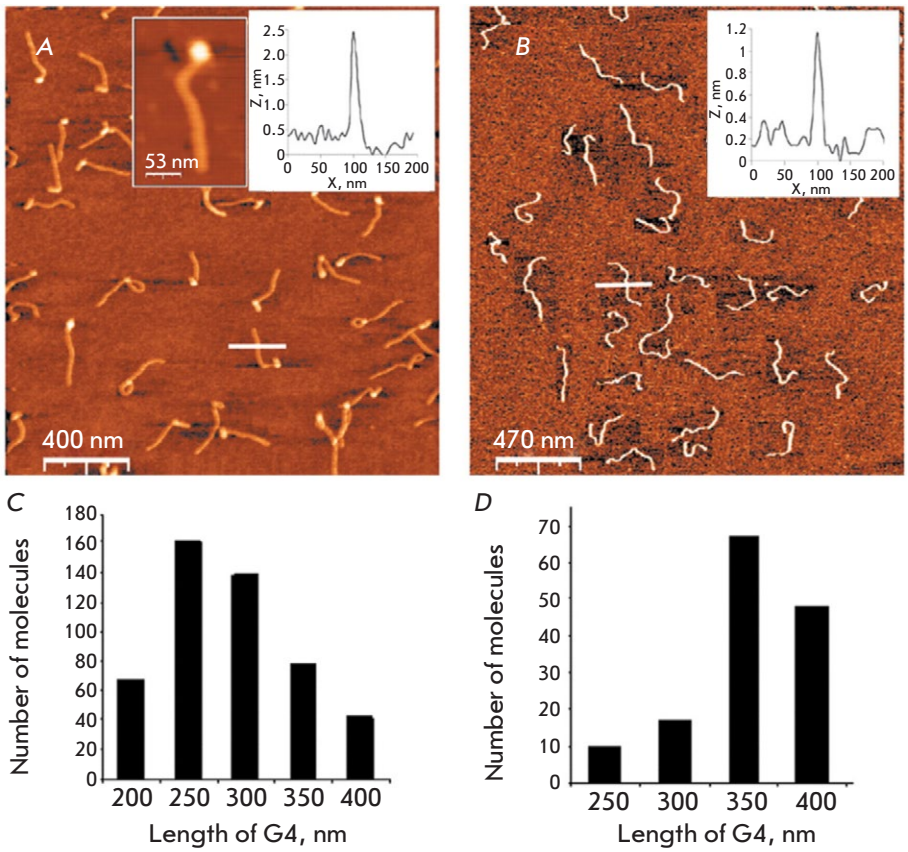

Fig. 6. Comparison of tetra- and monomolecular G-quadruplexes. AFM images of tetramolecular (insert: the zoomed-in tetramolecular complex) (*A*) and monomolecular (*B*) G-quadruplexes. Tetramolecular G-quadruplexes were prepared using a complex of four 1,400 bp long 5′-biotin-poly(dG)-poly(dC) molecules associated with avidin. Monomolecular G-quadruplexes were prepared using a 5,500-base-long G-chain. Molecules of both types were deposited on mica under the same conditions. Statistical analysis of the contour lengths of tetramolecular (*C*) and monomolecular (*D*) G-quadruplexes. Reproduced from [95] under the CC 4.0 license (http://creativecommons.org/licenses/by/4.0/)

and the number of such G-tetrads or double cytosine dimers in the stack can vary quite widely. The longest non-canonical DNA structure is the G-nanowire: it is formed from G-rich (e.g., poly(G)) nucleotide sequences due to spontaneous formation of a long DNA tetraplex and reaches micron lengths. The morphological characteristics of G-nanowires obtained from AFM images, such as diameter, length, and contour shape, make it possible to determine their structure (e.g., the number of DNA molecules involved in the formation of G-wire), persistent length, and can also be used as feedback when developing procedures for synthesizing these structures for biotechnological applications. A G-nanowire can be formed from a large number of oligonucleotides "interlocking" with each other in a tetraplex [91–94] from four parallel guanine sequences (a tetramolecular nanowire) [95], as well as from one long molecule of single-stranded DNA folded four times (a monomolecular nanowire) [96, 97]. In the first case, G-nanowires are characterized by a broad length distribution, whereas, in the other two cases, the distribution is narrow. The diameter of the G-nanowire measured according to its height in AFM images is usually ~ 2 nm [91, 95, 96], which, taking into account the effect of height underestimation caused by the interaction of the cantilever with a soft sample [98], is consistent with the size of 2.8 nm obtained from a X-ray diffraction analysis of the G-tetrad [99]. The examples of AFM images of G-nanowires are shown in *Fig. 6*.

Other nanowires based on non-canonical structures have also been described. Thus, hybrid nanowires consisting of fragments of G-nanowires and i-motifs have been synthesized [100]. AFM revealed

the polymorphism of such structures, which depends on the oligonucleotides used and the ionic environment, in particular, the supramolecular conformation of the hybrids, as well as the V-shaped, circular and linear configuration of the hybrids. Fibrils 0.45–4 nm high and up to 2 μm long were also found to form from two types of oligonucleotides: SQ1A (CAGTAGATGCTGCTGAGGGGGGGTGTGTCTTCAAGCG) and SQ1B (CTCTACGACGACTGGGGGGGACACGAAGTTCGCTACTG), which is attributed to the formation of numerous synapses based on quadruplexes [101].

Thanks to the possibility of feeding an electric potential to the cantilever of an atomic force microscope and measuring the current, the current–voltage curves of individual G-nanowires can be recorded. In particular, it has been shown that the G-nanowire is capable of conducting current from several tens to several hundreds of picoamps [11].

In nature, G- or C-rich nucleotide sequences prone to forming non-canonical structures are usually embedded in longer DNA molecules (e.g., the telomeric regions of chromosomes or near the promoter). In double-stranded DNA, G- and C-rich motifs always reside opposite to each other due to complementarity. Thus, AFM allowed one to visualize the simultaneous formation of a G-quadruplex and an i-motif on double-stranded DNA containing a G-rich VNTR motif: $CGC(GGGGCGGGG)_n$. These structures had a branched shape and were observed only in an acidic medium and in the presence of K^+ ions. The formation of a G-quadruplex and an i-motif in the VNTR sequence can occur during transcription or replication, when double-stranded DNA becomes single-stranded and, thus, affects the expression of the respective gene [102].

To study the formation of non-canonical structures and visualize them, G- and C-rich motifs are often "embedded" in a DNA molecule or a DNA-based nanostructure with a size much larger than that of the non-canonical structure per se. Therefore, it becomes possible to identify individual G-quadruplexes or i-motifs by changing the morphology of the larger DNA structures connected to them.

Thus, a single-stranded DNA region containing two C-tracts was inserted into a double-stranded circular DNA region from opposite sides of the "ring" [103]. The formation of various intra- and intermolecular i-motifs was shown, in particular, using AFM visualization of the architecture of the DNA rings. The mutual arrangement of these rings also made it possible to determine the role of the length of the C-repeats of a single-stranded DNA region in the formation of intra- or intermolecular i-motifs: the presence of two tracts of six or less cytosine bases gave rise to an intermolecular i-motif, while a larger number of repeats of cytosine tracts yielded an intramolecular i-motif.

For performing AFM visualization of the formation of individual non-canonical DNA structures, it was proposed to embed the G- and C-rich sequences of oligonucleotides into a rectangular DNA origami frame. Using high-speed AFM, the formation and dissociation of the G-quadruplex inside such a frame are visualized in real time. Meanwhile, the formation and dissociation of G-quadruplexes was identified according to the changes in the contours of two DNA molecules carrying a G-quadruplex sequence from the parallel to the X-shaped one (during the formation of a G-quadruplex), and vice versa (during its dissociation) [104]. Topologically controlled G-quadruplexes and i-motifs were formed on the basis of the DNA-nanoframe by moving the DNA chain, adding or removing K^+ ions, and using an acidic medium. Dissociation of double-stranded DNA with the formation of a G-quadruplex and an i-motif was visualized by high-speed AFM (*Fig.* 7) [105].

Investigation of individual short G- or C-rich oligonucleotides capable of forming non-canonical DNA structures, as well as their interaction with each other, is of no less fundamental and practical interest. AFM visualization of such sequences allows one to supplement the data obtained using the conventional methods for studying quadruplexes (such as circular dichroism, thermal melting, NMR, etc.) with the morphological parameters of individual structures and their statistical distribution. Nevertheless, AFM studies of non-canonical DNA structures consisting of short oligonucleotides are quite rare.

An AFM study of a synthetic oligonucleotide adsorbed onto a mica surface containing a G-rich CpG motif revealed that there are heterogeneous structures 1–6 nm high which most likely are the G-quadruplexes and their aggregates [106]. AFM visualization of oligonucleotides consisting of 16 telomeric TTAGGG repeats allowed one to infer that most of these oligonucleotides form only two quadruplexes out of the four possible ones, which resemble beads on a string in the AFM images [107]. G-quadruplexes of the oligonucleotides $d(G)_{10}$, $d(TG_9)$, and $d(TG_8T)$ were formed only in a Na^+-containing solution with a long incubation time or in a K^+-containing solution and looked like spherical aggregates 1.5–3 nm high or nanowires (for $d(G)_{10}$) [94].

AFM imaging can also be used to study the interaction between individual non-canonical DNA structures and various ligands. Investigating this interaction would be of great relevance because of the suspected role of G-quadruplexes in many intracellu-

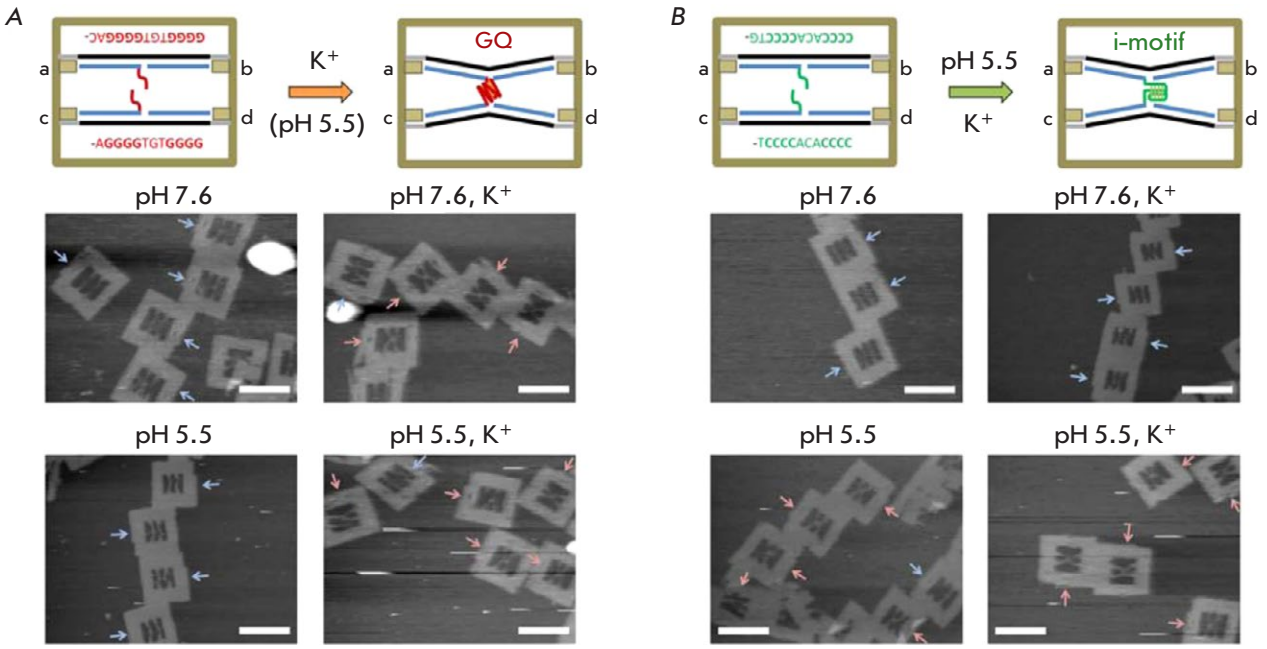

Fig. 7. Observation of the formation of a separate G-quadruplex and i-motif. (*A*) – AFM images of DNA frames containing the G-tracts required for the formation of an interstrand G-quadruplex in the presence of K^+. (*B*) – AFM images of DNA frames containing the C-tracts required for the formation of an interstrand i-motif in an acidic medium. The blue and red arrows show disconnected and connected (X-shaped) threads, respectively. The scale bars are 100 nm. Adapted with permission from [105]. Copyright (2015) American Chemical Society

lar processes, as well as their potential use as targets for antitumor drugs.

For example, when studying the interaction between G-quadruplexes and polyamines, aggregation of G-quadruplexes was visualized: the height of the observed structures increased from 3 to 4–11 nm, depending on the type of polyamine [108]. Another series of AFM experiments showed that the triazole-linked acridine ligand GL15 binding to G-quadruplexes stabilizes and accelerates the formation of quadruplexes in Na^+- and K^+-containing solutions [109]. It was also shown that prolinamide derivatives can selectively bind and stabilize G-quadruplexes. An AFM study showed that the *tris*-prolinamide derivative Pro-4 can drive the formation of structures from G-quadruplexes based on c-MYC [110].

The small number of AFM studies of individual G-quadruplexes formed from oligonucleotides and their associates infers that the size of these structures being close to the resolution limit of AFM in soft objects is the main roadblock in such studies. The spatial resolution of an atomic force microscope depends on a number of factors, including the cantilever tip radius. Therefore, one of the ways to increase the resolution of AFM images is to use super sharp

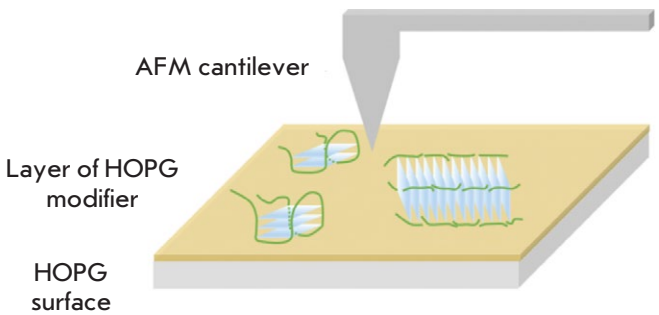

Fig. 8. Schematic representation of the sample surface for AFM studies of the quadruplexes and quadruplex-containing structures on the surface of the GM modified HOPG

cantilevers. Cantilevers with a radius of curvature of down to 1 nm are commercially available today [79, 111]. The nature of the substrate can also limit the resolution of an atomic force microscope: for example, the formation of a salt film on the mica surface can reduce the height of the adsorbed DNA structures in AFM images, thus worsening the contrast and reducing the spatial resolution.

The use of ultrasharp cantilevers and the GM-modified HOPG's surface as a substrate often allows

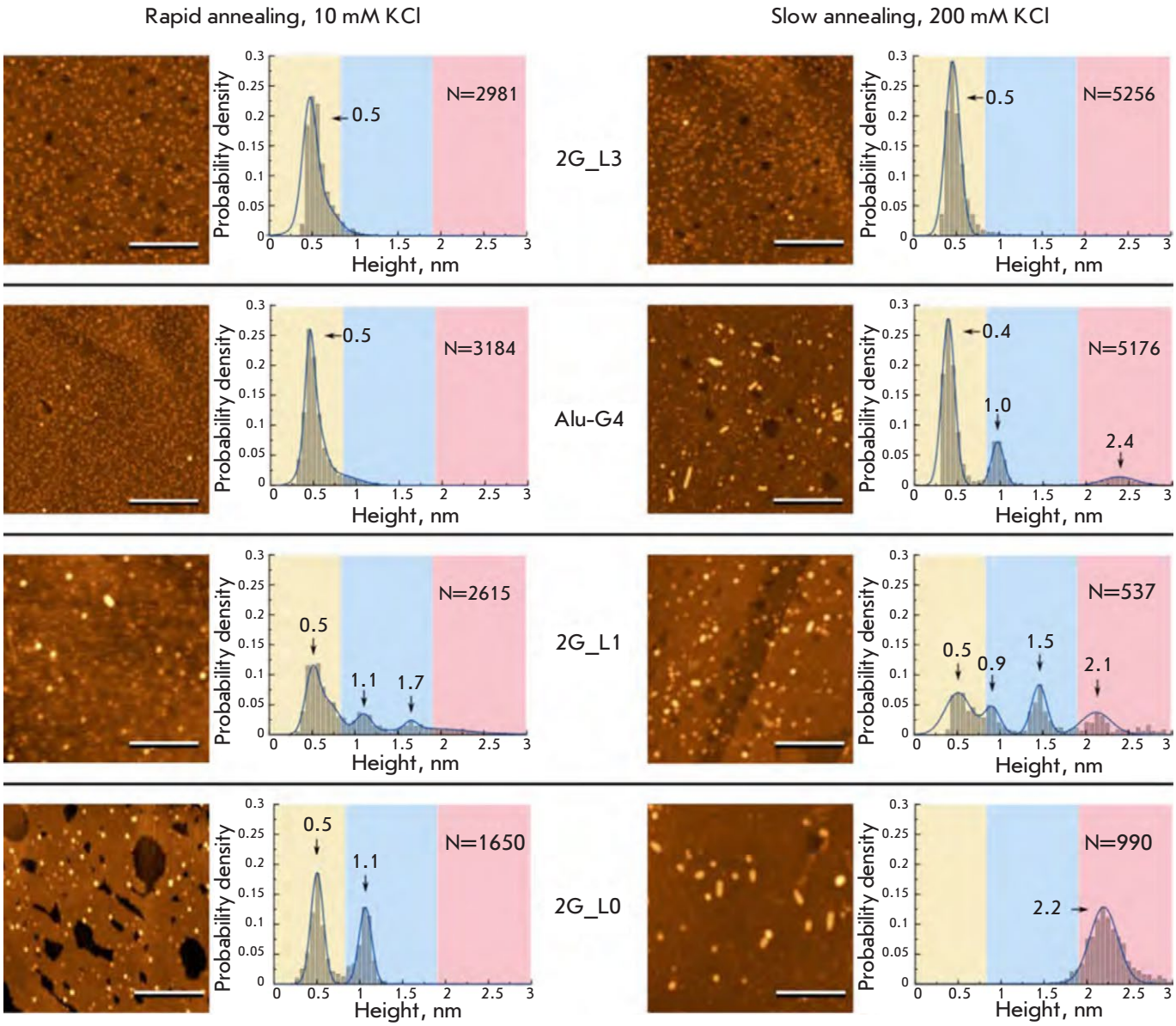

Fig. 9. AFM images and corresponding histograms of the height distribution of two tetrad G-quadruplexes formed after rapid annealing in the presence of 10 mM KCl (left-hand side) and slow annealing in the presence of 200 mM KCl (right-hand side). The scale bar is 100 nm. Reproduced from [112] under the CC 4.0 license (http://creativecommons.org/licenses/by/4.0/)

one to improve the quality of a structural analysis of biomolecules using AFM [79, 80]. This approach, illustrated in *Fig. 8*, has been applied in several studies of non-canonical DNA structures. The polymorphism of quadruplexes formed under different conditions from G-rich oligonucleotides with different lengths of the G-tracts and loops between them was analyzed by AFM [112]. An analysis of the morphology and histograms of the heights distribution of the visualized structures allowed one to distinguish from one to four types of the quadruplexes formed by each of the oligonucleotides and identify the patterns of formation of molecular associates (multimers of G-quadruplexes) from intramolecular G-quadruplexes (*Fig. 9*).

It has been shown using model oligonucleotides (fragments of the human genome containing a G/C-rich region in the middle) using AFM that synaptic contacts between DNA molecules emerge due to the formation of intermolecular G-quadruplexes or i-motifs [113]. The emergence of intermolecular

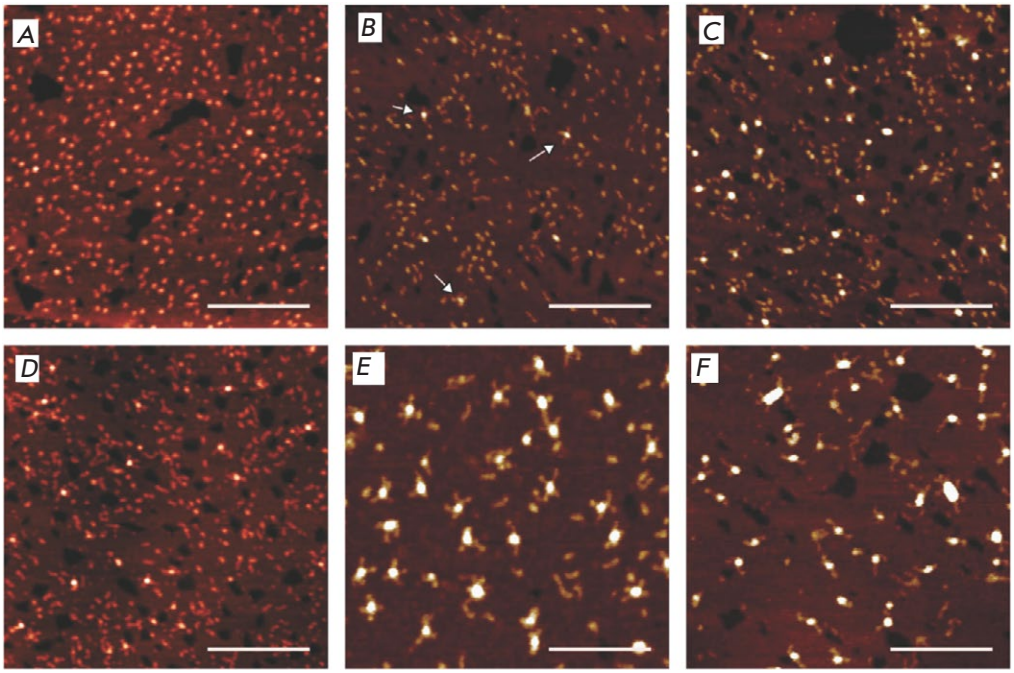

Fig. 10. AFM images of the nanostructures based on i-motifs formed by the following oligonucleotide sequences at pH 5.5: C_2T_{25} (*A*); C_5T_{25} (*B*); C_7T_{25} (*C*); C_9T_{25} (*D*); $C_{12}T_{25}$ (*E*); and $C_{25}T_{25}$ (*F*). The scale bar is 100 nm. Reproduced from [114] under the CC BY-NC 3.0 license (https://creativecommons.org/licenses/by-nc/3.0/)

i-motifs explains the structures formed by single-stranded C_nT_{25} oligonucleotides (n = 2, 5, 7, 9, 12, 25) at pH 5.5 and visualized by AFM (*Fig. 10*) [114]. Such structures consist of the i-motif "core" and the "arms" emerging from it. These structures may be of interest in bioengineering for synthesizing DNA-based molecular architectures.

CONCLUSIONS

The main methods currently used to visualize non-canonical DNA structures include fluorescence microscopy, TEM and AFM. Fluorescence microscopy allows one to visualize G-quadruplexes, including those in living cells, while visualization is carried out thanks to fluorescent label binding to the DNA-quadruplex. Therefore, much attention is paid to the development of fluorophores with high selectivity to G-quadruplexes and good optical properties. Among the types of fluorescence microscopy used to visualize quadruplexes, fluorescence lifetime imaging microscopy and immunofluorescence microscopy are worth noting. Anti-G-quadruplexes antibodies enhanced by secondary antibodies with fluorescent labels attached are used in the latter case. Over the past few years, fluorescence microscopy has provided a large amount of data proving that G-quadruplexes exist in living cells, with DNA quadruplexes localized mainly in the nucleolus; and RNA quadruplexes, in the cytoplasm.

Unlike fluorescence microscopy, TEM and AFM can help visualize non-canonical DNA structures without using labels. Both methods are characterized by a comparable lateral resolution, while AFM, unlike TEM, has a high height resolution. A number of structures based on non-canonical structures, such as G-loops, R-loops, and G-nanowires, have been visualized by TEM and AFM. Special approaches employing DNA origami nanoframes, in which oligonucleotides capable of forming noncanonical DNA structures are embedded, have been developed for real-time AFM visualization of the formation and dissociation of individual quadruplexes and i-motifs. These studies have allowed us to understand better the influence of conditions, such as the composition and concentration of ions, pH, the distance between interacting DNA fragments, etc., on the formation of G-quadruplexes or i-motifs. AFM and TEM visualization of individual non-canonical DNA structures and their smaller derivatives is the most challenging problem from the methodological standpoint, since the size of such structures is close to the resolution of these methods. AFM resolution for studying non-canonical DNA structures can be further increased by using special substrates (e.g., modified graphite) and ultrasharp AFM cantilevers. This approach has helped visualize the polymorphism of G-quadruplex structures and also detect the emergence of synaptic contacts between oligonucleotides thanks to the formation of intermolecular non-canonical DNA structures. ●

This work is supported by the Russian Science Foundation (project No. 22-23-00395).

REFERENCES

1. Gellert M., Lipsett M.N., Davies D.R. // Proc. Natl. Acad. Sci. USA. 1962. V. 48. № 12. P. 2013–2018.
2. Gehring K., Leroy J.-L., Guéron M. // Nature. 1993. V. 363. № 6429. P. 561–565.
3. Hänsel-Hertsch R., Di Antonio M., Balasubramanian S. // Nat. Rev. Mol. Cell Biol. 2017. V. 18. № 5. P. 279–284.
4. Abou Assi H., Garavís M., González C., Damha M.J. // Nucl. Acids Res. 2018. V. 46. № 16. P. 8038–8056.
5. Brown S.L., Kendrick S. // Pharmaceuticals. 2021. V. 14. № 2. P. 96.
6. Varshney D., Spiegel J., Zyner K., Tannahill D., Balasubramanian S. // Nat. Rev. Mol. Cell Biol. 2020. V. 21. № 8. P. 459–474.
7. Drygin D., Siddiqui-Jain A., O'Brien S., Schwaebe M., Lin A., Bliesath J., Ho C.B., Proffitt C., Trent K., Whitten J.P., et al. // Cancer Res. 2009. V. 69. № 19. P. 7653–7661.
8. Ohnmacht S.A., Marchetti C., Gunaratnam M., Besser R.J., Haider S.M., Di Vita G., Lowe H.L., Mellinas-Gomez M., Diocou S., Robson M., et al. // Sci. Rep. 2015. V. 5. № 1. P. 11385.
9. Shu B., Cao J., Kuang G., Qiu J., Zhang M., Zhang Y., Wang M., Li X., Kang S., Ou T.-M., et al. // Chem. Commun. 2018. V. 54. № 16. P. 2036–2039.
10. Kuang G., Zhang M., Kang S., Hu D., Li X., Wei Z., Gong X., An L.-K., Huang Z.-S., Shu B., et al. // J. Med. Chem. 2020. V. 63. № 17. P. 9136–9153.
11. Livshits G.I., Stern A., Rotem D., Borovok N., Eidelshtein G., Migliore A., Penzo E., Wind S.J., Di Felice R., Skourtis S.S., et al. // Nat. Nanotechnol. 2014. V. 9. № 12. P. 1040–1046.
12. Xu J., Yan C., Wang X., Yao B., Lu J., Liu G., Chen W. // Anal. Chem. 2019. V. 91. № 15. P. 9747–9753.
13. Li C., Chen H., Chen Q., Shi H., Yang X., Wang K., Liu J. // Anal. Chem. 2020. V. 92. № 14. P. 10169–10176.
14. Alberti P., Mergny J.-L. // Proc. Natl. Acad. Sci. USA. 2003. V. 100. № 4. P. 1569–1573.
15. Yang T., Peng S., Zeng R., Xu Q., Zheng X., Wang D., Zhou X., Shao Y. // Spectrochim. Acta. A. Mol. Biomol. Spectrosc. 2022. V. 270. P. 120845.
16. Huang J., Ying L., Yang X., Yang Y., Quan K., Wang H., Xie N., Ou M., Zhou Q., Wang K. // Anal. Chem. 2015. V. 87. № 17. P. 8724–8731.
17. Burge S., Parkinson G.N., Hazel P., Todd A.K., Neidle S. // Nucl. Acids Res. 2006. V. 34. № 19. P. 5402–5415.
18. Karsisiotis A.I., Hessari N.M., Novellino E., Spada G.P., Randazzo A., Webba da Silva M. // Angew. Chem. Int. Ed. 2011. V. 50. № 45. P. 10645–10648.
19. Binnig G., Quate C., Gerber C. // Phys. Rev. Lett. 1986. V. 56. № 9. P. 930–933.
20. Mirsaidov U.M., Zheng H., Casana Y., Matsudaira P. // Biophys. J. 2012. V. 102. № 4. P. L15–L17.
21. Transmission Electron Microscopy: Diffraction, Imaging, and Spectrometry / Eds Carter B., Williams D.B. Cham: Springer International Publ., 2016.
22. Alessandrini A., Facci P. // Meas. Sci. Technol. 2005. V. 16. № 6. P. R65–R92.
23. Lyubchenko Y.L. // J. Phys. Appl. Phys. 2018. V. 51. № 40. P. 403001.
24. Largy E., Granzhan A., Hamon F., Verga D., Teulade-Fichou M.-P. // Quadruplex Nucleic Acids / Eds Chaires J.B., Graves D. Berlin: Heidelberg Springer, 2013. P. 111–177.
25. Chang C.-C., Kuo I.-C., Ling I.-F., Chen C.-T., Chen H.-C., Lou P.-J., Lin J.-J., Chang T.-C. // Anal. Chem. 2004. V. 76. № 15. P. 4490–4494.
26. Chan Y.-C., Chen J.-W., Su S.-Y., Chang C.-C. // Biosens. Bioelectron. 2013. V. 47. P. 566–573.
27. Lubitz I., Zikich D., Kotlyar A. // Biochemistry. 2010. V. 49. № 17. P. 3567–3574.
28. Xu L., Shen X., Hong S., Wang J., Zhou L., Chen X., Pei R. // Asian J. Org. Chem. 2015. V. 4. № 12. P. 1375–1378.
29. Nygren J., Svanvik N., Kubista M. // Biopolymers. 1998. V. 46. № 1. P. 39–51.
30. Lee L.G., Chen C.-H., Chiu L.A. // Cytometry. 1986. V. 7. № 6. P. 508–517.
31. Mohanty J., Barooah N., Dhamodharan V., Harikrishna S., Pradeepkumar P.I., Bhasikuttan A.C. // J. Am. Chem. Soc. 2013. V. 135. № 1. P. 367–376.
32. Hanczyc P., Rajchel-Mieldzioć P., Feng B., Fita P. // J. Phys. Chem. Lett. 2021. V. 12. № 22. P. 5436–5442.
33. Barooah N., Mohanty J., Bhasikuttan A.C. // J. Indian Chem. Soc. 2021. V. 98. № 6. P. 100078.
34. Turaev A.V., Tsvetkov V.B., Tankevich M.V., Smirnov I.P., Aralov A.V., Pozmogova G.E., Varizhuk A.M. // Biochimie. 2019. V. 162. P. 216–228.
35. Yu K.-K., Li K., He H.-Z., Liu Y.-H., Bao J.-K., Yu X.-Q. // Sens. Actuators B Chem. 2020. V. 321. P. 128479.
36. Yan J., Tian Y., Tan J., Huang Z. // Analyst. 2015. V. 140. № 21. P. 7146–7149.
37. Platella C., Gaglione R., Napolitano E., Arciello A., Pirota V., Doria F., Musumeci D., Montesarchio D. // Int. J. Mol. Sci. 2021. V. 22. № 19. P. 10624.
38. Ma D.-L., Zhang Z., Wang M., Lu L., Zhong H.-J., Leung C.-H. // Chem. Biol. 2015. V. 22. № 7. P. 812–828.
39. Tseng T.-Y., Chien C.-H., Chu J.-F., Huang W.-C., Lin M.-Y., Chang C.-C., Chang T.-C. // J. Biomed. Opt. 2013. V. 18. № 10. P. 101309.
40. Shivalingam A., Izquierdo M.A., Marois A.L., Vyšniauskas A., Suhling K., Kuimova M.K., Vilar R. // Nat. Commun. 2015. V. 6. P. 8178.
41. Summers P.A., Lewis B.W., Gonzalez-Garcia J., Porreca R.M., Lim A.H.M., Cadinu P., Martin-Pintado N., Mann D.J., Edel J.B., Vannier J.B., et al. // Nat. Commun. 2021. V. 12. № 1. P. 162.
42. Zhang S., Sun H., Chen H., Li Q., Guan A., Wang L., Shi Y., Xu S., Liu M., Tang Y. // Biochim. Biophys. Acta – Gen. Subj. 2018. V. 1862. № 5. P. 1101–1106.
43. Yang S.Y., Amor S., Laguerre A., Wong J.M.Y., Monchaud D. // Biochim. Biophys. Acta BBA – Gen. Subj. 2017. V. 1861. № 5. Part B. P. 1312–1320.
44. Lu Y.-J., Hu D.-P., Zhang K., Wong W.-L., Chow C.-F. // Biosens. Bioelectron. 2016. V. 81. P. 373–381.
45. Kang Y., Wei C. // Chem. Biodivers. 2022. V. 19. № 3. e202101030.
46. Guo X., Chen H., Liu Y., Yang D., Li Q., Du H., Liu M., Tang Y., Sun H. // J. Mater. Chem. B. 2022. V. 10. № 3. P. 430–437.
47. Liu L.-Y., Liu W., Wang K.-N., Zhu B.-C., Xia X.-Y., Ji L.-N., Mao Z.-W. // Angew. Chem. 2020. V. 132. № 24. P. 9806–9813.
48. Laguerre A., Hukezalie K., Winckler P., Katranji F., Chanteloup G., Pirrotta M., Perrier-Cornet J.-M., Wong J.M.Y., Monchaud D. // J. Am. Chem. Soc. 2015. V. 137. № 26. P. 8521–8525.
49. Huang W.-C., Tseng T.-Y., Chen Y.-T., Chang C.-C., Wang Z.-F., Wang C.-L., Hsu T.-N., Li P.-T., Chen C.-T., Lin J.-J., et al. // Nucl. Acids Res. 2015. V. 43. № 21. P. 10102–10113.

50. Biffi G., Di Antonio M., Tannahill D., Balasubramanian S. // Nat. Chem. 2014. V. 6. № 1. P. 75–80.
51. Biffi G., Tannahill D., Miller J., Howat W.J., Balasubramanian S. // PLoS One. 2014. V. 9. № 7. P. e102711.
52. Henderson A., Wu Y., Huang Y.C., Chavez E.A., Platt J., Johnson F.B., Brosh R.M., Sen D., Lansdorp P.M. // Nucl. Acids Res. 2014. V. 42. № 2. P. 860–869.
53. Biffi G., Tannahill D., McCafferty J., Balasubramanian S. // Nat. Chem. 2013. V. 5. № 3. P. 182–186.
54. Zyner K.G., Simeone A., Flynn S.M., Doyle C., Marsico G., Adhikari S., Portella G., Tannahill D., Balasubramanian S. // Nat. Commun. 2022. V. 13. № 1. P. 142.
55. Tang W., Niu K., Yu G., Jin Y., Zhang X., Peng Y., Chen S., Deng H., Li S., Wang J., et al. // Epigenetics Chromatin. 2020. V. 13. № 1. P. 12.
56. Duquette M.L., Handa P., Vincent J.A., Taylor A.F., Maizels N. // Genes Dev. 2004. V. 18. № 13. P. 1618–1629.
57. Reddy K., Schmidt M.H.M., Geist J.M., Thakkar N.P., Panigrahi G.B., Wang Y.-H., Pearson C.E. // Nucl. Acids Res. 2014. V. 42. № 16. P. 10473–10487.
58. Hammondkosack M., Dobrinski B., Lurz R., Docherty K., Kilpatrick M. // Nucl. Acids Res. 1992. V. 20. № 2. P. 231–236.
59. Yatsunyk L.A., Piétrement O., Albrecht D., Tran P.L.T., Renčiuk D., Sugiyama H., Arbona J.-M., Aimé J.-P., Mergny J.-L. // ACS Nano. 2013. V. 7. № 7. P. 5701–5710.
60. Randall A., Griffith J.D. // J. Biol. Chem. 2009. V. 284. № 21. P. 13980–13986.
61. Artusi S., Perrone R., Lago S., Raffa P., Di Iorio E., Palù G., Richter S.N. // Nucl. Acids Res. 2016. V. 44. № 21. P. 10343–10353.
62. Scotuzzi M., Kuipers J., Wensveen D.I., Boer P. de, Hagen K. C. W., Hoogenboom J.P., Giepmans B.N.G. // Sci. Rep. 2017. V. 7. P. 45970.
63. Zhong Q., Inniss D., Kjoller K., Elings V. // Surf. Sci. 1993. V. 290. № 1–2. P. L688–L692.
64. Xu K., Sun W., Shao Y., Wei F., Zhang X., Wang W., Li P. // Nanotechnol. Rev. 2018. V. 7. № 6. P. 605–621.
65. Vesenka J., Guthold M., Tang C., Keller D., Delaine E., Bustamante C. // Ultramicroscopy. 1992. V. 42. P. 1243–1249.
66. Bustamante C., Vesenka J., Tang C., Rees W., Guthold M., Keller R. // Biochemistry. 1992. V. 31. № 1. P. 22–26.
67. Lyubchenko Y.L., Shlyakhtenko L.S. // Methods. 2009. V. 47. № 3. P. 206–213.
68. Rivetti C., Guthold M., Bustamante C. // J. Mol. Biol. 1996. V. 264. № 5. P. 919–932.
69. Vanderlinden W., De Feyter S. // Nanoscale. 2013. V. 5. № 6. P. 2264–2268.
70. Bustamante C., Guthold M., Zhu X.S., Yang G.L. // J. Biol. Chem. 1999. V. 274. № 24. P. 16665–16668.
71. Suzuki Y., Higuchi Y., Hizume K., Yokokawa M., Yoshimura S.H., Yoshikawa K., Takeyasu K. // Ultramicroscopy. 2010. V. 110. № 6. P. 682–688.
72. Valle F., Favre M., De Los Rios P., Rosa A., Dietler G. // Phys. Rev. Lett. 2005. V. 95. № 15. P. 158105.
73. Christenson H.K., Thomson N.H. // Surf. Sci. Rep. 2016. V. 71. № 2. P. 367–390.
74. Sorel I., Piétrement O., Hamon L., Baconnais S., Le Cam E., Pastré D. // Biochemistry. 2006. V. 45. № 49. P. 14675–14682.
75. Brett A.M.O., Chiorcea A.M. // Langmuir. 2003. V. 19. № 9. P. 3830–3839.
76. Jiang X.H., Lin X.Q. // Electrochem. Commun. 2004. V. 6. № 9. P. 873–879.
77. Klinov D.V., Dubrovin E.V., Yaminsky I.V. // Phys. Low-Dimens. Struct. 2003. V. 3–4. P. 119–124.
78. Klinov D.V., Dubrovin E.V., Yaminsky I.V. // AIP Conf. Proc. 2003 V. 696. P. 452–456.
79. Klinov D., Dwir B., Kapon E., Borovok N., Molotsky T., Kotlyar A. // Nanotechnology. 2007. V. 18. № 22. P. 225102.
80. Klinov D.V., Protopopova A.D., Andrianov D.S., Litvinov R.I., Weisel J.W. // Colloids Surf. B Biointerfaces. 2020. V. 196. P. 111321.
81. Barinov N.A., Tolstova A.P., Bersenev E.A., Ivanov D.A., Dubrovin E.V., Klinov D.V. // Colloids Surf. B Biointerfaces. 2021. V. 206. P. 111921.
82. Dubrovin E.V., Klinov D.V. // Polym. Sci. Ser. A. 2021. V. 63. № 6. P. 601–622.
83. Rabe J., Buchholz S. // Science. 1991. V. 253. № 5018. P. 424–427.
84. Cincotti S., Rabe J.P. // Appl. Phys. Lett. 1993. V. 62. № 26. P. 3531–3533.
85. van Hameren R., Schön P., van Buul A.M., Hoogboom J., Lazarenko S.V., Gerritsen J.W., Engelkamp H., Christianen P.C.M., Heus H.A., Maan J.C., et al. // Science. 2006. V. 314. № 5804. P. 1433–1436.
86. De Feyter S., De Schryver F.C. // J. Phys. Chem. B. 2005. V. 109. № 10. P. 4290–4302.
87. Adamcik J., Tobenas S., Di Santo G., Klinov D., Dietler G. // Langmuir. 2009. V. 25. № 5. P. 3159–3162.
88. Dubrovin E.V., Gerritsen J.W., Zivkovic J., Yaminsky I.V., Speller S. // Colloids Surf. B Biointerfaces. 2010. V. 76. № 1. P. 63–69.
89. Dubrovin E.V., Speller S., Yaminsky I.V. // Langmuir. 2014. V. 30. № 51. P. 15423–15432.
90. Dubrovin E.V., Schächtele M., Schäffer T.E. // RSC Adv. 2016. V. 6. № 83. P. 79584–79592.
91. Vesenka J., Marsh T., Miller R., Henderson E. // J. Vac. Sci. Technol. B. 1996. V. 14. № 2. P. 1413–1417.
92. Karimata H., Miyoshi D., Fujimoto T., Koumoto K., Wang Z.-M., Sugimoto N. // Nucl. Acids Symp. Ser. 2007. № 51. P. 251–252.
93. Ma'ani Hessari N., Spindler L., Troha T., Lam W.-C., Drevenšek-Olenik I., Webba da Silva M. // Chem. – Eur. J. 2014. V. 20. № 13. P. 3626–3630.
94. Chiorcea-Paquim A.-M., Santos P.V., Eritja R., Oliveira-Brett A.M. // Phys. Chem. Chem. Phys. PCCP. 2013. V. 15. № 23. P. 9117–9124.
95. Borovok N., Iram N., Zikich D., Ghabboun J., Livshits G.I., Porath D., Kotlyar A.B. // Nucl. Acids Res. 2008. V. 36. № 15. P. 5050–5060.
96. Kotlyar A.B., Borovok N., Molotsky T., Cohen H., Shapir E., Porath D. // Adv. Mater. 2005. V. 17. № 15. P. 1901–1905.
97. Borovok N., Molotsky T., Ghabboun J., Porath D., Kotlyar A. // Anal. Biochem. 2008. V. 374. № 1. P. 71–78.
98. Jiao Y., Schäffer T.E. // Langmuir. 2004. V. 20. № 23. P. 10038–10045.
99. Phillips K., Dauter Z., Murchie A.I.H., Lilley D.M.J., Luisi B. // J. Mol. Biol. 1997. V. 273. № 1. P. 171–182.
100. Cao Y., Gao S., Yan Y., Bruist M.F., Wang B., Guo X. // Nucl. Acids Res. 2017. V. 45. № 1. P. 26–38.
101. Mendez M.A., Szalai V.A. // Nanoscale Res. Lett. 2013. V. 8. № 1. P. 210.
102. Li Y., Syed J., Suzuki Y., Asamitsu S., Shioda N., Wada T., Sugiyama H. // ChemBioChem. 2016. V. 17. № 10. P. 928–935.
103. Li T., Famulok M. // J. Am. Chem. Soc. 2013. V. 135. № 4. P. 1593–1599.
104. Sannohe Y., Endo M., Katsuda Y., Hidaka K., Sug-

iyama H. // J. Am. Chem. Soc. 2010. V. 132. № 46. P. 16311–16313.
105. Endo M., Xing X., Zhou X., Emura T., Hidaka K., Tuesuwan B., Sugiyama H. // ACS Nano. 2015. V. 9. № 10. P. 9922–9929.
106. Costa L.T., Kerkmann M., Hartmann G., Endres S., Bisch P.M., Heckl W.M., Thalhammer S. // Biochem. Biophys. Res. Commun. 2004. V. 313. № 4. P. 1065–1072.
107. Wang H., Nora G.J., Ghodke H., Opresko P.L. // J. Biol. Chem. 2011. V. 286. № 9. P. 7479–7489.
108. Wen L.-N., Xie M.-X. // Biochimie. 2013. V. 95. № 6. P. 1185–1195.
109. Chiorcea-Paquim A.-M., Rodrigues Pontinha A.D., Eritja R., Lucarelli G., Sparapani S., Neidle S., Oliveira-Breet A.M. // Anal. Chem. 2015. V. 87. № 12. P. 6141–6149.
110. Chauhan A., Paladhi S., Debnath M., Dash J. // Org. Biomol. Chem. 2016. V. 14. № 24. P. 5761–5767.
111. Obraztsova E.A., Basmanov D.V., Barinov N.A., Klinov D.V. // Ultramicroscopy. 2019. V. 197. P. 11–15.
112. Varizhuk A.M., Protopopova A.D., Tsvetkov V.B., Barinov N.A., Podgorsky V.V., Tankevich M.V., Vlasenok M.A., Severov V.V., Smirnov I.P., Dubrovin E.V., et al. // Nucl. Acids Res. 2018. V. 46. № 17. P. 8978–8992.
113. Severov V.V., Tsvetkov V.B., Barinov N.A., Babenko V.V., Klinov D.V., Pozmogova G.E. // Polymers. 2022. V. 14(10). P. 2118.
114. Protopopova A.D., Tsvetkov V.B., Varizhuk A.M., Barinov N.A., Podgorsky V.V., Klinov D.V., Pozmogova G.E. // Phys. Chem. Chem. Phys. 2018. V. 20. № 5. P. 3543–3553.

The Role of a Pathological Interaction between β-amyloid and Mitochondria in the Occurrence and Development of Alzheimer's Disease

N. S. Nikolaeva*, E. Yu. Yandulova, Yu. R. Aleksandrova, A. S. Starikov, M. E. Neganova*
Federal State Budgetary Institution of Science Institute of Physiologically Active Compounds of the Russian Academy of Sciences, Chernogolovka, 142432 Russia
*E-mail: nikolaevans@bk.ru; neganova83@mail.ru
Received April 27, 2022; in final form, July 05, 2022
DOI: 10.32607/actanaturae.11723

ABSTRACT **Alzheimer's disease (AD) is one of the most common neurodegenerative diseases in existence. It is characterized by an impaired cognitive function that is due to a progressive loss of neurons in the brain. Extracellular β-amyloid (Aβ) plaques are the main pathological features of the disease. In addition to abnormal protein aggregation, increased mitochondrial fragmentation, altered expression of the genes involved in mitochondrial biogenesis, disruptions in the ER–mitochondria interaction, and mitophagy are observed. Reactive oxygen species are known to affect Aβ expression and aggregation. In turn, oligomeric and aggregated Aβ cause mitochondrial disorders. In this review, we summarize available knowledge about the pathological effects of Aβ on mitochondria and the potential molecular targets associated with proteinopathy and mitochondrial dysfunction for the pharmacological treatment of Alzheimer's disease.**
KEYWORDS **Alzheimer's disease, beta-amyloid, mitochondria, MAM, mitophagy.**
ABBREVIATIONS **AD – Alzheimer's disease; Aβ – beta-amyloid peptide; APP – beta-amyloid precursor protein; MAM – mitochondria-associated endoplasmic reticulum membrane; ER – endoplasmic reticulum; TOM – translocase of the outer membrane; TIM – translocase of the inner membrane; BACE1 – β-secretase 1; NEP – neprilysin, neutral endopeptidase; IDE – insulin-degrading enzyme; PreP – presequence protease (or pitrilysin metallopeptidase 1 (PITRM1)); ECE – endothelin-converting enzyme; ABAD – amyloid beta peptide-binding alcohol dehydrogenase, VDAC – voltage-dependent anion channel; PGC1α – peroxisome proliferator-activated receptor-γ coactivator 1-α; PINK1 – PTEN-induced kinase 1; GSK3β – glycogen synthase kinase-3β; Fis1 – mitochondrial fission protein 1; Drp1 – dynamin-related protein 1; OPA1 – optic atrophy type1; SOD – superoxide dismutase; GPx – glutathione peroxidase; CAT – catalase; GSH – glutathione; OS – oxidative stress; BBB – brain–blood barrier; LP – lipid peroxydation.**

INTRODUCTION

Neurodegenerative diseases are disorders characterized by the progressive death of the neurons associated with the deposition of proteins, with altered physicochemical properties and severe cognitive impairment. It is estimated that the number of people with dementia will increase to 131.5 million worldwide by 2050 [1]. Alzheimer's disease (AD) is the most common form of neurodegenerative diseases; it develops mainly in people over 65 years of age [2]. The key pathomorphological features of AD include deposition and accumulation of abnormally folded β-amyloid (Aβ) peptide and truncated/hyperphosphorylated tau proteins [3, 4]. The cause behind AD development remains controversial and not completely understood. Various hypotheses of AD pathogenesis have been proposed, the most common of which are the hypotheses of the amyloid [5, 6] and mitochondrial cascades [7]. The cholinergic [8] and tau [9] hypotheses, the theory of oxidative stress (OS) [10, 11], hypotheses of calcium homeostasis [12] and neuroinflammation [13], the neurovascular hypothesis [14], hypotheses based on metals with a variable oxidation state [15] and viral origin [16] were also proposed. To date,

there is no drug that can prevent AD from developing. Four drugs are used in clinical practice: three cholinesterase inhibitors (galantamine, rivastigmine, and donepezil) and memantine (a non-competitive NMDA receptor antagonist). However, these drugs have symptomatic effects only. Therefore, an intensive search for new potential drugs based on the data postulated in modern hypotheses of AD pathogenesis is currently under way.

There are sporadic (found in most cases) and familial (inherited in an autosomal dominant manner; has an early onset) forms of AD. The familial AD results from mutations in the genes encoding the β-amyloid precursor protein (*APP*; located on the chromosome 21) [17], presenilin 1 (*PSEN1*, located on the chromosome 14) [18], and presenilin 2 (*PSEN2*, located on the chromosome 1) [19]. The presence of one or more mutations in these genes leads to impaired APP cleavage, resulting in an increased ratio of $A\beta_{1-42}/A\beta_{1-40}$ peptides [20, 21], which, in turn, causes deposition of fibrillar Aβ and an early onset of the disease [22, 23]. The sporadic AD, which has a late onset, is a multifactorial pathological condition resulting from allelic variation in apolipoprotein E (*APOE*), vascular pathologies, immune system defects, mitochondrial dysfunction, and dyshomeostasis of metals with a variable oxidation state [24].

One of the important pathogenic mechanisms of AD is the malfunction of the main energy-generating organelle of the cell: the mitochondrion. Mitochondria are two-membrane organelles that undergo fission and fusion cycles, leading to changes in the organelle dynamics, morphology, and functions [25]. Mitochondrial dysfunction plays an important role in the pathology of neurodegenerative diseases [26–28]. The mitochondrial fission/fusion balance, their biogenesis, ubiquitin–proteasome pathways, as well as mitophagy and autophagy signaling proteins, determine the physiological state of newly formed mitochondria. Aβ and the hyperphosphorylated tau protein are involved in the oxidative damage inflicted on mitochondrial membranes and mtDNA, which ultimately leads to an imbalance in mitochondrial dynamics [29]. Aβ-induced OS alters mitochondrial fusion/fission, worsening the state of organelles and increasing the level of reactive oxygen species (ROS), molecular markers of OS. This, in turn, leads to the accumulation of pathological Aβ. The main routes through which Aβ enters mitochondria are the mitochondria-associated endoplasmic reticulum membrane (MAM) and the complex of outer and inner membrane translocases (TOM–TIM) [30, 31].

In our review, the main pathways of mitochondria–Aβ interaction are associated with the Aβ intake, excretion, and effect on the various mitochondrial functions. These pathways can serve as potential targets for neuroprotective drugs that can prevent both Aβ deposition and mitochondrial dysfunction, as well as delay AD progression.

PATHWAYS OF Aβ FORMATION FROM THE AMYLOID PRECURSOR PROTEIN

The Aβ peptide forms through sequential cleavage of APP by α-/β- and γ-secretases [32]. APP is a type I membrane protein (110–130 kDa) containing a large extracellular glycosylated N-terminal domain and a shorter cytoplasmic C-terminal region located towards the intracellular space. APP is synthesized in the ER and then transported to the Golgi complex, where it completes its maturation. Its mature form is then transported to the plasma membrane [33]. There are two pathways of APP cleavage: non-amyloidogenic, which prevents Aβ deposition, and amyloidogenic, which results in Aβ formation (*Fig. 1*).

In the non-amyloidogenic pathway, the first cleavage of APP is catalyzed by α-secretase, the enzyme

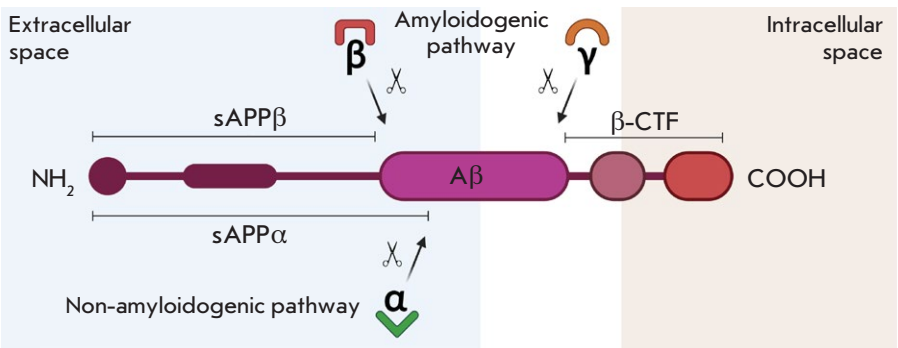

Fig. 1. Simplified representation of the APP structure and cleavage. APP undergoes sequential proteolysis by β-secretase (β), α-secretase (α), and γ-secretase (γ) to release Aβ from the neuronal plasma membrane. sAPPα – soluble alpha fragment of APP; sAPPβ – soluble beta fragment of APP; a CTF-β fragment (C99, membrane-associated)

that belongs to the disintegrin family, and ADAM metalloproteases (Disintegrin and the metalloproteinase domain-containing protein; ADAM10 [EC 3.4.24.81] and ADAM17 [EC 3.4.24.86] in neurons). The plasma membrane and the *trans*-Golgi network are considered to be the main sites of APP cleavage by α-secretase [34]. The α-secretase enzyme cleaves APP in the Aβ sequence between the amino acids 16 and 17 to form a small membrane-anchored 83-amino-acid C-terminal fragment of APP (α-CTF, C83) and soluble APP-α (sAPPα) [35]. sAPPα is known for its numerous neuroprotective functions; in particular, it counteracts the toxic effects of Aβ [36, 37]. Next, α-CTF is cleaved by γ-secretase to generate the hydrophobic P3 peptide (3 kDa) and intracellular domain of the amyloid precursor protein (AICD) [38]. The functional γ-secretase complex includes the following proteins: either presenilin 1 (PS-1) or presenilin 2 (PS-2), which belong to the catalytic domain; nicastrin, which serves as a substrate receptor [39]; presenilin-enhancer-1 (Pen-1, or aph-1; anterior pharynx-defective 1) and presenilin-enhancer-2 (Pen-2) [40]. Aph-1 and Pen-2 act similar to the transmembrane aspartate protease, playing an important role in the $A\beta_{1-40}/A\beta_{1-42}$ ratio [41].

The amyloidogenic pathway begins with N-terminal cleavage of APP by β-secretase (BACE1; β-Site APP-cleaving enzyme 1 [EC 3.4.23.46]) [42] resulting in the formation of soluble sAPPβ and the β-C-terminal fragment (β-CTF; 99-amino-acid C-terminal fragment of APP; C99). Next, the γ-secretase complex cleaves β-CTF to generate Aβ (4 kDa) and AICD [35]. The $A\beta_{1-42}$ form is more toxic than $A\beta_{1-40}$ due to its higher tendency to form aggregates [43]. $A\beta_{1-42}$ activates signaling pathways that lead to synaptic and mitochondrial dysfunction, disruption of Ca^{2+} homeostasis, onset of OS, and, ultimately, neuronal apoptosis [44]. Accumulation of Aβ and C99 stimulates neuroinflammation in a mouse model of AD [45, 46]. Aβ is localized in extracellular and intracellular compartments, including endosomes, lysosomes, and the mitochondrial membrane [47, 48].

Thus, Aβ is formed via the pathological amyloidogenic pathway, either in the case of mutations in the genes encoding γ-secretase complex proteins or in disrupted expression of the α- and β-secretase enzymes, resulting in the formation of a longer Aβ peptide capable of aggregation.

PATHWAYS OF Aβ INTAKE BY MITOCHONDRIA AND ITS EFFECT ON MITOCHONDRIAL TRANSPORT

Normal functioning of mitochondria requires a large number of proteins, the majority (about 99%) of which are synthesized in cytosolic ribosomes [49] and imported post-translationally into various subcompartments of organelles. To date, several pathways for Aβ (and many other mitochondrial proteins) import directly into mitochondria are known: via translocases of the outer (TOM) and inner (TIM) membranes and through MAM sites (*Fig. 2*). In addition, Aβ can form directly in mitochondria as a result of APP cleavage by γ-secretase [50, 51].

The TOM complex consists of the main protein TOM40 and adaptor TOM70, TOM22, and TOM20 (large) and the TOM7, TOM6, and TOM5 (small) proteins. Large TOMs are involved in protein recognition, while the small ones participate in pore formation [52]. Protein import from the inner membrane requires the recruitment of the TIM complexes (TIM23 and TIM22) [53]. A decrease in $A\beta_{1-40}$ and $A\beta_{1-42}$ import in the presence of antibodies to the mitochondrial receptors TOM20 and TOM70 or to the common mitochondrial import pore of the outer membrane, TOM40, confirms that Aβ enters mitochondria through the TOM–TIM complex [50]. The Aβ peptide does not affect the structure of translocase systems but significantly hinders mitochondrial preprotein transport via the extramitochondrial coaggregation mechanism [54].

Aβ is translocated from the ER membrane into mitochondria through the contact sites between these organelles called MAMs [55], which have the characteristics of a lipid raft and are rich in cholesterol and sphingomyelin [56]. The physiological functions of MAM include the regulation of phospholipid and Ca^{2+} homeostasis, mitochondrial fusion/fission, apoptosis, autophagy, and cholesterol esterification [57, 58]. MAM is enriched in sarco/ER Ca^{2+} ATPase (SERCA) [59] as well as the sigma-1 (Sig-1R) [60] and inositol-1,4,5-trisphosphate receptors (IP3R) [61]. The ER and mitochondria interact through mitofusin-2 (Mfn-2) and cytosolic chaperone Grp75 (a member of the heat shock protein 70 family), which is associated with IP3R on the ER membrane and with voltage-dependent anion-selective channel 1 (VDAC1) on the mitochondrial membrane. VDAC1 is a multifunctional protein expressed in mitochondria and other cell compartments, including the plasma membrane, and a key regulator of Ca^{2+} homeostasis, OS, and apoptosis [62]. The IP3R–GRP75–VDAC complex regulates Ca^{2+} transfer from the ER to mitochondria [63]. MAM functions are disturbed in cell pathologies, which leads to increased ER stress (accumulation of aberrant unfolded/misfolded proteins in the ER lumen, followed by their aggregation) [64], and disruption of Ca^{2+} homeostasis. Hedskog et al. demonstrated the ability of nanomolar concentrations of the Aβ peptide to increase both the expression of IP3Rs and VDAC and the number of ER–mitochondria contacts and, thereby, increase Ca^{2+} concentration in organelles [65]. The interaction

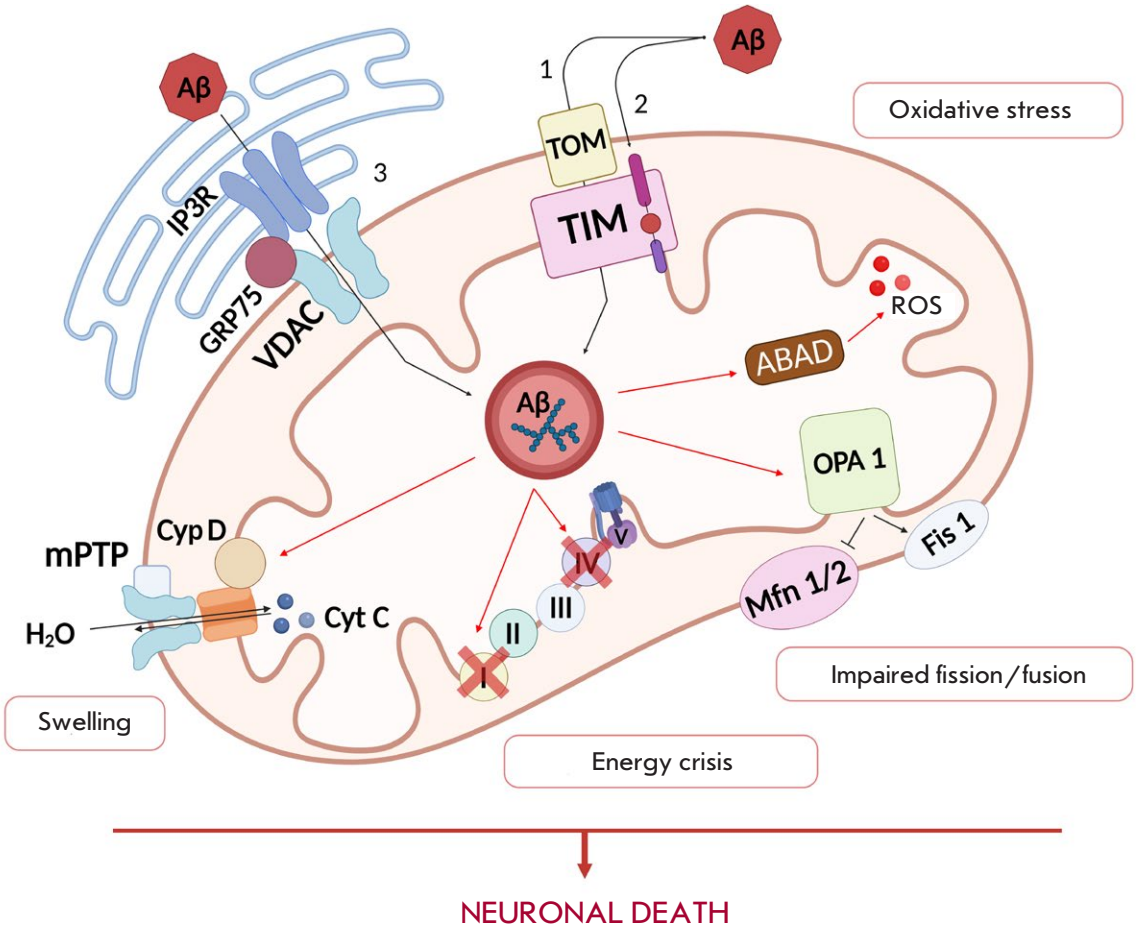

Fig. 2. Schematic representation of the pathways of β-amyloid (Aβ) entry into mitochondria and its pathological effects on these organelles. The first pathway is via the TOM–TIM complex. This pathway has two options: (1) Aβ enters the mitochondrial matrix; (2) Aβ binds to TIM, thus disrupting the import of important mitochondrial proteins. The second pathway is performed through the endoplasmic reticulum (ER)–mitochondria contact sites MAM (3). The formation of Aβ in MAM increases Ca^{2+} entry into mitochondria from the ER through the IP3R–GRP75–VDAC channel. The Aβ–alcohol dehydrogenase (ABAD) complex induces ROS formation. Aβ inhibits fusion proteins (OPA1 and Mfn1\2) and activates the fission protein (Fis1), resulting in the formation of abnormal mitochondria. Aβ binding to cyclophilin D (CypD) leads to the opening of the mitochondrial permeability transition pore (mPTP). Aβ accumulation in mitochondria disrupts the ETC function, which leads to the formation of ROS and further death of neurons

between VDAC1 and Aβ leads to mitochondrial pore dysfunction. This disrupts the transport of mitochondrial proteins and metabolites of up to 150 kDa (ADP and inorganic phosphate), which are necessary for the completion of oxidative phosphorylation and ATP synthesis. Abnormal transport of proteins and metabolites leads to impaired oxidative phosphorylation and mitochondrial dysfunction [66]. VDAC1 overexpression in the human cerebral cortex correlates with the stages of AD; this is also observed in mice transgenic for the *APP* gene and Aβ-exposed neuroblastoma cells. A decrease in VDAC1 expression is accompanied by a drop in the levels of APP and BACE1 mRNA [62].

Data on a possible formation of Aβ directly in MAM has been published [67]. The presence of presenilins and the C99 fragment, which is cleaved by γ-secretase [69], in MAM [68] may explain the mito-

chondrial localization of Aβ [50]. In addition, MAM is a lipid raft-like domain [70], while APP cleavage via the amyloidogenic pathway depends on the lipid raft [71, 72]. A change in γ-secretase activity leads to the accumulation of the C99 fragment in MAM, inducing esterification of cholesterol, hydrolysis of sphingolipids, and mitochondrial dysfunction [73]. It has been suggested that the synergetic effect of ceramide, a product of sphingomyelin hydrolysis, and Aβ can cause neuronal death in AD [74]. Mutations in *PSEN1*, *PSEN2*, and *APP* upregulate MAM function and significantly increase the ER – mitochondria interaction [75].

Takuma et al. showed that the receptor for advanced glycation endproducts (RAGE, type I transmembrane protein) also facilitates $Aβ_{1-40}$ translocation from the extracellular to the intracellular space, which can be one of the mechanisms of Aβ import into mitochondria [76]. Aβ accumulation in the brain leads to RAGE overexpression in the affected vessels, neurons, and microglia [77], which, in turn, induces ROS production, mainly due to the activity of NADPH oxidases [78].

Aβ accumulates on the inner mitochondrial membrane [79], hindering the import of the precursor proteins required for mitochondrial biogenesis [54]. Aβ also interacts with cytochrome *c* oxidase, F1α ATP synthase, and the subunits of the electron transport chain, while inhibiting the activity of the complexes [80]. For instance, 24 proteins were found to be dysregulated in transgenic pR5/AβPP/PS2 mice; one-third of these proteins are mitochondrial proteins associated mainly with oxidative phosphorylation system (OXPHOS) complexes I and IV [81]. It is noteworthy that complex IV dysregulation depends on the level and degree of Aβ activity. In addition, Aβ accumulation in mitochondria correlates with manifestations of early synaptic deficit in a mouse model of AD [82, 83].

The Aβ was shown to enter mitochondria through translocases of the mitochondrial membrane and at the ER–mitochondria contact points. Moreover, Aβ is synthesized directly in mitochondria as a result of APP cleavage by γ-secretase localized in them, which leads to mitochondrial transport dysfunction.

EFFECT OF Aβ ON MITOCHONDRIAL DYNAMICS AND BIOGENESIS

Mitochondrial biogenesis is a complex process involving the nuclear and mitochondrial genomes and resulting in an increased number of mitochondria in response to enhanced energy demand. Peroxisome proliferator-activated receptor-γ 1α coactivator (PGC-1α) is a master regulator of mitochondrial biogenesis, energy metabolism, and respiration through interactions with various transcription factors, including nuclear respiratory factors 1 (NRF-1) and 2 (NRF-2) [84]. Qin et al. were the first to show a decrease in PGC-1α expression in AD patients and a transgenic mouse model of AD [85]. Administration of PGC-1α in the hippocampus and the cerebral cortex of transgenic APP23 mice decreased the level of Aβ deposits owing to BACE1 downregulation and helped to preserve most neurons [86]. Exogenous PGC-1α expression in neuroblastoma N2a cells suppresses BACE1 transcription, which, in turn, reduces the level of secreted Aβ and increases the level of sAPPα [87]. PGC-1α activity is regulated by AMP-activated protein kinase (AMPK) and sirtuins (SIRTs). Aβ was found to cause overexpression of poly(ADP-ribose) polymerase 1 (PARP1 [EC 2.4.2.30]), which is accompanied by NAD^+ depletion followed by a reduction of SIRT1 activity. Inhibition of PARP1 induces SIRT1 expression, leading to an increase in α-secretase expression, downregulation of BACE1, and a decrease in the Aβ level [88]. Small interfering RNAs (siRNAs), a group of small single-stranded non-coding RNAs involved in mitochondrial biogenesis and post-transcriptional regulation of mRNAs by inhibiting their translation and degradation, also affect SIRT function [89]. These non-coding RNAs are also involved in AD pathogenesis [90–93].

Mitophagy is a process in which damaged mitochondria are specifically taken up by autophagosomes and subjected to lysosomal degradation, which prevents the accumulation of dysfunctional mitochondria [94]. The main mitophagy pathway is ubiquitin- and receptor-mediated mitophagy; PTEN-induced kinase 1 (PINK1) and Parkin play an important role in this process. An abnormal increase in the number of autophagic vacuoles containing defective (aberrant) mitochondria with an altered activity of PINK1 [EC 2.7.11.1] and Parkin [EC 2.3.2.31] is observed in AD [95]. Aβ and hyperphosphorylated tau cause oxidative damage to mitochondria, resulting in a reduced level of these proteins [96–98]. This leads to a decrease in the number of completed mitophagy processes and contributes to an increase in the number of Aβ and tau aggregates. Vaillant-Beuchot et al. showed that, independent of Aβ, the C-terminal fragments of APP trigger excessive disorganization of mitochondrial cristae, enhance ROS generation, and reduce the mitophagy associated with insufficient fusion of mitochondria with lysosomes [99].

Not only changes in mitochondrial morphology, but also disrupted distribution of these organelles in the brain cells are observed in AD. Anterograde (kinesin-based) transport promotes the delivery of newly

formed mitochondria to axons; retrograde (dynein-based) transport promotes the removal of damaged organelles and maintains a healthy level of their population [100]. Disruption of the transport system and the balance between healthy/damaged mitochondria can change the distribution of organelles, which, in turn, has a significant impact on the synaptic and neuronal functions [101]. Aβ reduces the expression of the anterograde KIF5A protein [102], while interaction between oligomeric Aβ and the dynein intermediate chain negatively affects dynein interaction with snapin (adaptor protein) [103]. Mutations in the *PSEN1* impair axonal transport by activating glycogen synthase kinase-3β (GSK-3β), which phosphorylates the kinesin light chain and releases it from the sites of its incorporation into the membrane [104].

Mitochondrial transport is important for neuronal survival, given the need for a proper distribution of mitochondria in areas with a higher demand for ATP and calcium. In addition, mitochondria are organized into a dynamic network through the continuous cycles of fusion and fission necessary for mitochondrial homeostasis and adaptation to cellular needs [105, 106]. Fusion and fission of mitochondria are regulated by proteins of the dynamin family, which have GTPase activity. Mitochondrial fission involves the proteins Fis1 (mitochondrial fission protein 1) and Drp1 (dynamin-like protein 1, DLP1), while fusion is mediated by mitofusins (mitofusins Mfn1 and Mfn2 are involved in outer membrane fusion) and the protein encoded by *OPA1* [107, 108]. The imbalance between mitochondrial fusion and fission has been confirmed in *in vivo* studies [109]. Overexpression of wild-type (APPwt) and mutant (APPswe) APP in M17 neuroblastoma cells and primary neurons leads to mitochondrial fragmentation and their perinuclear distribution through a decrease in the levels of the fusion proteins, in particular Drp1, OPA1, Mfn1, and Mfn2, and an increase in the level of mitochondrial Fis1. These effects are blocked by the BACE1 inhibitor, which indicates that Aβ affects mitochondrial fragmentation [110, 111].

Mitofusins, located on the outer mitochondrial membrane, are involved in fusion by forming homotypic and heterotypic interactions with the OPA1 protein of the inner mitochondrial membrane [112]. It has also been reported that Mfn2 is present in MAM; it regulates axonal transport [113] and modulates γ-secretase activity and Aβ formation [114].

Drp1 is a mitochondrial fission protein that is involved in cell fragmentation, phosphorylation, ubiquitination, and death [115, 116]. An interaction of oligomeric Aβ and hyperphosphorylated tau with Drp1 was uncovered in the brains of AD patients and transgenic mice [117]. ROS are formed during the interaction between Aβ and Drp1 and are further involved in mitochondrial fragmentation [118], followed by mitochondrial depletion in axons and dendrites, resulting in the loss of synapses [119]. At the same time, Aβ-induced OS and calcium entry into the cell lead to Drp1 phosphorylation, causing an increase in the activity of extracellular signal-regulated kinase (ERK) and Akt [20, 121].

Thus, pathological Aβ negatively affects many important mitochondrial functions, leading to a disruption of their biogenesis, transport system functioning, the balance between damaged and healthy mitochondria, and, as a result, changes the distribution of these organelles in neurons, which, in turn, affects the synaptic and neuronal function.

Aβ CLEAVING ENZYMES

An imbalance between Aβ formation and excretion results in its abnormal deposition in the brain tissue [122, 123]. The main pathways underlying Aβ elimination include its clearance through the blood–brain barrier (BBB), enzymatic degradation, cellular uptake, and subsequent degradation [124, 125]. The main enzymes involved in the extracellular cleavage of Aβ include the following zinc metallopeptidases: neprilysin (NEP [EC 3.4.24.11]), insulin-degrading enzyme (IDE [EC 3.4.24.56]), endothelin-converting enzyme (ECE [EC 3.4.24.71]), and matrix metalloproteinase-9 (MMP-9 [EC 3.4.24.35]) [126, 127]. Peptidases PreP [128] and transthyretin, which are capable of excreting amyloid by a mechanism similar to NEP [129], also exhibit catalytic activity against Aβ. Another peptidase neurolysin (NLN [EC 3.4.24.16]), which is capable of degrading mitochondrial precursor proteins (<20 amino acid residues long) and longer mitochondrial peptides, has been found in the mammalian mitochondrial matrix. An *in vitro* analysis of peptide cleavage revealed an interaction between NLN and PreP during the degradation of long peptides; in particular, the hydrophobic fragment of $A\beta_{35-40}$ [130].

IDE is an extracellular zinc metallopeptidase capable of regulating the plasma levels of insulin, as well as extracellular Aβ. IDE is localized mainly in the cell cytosol [131]. However, it is also found in mitochondria and endosomes [132]. IDE selectively interacts with Aβ monomers [133]. The activity of this enzyme is determined by the dynamic equilibrium between soluble Aβ monomers and its aggregates [134]. Decreased levels of IDE and angiotensin-converting enzyme (ACE [EC 3.4.15.1]) and an increased Aβ level (due to slower exogenous protein cleavage) are observed in transgenic CB2R-/-$A\beta_{1-42}$ mice lacking the cannabinoid receptor type 2 (CB2R)

compared to WT-$A\beta_{1-42}$ mice [135]. NEP is a type II integral membrane protein located in the plasma membrane; a larger part of this protein, including the active site, is located in the extracellular space [136]. Evidence has been obtained that the NEP and IDE activities are regulated by cholesterol levels. The enzymes IDE and NEP are sensitive to the OS caused by high cholesterol levels. In addition, their activity is also associated with *APOE*. High NEP activity was noted in the brain of people carrying the ε2 allele of *APOE*, while patients with the ε4 allele have decreased levels of IDE and NEP [137]. The activity of IDE and NEP is also affected by protein kinases A and C (PKA and PKC), which regulate the direct (enzymatic) cleavage of APP, thus decreasing the Aβ level. An experiment in a primary culture of rat astrocytes demonstrated that PKA activation impedes Aβ degradation by reducing the level of NEP but not IDE, while PKC activation stimulates NEP release into the extracellular space and IDE overproduction in astrocyte cell membranes [138].

Mitochondrial peptidasome (PreP, or PITRM1) is a metallopeptidase 1 located in the mitochondrial matrix and involved in the cleavage of protein pre-sequences after their import into mitochondria. Accumulation of Aβ was detected in the brain of mice heterozygous for *PITRM1* [139]. Recent studies have revealed the role of PreP in Aβ metabolism [140]. For instance, PreP cleaves $A\beta_{1-40}$, $A\beta_{1-42}$, Arctic Aβ (E22G), and the 53-amino-acid mitochondrial pre-sequence pF1β [141, 142]. A significant decrease in the proteolytic activity of PreP against both the Aβ and non-Aβ peptides in mitochondria of the brain of transgenic mAβPP and mAβPP/ABAD mice should be noted [143]. At the same time, overexpression and increased PreP activity contribute to a decrease in the mitochondrial Aβ level [140]. Increased PreP expression not only leads to a degradation of mitochondrial Aβ, but also affects the overall level of Aβ in the brain. A decrease in the PreP activity in brain mitochondria is associated with functional changes in it; for instance, it can be due to protein oxidation [26]. PreP inactivation in acidic conditions has been shown to be due to the oxidation of cysteine residues and subsequent oligomerization through the formation of intermolecular disulfide bonds [144]. Disruption of the PreP function in OS is confirmed by Teixeira et al., who revealed the concentration dependence of PreP activity inhibition by hydrogen peroxide [145]. Thus, one can assume that increased ROS generation resulting in the inhibition of PreP activity is due to Aβ accumulation in mitochondria [146].

In addition, the acidic environment in mitochondria prevents Aβ clearance owing to its rapid interaction with cyclophilin D (CypD) and/or Aβ-binding alcohol dehydrogenase (ABAD) [147]. ABAD is a mitochondrial protein that contributes to the toxic effect of Aβ in mitochondria of AD patients and in a mouse model of AD by increasing ROS production and decreasing ATP levels [148, 149]. The formation of the ABAD–Aβ complex disrupts the interaction between NAD^+ and ABAD, which changes mitochondrial membrane permeability [150] and accelerates mitochondrial dysfunction [151]. CypD is an important part of mPTP: it is responsible for its opening [152]. The formation of CypD–Aβ complexes causes mPTP opening, which leads to matrix swelling and ROS generation [153]. This, in turn, results in a disruption of the outer membrane and nonspecific release of such intermembrane proteins as cytochrome *c*, endonuclease G, procaspase, and Smac/DIABLO into the cytosol, where they activate apoptosis [154, 155]. A decrease in CypD expression leads to the suppression of Aβ-related disorders, in particular Ca^{2+}-dependent mitochondrial swelling, a decrease in the calcium uptake, and an impairment of the mitochondrial respiratory function [156].

Thus, the importance of regulating the performance of the enzymes cleaving Aβ in both extracellular and intracellular spaces, as well as the factors inhibiting their activity, in order to reduce the toxic effect of Aβ on neurons has been mentioned.

POTENTIAL NEUROPROTECTOR AGENTS ACTING ON BOTH Aβ DEPOSITION AND MITOCHONDRIAL DYSFUNCTION

One of the most common undertakings in the search for potential drugs against AD is the synthesis of compounds that reduce deposits of Aβ and prevent its accumulation in the first place. However, as various studies have shown, action on only one target is not enough to obtain a promising neuroprotector. For this reason, we studied the interaction between Aβ and mitochondria, in an attempt to combine the Aβ-aggregation-modulatory and mitoprotective effects in one molecule. By combining and systematizing data on compounds that could work against AD and are currently under study, one can outline promising fields and possible modifications to a molecule for the synthesis of more effective compounds.

Taking into account the multifactorial nature of AD, in particular the relationship between Aβ, mitochondria, and OS, pharmacological correction of mitochondrial dysfunction with a simultaneous effect on Aβ formation, deposition, and excretion seems a promising direction. Some potential multitarget compounds acting on the pathological processes described above are presented in *Table 1*.

Table 1. Potential multitarget agents for the treatment of Alzheimer's disease

Agent	Aβ-associated targets	Mitochondrial targets	Main effect	Ref.
Epigallo-catechin-3-gallate (EGCG)	NEP; BACE1	ROS and NO	↓ Aβ deposition; ↓ OS; ↑ learning and memory	[158] [160] [193]
Kai-Xin-San	NEP	LP; SOD, GPx, and CAT	↓ Aβ level; ↑ learning and memory; ↑ antioxidant system	[163, 164]
Curcumin	Aβ fibrils and oligomers; BACE1	ROS; SOD and GSH	prevents Aβ deposition; ↑ antioxidant system; ↓ OS	[178, 179] [216]
Silibinin	*APP* and *BACE* genes; NEP	LP; CAT, SOD, NO, and GSH	↑ antioxidant system; improves memory in animals	[183–187]
Quercetin	APP, BACE, APH1 and PSEN1; ADAM10 and ADAM17	ROS, MDA, GPx, and SOD	↓ mitochondrial dysfunction; ↓ Aβ level	[190–194]
Baicalein	Aβ; stimulates neurogenesis	OS	↓ neuronal death; improves memory in mice	[197, 198]
Berberin	BACE1	ROS; SOD	↓ Aβ level; improves cognitive function in mice	[202]
Resveratrol	APP; Aβ; microglia	CAT, SOD, NO, GSH; transition metal ions; ROS; PGC1-α	↓ Aβ aggregation in in the hippocampus and cortex of transgenic APP/PS1pa mice	[208, 209]
Ferulic acid	≠ BACE1 activity	SOD; LP; Drp1; Mfn2	↓ Aβ formation; maintains the functional state of mitochon-dria	[214–216]
Idebenone	ADAM17 and NEP; RAGE/ caspase-3	ROS	↓ Aβ deposition in 5xFAD mice; ↓ mitochondrial dysfunction	[217, 218]
α-lipoic acid	Aβ fibrils	ROS CAT, SOD, NO, GSH	↓ Aβ formation *in vitro*; ↓ OS	[219]
SS31	Aβ	Drp1 and Fis1; Mfn1/2 and OPA1; PGC1α and Nrf1/2	↓ Aβ formation; ↓ mitochondrial dysfunction; ↑ mitochondrial biogenesis	[220]
SkQ1	$Aβ_{1-40}$ and $Aβ_{1-42}$	Drp1 and Mfn2	↑ mitochondrial biogenesis; ↑ memory in OXYS rats; ↑ number of neurons in CA1 and CA3 areas and the dentate gyrus of OXYS rats; ↓ Aβ deposition	[221]

Note: ↓ – decreases; ↑ – increases; ≠ – inhibits.

NEP modulators [157], which facilitate Aβ clearance from the extracellular space, thus preventing Aβ entry into mitochondria and Aβ-induced mitochondrial dysfunction, are therapeutic targets in AD. Administration of the well-known antioxidant and HDAC inhibitor epigallocatechin-3-gallate (EGCG) reduces Aβ levels and increases NEP expression in the cerebral cortex of senescence accelerated (SAMP8) mice [158] and rats subjected to prenatal hypoxia [159]. In addition, EGCG suppresses BACE1 expression and decreases $Aβ_{1-42}$ levels, improving learning and memory in a rat model of AD [160]. Li et al. found that (E)-N-((6-aminopyridin-2-yl)methyl)-3-(4-hydroxy-3-methoxyphenyl)acrylamide inhibits BACE1 activity and exhibits strong antioxidant activity against 1,1-diphenyl- 2-picrylhydrazyl (DPPH) and 2,2'-azino-bis-(3-ethylbenzothiazoline-6-sulfonic acid) (ABTS), exceeding the effect of EGCG [161]. Another potential compound is Kai-Xin-San (KXS, a Chinese herbal decoction used to treat amnesia), which increases NEP levels in murine hippocampus [162]. A antioxidant activity of KXS was shown to exist in doxorubicin- [163] and scopolamine-induced models of OS [164]. KXS caused a simultaneous decrease in the malondialdehyde (MDA) level and increase in the activity of superoxide dismutase (SOD), glutathione peroxidase (GPx), and catalase (CAT). An antioxidant activity of KXS was also shown by Guo et al. [165].

A potential compound for the treatment of AD is the natural polyphenol curcumin, which has strong antioxidant activity [166, 167]. Curcumin neutralizes ROS, increases the levels of SOD, Na^+-K^+-ATPase, glutathione, and mitochondrial complex enzymes, and protects mitochondria from peroxynitrite [168–171]. Another important property of curcumin is its ability to inhibit Aβ oligomerization and Aβ fibril formation, as well as hinder Aβ-induced neurotoxicity in the brain of transgenic mice [172]. Curcumin binds strongly to Aβ peptides through a wide range of intermolecular interactions: hydrogen bonds, hydrophobic interactions, π-π stacking, and cation-π-attraction. Curcumin forms π–π interactions with aromatic residues (Phe4, Tyr10, Phe19, and Phe20) and cation–π interactions with cationic residues (Arg5, Lys16, and Lys28) in Aβ [173]. Zhao et al. studied the effect of curcumin on the stability of Aβ dimers and found that curcumin disrupts β-sheets, reducing their number in Aβ oligomers [174]. In addition, curcumin binds strongly to the Aβ fibril pre-form, occupying a binding pocket inside the fibril, where it forms hydrogen bonds and hydrophobic interactions with protofibrils and causes structural distortions [175–177]. *In vivo* and *in vitro* experiments revealed another mechanism of curcumin-induced reduction of Aβ accumulation and deposition: suppression of BACE1 expression [178, 179]. Hydroxylated derivatives of monocarbonyl curcumin containing cyclohexanone increase NEP levels [180]. Taken together, these data suggest that curcumin exhibits multi-targeted activity and warrants further study.

Another promising compound is the flavonoid silibinin (silybin), which has antioxidant activity [181]. Silibinin interacts with the mitochondrial membrane, preventing the dysfunction of isolated mitochondria [182]. Administration of silibinin decreases the MDA level and increases the activity of the antioxidant enzymes CAT, SOD, nitric oxide (NO), and glutathione (GSH) [183–186]. In addition to its antioxidant activity, silibinin can reduce Aβ deposition in the hippocampus of APP/PS1 mice by inhibiting *APP* and *BACE1* expression and increasing the NEP level. The issue regarding the previously discovered inability of silibinin to pass through the BBB was solved by its encapsulation in macrophage-derived exosomes (Exo-Slb). After entering the brain of AD mice, Exo-Slb selectively interacts with Aβ monomers, preventing their aggregation, and effectively improves the memory of the animals [187]. The effect of silibinin encapsulated in the nanoparticles of human serum albumin (HSA) was also studied. The neuroprotective and antioxidant activity of silibinin–HSA nanoparticles was found to be higher than that of free silibinin [188]. Another flavonoid, quercetin, which modulates gene expression and the signaling pathways, also exhibits antioxidant and iron chelating activities [189]. Quercetin protects neurons from the action of H_2O_2 by reducing lactate dehydrogenase (LDH) release, ROS and MDA levels, while simultaneously increasing GPx and SOD activity [190]. Quercetin reduces mitochondrial dysfunction by reducing ROS production, restoring mitochondrial membrane production and ATP synthesis; it regulates the expression of AMPK, which is involved in the modulation of energy metabolism, reduces Aβ deposition, facilitates its excretion, and regulates APP processing [191]. Studies of transgenic AD mice have shown that quercetin decreases the level of extracellular Aβ [192, 193]. Oral administration of quercetin in rats with $AlCl_3$-induced AD symptoms reduced Aβ aggregation in the hippocampus owing to a downregulation of *APP, BACE1, APH1*, and *PSEN1* and overexpression of *ADAM10* and *ADAM17* [194]. The flavonoids taxifolin and isorhamnetin inhibit BACE1 activity and exhibit an antioxidant effect [195]. Taxifolin inhibits Aβ fibril formation *in vitro* and improves the cerebral blood flow, facilitating Aβ clearance [196]. Baicalein exhibits a

number of important pharmacological properties as a neuroprotector: it reduces OS, inhibits Aβ aggregation, and stimulates neurogenesis [197]. Baicalein was also shown to prevent Aβ-induced neuronal atrophy and improve memory in mice [198]. The combination of baicalein and *trans*-chalcone significantly reduced the levels of ROS and $A\beta_{1-42}$ in yeast cells expressing $A\beta_{1-42}$ without affecting their growth in [199]. The neuroprotective mechanism of luteolin action consists in the direct inhibition of ROS and acetylcholinesterase (AChE) activity, as well as $A\beta_{42}$ accumulation [200].

Numerous *in vivo* studies performed recently have shown the neuroprotective effect of the isoquinoline alkaloid berberine [201]. Berberine inhibits BACE1 and AChE activity, reduces the ROS level, while increasing the glutathione level, preventing apoptosis, and improving cognitive functions [202, 203]. The incorporation of berberine into lipid nano-carriers increased its bioavailability and effectiveness in an *in vivo* experiment [204]. It was also established that another natural alkaloid, piperine, and its metabolites can inhibit BACE1 and reduce the ROS level, thus decreasing the damage to mitochondria [205]. The sesquiterpene alkaloid huperzine A (HupA) also has a multifunctional activity: it reduces Aβ deposition in the cortex and hippocampus, improves mitochondrial functions, and inhibits AChE activity in an AD model of transgenic APPswe/PS1dE9 mice [206]. Recently, synthesized HupA analogues have demonstrated even higher efficiency [207].

Numerous studies have shown that polyphenol resveratrol exhibits a variety of biological activities, including antioxidant and neuroprotective effects. Resveratrol increases the expression and activity of antioxidant enzymes, binds transition metal ions, inactivates free radicals, and improves the mitochondrial function by increasing the expression and activation of the main inducer of mitochondrial biogenesis, PGC1-α [208]. Resveratrol reduces Aβ deposition through the activation of the non-amyloidogenic pathway of APP cleavage and Aβ excretion; it also activates microglia in the hippocampus and cortex of transgenic APP/PS1 mice [209]. Promising compounds exhibiting both antioxidant activity and the ability to inhibit BACE1 have been identified among derivatives of styryl benzamide [210], N-cyclohexylimidazo[1,2-a] pyridine [211], and trimethoxylated halogenated chalcones [212, 213].

The neuroprotective effect of ferulic acid (FA) can be implemented through several mechanisms. FA exhibits the antioxidant and mitoprotective effects. FA administration in a mouse model of AD increased SOD activity and decreased the MDA level [215]. In addition, FA restores the balance between mitochondrial fission and fusion by regulating the activity of fission and fusion proteins (by decreasing Drp1 expression and increasing Mfn2 expression) [216] and the PGC-1α level [222]. Maintenance of the PGC-1 level prevents a loss of the mitochondrial membrane potential and reduces Drp-1-dependent mitochondrial fission. The second important action of FA is its ability to inhibit BACE1, which prevents Aβ formation [214]. Promising compounds with anti-aggregation and antioxidant activities have also been identified among FA derivatives [223, 224].

Another direction in the search for AD drugs is the study of compounds that are similar to endogenous antioxidants. An example is idebenone, a coenzyme Q10 analogue that can pass through the BBB, which is an FDA-approved antioxidant. Idebenone inhibits Aβ-induced ROS production and mitochondrial dysfunction [217]. Idebenone administration significantly reduces Aβ deposition in 5xFAD mice by increasing the levels of α-secretase ADAM17 and NEP; it also inhibits the RAGE/caspase-3 signaling pathway [218]. The glutathione precursor N-acetylcysteine (NAC) reduced the levels of Aβ, phosphorylated tau, and OS markers and improved cognitive functions in animals in *in vitro* and *in vivo* experiments [225]. Alpha-lipoic acid (α-LA), whose production decreases with age, is considered a promising agent for the prevention and treatment of AD. This acid neutralizes ROS, increases the glutathione level, chelates transition metals, disrupts Aβ synthesis, and promotes its excretion [219]. In addition, α-LA acts as an enzyme cofactor capable of regulating the metabolism, energy production, and mitochondrial biogenesis [226]. The results of a randomized placebo-controlled trial showed that the combination of omega-3 fatty acid and α-LA delayed cognitive impairment in AD patients when administered for 12 months [227].

The antioxidant peptide SS31 reduces Aβ peptide production and restores mitochondrial and synaptic functions in a mouse model of AD [228]. The combined use of this peptide and mitochondrial division 1 inhibitor (Mdivi1) has a positive effect on cultured cells. This result suggests that combined treatment with the use of antioxidants acting on mitochondria may be more effective [229]. SkQ (10-(6'-plastoquinonyl) decylrhodamine 19), which accumulates mainly in neuronal mitochondria, improves the structural and functional state of organelles, thereby preventing neuronal loss and synaptic damage, and reduces the Aβ level and hyperphosphorylation of the tau protein in the hippocampus; this, in turn, leads to improved learning and memory ability in animals [221].

ABAD inhibitors are also promising agents in the search for anti-AD drugs. They prevent rapid binding of Aβ to ABAD in the mitochondrial matrix, resulting in PreP normalization [230–234].

Thus, the approach to the designing and developing of neuroprotective drugs based on combining various pharmacophore fragments in one molecule capable of acting on targets associated with proteinopathy and mitochondrial dysfunction is considered a promising and relevant strategy for medicinal chemistry and pharmacology.

CONCLUSION

Due to the lack of effective drugs for the treatment of Alzheimer's that have not only a symptomatic effect, but also a drastic impact on the disease's pathological cascades, a targeted search for and development of drugs for a pharmacological correction of this neuronal disease remains relevant. In order to do this, it is necessary to understand not just individual pathogenetic processes, but their interrelation and how they mutually affect each other. For instance, the interaction between mitochondria and Aβ is a closely related process. Toxic forms of Aβ lead to mitochondrial dysfunction due to the impairment of Ca^{2+} homeostasis, mitochondrial fusion and fission, protein import, increased mitochondrial membrane permeability, and inhibition of mitochondrial respiratory chain complexes. At the same time, mitochondrial dysfunction leads to oxidative stress, energy crisis, and activation of cell death cascades. This, in turn, promotes processing of the precursor protein APP and leads to β-amyloid aggregation and deposition. Therefore, a more thorough understanding of the properties of potential neuroprotective drugs indicates that it is necessary to focus attention on the combination of pharmacophore fragments that can simultaneously affect the proteinopathy-associated cascades and prevent mitochondrial dysfunction in one molecule.

In this review, we tried to consolidate and analyze the currently available data on the role of Aβ interaction with mitochondria in the pathogenesis of Alzheimer's disease and judge the effectiveness of the search for potential neuroprotective drugs targeting the pathological processes associated with proteinopathy and mitochondrial dysfunction. ●

This work was supported by the Russian Science Foundation Grant No. 22-23-00995.

REFERENCES

1. Sengoku R. // Neuropathology. 2020. V. 40. № 1. P. 22–29.
2. Lane C.A., Hardy J., Schott J.M. // Eur. J. Neurol. 2018. V. 25. № 1. P. 59–70.
3. Chen S., Jiang Q., Huang P., Hu C., Shen H., Schachner M., ZhaoW. // Brain. Res. Bull. 2020. V. 162. P. 141–150.
4. Scheltens P., Blennow K., Breteler M.M.B., de Strooper B., Frisoni G.B., Salloway S., Vander Flier W.M. // Lancet. 2016. V. 388. P. 505–517.
5. Hardy J., Allsop D. // Trends Pharmacol. Sci. 1991. V. 12. P. 383–388.
6. Winblad B., Amouyel P., Andrieu S., Ballard C., Brayne C., Brodaty H., Cedazo Minguez A., Dubois B., Edvardsson D., Feldman H., et al. // Lancet. Neurol. 2016. V. 15. P. 455–532.
7. Swerdlow R.H., Burns J.M., Khan S.M. // Biochim. Biophys. Acta. 2014. V. 1842. № 8. P. 1219–1231.
8. Stanciu G.D., Luca A., Rusu R.N., Bild V., Chiriac S.I.B., Solcan C., Bild W., Ababei D.C. // Biomolecules. 2020. V. 10. № 1. P. 40.
9. Arnsten A.F.T., Datta D., Tredici K.D., Braak H. // Alzheimers Dement. 2021. V. 17. № 1. P. 115–124.
10. Cheignon C., Tomas M., Bonnefont-Rousselo D., Faller P., Hureau C., Collin F. // Redox. Biol. 2018. V. 14. P. 450–464.
11. Pohanka M. // Bratisl. Lek. Listy. 2018 . V. 119. № 9. P. 535–543.
12. Tong B.C., Wu A.J., Li M., Cheung K.H. // Biochim. Biophys. Acta. Mol. Cell. Res. 2018. V. 1865. № 11. Pt B. P. 1745–1760.
13. Akiyama H., Barger S., Barnum S., Bradt B., Bauer J., Cole G.M., Cooper N.R., Eikelenboom P., Emmerling M., Fiebich B.L., et al. // Neurobiol. Aging. 2000. V. 21. № 3. P. 383–421.
14. Scheffer S., Hermkens D.M.A., van der Weerd L., de Vries H.E., Daemen M.J.A.P. // Arterioscler. Thromb. Vasc. Biol. 2021. V. 41. P. 1265–1283.
15. Ward R.J., Zucca F.A., Duyn J.H., Crichton R.R., Zecca L. // Lancet. Neurol. 2014. V. 13. № 10. P. 1045–1060.
16. Seaks C.E., Wilcock D.M. // PLoS Pathog. 2020. V. 16. № 11. P. e1008596.
17. Asai M., Kawakubo T., Mori R., Nobuhisa I. // Yakugaku. Zasshi. 2017. V. 137. № 7. P. 801–805.
18. An S.S., Bagyinszky E., Kim H.R., Seok J.W., Shin H.W., Bae S., Kim S.,Youn Y.C. // BMC Neurol. 2016. V. 16. P. 71.
19. Cai Y., An S.S., Kim S. // Clin. Interv. Aging. 2015. V. 10. P. 1163–1172.
20. Sun L., Zhou R., Yang G., Shi Y. // Proc. Natl. Acad. Sci. USA. 2017. V. 114. № 4. P. E476–e85.
21. Dai M.H., Zheng H., Zeng L.D., Zhang Y. // Oncotarget.

2018. V. 9. № 19. P. 15132–15143.
22. Veugelen S., Saito T., Saido T.C., Chávez-Gutiérrez L., De Strooper B. // Neuron. 2016. V. 90. № 2. P. 410–416.
23. Szaruga M., Munteanu B., Lismont S., Veugelen S., Horré K., Mercken M., Saido T.C., Ryan N.S., De Vos T., Savvides S.N., et al. // Cell. 2017. V. 170. № 3. P. 443–456. e14.
24. Armstrong R.A. // Folia. Neuropathol. 2019. V. 57. № 2. P. 87–105.
25. Tilokani L., Nagashima S., Paupe V., Prudent J. // Essays Biochem. 2018. V. 62. № 3. P. 341–360.
26. Wang W., Zhao F., Ma X., Perry G., Zhu X. // Mol. Neurodegener. 2020. V. 15. № 1. P. 30.
27. Wang Y., Xu E., Musich P.R., Lin F. // CNS Neurosci. Ther. 2019. V. 25. № 7. P. 816–824.
28. Cheng H., Gang X., Liu Y., Wang G., Zhao X., Wang G. // Am. J. Physiol. Endocrinol. Metab. 2020. V. 318. № 5. P. E750–E764.
29. Cai Q., Tammineni P. // Front. Cell. Neurosci. 2016. V. 10. P. 24.
30. Del Prete D., Suski J.M., Oulès B., Debayle D., Gay A.S., Lacas-Gervais S., Bussiere R., Bauer C., Pinton P., Paterlini-Bréchot P., et al. // Alzheimers Dis. 2017. V. 55. № 4. P. 1549–1570.
31. Heinemeyer T., Stemmet M., Bardien S., Neethling A. // DNA Cell. Biol. 2019. V. 38. № 1. P. 23–40.
32. Cline E.N., Bicca M.A., Viola K.L., Klein W.L. // J. Alzheimers Dis. 2018. V. 64. P. 567–610.
33. Chen G.F., Xu T.H., Yan Y., Zhou Y.R., Jiang Y., Melcher K., Xu H.E. // Acta Pharmacol. Sin. 2017. V. 38. № 9. P. 1205–1235.
34. Tan J.Z.A., Gleeson P.A. // J. Biol. Chem. 2019. V. 294. № 5. P. 1618–1631.
35. Nhan H.S., Chiang K., Koo E.H. // Acta Neuropathol. 2015. V. 129. № 1. P. 1–19.
36. Habib A., Sawmiller D., Tan J. // J. Neurosci. Res. 2017. V. 95. № 4. P. 973–991.
37. Fol R., Braudeau J., Ludewig S., Abel T., Weyer S.W., Roederer J.P., Brod F., Audrain M., Bemelmans A.P., Buchholz C.J., et al. // Acta. Neuropathol. 2016. V. 131. № 2. P. 247–266.
38. Liu X., Liu Y., Ji S. // Membranes (Basel). 2021. V. 11. № 12. P. 983.
39. Bolduc D.M., Montagna D.R., Gu Y., Selkoe D.J., Wolfe M.S. // Proc. Natl. Acad. Sci. USA. 2016. V. 113. № 5. P. E509–E518.
40. Oikawa N., Walter J. // Cells. 2019. V. 8. № 3. P. 209.
41. Bai X.C., Yan C., Yang G., Lu P., Ma D., Sun L., Zhou R., Scheres S.H., Shi Y. // Nature. 2015. V. 525. № 7568. P. 212–217.
42. Hampel H., Vassar R., De Strooper B., Hardy J., Willem M., Singh N., Zhou J., Yan R., Vanmechelen E., De Vos A., et al. // Biol. Psychiatry. 2021. V. 89. № 8. P. 745–756.
43. Anand B.G., Wu Q., Karthivashan G., Shejale K.P., Amidian S., Wille H., Kar S. // Bioact. Mater. 2021. V. 6. № 12. P. 4491–4505.
44. Jarosz-Griffiths H.H., Noble E., Rushworth J.V., Hooper N.M. // J. Biol. Chem. 2016. V. 291. № 7. P. 3174–3183.
45. Lauritzen I., Pardossi-Piquard R., Bourgeois A., Pagnotta S., Biferi M.G., Barkats M., Lacor P., Klein W., Bauer C., Checler F. // Acta. Neuropathol. 2016. V. 132. № 2. P. 257–276.
46. van Gijsel-Bonnello M., Baranger K., Benech P., Rivera S., Khrestchatisky M., de Reggi M., Gharib B. // PLoS One. 2017. V. 12. № 4. P. e0175369.
47. Chadha S., Behl T., Sehgal A., Kumar A., Bungau S. // Mitochondrion. 2021. V. 56. P. 62–72.
48. Schützmann M.P., Hasecke F., Bachmann S., Zielinski M., Hänsch S., Schröder G.F., Zempel H., Hoyer W. // Nat. Commun. 2021. V. 12. № 1. P. 4634.
49. Avendaño-Monsalve M.C., Ponce-Rojas J.C., Funes S. // Biol. Chem 2020. V. 401. № 6–7. P. 645–661.
50. Hansson Petersen C.A., Alikhani N., Behbahani H., Wiehager B., Pavlov P.F., Alafuzoff I., Leinonen V., Ito A., Winblad B., Glaser E., et al. // Proc. Natl. Acad. Sci. USA. 2008. V. 105. № 35. P. 13145–13150.
51. Del Prete D., Suski J.M., Oulès B., Debayle D., Gay A.S., Lacas-Gervais S., Bussiere R., Bauer C., Pinton P., Paterlini-Bréchot P., et al. // J. Alzheimers Dis. 2017. V. 55. № 4. P. 1549–1570.
52. Araiso Y., Tsutsumi A., Qiu J., Imai K., Shiota T., Song J., Lindau C., Wenz L.S., Sakaue H., Yunoki K., et al. // Nature. 2019. V. 575. № 7782. P. 395–401.
53. Palmer C.S., Anderson A.J., Stojanovski D. // FEBS. Lett. 2021. V. 595. № 8. P. 1107–1131.
54. Cenini G., Rüb C., Bruderek M., Voos W. // Mol. Biol. Cell. 2016. V. 27. № 21. P. 3257–3272.
55. Zhang Z., Cui D., Zhang T., Sun Y., Ding S. // Diabetes. Metab. Syndr. Obes. 2020. V. 13. P. 1417–1428.
56. Area-Gomez E., Schon E.A. // FASEB J. 2017. V. 31. № 3. P. 864–867.
57. Yang S., Zhou R., Zhang C., He S., Su Z. // Front. Cell. Dev. Biol. 2020. V. 8. P. 571554.
58. Luan Y., Luan Y., Yuan R.X., Feng Q., Chen X., Yang Y. // Oxid. Med. Cell. Longev. 2021 V. 2021. P. 4578809.
59. Wang N., Wang C., Zhao H., He Y., Lan B., Sun L., Gao Y. // Cells. 2021. V. 10. № 3. P. 657.
60. Weng T.Y., Tsai S.A., Su T.P. // J. Biomed. Sci. 2017. V. 24. № 1. P. 74.
61. Mangla A., Guerra M.T., Nathanson M.H. // Cell. Calcium. 2020. V. 85. P. 102132.
62. Shoshan-Barmatz V., Nahon-Crystal E., Shteinfer-Kuzmine A., Gupta R. // Pharmacol. Res. 2018. V. 131. P. 87–101.
63. Veeresh P., Kaur H., Sarmah D., Mounica L., Verma G., Kotian V., Kesharwani R., Kalia K., Borah A., Wang X., et al. // Ann. N.Y. Acad. Sci. 2019. V. 1457. № 1. P. 41–60.
64. Giacomello M., Pellegrini L. // Cell. Death. Differ. 2016. V. 23. № 9. P. 1417–1427.
65. Hedskog L., Pinho C.M., Filadi R., Ronnback A., Hertwig L., Wiehager B., Larssen P., Gellhaar S., Sandebring A., Westerlund M., et al. // Proc. Natl. Acad. Sci. USA. 2013. V. 110. № 19. P. 7916–7921.
66. Manczak M., Reddy P.H. // Hum. Mol. Genet. 2012. V. 21. № 23. P. 5131–5146.
67. Schreiner B., Hedskog L., Wiehager B., Ankarcrona M. // J. Alzheimers Dis. 2015. V. 43. № 2. P. 369–374.
68. Pera M., Larrea D., Guardia-Laguarta C., Montesinos J., Velasco K.R., Agrawal R.R., Xu Y., Chan R.B., Paolo G.D., Mehler M.F., et al. // EMBO J. 2017. V. 36. № 22. P. 3356–3371.
69. Area-Gomez E., de Groof A., Bonilla E., Montesinos J., Tanji K., Boldogh I., Pon L., Schon E.A. // Cell Death Dis. 2018. V. 9. № 3. P. 335.
70. Annunziata I., Sano R., d'Azzo A. // Cell Death Dis. 2018. V. 9. № 3. P. 328.
71. Cho Y.Y., Kwon O.H., Chung S. // Molecules. 2020. V. 25. № 23. P. 5490.
72. Brandimarti R., Hill G.S., Geiger J.D., Meucci O. // Sci. Rep. 2017. V. 7. № 1. P. 15103.

73. Montesinos J., Pera M., Larrea D., Guardia-Laguarta C., Agrawal R.R., Velasco K.R., Yun T.D., Stavrovskaya I.G., Xu Y., Koo S.Y., et al. // EMBO J. 2020. V. 39. № 20. P. e103791.
74. Di Pardo A., Maglione V. // Front. Neurosci. 2018. V. 12. P. 249.
75. Area-Gomez E, Del Carmen Lara Castillo M., Tambini M.D., Guardia-Laguarta C., de Groof A.J., Madra M., Ikenouchi J., Umeda M., Bird T.D., Sturley S.L., et al. // EMBO J. 2012. V. 31. № 21. P. 4106–4123.
76. Takuma K., Fang F., Zhang W., Yan S., Fukuzaki E., Du H., Sosunov A., McKhann G., Funatsu Y., Nakamichi N., et al. // Proc. Natl. Acad. Sci. USA. 2009. V. 106. №47. P. 20021–20026.
77. Fang F., Yu Q., Arancio O., Chen D., Gore S.S., Yan S.S., Yan S.F. // Hum. Mol. Genet. 2018. V. 27. № 6. P. 1002–1014.
78. Piras S., Furfaro A.L., Domenicotti C., Traverso N., Marinari U.M., Pronzato M.A., Nitti M. // Oxid. Med. Cell. Longevity. 2016. V. 2016. P. 9348651.
79. Manczak M., Anekonda T.S., Henson E., Park B.S., Quinn J., Reddy P.H. // Hum. Mol. Genet. 2006. V. 15. № 9. P. 1437–1449.
80. Hu W., Wang Z., Zheng H. // J. Biol. Chem. 2018. V. 293. № 33. P. 12681–12689.
81. Rhein V., Song X., Wiesner A., Ittner L.M., Baysang G., Meier F., Ozmen L., Bluethmann H., Dröse S., Brandt U., et al. // Proc. Natl. Acad. Sci. USA. 2009. V. 106. № 47. P. 20057–20062.
82. Pickett E.K., Koffie R.M., Wegmann S., Henstridge C.M., Herrmann A.G., Colom-Cadena M., Lleo A., Kay K.R., Vaught M., Soberman R., et al. // J. Alzheimers Dis. 2016. V. 53. № 3. P. 787–800.
83. Spires-Jones T.L., Hyman B.T. // Neuron. 2014. V. 82. № 4. P. 756–771.
84. Grimm A., Eckert A. // J. Neurochem. 2017. V. 143. № 4. P. 418–431.
85. Qin W., Haroutunian V., Katsel P., Cardozo C.P., Ho L., Buxbaum J.D., Pasinetti G.M. // Arch. Neurol. 2009. V. 66. № 3. P. 352–361.
86. Katsouri L., Lim Y.M., Blondrath K., Eleftheriadou I., Lombardero L., Birch A.M., Mirzaei N., Irvine E.E., Mazarakis N.D., Sastre M. // Proc. Natl. Acad. Sci. USA. 2016. V. 113. № 43. P. 12292–12297.
87. Katsouri L., Parr C., Bogdanovic N., Willem M., Sastre M. // J. Alzheimers Dis. 2011. V. 25. № 1. P. 151–162.
88. Motyl J., Wencel P.L., Cieslik M., Strosznajder R.P., Strosznajder J.B. // Mol. Neurobiol. 2018. V. 55. № 1. P. 727–740.
89. Mohamed J.S., Hajira A., Pardo P.S., Boriek A.M. // Diabetes. 2014. V. 63. № 5. P. 1546–1559.
90. Long J.M., Maloney B., Rogers J.T., Lahiri D.K. // Mol. Psychiatry. 2019. V. 24. № 3. P. 345–363.
91. Chen F.Z., Zhao Y., Chen H.Z. // Int. J. Mol. Med. 2019. V. 43. № 1. P. 91–102.
92. Kumar S., Reddy P.H. // Biochim. Biophys. Acta. Mol. Basis. Dis. 2020. V. 1866. № 12. P. 165937.
93. John A., Kubosumi A., Reddy P.H. // Cells. 2020. V. 9. № 6. P. 1345.
94. Wang Y., Liu N., Lu B. // CNS. Neurosci. Ther. 2019. V. 25. № 7. P. 859–875.
95. Pradeepkiran J.A., Reddy H.P. // Ageing. Res. Rev. 2020. V. 64. P. 101191.
96. Cai Q., Jeong Y.Y. // Cells. 2020. V. 9. № 1. P. 150.
97. Liu L., Liao X., Wu H., Li Y., Zhu Y., Chen Q. // Antioxid. Redox Signal. 2020. V. 32. № 12. P. 906–927.
98. Du F., Yu Q., Yan S., Hu G., Lue L.F., Walker D.G., Wu L., Yan S.F., Tieu K., Yan S.S. // Brain. 2017. V. 140. № 12. P. 3233–3251.
99. Vaillant-Beuchot L., Mary A., Pardossi-Piquard R., Bourgeois A., Lauritzen I., Eysert F., Kinoshita P.F., Cazareth J., Badot C., Fragaki K., et al. // Acta. Neuropathol. 2021. V. 141. № 1. P. 39–65.
100. Guillaud L., El-Agamy S.E., Otsuki M., Terenzio M. // Front. Mol. Neurosci. 2020. V. 13. P. 556175.
101. Cagin U., Duncan O.F., Gatt A.P., Dionne M.S., Sweeney S.T., Bateman J.M. // Proc. Natl. Acad. Sci. USA. 2015. V. 112. № 44. P. E6000–E6009.
102. Wang Q., Tian J., Chen H., Du H., Guo L. // Neurobiol. Dis. 2019. V. 127. P. 410–418.
103. Tammineni P., Ye X., Feng T., Aikal D., Cai Q. // Elife. 2017. V. 6. P. e21776.
104. Pigino G., Morfini G., Pelsman A., Mattson M.P., Brady S.T., Busciglio J. // J. Neurosci. 2003. V. 23. № 11. P. 4499–4508.
105. Yu S.B., Pekkurnaz G. // J. Mol. Biol. 2018. V. 430. № 21. P. 3922–3941.
106. Glancy B., Kim Y., Katti P., Willingham T.B. // Front. Physiol. 2020. V. 11. P. 541040.
107. Oliver D., Reddy P.H. // Cells. 2019. V. 8. № 9. P. 961.
108. Harland M., Torres S., Liu J., Wang X. // J. Neurosci. 2020. V. 40. № 8. P. 1756–1765.
109. Wang W., Yin J., Ma X., Zhao F., Siedlak S.L., Wang Z., Torres S., Fujioka H., Xu Y., Perry G., et al. // Hum. Mol. Genet. 2017. V. 26. № 21. P. 4118–4131.
110. Wang X., Su B., Siedlak S.L., Moreira P.I., Fujioka H., Wang Y., Casadesus G., Zhu X. // Proc. Natl. Acad. Sci. USA. 2008. V. 105. № 49. P. 19318–19323.
111. Pradeepkiran J.A., Reddy A.P., Yin X., Manczak M., Reddy P.H. // Hum. Mol. Genet. 2020. V. 29. № 1. P. 49–69.
112. Eysert F., Kinoshita P.F., Mary A., Vaillant-Beuchot L., Checler F., Chami M. // Int. J. Mol. Sci. 2020. V. 21. № 24. P. 9521.
113. Wang L., Gao J., Liu J., Siedlak S.L., Torres S., Fujioka H., Huntley M.L., Jiang Y., Ji H., Yan T., et al. // Cell Metab. 2018. V. 28. № 3. P. 400-414.e8.
114. Leal N.S., Schreiner B., Pinho C.M., Filadi R., Wiehager B., Karlström H., Pizzo, P., Ankarcrona M. // J. Cell. Mol. Med. 2016. V. 20. № 6. P. 1686–1695.
115. Yu R., Liu T., Jin S.B., Ning C., Lendahl U., Nister M., Zhao J. // Sci. Rep. 2017. V. 7. № 1. P. 880.
116. Panes J.D., Godoy P.A., Silva-Grecchi T., Celis M.T., Ramirez-Molina O., Gavilan J., Munoz-Montecino C., Castro P.A., Moraga-Cid G., Yevenes G.E., et al. // Front. Pharmacol. 2020. V. 11. P. 709.
117. Manczak M., Reddy P.H. // Hum. Mol. Genet. 2012. V. 21. № 11. P. 2538–2547.
118. Kuruva C.S., Manczak M., Yin X., Ogunmokun G., Reddy A.P., Reddy P.H. // Hum. Mol. Genet. 2017. V. 26. № 17. P. 3375–3395.
119. Joshi A.U., Saw N.L., Shamloo M., Mochly-Rosen D. // Oncotarget. 2018. V. 9. № 5. P. 6128–6143.
120. Kim B., Park J., Chang K.T., Lee D.S. // Free. Radic. Biol. Med. 2016. V. 90. P. 184–194.
121. Kim D.I., Lee K.H., Gabr A.A., Choi G.E., Kim J.S., Ko S.H., Han H.J. // Biochim. Biophys. Acta. 2016. V. 1863. № 11. P. 2820–2834.
122. Kikuchi K., Kidana K., Tatebe T., Tomita T. // J. Cell. Biochem. 2017. V. 118. № 12. P. 4183–4190.
123. Jagust W. // Nat. Rev. Neurosci. 2018. V. 19. № 11.

P. 687–700.
124. Tarasoff-Conway J.M., Carare R.O., Osorio R.S., Glodzik L., Butler T., Fieremans E., Axel L., Rusinek H., Nicholson C., Zlokovic B.V., et al. // Nat. Rev. Neurol. 2015. V. 11. № 8. P. 457–470.
125. Xin S.H., Tan L., Cao X., Yu J.T., Tan L. // Neurotox. Res. 2018. V. 34. № 3. P. 733–748.
126. Porter K.N., Sarkar S.N., Dakhlallah D.A., Vannoy M.E., Quintana D.D., Simpkins J.W. // Front. Aging. Neurosci. 2020. V. 12. P. 92.
127. Zuroff L., Daley D., Black K.L., Koronyo-Hamaoui M. // Cell. Mol. Life. Sci. 2017. V. 74. № 12. P. 2167–2201.
128. Brunetti D., Torsvik J., Dallabona C., Teixeira P., Sztromwasser P., Fernandez-Vizarra E., Cerutti R., Reyes A., Preziuso C., D'Amati G., et al. // EMBO. Mol. Med. 2016. V. 8. № 3. P. 176–190.
129. Ciccone L., Shi C., di Lorenzo D., van Baelen A.C., Tonali N. // Molecules. 2020. V. 25. № 10. P. 2439.
130. Teixeira P.F., Masuyer G., Pinho C.M., Branca R.M.M., Kmiec B., Wallin C., Wärmländer S.K.T.S., Berntsson R.P., Ankarcrona M., Gräslund A., et al. // J. Mol. Biol. 2018. V. 430. № 3. P. 348–362.
131. Song E.S., Rodgers D.W., Hersh L.B. // Sci. Rep. 2018. V. 8. № 1. P. 2335.
132. Song E.S., Jang H., Guo H.F., Juliano M.A., Juliano L., Morris A.J., Galperin E., Rodgers D.W., Hersh L.B. // Proc. Natl. Acad. Sci. USA. 2017. V. 114. № 14. P. E2826–E2835.
133. Kurochkin I.V., Guarnera E., Wong J.H., Eisenhaber F., Berezovsky I.N. // Biochemistry. 2017. V. 56. № 1. P. 228–239.
134. Deprez-Poulain R., Hennuyer N., Bosc D., Liang W.G., Enée E., Marechal X., Charton J., Totobenazara J., Berte G., Jahklal J., et al. // Nat. Commun. 2015. V. 6. P. 8250.
135. Wang L., Shi F.X., Xu W.Q., Cao Y., Li N., Li M., Wang Q., Wang J.Z., Tian Q., Yu L.K. // J. Alzheimers. Dis. 2018. V. 64. № 3. P. 957–971.
136. Nalivaeva N.N., Zhuravin I.A., Turner A.J. // Mech. Ageing. Dev. 2020. V. 192. P. 111363.
137. de Dios C., Bartolessis I., Roca-Agujetas V., Barbero-Camps E., Mari M., Morales A., Colell A. // Redox. Biol. 2019. V. 26. P. 101283.
138. Yamamoto N., Nakazawa M., Nunono N., Yoshida N., Obuchi A., Tanida M., Suzuki K., Ikeda-Matsuo Y., Sobue K. // Neurosci. Res. 2021. V. 166. P. 62–72.
139. Brunetti D., Catania A., Viscomi C., Deleidi M., Bindoff L.A., Ghezzi D., Zeviani M. // Biomedicines. 2021. V. 9. № 7. P. 833.
140. Fang D., Wang Y., Zhang Z., Du H., Yan S., Sun Q., Zhong C., Wu L., Vangavaragu J.R., Yan S., et al. // Hum. Mol. Genet. 2015. V. 24. № 18. P. 5198–5210.
141. Falkevall A., Alikhani N., Bhushan S., Pavlov P.F., Busch K., Johnson K.A., Eneqvist T., Tjernberg L., Ankarcrona M., Glaser E. // J. Biol. Chem. 2006. V. 281. № 39. P. 29096–29104.
142. Alikhani N., Ankarcrona M., Glaser E. // J. Bioenerg. Biomembr. 2009. V. 41. № 5. P. 447–451.
143. Alikhani N., Guo L., Yan S., Du H., Pinho C.M., Chen J.X., Glaser E., Yan S.S. // J. Alzheimers Dis. 2011. V. 27. № 1. P. 75–87.
144. Chen J., Teixeira P.F., Glaser E., Levine R.L. // Free. Radic. Biol. Med. 2014. V. 77. P. 57–63.
145. Teixeira P.F., Pinho C.M., Branca R.M., Lehtiö J., Levine R.L., Glaser E. // Free. Radic. Biol. Med. 2012. V. 53. № 11. P. 2188–2195.
146. Xu Y.J., Mei Y., Qu Z.L., Zhang S.J., Zhao W., Fang J.S., Wu J., Yang C., Liu S.J., Fang Y.Q., et al. // Biomed. Res. Int. 2018. V. 2018. P. 4606752.
147. Hemmerová E., Špringer T., Krištofiková Z., Homola J. // Sci. Rep. 2019. V. 9. № 1. P. 16700.
148. Zakaria A., Hamdi N., Abdel-Kader R.M. // Mol. Neurobiol. 2016. V. 53. № 2. P. 1220–1228.
149. Xiao X., Chen Q., Zhu X., Wang Y. // Neurobiol. Aging. 2019. V. 81. P. 77–87.
150. Morsy A., Trippier P.C. // J. Med. Chem. 2019. V. 62. № 9. P. 4252–4264.
151. Reiss A.B., Arain H.A., Stecker M.M., Siegart N.M., Kasselman L.J. // Rev. Neurosci. 2018. V. 29. № 6. P. 613–627.
152. Park I., Londhe A.M., Lim J.W., Park B.G., Jung S.Y., Lee J.Y., Lim S.M., No K.T., Lee J., Pae A.N. // J. Comput. Aided. Mol. Des. 2017. V. 31. № 10. P. 929–941.
153. Rottenberg H., Hoek J.B. // Aging. Cell. 2017. V. 16. № 5. P. 943–955.
154. Marroquin L., Swiss R., Will Y. // Curr. Protoc. Toxicol. 2014. V. 60. № 1. P. 25.4.1–25.4.17.
155. Bhatia V., Sharma S. // J. Neurol. Sci. 2021. V. 421. P. 117253.
156. Guo L., Du H., Yan S., Wu X., McKhann G.M., Chen J.X., Yan S.S. // PLoS One. 2013. V. 8. № 1. P. e54914.
157. Nalivaeva N.N., Turner A.J. // Br. J. Pharmacol. 2019. V. 176. № 18. P. 3447–3463.
158. Chang X., Rong C., Chen Y., Yang C., Hu Q., Mo Y., Zhang C., Gu X., Zhang L., He W., et al. // Exp. Cell. Res. 2015. V. 334. № 1. P. 136–145.
159. Zhuravin I.A., Dubrovskaya N.M., Vasilev D.S., Kozlova D.I., Kochkina E.G., Tumanova N.L., Nalivaeva N.N. // Neurochem. Res. 2019. V. 44. № 6. P. 1387–1398.
160. Nan S., Wang P., Zhang Y., Fan J. // Drug. Des. Devel. Ther. 2021. V. 15. P. 2013–2024.
161. Li H., Yu S., Fan T., Zhong Y., Gu T., Wu W., Wang X. // Drug. Dev. Res. 2020. V. 81. № 2. P. 206–214.
162. Wang N., Jia Y., Zhang B., Li Y., Murtaza G., Huang S., Liu X. // Evid. Based. Complement. Alternat. Med. 2020. V. 2020. P. 3862342.
163. Lyu W., Ouyang M., Ma X., Han T., Pi D., Qiu S. // Evid. Based. Complement. Alternat. Med. 2021. V. 2021. P. 5521739.
164. Xu Y.M., Wang X.C., Xu T.T., Li H.Y., Hei S.Y., Luo N.C., Wang H., Zhao W., Fang S.H., Chen Y.B., et al. // Neural. Regen. Res. 2019. V. 14. № 5. P. 794–804.
165. Guo S., Wang J., Wang Y., Zhang Y., Bi K., Zhang Z., Li Q. // Oxid. Med. Cell Longev. 2019. V. 2019. P. 1707218.
166. Farkhondeh T., Samarghandian S., Pourbagher-Shahri A.M., Sedaghat M. // J. Cell. Physiol. 2019. V. 234. № 10. P. 16953–16965.
167. Amalraj A., Pius A., Gopi S., Gopi S. // J. Tradit. Complement. Med. 2017. V. 7. № 2. P. 205–233.
168. Zia A., Farkhondeh T., Pourbagher-Shahri A.M., Samarghandian S. // Biomed. Pharmacother. 2021. V. 134. P. 111119.
169. Ege D. // Materials (Basel). 2021. V. 14. № 12. P. 3332.
170. Amato A., Terzo S., Mulè F. // Antioxidants (Basel). 2019. V. 8. № 12. P. 608.
171. Teter B., Morihara T., Lim G.P., Chu T., Jones M.R., Zuo X., Paul R.M., Frautschy S.A., Cole G.M. // Neurobiol. Dis. 2019. V. 127. P. 432–448.
172. Ege D. // Materials (Basel). 2021. V. 14. № 12. P. 3332.
173. Doytchinova I., Atanasova M., Salamanova E., Ivanov S., Dimitrov I. // Biomolecules. 2020. V. 10. № 9. P. 1323.
174. Zhao L.N., Chiu S.W., Benoit J., Chew L.Y., Mu Y. // J.

Phys. Chem. B. 2012. V. 116. P. 7428–7435.
175. Ngo S.T., Li M.S. // J. Phys. Chem B. 2012. V. 116. P. 10165–10175.
176. Kundaikar H.S., Degani M.S. // Chem. Biol. Drug Des. 2015. V. 86. P. 805–812.
177. Tavanti F., Pedone A., Menziani M.C. // Molecules. 2018. V. 23. P. 1320.
178. Zheng K., Dai X., Xiao N., Wu X., Wei Z., Fang W., Zhu Y., Zhang J., Chen X. // Mol Neurobiol. 2017. V. 54. № 3. P. 1967–1977.
179. Huang P., Zheng N., Zhou H.B., Huang J. // Mol. Cell. Biochem. 2020. V. 463. № 1–2. P. 161–173.
180. Matiadis D., Ng S.T., Chen E.H., Nigianni G., Vidali V.P., Canko A., Chen R.P., Sagnou M. // Biomedicines. 2021. V. 9. № 8. P. 955.
181. Amato A., Terzo S., Mulè F. // Antioxidants (Basel). 2019. V. 8. № 12. P. 608.
182. Esselun C., Bruns B., Hagl S., Grewal R., Eckert G.P. // Antioxidants (Basel). 2021. V. 10. № 10. P. 1520.
183. Bai D., Jin G., Zhang D., Zhao L., Wang M., Zhu Q., Zhu L., Sun Y., Liu X., Chen X., et al. // J. Physiol. Sci. 2019. V. 69. № 4. P. 643–652.
184. Saravanan K., Sugarthi S., Suganya S., Kumaradhas P. // J. Biomol. Struct. Dyn. 2021. V. 12. № 1. P. 15.
185. Shen L., Liu L., Li X.Y., Ji H.F. // Appl. Microbiol. Biotechnol. 2019. V. 103. № 17. P. 7141–7149.
186. Wang X.-L., Lin F.-L., Xu W., Wang C., Wang Q., Jiang R.W. // Eur. J. Pharmacol. 2022. V. 288. P. 114938.
187. Huo Q., Shi Y., Qi Y., Huang L., Sui H., Zhao L. // Mater. Sci. Eng. C. Mater. Biol. Appl. 2021. V. 129. P. 112365.
188. Pan Q., Ban Y., Xu L. // J. Biomed. Nanotechnol. 2021. V. 17. № 6. P. 1123–1130.
189. Alizadeh S.R., Ebrahimzadeh M.A. // Phytother. Res. 2022. V. 36. № 2. P. 778–807.
190. Ghafouri-Fard S., Shoorei H., Khanbabapour Sasi A., Taheri M., Ayatollahi S.A. // Biomed. Pharmacother. 2021. V. 141. P. 111847.
191. Khan H., Ullah H., Aschner M., Cheang W.S., Akkol E.K. // Biomolecules. 2020. V. 10. № 1. P. 59.
192. Zhang X.W., Chen J.Y., Ouyang D., Lu J.H. // Int. J. Mol. Sci. 2020. V. 21. № 2. P. 493.
193. Maccioni R.B., Calfío C., González A., Lüttges V. // Biomolecules. 2022. V. 12. № 2. P. 249.
194. Elfiky A.M., Mahmoud A.A., Elreedy H.A., Ibrahim K.S., Ghazy M.A. // Life. Sci. 2021. V. 285. P. 119964.
195. Das S., Majumder T., Sarkar A., Mukherjee P., Basu S. // Int. J. Mol. Sci. 2020. V. 165. P. 1323–1330.
196. Tanaka M., Saito S., Inoue T., Satoh-Asahara N., Ihara M. // Int. J. Mol. Sci. 2020. V. 21. № 6. P. 1992.
197. Li Y., Zhao J., Hölscher C. // CNS Drugs. 2017. V. 31. № 8. P. 639–652.
198. Shi J., Li Y., Zhang Y., Chen J., Gao J., Zhang T., Shang X., Zhang X. // Front. Pharmacol. 2021. V. 12. P. 794458.
199. Dhakal S., Ramsland P.A., Adhikari B., Macreadie I. // Int. J. Mol. Sci. 2021. V. 22. № 17. P. 9456.
200. Ali F., Rahul., Jyoti S., Naz F., Ashafaq M., Shahid M., Siddique Y.H. // Neurosci. Lett. 2019. V. 692. P. 90–99.
201. Akbar M., Shabbir A., Rehman K., Akash M.S.H., Shah M.A. // J. Food Biochem. 2021. V. 45. № 10. P. e13936.
202. Liang Y., Ye C., Chen Y., Chen Y., Diao S., Huang M. // ACS Chem. Neurosci. 2021. V. 12. № 11. P. 1894–1904.
203. Fang Z., Tang Y., Ying J., Tang C., Wang Q. // Chin. Med. 2020. V. 15. P. 82.
204. Raju M., Kunde S.S., Auti S.T., Kulkarni Y.A., Wairkar S. // Life Sci. 2021. V. 285. P. 119990.
205. Azam S., Park J.Y., Kim I.S., Choi D.K. // Biomedicines. 2022. V. 10. № 1. P. 154.
206. Chetia P., Mazumder M.K., Mahanta S., De B., Choudhury M.D. // Med. Hypotheses. 2020. V. 142. № 2. P. 109839.
207. Miao S.X., Wan L.X., He Z.X., Zhou X.L., Li X., Gao F. // J. Nat. Prod. 2021. V. 84. № 8. P. 2374–2379.
208. Zhou D.D., Luo M., Huang S.Y., Saimaiti A., Shang A., Gan R.Y., Li H.B. // Oxid. Med. Cell. Longev. 2021. V. 2021. P. 9932218.
209. Noori T., Dehpour A.R., Sureda A., Sobarzo-Sanchez E., Shirooie S. // Eur. J. Pharmacol. 2021. V. 898. P. 173974.
210. Mphahlele M.J., Agbo E.N., More G.K., Gildenhuys S. // Antioxidants (Basel). 2021. V. 10. № 5. P. 647.
211. Haghighijoo Z., Akrami S., Saeedi M., Zonouzi A., Iraji A., Larijani B., Fakherzadeh H., Sharifi F., Arzaghi S.M., Mahdavi M., et al. // Bioorg. Chem. 2020. V. 103. P. 104146.
212. Vishal P.K., Oh J.M., Khames A., Abdelgawad M.A., Nair A.S., Nath L.R., Gambacorta N., Ciriaco F., Nicolotti O., Kim H., et al. // Pharmaceutics. 2021. V. 13. № 6. P. 850.
213. Singh N.A., Bhardwaj V., Ravi C., Ramesh N., Mandal A.K.A., Khan Z.A. // Front. Aging Neurosci. 2018. V. 10. P. 244.
214. Mori T., Koyama N., Tan J., Segawa T., Maeda M., Town T. // J. Biol. Chem. 2019. V. 294. № 8. P. 2714–2731.
215. Yue W., Xu W., Song Y.U., Chun W. // Nat. Prod. Res. Dev. 2017. V. 29. P. 762–766.
216. Qian W., Wei-wei Q., Jie-wen Z. // Chin. Pharm. J. 2019. V. 54. P. 703–710.
217. Wang H., Li L., Jia K., Wang Q., Sui S., Lin Y., He Y. // Neuroreport. 2020. V. 31. P. 1104–1110.
218. Lee H.J., Jeong H.R., Park J.H., Hoe H.S. // Biology (Basel). 2021. V. 10. № 9. P. 938.
219. Kaur D., Behl T., Sehgal A., Singh S., Sharma N., Chigurupati S., Alhowail A., Abdeen A., Ibrahim S.F., Vargas-De-La-Cruz C., et al. // Life. Sci. 2021. V. 284. P. 119899.
220. Reddy P.H., Manczak M., Kandimalla R. // Hum. Mol. Genet. 2017. V. 26. № 8. P. 1483–1496.
221. Stefanova N.A., Muraleva N.A., Maksimova K.Y., Rudnitskaya E.A., Kiseleva E., Telegina D.V., Kolosova N. // Aging (Albany NY). 2016. V. 8. № 11. P. 2713–2733.
222. Zafeer M.F., Firdaus F., Anis E., Mobarak Hossain M. // Neurotoxicology. 2019. V. 73. P. 246–257.
223. Lan J.S., Zeng R.F., Jiang X.Y., Hou J.W., Liu Y., Hu Z.H., Li H.X., Li Y., Xie S.S., Ding Y., Zhang T. // Bioorg. Chem. 2020. V. 94. P. 103413.
224. Benchekroun M., Pachón-Angona I., Luzet V., Martin H., Oset-Gasque M.J., Marco-Contelles J., Ismaili L. // Bioorg. Chem. 2019. V. 85. P. 221–228.
225. Costa M., Bernardi J., Fiuza T., Costa L., Brandão R., Pereira M.E. // Chem. Biol. Interact. 2016. V. 253. P. 10–17.
226. Dos Santos S.M., Romeiro C.F.R., Rodrigues C.A., Cerqueira A.R.L., Monteiro M.C. // Oxid. Med. Cell. Longev. 2019. V. 2019. P. 8409329.
227. Shinto L., Quinn J., Montine T., Dodge H.H., Woodward W., Baldauf-Wagner S., Waichunas D., Bumgarner L., Bourdette D., Silbert L., et al. // J. Alzheimers. Dis. 2014. V. 38. № 1. P. 111–120.
228. Reddy P.H., Manczak M., Kandimalla R. // Hum. Mol. Genet. 2017. V. 26. № 8. P. 1483–1496.
229. Reddy P.H., Manczak M., Yin X., Reddy A.P. // J. Alzheimers Dis. 2018. V. 62. № 4. P. 1549–1565.

230. Hroch L., Benek O., Guest P., Aitken L., Soukup O., Janockova J., Musil K., Dohnal V., Dolezal R., Kuca K., et al. // Bioorg. Med. Chem. Lett. 2016. V. 26. № 15. P. 3675–3678.
231. Aitken L., Benek O., McKelvie B.E., Hughes R.E., Hroch L., Schmidt M., Major L.L., Vinklarova L., Kuca K., Smith T.K., et al. // Molecules. 2019. V. 24. № 15. P. 2757.
232. Benek O., Hroch L., Aitken L., Dolezal R., Guest P., Benkova M., Soukup O., Musil K., Kuca K., Smith T.K., et al. // Med. Chem. 2017. V. 13. № 4. P. 345–358.
233. Xiao X., Chen Q., Zhu X., Wang Y. // Neurobiol. Aging. 2019. V. 81. P. 77–87.
234. Yao J., Du H., Yan S., Fang F., Wang C., Lue L.F., Guo L., Chen D., Stern D.M., Moore F.J., et al. // J. Neurosci. 2011. V. 31. № 6. P. 2313–2320.

Human Artificial Chromosomes and Their Transfer to Target Cells

S. V. Ponomartsev[1], S. A. Sinenko[1*], A. N. Tomilin[1,2*]
[1]Institute of Cytology Russian Academy of Sciences, St. Petersburg, 194064 Russia
[2]Institute of Translational Biomedicine, St. Petersburg State University, St. Petersburg, 199034 Russia
[*]E-mail: s.sinenko@incras.ru, a.tomilin@incras.ru
Received December 27, 2021; in final form, July 12, 2022
DOI: 10.32607/actanaturae.11670

ABSTRACT **Human artificial chromosomes (HACs) have been developed as genetic vectors with the capacity to carry large transgenic constructs or entire gene loci. HACs represent either truncated native chromosomes or *de novo* synthesized genetic constructs. The important features of HACs are their ultra-high capacity and ability to self-maintain as independent genetic elements, without integrating into host chromosomes. In this review, we discuss the development and construction methods, structural and functional features, as well as the areas of application of the main HAC types. Also, we address one of the most technically challenging and time-consuming steps in this technology – the transfer of HACs from donor to recipient cells.**
KEYWORDS **human artificial chromosomes, microcell-mediated chromosome transfer, tetracycline operator, transformation-associated recombination.**
ABBREVIATIONS **HAC – human artificial chromosome; BAC – bacterial artificial chromosome; YAC – yeast artificial chromosome; MMCT – microcell-mediated chromosome transfer; TAR – transformation-associated recombination; CENP-B – centromere protein B; ESCs – embryonic stem cells; iPSCs – induced pluripotent stem cells; CHO – Chinese hamster ovary; *tetO* – tetracycline operator; HSV-1 – herpes simplex virus 1; HVJ-E – hemagglutinating virus of Japan envelope; MLV – murine leukemia retrovirus; TACF – telomere associated chromosome fragmentation; FSCT – flow sorted chromosome transfer; MWCF – micronucleated whole cell fusion; iMCT – isolated metaphase chromosome transfection; PEG – polyethylene glycol; HPRT – hypoxanthine-guanine phosphoribosyltransferase; FACS – fluorescence activated cell sorting; GFP – green fluorescent protein; DNA – deoxyribonucleic acid; bp – base pairs.**

INTRODUCTION

Human artificial chromosomes (HACs) were conceived primarily as expression vector systems for the transfer of transgenes into eukaryotic cells. To date, many vector systems have been created that differ in their main characteristics: (1) the ability to integrate into the chromosomes of host cells or remain in episomal form; (2) the genetic capacity that restricts the maximum transgene size; (3) and the method of vector delivery. Integrating vectors are inserted into the host cell's DNA and, consequently, are inherited by daughter cells. The disadvantages of these vector systems include their random integration into the genome, which comes with the risk of insertional mutagenesis and epigenetic repression of transgene expression. Integrating vectors include linearized plasmids and vector systems based on retroviruses [1–3] and transposons, such as piggy-Bac, Sleeping Beaty, and Tol2 [4–6].

Non-integrating vectors are present in episomal state in the host cells. During cell division, these vectors are unevenly distributed between daughter cells and gradually lost. These systems are convenient for transient transfection of cells, but they are not suitable for long-term expression of transgenes. These vector systems are exemplified by circular plasmids and vectors based on adenoviruses, alphaviruses, herpesviruses, baculoviruses, poxviruses, and bacteriophages [1, 2, 7]. An important parameter of vector systems is their capacity that is defined as the maximum size of an inserted transgene. Plasmids can be used to transfer transgenes of up to 20 kilo base pairs (kbp) in length. Transposon-based vectors can be used to deliver transgenic DNA of up to 9 kbp, whereas viral DNA-based vector systems can accommodate transgenes of up to 150 kbp [12]. There are various methods for the transfer of expression vector systems

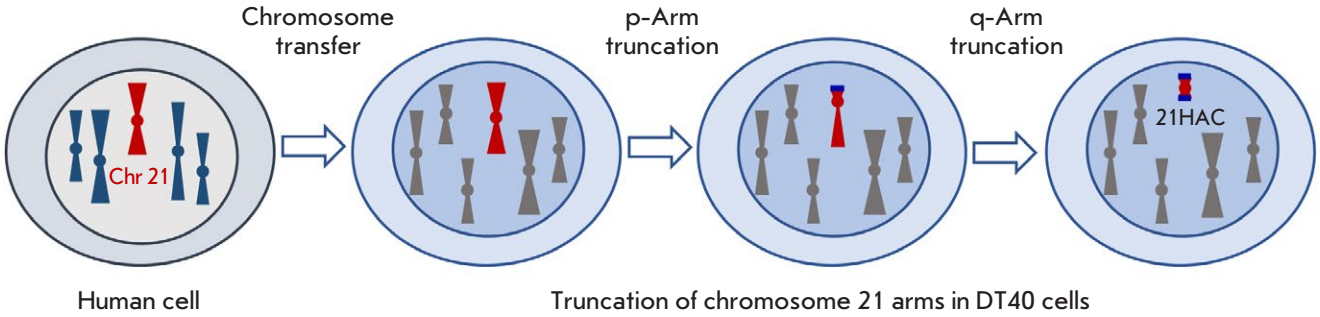

Fig. 1. Schematic representation of 21HAC assembly using telomere-associated chromosome truncation. Human chromosome 21 was transferred to DT40 cells. Then, telomeric sequences (shown in blue) were inserted into the pericentromeric site using homologous recombination, which led to truncation of the chromosome. Thus, the 21HAC was generated using successive truncation of chromosome arms and their replacement with telomeric sequences

into target cells. Plasmids and DNA transposon-based vectors are transferred using calcium phosphate transfection, electroporation, lipofection, sonoporation, microinjection, magnetofection, and the so-called gene gun. Delivery of viral DNA-based vectors, which is called transduction, is performed using the host cell infection mechanisms typical of viruses.

Human artificial chromosomes are vector constructs that possess the following crucial chromosomal characteristics: (1) the ability to self-maintain autonomously, i.e., as an additional chromosome, in the cell and (2) the ability to replicate and be transmitted to both daughter cells during cell division. Thus, the use of HACs skirts the risks of insertional mutagenesis and ensures a stable expression of transgenes. A unique feature of HACs is their ultra-high capacity that enables the transfer of transgenes up to several-million-base-pairs long, in particular entire gene loci with *cis*-regulatory elements, which ensures an accurate expression of endogenous loci. Although many structurally diverse HACs have been developed to date, these vector systems are still being intensively improved and modified [8–13]. Two approaches are used to produce HACs. The first is the so-called top-down approach that is based on the production of HACs from native chromosomes by their maximal truncation, leaving only the centromeric and telomeric regions that are necessary for their stable replication in the cell [14–16]. The second is the synthetic bottom-up approach that is used to produce linear or circular HACs through the synthesis and assembly of large regions of pericentromeric alpha-satellite DNA *in vitro* [13, 17–19]. It should be noted that, despite the obvious advantages of HACs over other vector systems, there is a number of technical limitations standing in the way of their extensive use both in scientific research and in biomedical applications. One of the main limitations of the system is the inefficiency and laboriousness of the methods used to transfer HAC into target cells. This review describes different HAC types, methods of delivery into cells, and prospects for the application of these ultra-high capacity episomal vectors in medical practice.

MAIN HAC TYPES AND METHODS FOR THEIR PRODUCTION

HACs produced by reduction of native human chromosomes

Eukaryotic chromosomes can be truncated using telomere-associated chromosome fragmentation (TACF) [20]. To date, these are the most characterized and improved HACs in terms of their use as stable expression-vector systems. The top-down approach enables truncation of chromosome arms and their replacement with new telomere-containing regions that are inserted into selected loci using homologous recombination. The resulting HACs may contain some cryptic genes and non-coding sequences, but they always involve the elements necessary for their stable maintenance in the cell nucleus (telomeres) and equal distribution between daughter cells during cell division (centromeres). For site-specific integration of transgenes into these constructs, appropriate sequences, e.g., *loxP* sites, which mediate transgene integration through Cre-dependent recombination, are preliminarily introduced in the transgenes. Also, HACs often contain selective markers that enable positive selection of HAC-containing cells. The use of TACF has enabled the production of artificial chromosomes based on human chromosomes 14 [21] and 21 [16, 22, 23] and mouse chromosome 11 (mouse artificial chromosomes) [24]. The HAC based on human chromosome 21, 21HAC [16], which was produced in several stages (*Fig. 1*),

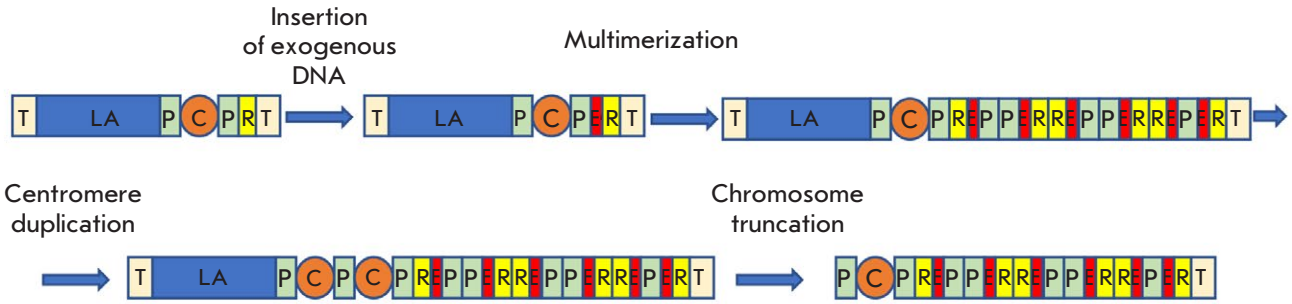

Fig. 2. Diagram of generation of a satellite DNA-based artificial chromosome (SATAC). Exogenous DNA bearing site-specific recombination sites, a selective marker, and other sequences is inserted into the pericentromeric region of an acrocentric chromosome using homologous recombination. This insertion results in the amplification of pericentromeric, ribosomal, and exogenous DNA regions. Centromere duplication is followed by chromosome truncation, which leads to HAC formation. Symbols: T – telomere; LA – long arm of the acrocentric chromosome; P – pericentromeric region; C – centromere; R – ribosomal DNA; E – exogenous DNA

is the most technically advanced construct to date. Native human chromosome 21 was first transferred into chicken DT40 cells suitable for homologous DNA recombination [25]. Then, the p-arm was deleted from the transferred chromosome using TACF; for that purpose, a telomeric sequence was inserted into the pericentromeric region using homologous recombination. Along with the telomeric sequence, a selective marker was also inserted; the marker enables selection of the cells in which recombination has occurred. The q-arm was deleted in a similar way (*Fig. 1*). In addition to the telomeric region, the *loxP* site, a fragment of the hypoxanthine-guanine-phosphoribosyltransferase (*HPRT*) gene, and other elements were also introduced into the 21HAC. Using sequencing, the resulting 21HAC was shown to contain not only the centromeric region and inserted elements, but also an insignificant amount of residual genetically inert material [26]. The resulting HAC was transferred from DT40 cells to CHO cells for the final stage of HAC assembly, which includes loading of an appropriate transgene using site-specific recombination, as well as maintenance and production of this HAC. Then, the HAC was transferred to the target cells using microcell-mediated chromosome transfer (MMCT) as described below.

There are several 21HAC modifications that have been generated using different selective markers: the green fluorescent protein (*GFP*) gene, thymidine kinase (*tk*) gene of the herpes simplex virus, and resistance genes to neomycin, hygromycin, and blasticidin [26]. There is also a 21HAC containing a multi-integrase locus involving the *loxP*, *FRT*, *φC31attP*, *R4attP*, *TP901-1attP*, and *Bxb1attP* sites [23]. This HAC has been used in various research and gene therapy models [8], the development of expression vectors for correction of Duchenne muscular dystrophy [22, 27, 28], hemophilia A [29], and the reprogramming of mouse embryonic fibroblasts [30].

Satellite-based HACs

Another HAC type generated using the top-down approach is produced by inserting a transgene into the ribosomal DNA gene cluster in the short arms of acrocentric chromosomes [31, 32] (*Fig. 2*). This insertion may be associated with replication errors, which results in the formation of long inverted repeats [33]. Along with this, the centromere doubles, the chromosome breaks off, and the short arm fragment forms a separate chromosome that behaves as an independent replicative unit [34, 35] and enables a stable expression of the inserted transgene [36]. The resulting HACs, called satellite DNA-based artificial chromosomes (SATACs), are isolated from donor cells using flow cytofluorometry and transferred to target cells using dendrimers and cationic particles [37] or microinjection [38, 39]. Mouse embryonic stem cells (ESCs) with transferred SATACs were able to participate in normal embryonic development [38, 40].

Alphoid HACs

A fundamentally different way to create HACs is based on the synthesis of extended nucleotide sequences possessing the main functions of chromosomes. The main difficulty in the bottom-up approach is the design of a functional artificial centromere sequence. In human chromosomes, this sequence is known to consist of alpha-satellite DNA tandem repeats 230 kbp to several mega base pairs (Mbp) in length [41]. These sequences are very difficult to

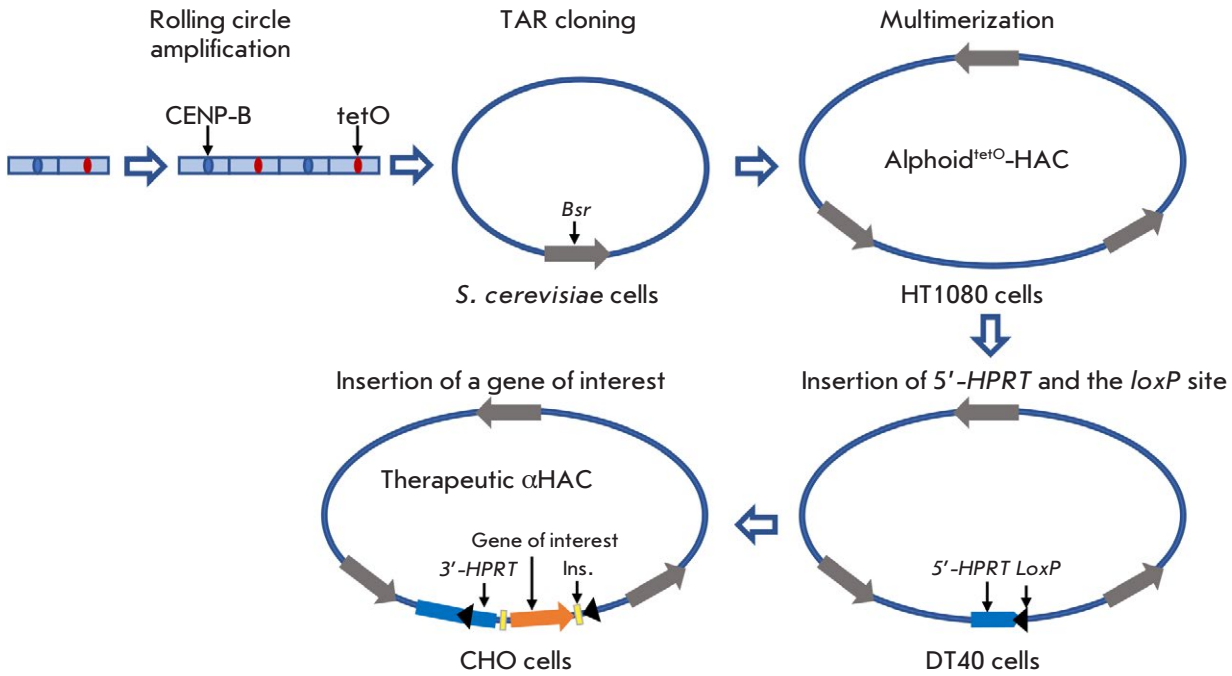

Fig. 3. Representation of alphoid^{tetO}-HAC assembly. At the first step, a tandem array comprising two units is synthesized: one unit is a 170-bp *CENP-B-box*-containing (blue oval) alphoid repeat from the human chromosome 17 centromere, and the second unit contains the same repeat in which the *CENP-B-box* is replaced with the tetracycline operator (*tetO*, red oval). Rolling circle amplification of the array produces a 10-kbp fragment. These fragments are cloned by TAR cloning in yeast cells, which provides a 50-kbp circular construct containing the blasticidin resistance gene (*Bsr*, gray arrow). The circular construct is multimerized in HT1080 cells, which results in the formation of a 1.1-Mbp alphoid^{tetO}-HAC. Fusion of HT1080 cells with DT40 cells (black arrow) is accompanied by the insertion of the *loxP* site into the HAC. The alphoid^{tetO}-HAC is transferred to CHO cells, where the construct is loaded with a gene of interest (orange arrow), together with the flanking insulator sequences (yellow boxes) and a 3′ fragment of the *HPRT* gene (blue line). The alphoid^{tetO}-HAC is transferred to target cells using MMCT

clone, due to spontaneous recombination [42]. The first successful attempt to clone human centromeric DNA was undertaken in 1997 [43]. Using multiple ligation rounds, long (several kbp) alpha-satellite DNA tandem repeats from the centromeres of human chromosomes 17 and Y were cloned into a bacterial artificial chromosome (BAC), resulting in repeats of up to 173 kbp in length. Ligation of these fragments provided human alpha-satellite DNA sequences more than 1 Mbp in length. The cloned centromeric repeats, telomeric sequences, and human genomic DNA fragments were transferred to human fibrosarcoma HT1080 cells, where they nonspecifically recombined with each other. In some cases, small HACs were formed, which remained stable in the cell nucleus and were inherited by both daughter cells. Thus, the fundamental possibility of *de novo* HAC assembly was shown for the first time, which gave impetus to further research in this direction.

Alphoid^{tetO}-HAC

This HAC type is assembled using alpha-satellite DNA amplification by rolling circle replication and transformation-associated recombination (TAR) [44–46] (*Fig. 3*). The former method is used to multimerize a DNA dimer, one monomer of which is a 170-bp alpha-satellite DNA sequence from human chromosome 17, which contains the *CENP-B box* (required for the assembly of the kinetochore complex), and the other monomer is the same sequence where the *CENP-B box* is replaced with the *tetO* site. Next, the multimerized alpha-satellite DNA repeats and linearized vector for TAR cloning were transferred to *Saccharomyces cerevisiae* yeast cells, where the DNA

repeats recombined with each other. This event resulted in the formation of longer sequences that were inserted into the TAR vector containing the blasticidin resistance gene [47–50]. The resulting constructs were transferred to HT1080 human fibrosarcoma cells, where they additionally multimerized and formed circular DNA molecules 1–2.5 Mbp in length. Thus, the main sequence of these molecules was centromeric alpha-satellite DNA. The produced genetic constructs were shown to be stable and act as independent genetic elements in cells: i.e., they were HACs [51, 52]. For further genetic manipulations, HT1080 cells containing the resulting HACs were fused with DT40 cells that are commonly used for homologous recombination of genetic elements. This resulted in the formation of HACs with an inserted *loxP* site and a 5'-fragment of the *HPRT* gene. These HACs were transferred to *HPRT*-mutant CHO cells using the MMCT procedure (see below). A desired transgene can be inserted into HACs within these cells by Cre-mediated recombination at the *loxP* site. For this purpose, this transgene containing regulatory sequences, flanking insulators, and a 3'-fragment of the *HPRT* gene are inserted into a HAC (*Fig. 3*). Thus, correct transgene insertion into a HAC is accompanied by *HPRT* gene restoration, which enables selection of target clones in the presence of hypoxanthine-aminopterin-thymidine (HAT). It should be noted that the presence of *tetO* sites in alphoid^{tetO} HAC enables, if necessary, deletion of these chromosomes during cell division. For this purpose, cells are induced to express TetR repressors that bind *tetO*, repress centromeric chromatin, and, thus, inhibit kinetochore complex formation [18, 52–54].

Full-length genes containing their own *cis*-regulatory sequences were transferred to target cells using alphoid^{tetO} HACs, and stable expression of these genes was demonstrated [19, 54–56]. In our studies, GFP-expressing alphoid^{tetO} HACs were transferred to mouse ESCs. Teratomas and chimeric mice generated using these cells stably maintained this HAC and expressed GFP in differentiated progeny of ESCs [57]. Also, the alphoid^{tetO} HAC was successfully transferred to human iPSCs that retained

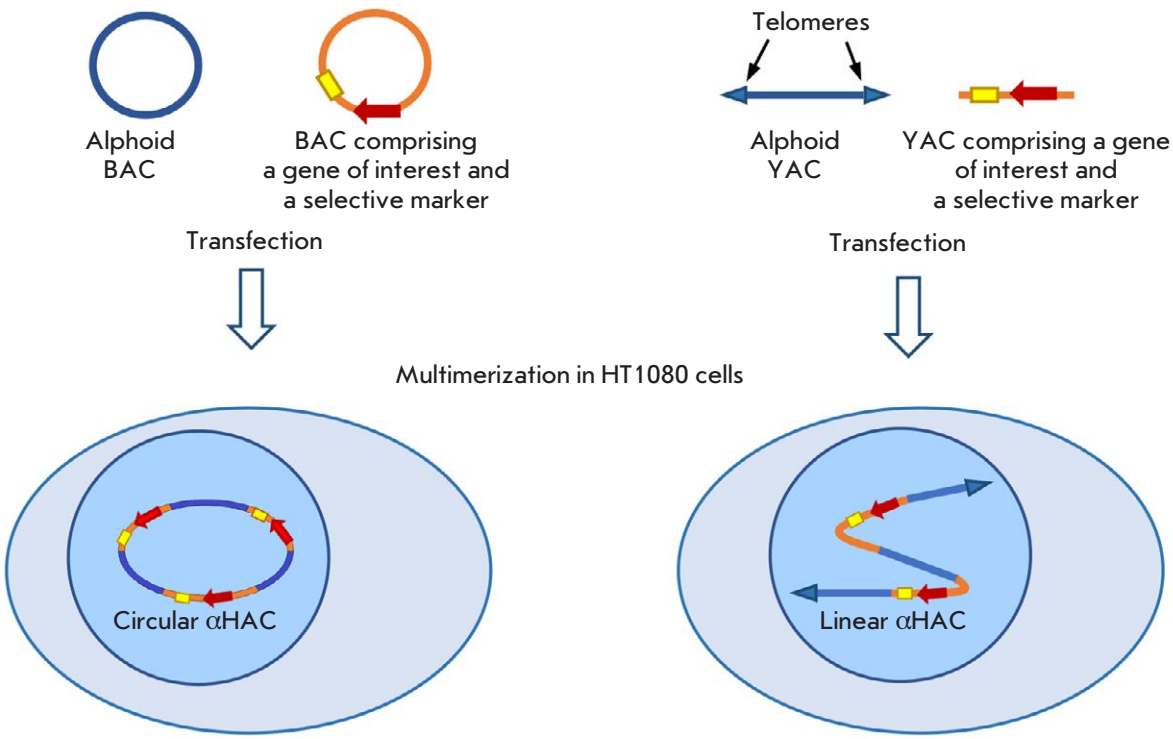

Fig. 4. Diagram of HAC assembly using bacterial and yeast artificial chromosomes (BACs and YACs, respectively). Circular BACs or linear YACs are used to assemble two vectors: one vector contains alphoid DNA, and the other contains a gene of interest. These constructs co-transfected into HT1080 cells undergo recombination and multimerization to form circular or linear alphoid HACs (αHACs)

pluripotent properties in the presence of this HAC [58]. Thus, we have shown that the introduction of alphoid^{tetO} HACs does not affect the pluripotent properties of mouse and human cells. Finally, we created an alphoid^{tetO} HAC expressing blood coagulation factor VIII, which may be further used to develop stem cell-based gene therapy methods for the treatment of hemophilia A [56].

Bacterial and yeast artificial chromosome-based HACs

The first study on the construction of yeast artificial chromosome (YAC)-based HACs was performed in 1998 [59]. A 100-kbp human chromosome 21 centromeric DNA sequence containing multiple CENP-B protein binding sequences (*CENP-B boxes*) was cloned into YACs. The resulting construct was modified in yeast cells by truncating the distal regions and replacing them with the telomeric regions of human chromosomes. Additionally, selective markers were inserted, after which the constructs were transferred to human fibrosarcoma HT1080 cells using lipofection (*Fig. 4*). In these cells, YACs underwent further multimerization, which led to the formation of 5 Mbp HACs that were stable in HT1080 cells and were stably inherited during cell divisions [13].

Later, there were successful attempts to generate BAC-based HACs [60] (*Fig. 4*). In this approach, HT1080 cells were co-transfected with a BAC that contained human chromosome 21 centromeric regions and sequences comprising full-length genes and their regulatory elements. In these cells, there was recombination of the introduced DNA molecules, followed by their subsequent multimerization, which led to the formation of circular HACs that stably replicated, were inherited by daughter cells, and maintained expression of target genes. Circular BAC-based HACs and linear YAC-based HACs were shown to be successfully transferred to mouse ESCs. Chimeric animals were produced by injection of these cells into blastocysts; differentiated progeny of ESCs stably maintained both a HAC and expression of a transgene introduced with the HAC [60].

In 2009, this approach was used to generate a HAC that carried the elements necessary for its use as an expression vector system, which included a sequence for site-specific recombination, a selective marker, and transcriptional insulators [61]. This HAC was used to develop vector constructs with different sites for site-specific recombination [62]. These types of HACs were used to develop a number of gene therapy models: transfer of a globin gene cluster to K562 cells [63], conducting cell immortalization [13, 64], generating a transgenic mouse model for Down syndrome [65], and identifying a genetic locus that provides silencing of the *HLA-G* gene in most tissues [66]. Finally, the possibility of transferring this HAC to human iPSCs was confirmed, opening a possibility of their applications in gene therapy [67].

HSV-1 amplicon-based HACs

A unique method for a direct HAC assembly in mammalian cells with the use of a herpes simplex virus type 1 (HSV-1) amplicon-based vector has been proposed [68]. This vector contains the *Pac* signal, which is necessary for its assembly into the viral capsid, and the viral replication origin, *OriS* [69]. The transgene-containing vector and two additional genetic constructs were co-transfected into green monkey cells to produce the vector amounts necessary for the transfection and package of the vector into the viral capsid. These additional constructs were expression vectors, one of which contained most of the HSV-1 genes required to assemble the viral capsid and pack the viral DNA into it. The other vector contained the *ICP27* gene required to regulate the expression of viral genes. Both accessory constructs lacked the *Pac* and *OriS* signals, which prevented them from replicating and packaging into the viral capsid. Viral amplicon vectors are able to accommodate a transgene of about 152 kbp in length [70, 71].

To assemble a HAC, human chromosome 17 and 21 centromeric sequences, a target gene, and selective markers were introduced into a BAC-containing *OriS* and *Pac* signals [68]. This vector and two auxiliary plasmids were transferred to green monkey cells, which ensured production of the vector and its packaging into the viral capsid that was then transduced into human cells (*Fig. 5*). The produced genetic construct was shown to act as a HAC, being maintained during cell division and providing stable transgene expression. Also, mitotic stability of the HAC was found to be mediated by an alpha-satellite sequence in a 40-kbp vector. Given that the maximum capacity of HSV-1-based vectors is 152 kbp, and that the centromeric region length is approximately 42 kbp, a target transgene of up to 110 kbp in length can be inserted into the considered HAC. An important indication that the HSV-1 replicon-based HAC may be used in cell therapy in the future was its successful transfer to human ESCs [72] and iPSCs [73].

Recently, the method for assembling this HAC has been improved. Human cells were transduced with two different vectors, one of which contained the alpha satellite sequence of human chromosome 17, and the other contained target genes [73]. When these vector constructs met in the cell nucleus, they recombined with each other to form a stable HAC with

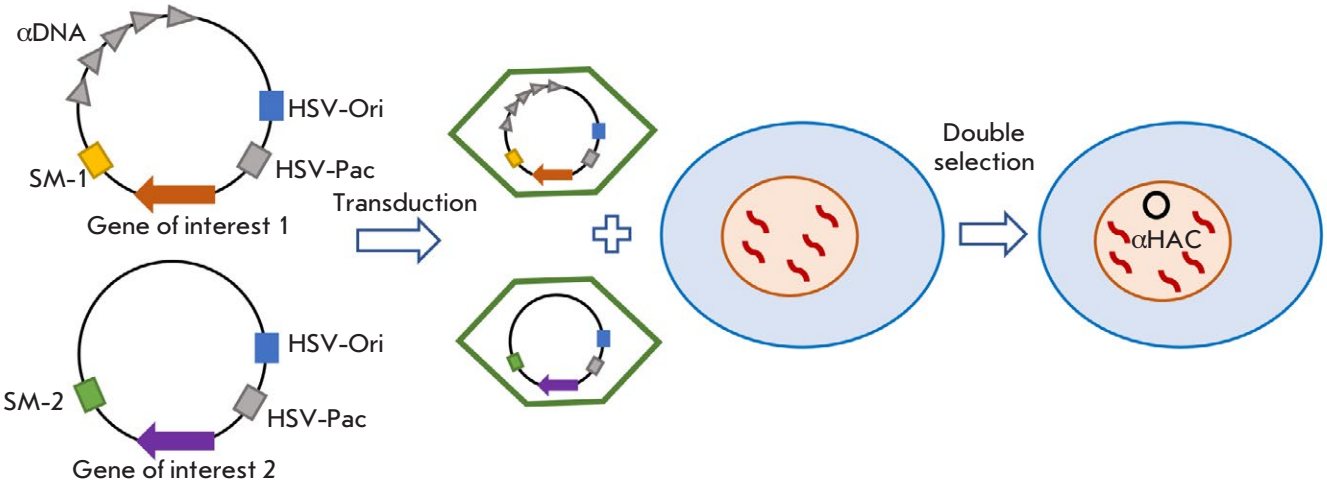

Fig. 5. Schematic representation of HSV-1 amplicon-based HAC assembly. Two vectors were constructed on the basis of herpes simplex virus (HSV-1) amplicons. One vector contained the origin of the replication signal (*Ori*), viral capsid packaging signal (*Pac*), selective markers (SM-1 and 2), and genes of interest. The second vector contained a 120-kbp sequence comprising alpha satellite repeats from human chromosome 17 (αDNA). The resulting viruses were co-transduced into target cells. Double selection was used to select cells in which two vector constructs recombined to form the target alphoid HAC (αHAC)

double the size of the initial one (*Fig. 5*). Therefore, this approach can be used to transfer transgenes of up to 260 kbp in length [11].

Methods of HAC transfer to target cells

The main method used to transfer HACs and other vectors of 1 Mbp or more in length is microcell-mediated chromosome transfer (MMCT), which enables the transfer of these vectors from donor cells to target cells using the so-called microcells (*Fig. 6A*) [74]. In donor cells, the formation of micronuclei, which are individual chromosomes surrounded by a nuclear envelope, is initiated. For this purpose, donor cells are incubated with cytostatic agents, colcemid [75] or griseofulvin, and TN-16 [76, 77], which cause cell cycle arrest at the metaphase stage. A9 (mouse subcutaneous tissue) or CHO cells are used as donor cells [8]. Donor cells are then fragmented into microcells by treatment with actin filament assembly inhibitors (cytochalasin B [75] or latrunculin B [76, 77]), followed by prolonged centrifugation. The microcell fraction is isolated using filtration [75] or a percoll gradient [60]. Microcells are then fused with target cells using polyethylene glycol (PEG) [75] or the hemagglutinating virus of the Japan envelope (HVJ-E) [23, 56, 57]. A retro-MMCT method (*Fig. 6B*) based on the use of the murine leukemia virus (MLV) envelope protein demonstrated improved efficiency compared with that of the original method. The MLV protein on the surface of microcells mediates their binding to the plasma membrane protein present on the surface of almost all types of mammalian cells, thus increasing the efficiency of cell–microcell fusion [78]. Using this MMCT variant, the alphoid^{tetO}-HAC was successfully transferred to human iPSCs [58]. It is important to note that various modifications of MMCT can be combined at its different stages, thereby increasing the efficiency of HAC transfer [12, 56, 58, 77, 78]. Cells bearing a target HAC are selected by culturing in the presence of antibiotics (blasticidin, G418, etc.) resistance to which is provided by the HAC.

Apart from MMCT, there are also methods for HAC transfer that do not use microcells. For example, in micronucleated whole cell fusion (MWCF), donor cells are fused with target cells using PEG after successive exposure to colcemid and cytochalasin B [79]. This method was developed to transfer HACs from cells that are not resistant to long-term exposure to cytostatics. The advantage of this method is high (compared with MMCT) efficiency and ease of use. However, a major limitation of this method is the need to use for the fusion cells of different animal species. Isolated metaphase chromosome transfer (iMCT) allows HAC transfer from donor cells incapable of forming micronuclei. In this method, HACs are isolated from a lysate of colcemid-pretreated cells using separation in the sucrose gradient [80]. The isolated HACs are transfected into target cells using li-

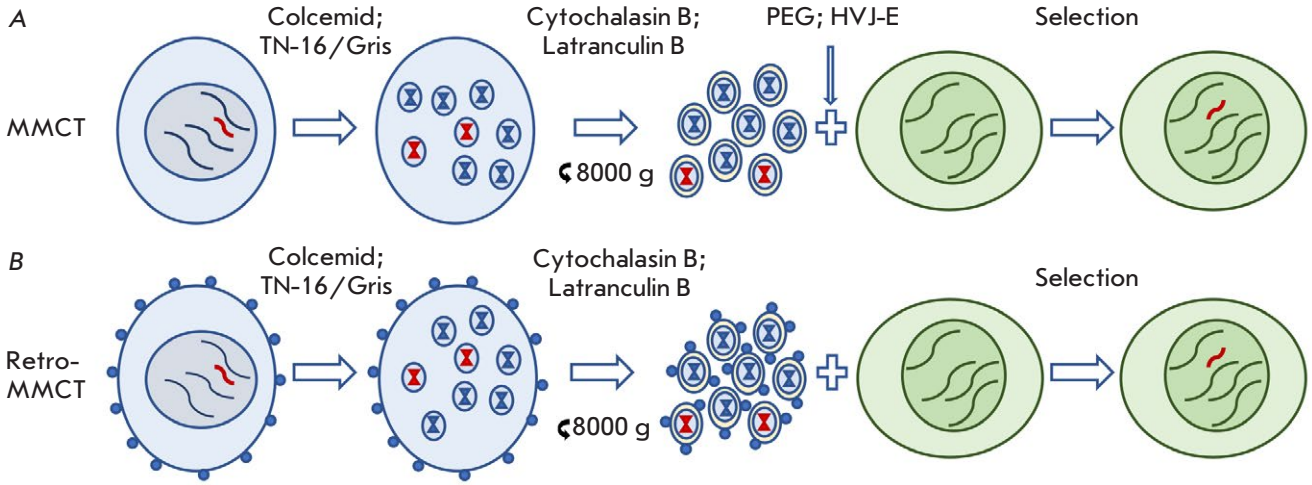

Fig. 6. Methods for HAC transfer from donor to recipient cells using MMCT. Donor cells are depicted as blue ovals, and recipient cells are shown as green ovals. HACs are marked in red. (*A*) The original MMCT method. At the first step, cells are treated with colcemid or TN-16/griseofulvin (Gris) to produce metaphase micronuclei. After treatment of cells with cytochalasin B or latrunculin B, the microcell fraction is isolated by centrifugation and filtration. Microcells are fused with recipient cells using PEG or HVJ envelopes. Cells containing HACs are selected using the appropriate selective medium. (*B*) In retro-MMCT, donor cells are pre-transduced with lentiviruses encoding the MLV protein (blue circles on the surface of donor cells)

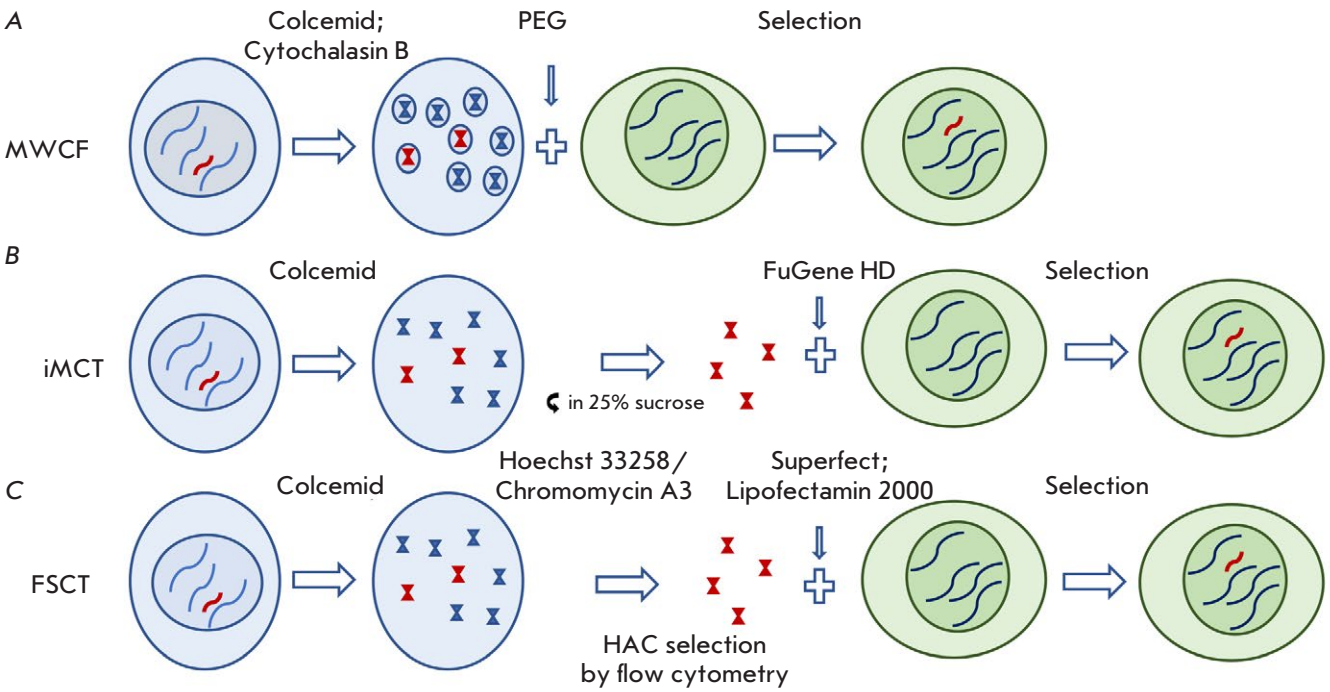

Fig. 7. Methods of HAC transfer that do not use microcells. (*A*) MWCF – fusion of donor cells with recipient cells. (*B*) iMCT – transfection of isolated chromosomes into target cells using lipofection. Colcemid-pretreated donor cells are lysed, and HACs isolated on a sucrose gradient are transferred to recipient cells using the FuGene HD reagent. (*C*) In FSCT, HACs are stained with Hoechst 33258 and chromomycin A3, collected by flow cytometry, and transfected into target cells using lipofection

pofection. This method has been sparsely used due to its low efficiency. Finally, Flow sorted chromosome transfer (FSCT) was developed for HACs containing C-G-rich sequences. In this case, HACs pretreated with Hoechst 33258 and chromomycin A3 dyes are isolated by flow cytometry (*Fig. 7C*). The isolated HACs are then transfected into target cells by lipofection [37, 81].

CONCLUSION

Currently, HACs are considered promising expression vector systems. The unique properties of HACs are their inertness and autonomy in the genome of target cells and the ability to bear large-sized transgenes. These properties of HAC-based genetic vectors are in demand in many areas of modern biology and medicine. HACs have been used in the development of approaches to the reprogramming of cells into iPSCs, creation of transgenic animals, and the generation of experimental models for the treatment of genetic diseases. HACs have been also extensively used to study chromosome functions and chromosomal instability.

However, despite the huge demand for HACs, the technologies of their production and transfer still need significant improvement before their implementation and wide application in laboratory practice and biomedicine. First of all, the transfer of HACs to recipient cells remains laborious and inefficient. Successful optimization of the methods for HAC transfer to recipient cells will increase the overall value and use of these genetic vectors in research and therapeutic applications. ●

This study was financially supported by a research project from Saint-Petersburg State University (No. 93024558), a grant of the Russian Science Foundation (No. 20-14-00242), and an Agreement with the Ministry of Science and Higher Education of the Russian Federation (No. 075-15-2021-1075 of September 28, 2021).

REFERENCES

1. Bouard D., Alazard-Dany N., Cosset F.L. // Brit. J. Pharmacol. 2009. V. 157. № 2. P. 153–165.
2. Ghosh S., Brown A.M., Jenkins C., Campbell K. // Appl. Biosafety. 2020. V. 25. № 1. P. 7–18.
3. Lundstrom K. // Genes (Basel). 2019. V. 10. № 3. P. 1–15.
4. Hackett P.B., Largaespada D.A., Cooper L.J. // Mol. Therapy. 2010. V. 18. № 4. P. 674–683.
5. Ivics Z., Izsvák Z. // Mob. DNA. 2010. V. 1. № 25. P. 1–15.
6. Skipper K.A., Andersen P.R., Sharma N., Mikkelsen J.G. // J. Biomed. Sci. 2013. V. 20. № 1. P. 92.
7. Blanc F., Mondain M., Bemelmans A.-P., Affortit C., Puel J.-L., Wang J. // J. Clin. Med. 2020. V. 9. № 2. P. 589.
8. Oshimura M., Kazuki Y., Iida Y., Uno N. // eLS. 2013. P. 1–12.
9. Kouprina N., Larionov V. // Chromosome Res. 2015. V. 23. № 1. P. 1–5.
10. Katona R.L. // Chromosome Res. 2015. V. 23. № 1. P. 143–157.
11. Moralli D., Monaco Z.L. // Exp. Cell Res. 2020. V. 390. № 1. P. 111931.
12. Sinenko S.A., Ponomartsev S.V., Tomilin A.N. // Exp. Cell Res. 2020. V. 389. № 1. P. 111882. https://www.ncbi.nlm.nih.gov/pubmed/32017931
13. Ikeno M., Hasegawa Y. // Exp. Cell Res. 2020. V. 390. № 1. P. 111793. https://www.ncbi.nlm.nih.gov/pubmed/31874174
14. Kazuki Y., Oshimura M. // Mol. Therapy. 2011. V. 19. № 9. P. 1591–1601. https://www.ncbi.nlm.nih.gov/pubmed/21750534
15. Koi M., Shimizu M., Morita H., Yamada H., Oshimura M. // Jpn. J. Cancer Res. 1989. V. 80. № 5. P. 413–418. http://www.ncbi.nlm.nih.gov/pubmed/2502516
16. Katoh M., Ayabe F., Norikane S., Okada T., Masumoto H., Horike S., Shirayoshi Y., Oshimura M. // Biochem. Biophys. Res. Commun. 2004. V. 321. № 2. P. 280–290. http://www.ncbi.nlm.nih.gov/pubmed/15358173
17. Suzuki N., Nishii K., Okazaki T., Ikeno M. // J. Biol. Chem. 2006. V. 281. № 36. P. 26615–26623. http://www.ncbi.nlm.nih.gov/pubmed/16837455
18. Iida Y., Kim J.H., Kazuki Y., Hoshiya H., Takiguchi M., Hayashi M., Erliandri I., Lee H.S., Samoshkin A., Masumoto H., et al. // DNA Res. 2010. V. 17. № 5. P. 293–301. http://www.ncbi.nlm.nih.gov/pubmed/20798231
19. Sinenko S.A., Ponomartsev S.V., Tomilin A.N. // Cell. Mol. Life Sci. 2021. V. 78. № 4. P. 1207–1220.
20. Farr C.J., Stevanovic M., Thomson E.J., Goodfellow P.N., Cooke H.J. // Nat. Genet. 1992. V. 2. № 4. P. 275–282.
21. Kuroiwa Y., Tomizuka K., Shinohara T., Kazuki Y., Yoshida H., Ohguma A., Yamamoto T., Tanaka S., Oshimura M., Ishida I. // Nat. Biotechnol. 2000. V. 18. № 10 SUPPL. P. 1086–1090.
22. Kazuki Y., Hiratsuka M., Takiguchi M., Osaki M., Kajitani N., Hoshiya H., Hiramatsu K., Yoshino T., Kazuki K., Ishihara C., et al. // Mol. Therapy. 2010. V. 18. № 2. P. 386–393.
23. Yamaguchi S., Kazuki Y., Nakayama Y., Nanba E., Oshimura M., Ohbayashi T. // PLoS One. 2011. V. 6. № 2. P. 1–11.
24. Takiguchi M., Kazuki Y., Hiramatsu K., Abe S., Iida Y., Takehara S., Nishida T., Ohbayashi T., Wakayama T., Oshimura M. // ACS Synthetic Biol. 2012. V. 3. № 12. P. 903–914.
25. Buerstedde J.M., Takeda S. // Cell. 1991. V. 67. № 1. P. 179–188.
26. Kazuki Y., Hoshiya H., Takiguchi M., Abe S., Iida Y., Osaki M., Katoh M., Hiratsuka M., Shirayoshi Y., Hiramatsu K., et al. // Gene Therapy. 2011. V. 18. № 4. P. 384–393.
27. Tedesco F.S., Gerli M.F.M., Perani L., Benedetti S.,

Ungaro F., Cassano M., Antonini S., Tagliafico E., Artusi V., Longa E., et al. // Sci. Translat. Med. 2012. V. 4. № 140. P. 1–13.
28. Benedetti S., Uno N., Hoshiya H., Ragazzi M., Ferrari G., Kazuki Y., Moyle L.A., Tonlorenzi R., Lombardo A., Chaouch S., et al. // EMBO Mol. Med. 2018. V. 10. № 2. P. 254–275.
29. Yakura Y., Ishihara C., Kurosaki H., Kazuki Y., Komatsu N., Okada Y., Doi T., Takeya H., Oshimura M. // Biochem. Biophys. Res. Commun. 2013. V. 431. № 2. P. 336–341.
30. Hiratsuka M., Uno N., Ueda K., Kurosaki H., Imaoka N., Kazuki K., Ueno E., Akakura Y., Katoh M., Osaki M., et al. // PLoS One. 2011. V. 6. № 10. P. 1–14.
31. Lindenbaum M., Perkins E., Csonka E., Fleming E., Garcia L., Greene A., Gung L., Hadlaczky G., Lee E., Leung J., et al. // Nucl. Acids Res. 2004. V. 32. № 21. P. 1–15.
32. Csonka E. // Mammal. Chromosome Engin.: Meth. Protocols, Meth. Mol. Biol. 2011. V. 738. P. 141–149.
33. Holló G., Keresõ J., Praznovszky T., Cserpán I., Fodor K., Katona R., Csonka E., Fãtyol K., Szeles A., Szalay A.A., et al. // Chromosome Res. 1996. V. 4. № 3. P. 240–247.
34. Vanderbyl S., MacDonald G.N., Sidhu S., Gung L., Telenius A., Perez C., Perkins E. // STEM CELLS. 2004. V. 22. № 3. P. 324–333.
35. Vanderbyl S.L., Sullenbarger B., White N., Perez C.F., MacDonald G.N., Stodola T., Bunnell B.A., Ledebur H.C., Lasky L.C. // Exp. Hematol. 2005. V. 33. № 12. P. 1470–1476.
36. Kennard M.L., Goosney D.L., Monteith D., Roe S., Fischer D., Mott J. // Biotechnol. Bioengin. 2009. V. 104. № 3. P. 526–539.
37. de Jong G., Telenius A., Vanderbyl S., Meitz A., Drayer J. // Chromosome Res. 2001. V. 9. № 6. P. 475–485. https://www.ncbi.nlm.nih.gov/pubmed/11592482
38. Co D.O., Borowski A.H., Leung J.D., van der Kaa J., Hengst S., Platenburg G.J., Pieper F.R., Perez C.F., Jirik F.R., Drayer J.I. // Chromosome Res. 2000. V. 8. № 3. P. 183–191.
39. Blazso P., Sinko I., Katona R.L. // Meth. Mol. Biol. 2011. V. 738. № 2. P. 161–181.
40. Katona R.L., Sinkó I., Holló G., Szucs K.S., Praznovszky T., Kereso J., Csonka E., Fodor K., Cserpán I., Szakál B., et al. // Cell. Mol. Life Sci. 2008. V. 65. № 23. P. 3830–3838.
41. Mehta G.D., Agarwal M.P., Ghosh S.K. // Mol. Genet. Genom. 2010. V. 284. № 2. P. 75–94.
42. Neil D.L., Villasante A., Fisher R.B., Vetrie D., Cox B., Tyler-Smit C. // Nucl. Acids Res. 1990. V. 18. № 6. P. 1421–1428.
43. Harrington J.J., Van Bokkelen G., Mays R.W., Gustashaw K., Willard H.F. // Nat. Genet. 1997. V. 15. № 4. P. 345–355.
44. Kouprina N., Larionov V. // Curr. Protocols Hum. Genet. 2006. Chapter 5:Unit 5.17. doi: 10.1002/0471142905.hg0517s49.
45. Larionov V., Kouprina N., Graves J., Resnick M.A.// Proc. Natl. Acad. Sci. USA. 1996. V. 93. № 24. P. 13925–13930. https://doi.org/10.1073/pnas.93.24.13925
46. Kouprina N., Larionov V. // Chromosoma. 2016. V. 125. № 4. P. 621–632. http://www.ncbi.nlm.nih.gov/pubmed/27116033
47. Ebersole T., Okamoto Y., Noskov V.N., Kouprina N., Kim J.H., Leem S.H., Barrett J.C., Masumoto H., Larionov V. // Nucl. Acids Res. 2005. V. 33. № 15. P. 1–8.
48. Kouprina N., Larionov V. // Mol. Ther. Methods Clin. Dev. 2019. V. 14. P. 16–26. https://www.ncbi.nlm.nih.gov/pubmed/31276008
49. Kouprina N., Kim J., Larionov V. // Curr. Protocols. 2021. V. 1. № 8. P. 1–27.
50. Kouprina N., Lee N.C.O., Kononenko A.V., Samoshkin A., Larionov V. // Methods Mol. Biol. 2015. V. 1227. P. 3–26. https://doi.org10.1007/978-1-4939-1652-8_1.
51. Nakano M., Cardinale S., Noskov V.N. // Chemtracts. 2008. V. 21. № 3. P. 87–88.
52. Kouprina N., Earnshaw W.C., Masumoto H., Larionov V. // Cell. Mol. Life Sci. 2013. V. 70. № 7. P. 1135–1148.
53. Kononenko A.V., Lee N.C., Liskovykh M., Masumoto H., Earnshaw W.C., Larionov V., Kouprina N. // Nucl. Acids Res. 2015. V. 43. № 9. P. 1–14. http://www.ncbi.nlm.nih.gov/pubmed/25712097
54. Lee N.C.O., Petrov N.S., Larionov V., Kouprina N. // Curr. Protocols. 2021. V. 1. № 12. P. 1–36.
55. Kim J.H., Kononenko A., Erliandri I., Kim T.A., Nakano M., Iida Y., Barrett J.C., Oshimura M., Masumoto H., Earnshaw W.C., et al. // Proc. Natl. Acad. Sci. USA. 2011. V. 108. № 50. P. 20048–20053.
56. Ponomartsev S.V., Sinenko S.A., Skvortsova E.V., Liskovykh M.A., Voropaev I.N., Savina M.M., Kuzmin A.A., Kuzmina E.Y., Kondrashkina A.M., Larionov V., et al. // Cells. 2020. V. 9. № 4. P. 1–17. https://www.ncbi.nlm.nih.gov/pubmed/32260189
57. Liskovykh M., Ponomartsev S., Popova E., Bader M., Kouprina N., Larionov V., Alenina N., Tomilin A. // Cell Cycle. 2015. V. 14. № 8. P. 1268–1273. http://www.ncbi.nlm.nih.gov/pubmed/25695642
58. Sinenko S.A., Skvortsova E.V., Liskovykh M.A., Ponomartsev S.V., Kuzmin A.A., Khudiakov A.A., Malashicheva A.B., Alenina N., Larionov V., Kouprina N., et al. // Cells. 2018. V. 7. № 12. P. 1–14. http://www.ncbi.nlm.nih.gov/pubmed/30544831
59. Ikeno M., Grimes B., Okazaki T., Nakano M., Saitoh K., Hoshino H., McGill N.I., Cooke H., Masumoto H. // Nat. Biotechnol. 1998. V. 16. № 5. P. 431–439.
60. Suzuki N., Nishii K., Okazaki T., Ikeno M. // J. Biol. Chem. 2006. V. 281. № 36. P. 26615–26623.
61. Ikeno M., Suzuki N., Hasegawa Y., Okazaki T. // Nucl. Acids Res. 2009. V. 37. № 6. P. 1–9.
62. Suzuki E., Nakayama M. // Nucl. Acids Res. 2011. V. 39. № 8. P. 1–11.
63. Suzuki N., Itou T., Hasegawa Y., Okazaki T., Ikeno M. // Nucl. Acids Res. 2009. V. 38. № 5. P. 1–9.
64. Ito M., Ito R., Yoshihara D., Ikeno M., Kamiya M., Suzuki N., Horiguchi A., Nagata H., Yamamoto T., Kobayashi N., et al. // Cell Transplant. 2008. V. 17. № 1–2. P. 165–171. https://www.ncbi.nlm.nih.gov/pubmed/18468246
65. Miyamoto K., Suzuki N., Sakai K., Asakawa S., Okazaki T., Kudoh J., Ikeno M., Shimizu N. // Transgenic Res. 2014. V. 23. № 2. P. 317–329.
66. Ikeno M., Suzuki N., Kamiya M., Takahashi Y., Kudoh J., Okazaki T. // Nucl. Acids Res. 2012. V. 40. № 21. P. 10742–10752.
67. Hasegawa Y., Ikeno M., Suzuki N., Nakayama M., Ohara O. // Biol. Meth. Protocols. 2018. V. 3. № 1. P. 1–10.
68. Moralli D., Simpson K.M., Wade-Martins R., Monaco Z.L. // EMBO Repts. 2006. V. 7. № 9. P. 911–918.
69. Frenkel N. // Curr. Gene Therapy. 2006. V. 6. № 3. P. 277–299.
70. Wade-Martins R., Smith E.R., Tyminski E., Chiocca E.A., Saeki Y. // Nat. Biotechnol. 2001. V. 19. № 11.

P. 1067–1070.
71. Zaupa C., Revol-Guyot V., Epstein A.L. // Hum. Gene Therapy. 2003. V. 14. № 11. P. 1049–1063.
72. Moralli D., Monaco Z.L. // Chromosome Res. 2015. V. 23. № 1. P. 105–110.
73. Chan D.Y., Moralli D., Wheatley L., Jankowska J.D., Monaco Z.L. // Exp. Cell Res. 2020. V. 388. № 2. P. 111840.
74. Doherty A.M., Fisher E.M. // Mamm. Genome. 2003. V. 14. № 9. P. 583–592. http://www.ncbi.nlm.nih.gov/pubmed/14629108
75. Fournier R.E.K., Ruddle F.H. // Proc. Natl. Acad. Sci. USA. 1977. V. 74. № 1. P. 319–323.
76. Liskovykh M., Lee N.C., Larionov V., Kouprina N. // Mol. Therapy – Meth. Clin. Dev. 2016. V. 3. P. 1–9.
77. Liskovykh M., Larionov V., Kouprina N. // Curr. Protocols. 2021. V. 1. № 9. P. 1–25.
78. Suzuki T., Kazuki Y., Oshimura M., Hara T. // PLoS One. 2016. V. 11. № 6. P. e0157187. http://www.ncbi.nlm.nih.gov/pubmed/27271046
79. Paulis M., Bensi M., Orioli D., Mondello C., Mazzini G., D'Incalci M., Falcioni C., Radaelli E., Erba E., Raimondi E., et al. // Stem Cells. 2007. V. 25. № 10. P. 2543–2550.
80. Suzuki N., Itou T., Hasegawa Y., Okazaki T., Ikeno M. // Nucl. Acids Res. 2010. V. 38. № 5. P. e33. http://www.ncbi.nlm.nih.gov/pubmed/20007595
81. Klobutcher L.A., Miller C.L., Ruddle F.H. // Proc. Natl. Acad. Sci. USA. 1980. V. 77. P. 3610–3614.

Reporter Transgenes for Monitoring the Antitumor Efficacy of Recombinant Oncolytic Viruses

A. V. Semenova*, G. F. Sivolobova, A. A. Grazhdantseva, A. P. Agafonov, G. V. Kochneva
Federal Budgetary Research Institution «State Research Center of Virology and Biotechnology «Vector», Koltsovo, Novosibirsk region, 630559, Russia
*E-mail: tkacheva_av@mail.ru
Received May 16, 2022; in final form, July 05, 2022
DOI: 10.32607/actanaturae.11719

ABSTRACT **Accurate measurement of tumor size and margins is crucial for successful oncotherapy. In the last decade, non-invasive imaging modalities, including optical imaging using non-radioactive substrates, deep-tissue imaging with radioactive substrates, and magnetic resonance imaging have been developed. Reporter genes play the most important role among visualization tools; their expression in tumors and metastases makes it possible to track changes in the tumor growth and gauge therapy effectiveness. Oncolytic viruses are often chosen as a vector for delivering reporter genes into tumor cells, since oncolytic viruses are tumor-specific, meaning that they infect and lyse tumor cells without damaging normal cells. The choice of reporter transgenes for genetic modification of oncolytic viruses depends on the study objectives and imaging methods used. Optical imaging techniques are suitable for *in vitro* studies and small animal models, while deep-tissue imaging techniques are used to evaluate virotherapy in large animals and humans. For optical imaging, transgenes of fluorescent proteins, luciferases, and tyrosinases are used; for deep-tissue imaging, the most promising transgene is the sodium/iodide symporter (NIS), which ensures an accumulation of radioactive isotopes in virus-infected tumor cells. Currently, NIS is the only reporter transgene that has been shown to be effective in monitoring tumor virotherapy not only in preclinical but also in clinical studies.**

KEYWORDS **oncolytic viruses, reporter transgenes, optical imaging, tumor cell, deep-tissue imaging, NIS.**

ABBREVIATIONS **GFP – green fluorescent protein; NIR – near-infrared; ADV – adenovirus; HSV-1 – herpes simplex virus 1; MV – measles virus; NDV – Newcastle disease virus; NIS – sodium/iodide symporter; VACV – vaccinia virus; VSV – vesicular stomatitis virus; FGS – fluorescence-guided surgery; CT – computed tomography; MRI – magnetic resonance imaging; SPECT – single-photon emission computed tomography; PET – positron emission tomography; Tyr – tyrosinase; PCa – prostate cancer.**

INTRODUCTION

To date, the use of oncolytic viruses is one of the most promising areas in cancer therapy. A great advantage of oncolytic virotherapy is that oncolytic viruses can specifically target tumor cells and lyse them without damaging healthy tissue during the entire treatment course [1]. Oncolytic viruses surpass the heterogeneity of tumor cells; they can lyse tumor stem cells, which are practically not amenable to other types of oncotherapy [2]. On the contrary, similar to the disruption of interferon signaling pathways in tumor cells, the immunosuppressive tumor microenvironment, which hinders effective immunotherapy, promotes virus replication [3]. At the same time, successful virus replication in the tumor inevitably makes the tumor more immunogenic due to pathogen-associated danger signals sent by infected cells (PAMP and DAMP). During tumor cell lysis, tumor-associated neoantigens are also released and an adaptive T-cell response to these antigens is formed [4]. Oncolytic viruses can act synergistically with other anticancer drugs, in particular, with checkpoint inhibitors (ipilimumab, atezolizumab, nivolumab, etc.) and CAR T-cell therapy [1, 5, 6].

Both natural and genetically modified virus strains of different taxonomic groups have oncolytic properties. The transgene insertion makes it possible to alter the properties of oncolytic viruses in a target-

ed manner, thus enhancing their tumor-specificity [7], ability to proliferate inside a tumor [8], as well as their immunostimulatory [9–11] and cytolytic activities [12, 13]. Reporter transgenes, which can be used for non-invasive instrumental monitoring of the antitumor and antimetastatic activities of the virus, as well as its safety for other body organs and tissues, occupy a special place in the genetic modification of viruses [14, 15].

Non-invasive imaging studies are of great importance in the diagnosis and management of cancer patients [16]. The effectiveness of antitumor therapy directly depends on a timely and accurate diagnosis of tumor nodes and metastases, and monitoring of tumor response to therapy can help in selecting the optimal treatment strategy. Since reporter transgene expression is associated with viral replication, imaging can be used in preclinical and clinical studies as an early indicator of the therapeutic effect of oncolytic viruses [17]. Non-invasive imaging of the whole body of an experimental animal at a number of time points will help evaluate the efficiency of virus delivery to tissues of interest and allow monitoring and quantifying infection and expression of therapeutic transgenes during the treatment course.

Imaging techniques can be divided into the following categories: optical imaging using non-radioactive substrates, deep-tissue imaging using radioactive substrates, and magnetic resonance imaging (*Fig. 1*). In the following sections, we will focus on the most studied reporter transgenes from oncolytic viruses used in various non-invasive imaging techniques.

OPTICAL IMAGING

Optical imaging is based on the use of light in the infrared, visible, and ultraviolet spectra. For this reason, it is best suited for imaging of surface than deep tissues. Optical imaging techniques used to detect reporter transgenes from oncolytic viruses include fluorescence, bioluminescence, and photoacoustic imaging (*Fig. 1*). The depth of the possible imaging of optical techniques varies over a fairly wide range: from fractions of a millimeter to several centimeters, and depends both on the chosen technique and absorption/scattering of excitation light and/or light emitted by surrounding tissues.

Fluorescence imaging

Fluorescence requires incident light of appropriate excitation wavelength to reach the fluorophore, causing the fluorophore to emit a photon of a specific wavelength. The emitted photons are detected using a highly sensitive CCD camera installed in a light-tight box.

Genes encoding such fluorescent proteins as the green fluorescent protein (GFP) and its enhanced variants, red fluorescent protein (RFP), yellow fluorescent protein (YFP), mCherry, and many others, are used as reporter genes for fluorescence imaging [18, 19].

GFP, first isolated from the *Aequorea victoria* jellyfish in 1960 [20], quickly became one of the most widely used and studied proteins in biochemistry and cell biology [21]. The protein is used because of its ability to generate a highly visible and efficiently emitting internal fluorophore. However, the sensitivity of the GFP reporter system is limited by the lack of amplification, because each GFP molecule produced by the reporter system yields only one fluorophore. It has been calculated that the concentration of natural unmodified GFP molecules should amount to 1 μM in order to match the endogenous autofluorescence of a typical mammalian cell [22]. Mutant (enhanced) GFPs with improved extinction coefficients increase the imaging efficiency by 6–10 times [23], which makes it possible to overcome the limitations associated with cell autofluorescence.

Mammalian tissues have the highest transparency in the so-called "near-infrared (NIR) transparency window" (λ ~ 650–900 nm) [24]. The absorption of light by hemoglobin, water, lipids, and melanin is the lowest in the NIR spectrum region. For this reason, the NIR light has a greater penetrating power than visible light. Moreover, autofluorescence of biological tissues and light scattering are also significantly lower in the NIR region compared to the visible spectrum. To date, fluorescent proteins emitting light in the NIR range are being developed in order to improve the fluorescence intensity *in vivo* [25]. An example of such proteins is the new NIR fluorescent proteins (iRFPs) developed based on bacterial phytochrome photoreceptors [26]. These proteins provide tissue-specific contrast without the need for any additional substances. Compared to conventional GFP-like red-shifted fluorescent proteins, iRFP670 and iRFP720 show stronger photoacoustic signals at longer wavelengths and can be spectrally distinguished from each other and hemoglobin. Moreover, iRFP670 and iRFP720 do not require oxygen to form chromophores, which gives them an advantage in imaging hypoxic tumors [27, 28].

A number of recombinant oncolytic viruses, including Newcastle disease virus (NDV), vesicular stomatitis virus (VSV), herpes simplex virus type I (HSV-1 or *Human alphaherpesvirus 1* according to the new taxonomy of viruses), measles virus (MV), adenovirus (ADV), and vaccinia virus (VACV), encoding fluorescent protein transgenes, have been constructed.

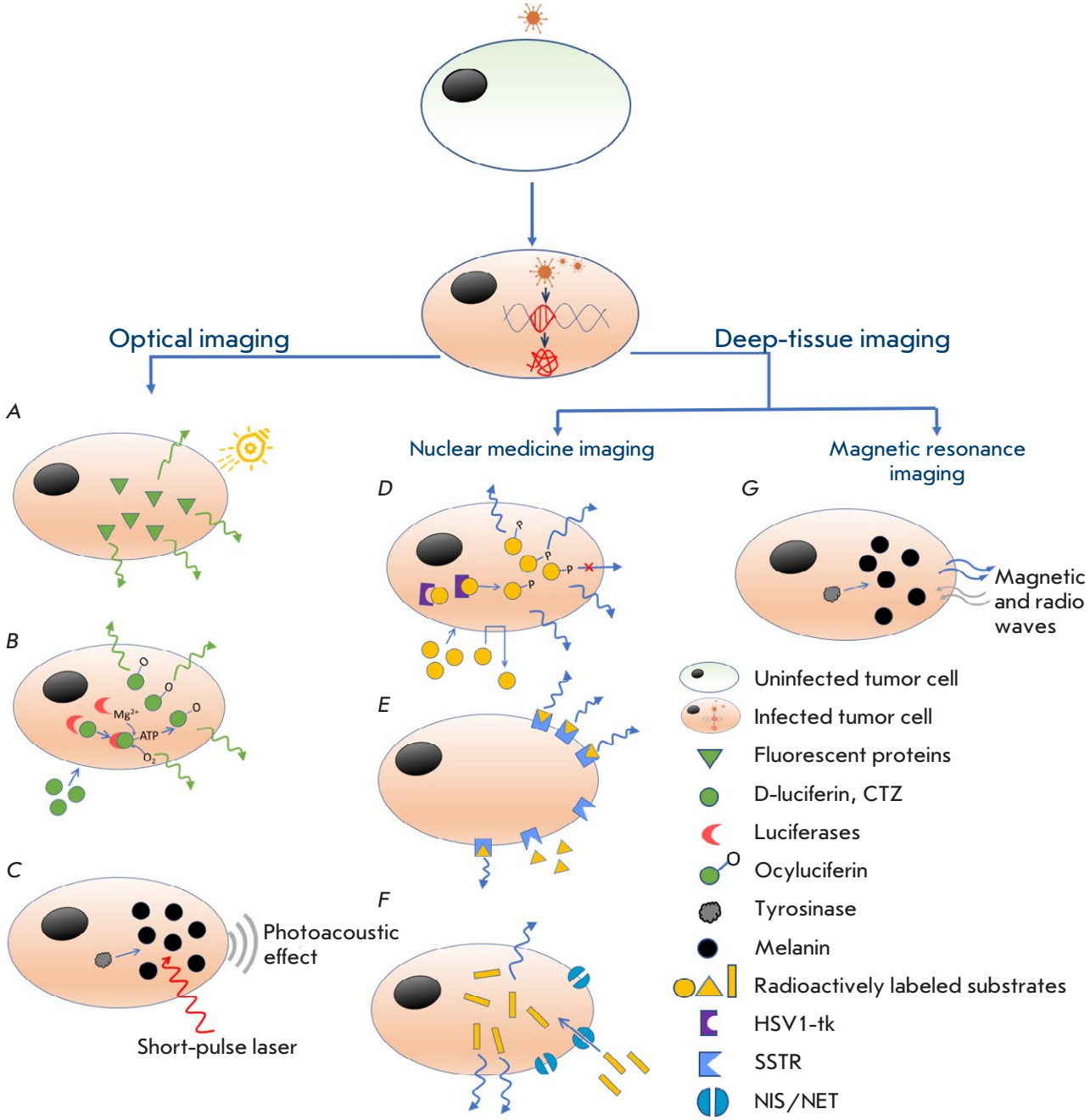

Fig. 1. Tumor cell imaging methods using oncolytic viruses expressing protein reporter transgenes. Optical imaging methods: (*A*) – fluorescence imaging: fluorescent proteins emit fluorescence when irradiated with light of a certain wavelength; (*B*) – bioluminescence imaging: light is produced when exogenous substrates are oxidized by a bioluminescent reporter enzyme; (*C*) – photoacoustic imaging: a photoacoustic effect is achieved by irradiating a target tissue with a short-pulsed laser. Deep-tissue imaging techniques (*D–F*) – SPECT, PET; (*G*) – MRI; (*D*) – the HSV1-tk enzyme interacts with radioactively labeled substrates and converts them into a metabolite incapable of leaving the cell; (*E*) – the SSTR2 receptor binds radioactively labeled synthetic peptide substrates; (*F*) – NIS/NET transporters ensure the absorption and accumulation of radioactive substrates inside the cell; (*G*) – melanin enhances the magnetic resonance signal

These viruses were tested in various tumor models in order to directly assess the effectiveness of viral oncotherapy, and were also used as an additional control to evaluate the effects of other imaging technologies [29–31]. One of oncolytic viruses, namely VACV encoding the GFP transgene (GLV-1h68), is currently undergoing phase I and II clinical trials, which use GFP fluorescence to confirm virus localization in superficial tumor sites and biopsy samples from internal tumors (*Table 1*) [32].

A group of Japanese researchers used an oncolytic ADV expressing the GFP transgene (OBP-401 strain) to study a new technology of fluorescence-guided surgery (FGS) for accurate tumor imaging in mice [33]. Surgical resection remains the most effective method for most solid tumors; however, even after radical resection of malignant tumors, relapses often occur, which in some cases may be due to the difficulty of correctly imaging the tumor margin [34, 35]. Preinjection of a fluorescent oncolytic virus can provide intraoperative real-time fluorescence control and is ideal for an accurate and complete resection of malignant cells. In addition, it allows for further reduction of the resection area due to tumor lysis. Kishimoto et al. used OBP-401-based FGS for a human glioblastoma xenograft in the orthotopic mouse model. The use of a fluorescent oncolytic virus can enable accurate resection of glioblastoma with an indistinct margin by FGS with preservation of brain function and the absence of relapses for more than 120 days. For comparison, 85% of mice with a tumor removed using standard surgical methods had relapses. The OBP-401 strain was also used to study the effectiveness of FGS technology in mouse models of disseminated colon and lung cancer, as well as in soft tissue sarcoma [36].

Bioluminescence imaging

Unlike fluorescence, bioluminescence imaging does not require excitation light to emit photons from the fluorophore. Light is produced through substrate oxidation by a bioluminescent reporter enzyme whose gene can be cloned into the genome of an oncolytic virus. The bioluminescence approach features a higher sensitivity (it requires as low as 10^{-17} M of luciferase) and lower background luminescence compared to fluorescence [37, 38].

Firefly luciferase (*Photinus pyralis*, FLuc) is the most widely used reporter enzyme for bioluminescence [39]. *D*-luciferin is used, along with the ATP, Mg^{2+}, and O_2 cofactors, as a FLuc substrate. FLuc catalyzes the formation of the luciferin–ATP complex, whose oxidation leads to production of high-energy oxyluciferin. Oxyluciferin emits photons of the yellow-green spectrum (λ_{max} ~ 560 nm) [40]. Light emission reaches its peak 10–12 min after luciferin injection and gradually decreases over the next 60 min [41]. In addition, ATP-independent luciferases such as sea pansy luciferase (*Renilla reniformis*,

Table 1. Reporter transgenes of oncolytic viruses

Imaging technique		Reporter transgene	Oncolytic viruses encoding a reporter transgene	Ref.
Optical imaging	Fluorescence imaging	Fluorescent proteins (GFP, eGFP, iRFP)	NDV, MV, HSV-1, ADV, VACV (GLV-1h68), VSV	[14, 29, 55]
	Bioluminescence imaging	Luciferases (FLuc, RLuc, GLuc)	HSV-1, VACV, ADV, MV	[47, 50, 56, 57]
	Photoacoustic imaging	Melanogenic enzymes (Tyr, Tyrp1, Tyrp2)	VACV	[53]
Deep-tissue imaging	SPECT and PET	Enzymes (HSV1-tk)	VSV, ADV, HSV-1	[58–60]
	PET	Receptors (SSTR2)	ADV, VACV	[61, 62]
	SPECT and PET	Carrier proteins (NET, NIS)	ADV, VACV, HSV-1, MV	[63–70]
	MRI	Melanogenic enzymes (Tyr)	VACV	[53]

RLuc) [42], marine copepod (*Gaussia princeps*, GLuc), and click beetle (*Pyrophorus plagiophthalamus*) luciferases are known [43]. RLuc and GLuc use coelenterazine (CTZ) as a substrate and emit mainly blue light (λ_{max} ~ 460–480 nm), which penetrates tissues worse than the yellow-green light of FLuc [44]. Additional disadvantages of ATP-independent luciferases include their limited distribution, fast kinetics, and higher background noise [37]. New variants of enzymes and substrates with improved bioluminescence are constantly being developed. An example of a new enzyme variant is NanoLuc (λ_{max} ~ 460 nm), whose gene has a shortened coding sequence. This is the only bioluminescent transgene variant for oncolytic viruses with a small genomic capacity, such as adeno-associated virus and other parvoviruses [45]. The use of several types of luciferases allows for simultaneous monitoring of different but related biological events. In particular, the method of labeling tumor cells and an oncolytic virus with various types of luciferases is widely used to determine the antitumor and antimetastatic activities of the virus in *in vivo* experiments [46].

The first oncolytic virus whose properties were studied by bioluminescence was HSV-1 [47]. Using recombinant HSV-1 variants expressing the FLuc and RLuc transgenes in mouse models, FLuc was shown to provide a more effective monitoring of viral infection than RLuc [48]. Treatment of virus-infected mice with the antiviral drug valaciclovir caused a dose-dependent decrease in the Fluc signal, which was a demonstration of the possibility of quantifying the effectiveness of antiviral therapy in animal models using bioluminescence [48]. In order to obtain more comprehensive quantitative data, bioluminescence is combined with *ex vivo* imaging of animal organs and a determination of their absolute viral load by real-time PCR [49].

Bioluminescence imaging has been successfully used to determine the effect of combination therapy on mouse tumors using oncolytic VACV together with a blockade of immune checkpoints [50], as well as to monitor replication of oncolytic parvoviruses, adenoviruses, HSV-1, VACV, MV, and VSV within a tumor in mouse models (*Table*) [37].

Photoacoustic imaging

Photoacoustic imaging, or optoacoustic imaging, is a recently developed imaging modality that uses the photoacoustic effect produced by irradiation of the target tissue with a short-pulsed laser. The tissue, depending on its physical properties, absorbs different amounts of light, which causes molecular vibration and thermoelastic expansion [24, 51]. Acoustic waves resulting from this process are less scattered than photons passing through tissue, which greatly increases image resolution [24]. Sometimes contrast agents are used to increase the molecular specificity of photoacoustic imaging [52].

To date, photoacoustic imaging experiments have been conducted using only one oncolytic virus, VACV, which expresses the key genes for melanin production: the tyrosinase (Tyr) gene and genes encoding the Tyr-related proteins 1 (Tyrp1) and 2 (Tyrp2) (*Table*) [53]. Melanin is an ideal contrast agent for photoacoustic imaging, while expression and accumulation of melanin in tumors make it possible to use photoacoustic imaging in oncotherapy experiments in animal models [53]. However, high concentrations of melanin inhibit viral replication; therefore, in order to reduce this inhibitory effect, an inducible system regulated by doxycycline is used to express Tyr group transgenes [54]. The complexity of choosing transgenes for photoacoustic imaging still limits the use of this technique in oncolytic virotherapy, despite its high resolution.

DEEP-TISSUE IMAGING

The transition from *in vitro* and preclinical studies to clinical trials requires appropriate translational animal models to adequately evaluate safety and efficacy. For this purpose, it is necessary to use large animals that are physiologically close to humans, such as dogs, pigs, and primates, since they allow one to better predict the clinical outcome of a therapy than when using small animals like mice and rats [71]. Optical imaging modalities used in small animals are not applicable to large animals because visible light cannot penetrate the tissues of large animals [18, 72]. For this, deep-tissue imaging techniques such as single-photon emission computed tomography (SPECT), positron emission tomography (PET), and magnetic resonance imaging (MRI) are required (*Fig. 1*) [73].

Imaging by nuclear medicine techniques (PET and SPECT) is based on a recognition and localization of the gamma rays emitted during the decay of a radioactive tracer introduced into the patient's body and accumulated specifically in various organs and tissues [74]. Specialists can draw a conclusion about the state of health of the organ under study and its metabolic activity based on how the cell reacts to the introduction of a radioactive drug, how this drug accumulates, and how it is being excreted. The spatiotemporal pattern of radiopharmaceutical distribution provides an idea of the organ's shape, size, and position, as well as the presence of pathological lesions in it [16].

SPECT uses radiopharmaceuticals labeled with radioisotopes, whose nuclei emit only one gamma quan-

tum (photon) during each radioactive decay act. PET utilizes radioisotopes emitting positrons, which, in turn, when annihilated with an electron, yield two gamma quanta moving in different directions along the same line; this increases PET sensitivity compared to that of SPECT [75]. SPECT and PET are often combined with computed tomography (CT) for co-registration of anatomical and functional images. A large set of detectors located around the object under study during PET and computer processing of the signals received from them make it possible to perform a more accurate three-dimensional reconstruction of the radionuclide distribution in the scanned object compared to SPECT [16].

MRI uses strong magnetic fields and radio waves to excite the nuclear–spin energy transition of hydrogen molecules. Hydrogen nuclei are present in large quantities in the human body in the composition of water and other substances. The rate of relaxation of nuclear hydrogen atoms from their excited state depends on tissue density, and this difference makes it possible to obtain sufficiently high-resolution images [76]. The disadvantages of MRI include the high cost of the devices and the long time required to obtain images (15–90 min).

Most oncolytic virus transgenes utilized in deep-tissue imaging can be studied using various techniques depending on the substrate. These transgenes encode HSV1 thymidine kinase (HSV1-tk), somatostatin receptor 2 (hSSRT2), enzymes catalyzing melanin synthesis (Tyr), and such transporter proteins as the human norepinephrine transporter (hNET) and the sodium/iodide symporter (NIS) [14, 63, 73].

Enzyme reporter transgenes

One of the first reporter genes proposed for non-invasive radionuclide imaging was the HSV1-tk gene. Its product, thymidine kinase, phosphorylates thymidine to thymidine 5'-monophosphate. Unlike mammalian thymidine kinase type 1, which has a high affinity mainly for thymidine, HSV1-tk exhibits specificity to various nucleosides. For example, HSV1-tk can phosphorylate both pyrimidine analogs (5-iodo-(2'-deoxy-2-fluoro-β-*D*-arabinofuranosyl)uracil, FIAU; 2'-deoxy-2-fluoro-arabinofuranosyl-5-ethyluracil, FEAU; (E)-5-(2-bromovinyl)-2'-deoxyuridine, BVDU) and acycloguanosine derivatives: acyclovir (ACV), ganciclovir (GCV), and 9-[4-fluoro-3-(hydroxymethyl) butyl]guanine (FHBG). HSV1-tk specifically interacts with radioactively labeled pyrimidine analogs, converting them into a metabolite incapable of leaving the cell, resulting in accumulation of the transformed radioactive substrate in the cells expressing HSV1-tk [77, 78]. Since HSV1-tk is one of the first well-characterized reporter genes, it has a wide range of substrates for PET and SPECT, as well as mutant forms such as HSV1-sr39tk, which have increased activity *in vivo* [73].

The HSV1-tk transgene was used to assess the biodistribution of recombinant oncolytic VSV in rat models of hepatocellular carcinoma [58]. HSV1-tk-expressing ADV capable of displaying virus localization using PET scanning was also obtained (*Table 1*) [59]. The first clinical studies were performed to evaluate the possibility of using the recombinant oncolytic HSV1-tk strain HSV1716 as a reporter transgene to monitor viral replication during treatment of glioma patients [60]. However, increased substrate (^{123}I-FIAU) accumulation in tumor cells was not registered by SPECT, which may be due to both insufficient virus replication and the low sensitivity of the method. In addition, HSV1-tk, as a foreign protein, can elicit an immune response, making it unsuitable for long-term imaging, which is important for gene therapy.

Receptor proteins as reporter transgenes

SSTR2, one of the receptors for the peptide hormone somatostatin, is expressed on neuroendocrine and other cells, where it is involved in neurotransmission, hormone secretion, and cell proliferation [3, 72]. The human hSSTR2 protein was used for SPECT imaging with indium-111-labeled synthetic peptide substrates such as octreotide, pentetreotide, and lanreotide, as well as PET imaging with gallium-68-labeled peptides [79]. Researchers integrated the SSTR2 transgene into the genomes of the oncolytic viruses ADV and VACV and demonstrated the possibility of long-term monitoring of the localization and persistence of these viruses in the syngeneic mouse models of several cancers [62, 73]. The expression of the SSTR2 transgene in the adeno-associated virus makes it possible to obtain PET images even six months after the end of therapy [61]. The disadvantages of SSTR2 include its endogenous expression, which can reduce the diagnostic performance, and the fact that each receptor can bind only one radiolabeled ligand, making signal amplification impossible and, thereby, limiting the imaging sensitivity [3, 18].

Contrast agents as transgenes

The genes of melanogenesis, such as the tyrosinase gene *Tyr*, which is also used in photoacoustic imaging, can be utilized as reporter genes for MRI imaging [73, 80]. Tyr-induced melanin production enhances the chelation of metal ions, resulting in a significant improvement in MRI contrast. Because the contrast

agent is produced directly in the transduced cells, imaging becomes possible without the use of an exogenous contrast agent.

The use of a recombinant VACV strain expressing melanin overproduction transgenes made it possible to carry out MRI imaging of the tumor and metastases in the xenograft model of human metastatic A549 lung cancer cells inoculated in immunodeficient mice. This VACV strain has also been successfully used for photoacoustic imaging (see section "Photoacoustic imaging") [53].

Melanin is present in all the kingdoms of living organisms. Therefore, melanin synthesis can possibly be used as a diagnostic/theranostic marker for most known species, including humans. [14, 81].

Carrier proteins as reporter transgenes

The Na^+/Cl^--dependent membrane protein NET transports norepinephrine (NE), epinephrine, dopamine, and other structurally related compounds into the cell. Most cells of neuroblastoma (the most common extracranial solid tumor in children, which accounts for 15% of the deaths among all childhood cancers) express NET on their membrane [82]. Metaiodobenzylguanidine (MIBG), also known as iobenguane, is a structural analog of NE, a natural NET substrate. MIBG was first adapted for the imaging of the adrenal medulla by scintigraphy in the 1980s [83]. Radioactively labeled MIBG (^{123}I-MIBG) can be effectively used for neuroblastoma imaging in the whole body. Currently, gamma scanning with ^{123}I-MIBG is considered to be the preferred method of detecting primary tumors and identifying metastatic neuroblastoma cells [84].

The human *NET* transgene (hNET) was introduced into the genomes of oncolytic VACV, ADV, and herpes viruses and used for the nuclear imaging of not only neuroendocrine, but also other human cancers in immunodeficient mouse models [64–66]. However, the use of exogenous NET for tumor imaging remains extremely limited, which is probably due to the existence of other reporter genes that are more accessible to radioactive tracers and have better expression profiles [85].

Sodium/iodide symporter (NIS) is a transmembrane glycoprotein that mediates iodide uptake and accumulation for organification of thyroid hormones; it plays a central role in the metabolism of thyroid hormones and is also expressed in other tissues, including the salivary gland, gastric mucosa, and the mammary gland [86]. Thanks to its ability to accumulate iodide, NIS has been used to detect and treat thyroid diseases, demonstrating the clinical versatility and practicality of the NIS-mediated iodide uptake, for more than 75 years [87]. Vector delivery of *NIS* allows for iodide accumulation in the tissues of other organs, where *NIS* is not normally expressed. NIS is responsible for the intracellular transportation of various types of gamma-emitting radioisotopes that are readily available and approved for use in humans. These radioisotopes include radioactive iodine (^{123}I, ^{124}I, ^{125}I, and ^{131}I), technetium in the form of anionic pertechnetate ($^{99m}TcO_4^-$), and perrhenate ($^{186, 188}$Re), which are suitable for non-invasive SPECT and PET imaging [14]. Ectopic expression of NIS ensures the accumulation of radioactive iodide either at a comparable or higher level as that of thyroid cells without affecting the main biochemical processes taking place in the cell [88]. This expands the scope of radiotherapy and NIS imaging use beyond the thyroid gland.

The use of NIS has potential advantages over other reporter gene systems. Unlike receptor-based reporters with stoichiometric linkages such as hSSTR2 (in which the receptor can only bind one radiolabeled ligand, preventing signal amplification and limiting imaging sensitivity), transporters such as NIS provide signal amplification via the intracellular transport-mediated accumulation of the substrate, thereby increasing detection sensitivity [73, 89]. NIS imaging was also proved to be more sensitive and longer lasting compared to HSV1-tk imaging [90]. NIS can show cell viability, since the accumulation effect of NIS is lost during cell apoptosis, while enzymes and receptors can still retain their functional activity [63]. NIS is found in all vertebrates, which makes it possible to use the species-specific NIS transgene in the vast majority of model systems [91, 92].

NIS not only has the advantages described; it is also the most abundant human reporter transgene. Many NIS-expressing recombinant viruses have been developed. NIS-encoding non-replicating ADV, which was studied in the xenografts of various human cancers, including cervical cancer, breast cancer, and prostate cancer (PCa), as well as in immunodeficient mouse models, was the first NIS-expressing virus obtained [67]. Shortly thereafter, a high-resolution SPECT image of canine prostate cancer tissue was obtained using replication-competent ADV expressing the NIS symporter (Ad5-yCD/mutTK[SR39]rep-hNIS) [93]. Phase 1 clinical trials of Ad5-yCD/mutTK[SR39] rep-hNIS were also conducted in a group of men with clinically localized PCa, which proved the possibility and safety of non-invasive SPECT imaging for monitoring the effectiveness of ADV-mediated gene therapy in humans [94]. The replication and distribution of recombinant oncolytic VSV (VSVd51-NIS) was monitored in mice transplanted with subcutaneous 5TGM1 myeloma by serial ^{123}I-γ-scintigraphy

after systemic and intratumoral administration [68]. Clinical trials showed the efficacy of using another recombinant VSV strain, VSV-IFNβ-NIS, to image metastatic colorectal and pancreatic cancers [95]. VACV expressing the *hNIS* transgene successfully inhibited the growth of several cancers in preclinical models, including pancreatic cancer, triple-negative breast cancer, gastric cancer, and malignant pleural mesothelioma [96–98]. Recombinant MV (Edmonston strain) expressing *hNIS* has undergone and is currently undergoing the largest number of phase 1 and 2 clinical trials in various cancers, including ovarian cancer (NCT02068794), head and neck squamous cell carcinoma and breast cancers (NCT01846091), malignant peripheral nerve sheath tumor (NCT02700230), multiple myeloma (NCT00450814), and urothelial carcinoma (NCT02364713) [3, 69, 70].

A major limitation of NIS imaging is the accumulation of radioisotopes in such NIS-expressing non-target tissues as thyroid and salivary glands and stomach. If the transduced tissue is adjacent to endogenous NIS-expressing tissues, then interpretation and quantification of NIS signals are technically difficult. Several studies have explored ways to improve NIS expression and block endogenous NIS expression in order to tackle these issues [99, 100].

CONCLUSION

As we can conclude from the presented data, the introduction of reporter transgenes into the genome of oncolytic viruses is a promising tool for a non-invasive molecular imaging of tumor tissue to assess tumor localization, size, and the effectiveness of its treatment. The choice of a reporter transgene depends on the imaging techniques used, which can be divided into two main categories: optical imaging and deep-tissue imaging.

Optical imaging techniques are amiable due to their short acquisition times, low cost, high throughput capacity, lack of toxicity in animal models, multispectral imaging capabilities, and ease of use compared to the radioisotopes required for deep-tissue imaging. These properties make optical imaging an extremely popular approach for *in vitro* and preclinical studies in small animals.

Transgenes of fluorescent proteins (fluorescence imaging), luciferase (bioluminescence imaging), and Tyr enzymes (photoacoustic imaging) are used for optical imaging of the antitumor properties of oncolytic viruses.

The limitations of optical imaging techniques include a shallow penetration depth, the absorption and scattering of the excitation and/or emitted light, especially in deep tissues; and the presence of cell autofluorescence, including that of dead cells, which is of particular importance when using oncolytic viruses that lyse tumor cells. Although the attenuation of the light flux and autofluorescence can be minimized within the infrared "window," optical imaging methods have a low spatial resolution and limited sensitivity. These problems, as well as the risk of developing immune responses to the foreign reporter proteins encoded by the transgenes of oncolytic viruses, prevent the adaptation of optical imaging modality for large animal and human models and, therefore, their use in the clinic.

Deep-tissue imaging techniques (SPECT, PET, and MRI) have the most translational potential, thus making it possible to study animals of any size, including humans. The same reporter transgenes of oncolytic viruses can be used for deep-tissue imaging by different methods depending on the contrast agent used. Melanin is an ideal MRI contrast agent; therefore, melanin-producing Tyr genes are used as transgenes of oncolytic viruses. However, melanin at high concentrations inhibits viral replication, which significantly limits the use of these imaging modalities in tumor virotherapy. Nuclear imaging methods (SPECT and PET) use radioactive isotopes as a substrate; a number of oncolytic virus transgenes have been developed for accumulation of these isotopes in tumor cells. These transgenes encode enzymes (HSV1-tk and its modifications), receptors (hSSRT2), as well as carrier proteins such as hNET and NIS.

One of the oldest and most effective reporter genes, *NIS*, is used for molecular imaging and targeted radionuclide therapy. *NIS* is found in all vertebrates, which makes it possible to use the species-specific *NIS* transgene in the vast majority of model systems. Not only preclinical, but also clinical studies confirm that *NIS*, expressed in oncolytic viruses, can be used to accurately determine tumor localization and response to therapy, as well as detect metastases using deep-tissue nuclear imaging. ●

This study was supported by the Ministry of Science and Higher Education of the Russian Federation (Agreement No. 075-15-2021-1355 dated 12 October, 2021, "Use of synchrotron radiation for virology research") as part of implementation of certain activities of the Federal Scientific and Technical Program for the Development of Synchrotron and Neutron Research and Research Infrastructure for 2019–2027.

REFERENCES

1. Lawler S.E., Speranza M.-C., Cho C.-F., Chiocca E.A. // JAMA Oncol. 2017. V. 3. № 6. P. 841.
2. Romanenko M.V., Dolgova E.V., Osipov I.D., Ritter G.S., Sizova M.S., Proskurina A.S., Efremov Y.R., Bayborodin S.I., Potter E.A., Taranov O.S., et al. // Anticancer Res. 2019. V. 39. № 11. P. 6073–6086.
3. Pelin A., Wang J., Bell J., Le Boeuf F. // Oncolytic Virotherapy. 2018. V. 7. P. 25–35.
4. Kochneva G.V., Sivolobova G.F., Tkacheva A.V., Gorchakov A.A., Kulemzin S.V. // Journal of Molecular Biology 2020. V. 54. № 1. P. 3–16.
5. Watanabe N., McKenna M.K., Rosewell Shaw A., Suzuki M. // Mol. Ther. 2021. V. 29. № 2. P. 505–520.
6. Evgin L., Vile R.G. // Cancers (Basel). 2021. V. 13. № 5. P. 1106.
7. Montaño-Samaniego M., Bravo-Estupiñan D.M., Méndez-Guerrero O., Alarcón-Hernández E., Ibáñez-Hernández M. // Front. Oncol. 2020. V. 10.
8. Guedan S., Grases D., Rojas J.J., Gros A., Vilardell F., Vile R., Mercade E., Cascallo M., Alemany R. // Gene Ther. 2012. V. 19. № 11. P. 1048–1057.
9. Stephenson K.B., Barra N.G., Davies E., Ashkar A.A., Lichty B.D. // Cancer Gene Ther. 2012. V. 19. № 4. P. 238–246.
10. Li J., O'Malley M., Urban J., Sampath P., Guo Z.S., Kalinski P., Thorne S.H., Bartlett D.L. // Mol. Ther. 2011. V. 19. № 4. P. 650–657.
11. Zamarin D., Holmgaard R.B., Ricca J., Plitt T., Palese P., Sharma P., Merghoub T., Wolchok J.D., Allison J.P. // Nat. Commun. 2017. V. 8. № 1. P. 14340.
12. Kochneva G., Zonov E., Grazhdantseva A., Yunusova A., Sibolobova G., Popov E., Taranov O., Netesov S., Chumakov P., Ryabchikova E. // Oncotarget. 2014. V. 5. № 22. P. 11269–11282.
13. Kochneva G., Sivolobova G., Tkacheva A., Grazhdantseva A., Troitskaya O., Nushtaeva A., Tkachenko A., Kuligina E., Richter V., Koval O. // Oncotarget. 2016. V. 7. № 45. P. 74171–74188.
14. Haddad D., Fong Y. // Mol. Ther. – Oncolytics. 2014. V. 1. P. 14007.
15. Kirn D.H., Thorne S.H. // Nat. Rev. Cancer. 2009. V. 9. № 1. P. 64–71.
16. Histed S.N., Lindenberg M.L., Mena E., Turkbey B., Choyke P.L., Kurdziel K.A. // Nucl. Med. Commun. 2012. V. 33. № 4. P. 349–361.
17. Luker K.E., Hutchens M., Schultz T., Pekosz A., Luker G.D. // Virology. 2005. V. 341. № 2. P. 284–300.
18. Serganova I., Blasberg R.G. // J. Nucl. Med. 2019. V. 60. № 12. P. 1665–1681.
19. Chudakov D.M., Lukyanov S., Lukyanov K.A. // Trends Biotechnol. 2005. V. 23. № 12. P. 605–613.
20. Shimomura O., Johnson F.H., Saiga Y. // J. Cell. Comp. Physiol. 1962. V. 59. № 3. P. 223–239.
21. Remington S.J. // Protein Sci. 2011. V. 20. № 9. P. 1509–1519.
22. Niswender K.D., Blackman S.M., Rohde L., Magnuson M.A., Piston D.W. // J. Microsc. 1995. V. 180. Pt 2. P. 109–116.
23. Patterson G.H., Knobel S.M., Sharif W.D., Kain S.R., Piston D.W. // Biophys. J. 1997. V. 73. № 5. P. 2782–2790.
24. Pirovano G., Roberts S., Kossatz S., Reiner T. // J. Nucl. Med. 2020. V. 61. № 10. P. 1419–1427.
25. Klohs J., Wunder A., Licha K. // Basic Res. Cardiol. 2008. V. 103. № 2. P. 144–151.
26. Shcherbakova D.M., Verkhusha V.V. // Nat. Methods. 2013. V. 10. № 8. P. 751–754.
27. Krumholz A., Shcherbakova D.M., Xia J., Wang L.V., Verkhusha V.V. // Sci. Rep. 2015. V. 4. № 1. P. 3939.
28. Wilson A., Wilson K., Bilandzic M., Moffitt L., Makanji M., Gorrell M., Oehler M., Rainczuk A., Stephens A., Plebanski M. // Cancers (Basel). 2018. V. 11. № 1. P. 32.
29. Rojas J.J., Thorne S.H. // Theranostics. 2012. V. 2. № 4. P. 363–373.
30. Patel M.R., Jacobson B.A., Ji Y., Drees J., Tang S., Xiong K., Wang H., Prigge J.E., Dash A.S., Kratzke A.K., et al. // Oncotarget. 2015. V. 6. № 32. P. 33165–33177.
31. Jun K.-H., Gholami S., Song T.-J., Au J., Haddad D., Carson J., Chen C.-H., Mojica K., Zanzonico P., Chen N.G., et al. // J. Exp. Clin. Cancer Res. 2014. V. 33. № 1. P. 2.
32. Khan K.H., Young A.-M., Mateo J., Tunariu N., Yap T.A., Tan D.S.P., Mansfield D., Wong M., Riisnaes R., Harrington K.J., et al. // J. Clin. Oncol. 2013. V. 31. № 15_suppl. P. 3062.
33. Yano S., Tazawa H., Kishimoto H., Kagawa S., Fujiwara T., Hoffman R.M. // Int. J. Mol. Sci. 2021. V. 22. № 2. P. 1–13.
34. Esposito I., Kleeff J., Bergmann F., Reiser C., Herpel E., Friess H., Schirmacher P., Büchler M.W. // Ann. Surg. Oncol. 2008. V. 15. № 6. P. 1651–1660.
35. Vos E.L., Gaal J., Verhoef C., Brouwer K., van Deurzen C.H.M., Koppert L.B. // Eur. J. Surg. Oncol. 2017. V. 43. № 10. P. 1846–1854.
36. Kishimoto H., Zhao M., Hayashi K., Urata Y., Tanaka N., Fujiwara T., Penman S., Hoffman R.M. // Proc. Natl. Acad. Sci. USA. 2009. V. 106. № 34. P. 14514–14517.
37. Coleman S.M., McGregor A. // Future Virol. 2015. V. 10. № 2. P. 169–183.
38. Sandhu G.S., Solorio L., Broome A.M., Salem N., Kolthammer J., Shah T., Flask C., Duerk J.L. // Wiley Interdiscip. Rev. Syst. Biol. Med. 2010. V. 2. № 4. P. 398–421.
39. de Wet J.R., Wood K.V., Helinski D.R., DeLuca M. // Proc. Natl. Acad. Sci. USA. 1985. V. 82. № 23. P. 7870–7873.
40. Luker G.D., Luker K.E. // J. Nucl. Med. 2008. V. 49. № 1. P. 1–4.
41. Paroo Z., Bollinger R.A., Braasch D.A., Richer E., Corey D.R., Antich P.P., Mason R.P. // Mol. Imaging. 2004. V. 3. № 2. P. 117–124.
42. Lorenz W.W., McCann R.O., Longiaru M., Cormier M.J. // Proc. Natl. Acad. Sci. USA. 1991. V. 88. № 10. P. 4438–4442.
43. Venisnik K.M., Olafsen T., Gambhir S.S., Wu A.M. // Mol. Imaging Biol. 2007. V. 9. № 5. P. 267–277.
44. Love A.C., Prescher J.A. // Cell Chem. Biol. 2020. V. 27. № 8. P. 904–920.
45. Hall M.P., Unch J., Binkowski B.F., Valley M.P., Butler B.L., Wood M.G., Otto P., Zimmerman K., Vidugiris G., Machleidt T., et al. // ACS Chem. Biol. 2012. V. 7. № 11. P. 1848–1857.
46. Power A.T., Wang J., Falls T.J., Paterson J.M., Parato K.A., Lichty B.D., Stojdl D.F., Forsyth P.A.J., Atkins H., Bell J.C. // Mol. Ther. 2007. V. 15. № 1. P. 123–130.
47. Summers B.C., Leib D.A. // J. Virol. 2002. V. 76. № 14. P. 7020–7029.
48. Luker G.D., Bardill J.P., Prior J.L., Pica C.M., Piwnica-Worms D., Leib D.A. // J. Virol. 2002. V. 76. № 23. P. 12149–12161.

49. Burgos J.S., Guzman-Sanchez F., Sastre I., Fillat C., Valdivieso F. // Microbes Infect. 2006. V. 8. № 5. P. 1330–1338.
50. Rojas J.J., Sampath P., Hou W., Thorne S.H. // Clin. Cancer Res. 2015. V. 21. № 24. P. 5543–5551.
51. Zhang H.F., Maslov K., Stoica G., Wang L.V. // Nat. Biotechnol. 2006. V. 24. № 7. P. 848–851.
52. Upputuri P.K., Pramanik M. // WIREs Nanomed. Nanobiotechnol. 2020. V. 12. № 4. P. e1618.
53. Stritzker J., Kirscher L., Scadeng M., Deliolanis N.C., Morscher S., Symvoulidis P., Schaefer K., Zhang Q., Buckel L., Hess M., et al. // Proc. Natl. Acad. Sci. USA. 2013. V. 110. № 9. P. 3316–3320.
54. Kirscher L., Deán-Ben X.L., Scadeng M., Zaremba A., Zhang Q., Kober C., Fehm T.F., Razansky D., Ntziachristos V., Stritzker J., et al. // Theranostics. 2015. V. 5. № 10. P. 1045–1057.
55. Le Boeuf F., Diallo J.-S., McCart J.A., Thorne S., Falls T., Stanford M., Kanji F., Auer R., Brown C.W., Lichty B.D., et al. // Mol. Ther. 2010. V. 18. № 5. P. 888–895.
56. Guse K., Dias J.D., Bauerschmitz G.J., Hakkarainen T., Aavik E., Ranki T., Pisto T., Särkioja M., Desmond R.A., Kanerva A., et al. // Gene Ther. 2007. V. 14. № 11. P. 902–911.
57. Msaouel P., Opyrchal M., Domingo Musibay E., Galanis E. // Expert Opin. Biol. Ther. 2013. V. 13. № 4. P. 483–502.
58. Muñoz-Álvarez K.A., Altomonte J., Laitinen I., Ziegler S., Steiger K., Esposito I., Schmid R.M., Ebert O. // Mol. Ther. 2015. V. 23. № 4. P. 728–736.
59. Abate-Daga D., Andreu N., Camacho-Sánchez J., Alemany R., Herance R., Millán O., Fillat C. // PLoS One. 2011. V. 6. № 10. P. e26142.
60. Dempsey M.F., Wyper D., Owens J., Pimlott S., Papanastassiou V., Patterson J., Hadley D.M., Nicol A., Rampling R., Brown S.M. // Nucl. Med. Commun. 2006. V. 27. № 8. P. 611–617.
61. Cotugno G., Aurilio M., Annunziata P., Capalbo A., Faella A., Rinaldi V., Strisciuglio C., Tommaso M.Di, Aloj L., Auricchio A. // Hum. Gene Ther. 2011. V. 22. № 2. P. 189–196.
62. Andrea McCart J., Mehta N., Scollard D., Reilly R.M., Carrasquillo J.A., Tang N., Deng H., Miller M., Xu H., Libutti S.K., et al. // Mol. Ther. 2004. V. 10. № 3. P. 553–561.
63. Montiel-Equihua C.A., Martín-Duque P., de la Vieja A., Quintanilla M., Burnet J., Vassaux G., Lemoine N.R. // Cancer Gene Ther. 2008. V. 15. № 7. P. 465–473.
64. Jia Z.-Y., Deng H.-F., Huang R., Yang Y.-Y., Yang X.-C., Qi Z.-Z., Ou X.-H. // Cancer Gene Ther. 2011. V. 18. № 3. P. 196–205.
65. Chen N., Zhang Q., Yu Y.A., Stritzker J., Brader P., Schirbel A., Samnick S., Serganova I., Blasberg R., Fong Y., et al. // Mol. Med. 2009. V. 15. № 5–6. P. 144–151.
66. Sorensen A., Mairs R.J., Braidwood L., Joyce C., Conner J., Pimlott S., Brown M., Boyd M. // J. Nucl. Med. 2012. V. 53. № 4. P. 647–654.
67. Boland A., Ricard M., Opolon P., Bidart J.M., Yeh P., Filetti S., Schlumberger M., Perricaudet M. // Cancer Res. 2000. V. 60. № 13. P. 3484–3492.
68. Goel A., Carlson S.K., Classic K.L., Greiner S., Naik S., Power A.T., Bell J.C., Russell S.J. // Blood. 2007. V. 110. № 7. P. 2342–2350.
69. Msaouel P., Opyrchal M., Dispenzieri A., Peng K.W., Federspiel M.J., Russell S.J., Galanis E. // Curr. Cancer Drug Targets. 2018. V. 18. № 2. P. 177–187.
70. Dispenzieri A., Tong C., LaPlant B., Lacy M.Q., Laumann K., Dingli D., Zhou Y., Federspiel M.J., Gertz M.A., Hayman S., et al. // Leukemia. 2017. V. 31. № 12. P. 2791–2798.
71. Ribitsch I., Baptista P.M., Lange-Consiglio A., Melotti L., Patruno M., Jenner F., Schnabl-Feichter E., Dutton L.C., Connolly D.J., van Steenbeek F.G., et al. // Front. Bioeng. Biotechnol. 2020. V. 8. P. 972.
72. Wu Z.J., Tang F.R., Ma Z.-W., Peng X.-C., Xiang Y., Zhang Y., Kang J., Ji J., Liu X.Q., Wang X.-W., et al. // Hum. Gene Ther. 2018. V. 29. № 2. P. 204–222.
73. Concilio S.C., Russell S.J., Peng K.-W. // Mol. Ther. – Oncolytics. 2021. V. 21. P. 98–109.
74. Maurer A.H. // Health Phys. 2008. V. 95. № 5. P. 571–576.
75. Cherry S., Sorenson J., Phelps M. Physics in Nuclear Medicine. 4th ed. Philadelphia: Saunders/Elsevier, 2012. 683 p.
76. McRobbie D.W., Moore E.A., Graves M.J., Prince M.R. MRI from picture to proton. 3rd ed. Cambridge, UK: Cambridge University Press, 2017.
77. Serganova I., Ponomarev V., Blasberg R. // Nucl. Med. Biol. 2007. V. 34. № 7. P. 791–807.
78. Keshavarz M., Sabbaghi A., Miri S.M., Rezaeyan A., Arjeini Y., Ghaemi A. // Cancer Cell Int. 2020. V. 20. № 1. P. 1–17.
79. Xu C., Zhang H. // Biomed. Res. Int. 2015. V. 2015. P. 1–14.
80. Paproski R.J., Forbrich A.E., Wachowicz K., Hitt M.M., Zemp R.J. // Biomed. Opt. Express. 2011. V. 2. № 4. P. 771.
81. Yang C., Tian R., Liu T., Liu G. // Molecules. 2016. V. 21. № 5. P. 580.
82. Park J.R., Eggert A., Caron H. // Hematol. Oncol. Clin. North Am. 2010. V. 24. № 1. P. 65–86.
83. Wieland D.M., Wu J., Brown L.E., Mangner T.J., Swanson D.P., Beierwaltes W.H. // J. Nucl. Med. 1980. V. 21. № 4. P. 349–353.
84. Parisi M.T., Eslamy H., Park J.R., Shulkin B.L., Yanik G.A. // Semin. Nucl. Med. 2016. V. 46. № 3. P. 184–202.
85. Zhang Y., Wang J. // Acta Pharm. Sin. B. 2020. V. 10. № 1. P. 79–90.
86. Spitzweg C., Nelson P.J., Wagner E., Bartenstein P., Weber W.A., Schwaiger M., Morris J.C. // Endocr. Relat. Cancer. 2021. V. 28. № 10. P. T193–T213.
87. Miller A., Russell S.J. // Expert Opin. Biol. Ther. 2016. V. 16. № 1. P. 15–32.
88. Dadachova E., Carrasco N. // Semin. Nucl. Med. 2004. V. 34. № 1. P. 23–31.
89. Haddad D., Chen N.G., Zhang Q., Chen C.-H., Yu Y.A., Gonzalez L., Carpenter S.G., Carson J., Au J., Mittra A., et al. // J. Transl. Med. 2011. V. 9. № 1. P. 36.
90. Miyagawa M., Anton M., Wagner B., Haubner R., Souvatzoglou M., Gansbacher B., Schwaiger M., Bengel F.M. // Eur. J. Nucl. Med. Mol. Imaging. 2005. V. 32. № 9. P. 1108–1114.
91. Concilio S.C., Zhekova H.R., Noskov S.Y., Russell S.J. // PLoS One. 2020. V. 15. № 2. P. 1–25.
92. Portulano C., Paroder-Belenitsky M., Carrasco N. // Endocr. Rev. 2014. V. 35. № 1. P. 106–149.
93. Barton K.N., Tyson D., Stricker H., Lew Y.S., Heisey G., Koul S., de la Zerda A., Yin F.-F., Yan H., Nagaraja T.N., et al. // Mol. Ther. 2003. V. 8. № 3. P. 508–518.
94. Barton K.N., Stricker H., Brown S.L., Elshaikh M., Aref I., Lu M., Pegg J., Zhang Y., Karvelis K.C., Siddiqui F., et al. // Mol. Ther. 2008. V. 16. № 10. P. 1761–1769.
95. Merchan J., Patel M.R., Powell S.F., Strauss J., Cripe T.P., Old M.O., Diaz R.M., Russell S.J., Bexon A.S., Suk-

sanpaisan L., et al. // Ann. Oncol. 2018. V. 29. P. 479–480.
96. Belin L.J., Ady J.W., Lewis C., Marano D., Gholami S., Mojica K., Eveno C., Longo V., Zanzonico P.B., Chen N.G., et al. // Surgery. 2013. V. 154. № 3. P. 486–495.
97. Gholami S., Chen C.-H., Lou E., Belin L.J., Fujisawa S., Longo V.A., Chen N.G., Gönen M., Zanzonico P.B., Szalay A.A., et al. // FASEB J. 2014. V. 28. № 2. P. 676–682.
98. Gholami S., Haddad D., Chen C.-H., Chen N.G., Zhang Q., Zanzonico P.B., Szalay A.A., Fong Y. // Surgery. 2011. V. 150. № 6. P. 1040–1047.
99. Suksanpaisan L., Pham L., McIvor S., Russell S.J., Peng K.-W. // Cancer Gene Ther. 2013. V. 20. № 11. P. 638–641.
100. Kim Y.-H., Youn H., Na J., Hong K.-J., Kang K.W., Lee D.S., Chung J.-K. // Theranostics. 2015. V. 5. № 1. P. 86–96.

Type 2 Diabetes Mellitus: Pathogenic Features and Experimental Models in Rodents

I. G. Gvazava[1*], M. V. Karimova[1], A. V. Vasiliev[1,2], E. A. Vorotelyak[1]
[1]Institute of Developmental Biology, Russian Academy of Sciences, Moscow, 119334 Russia
[2]Lomonosov Moscow State University, Faculty of Biology, Moscow, 119234 Russia
*E-mail: gvazava.inessa@yandex.ru
Received June 09, 2022; in final form, July 19, 2022
DOI: 10.32607/actanaturae.11751

ABSTRACT **Type 2 diabetes mellitus (T2DM) is the most common endocrine disorder (90%) in the world; it has numerous clinical, immunological, and genetic differences from type 1 diabetes mellitus. The pathogenesis of T2DM is complex and not fully clear. To date, animal models remain the main tool by which to study the pathophysiology and therapy of T2DM. Rodents are considered the best choice among animal models, because they are characterized by a small size, short induction period, easy diabetes induction, and economic efficiency. This review summarizes data on experimental models of T2DM that are currently used, evaluates their advantages and disadvantages vis-a-vis research, and describes in detail the factors that should be taken into account when using these models. Selection of a suitable model for tackling a particular issue is not always trivial; it affects study results and their interpretation.**
KEYWORDS **type 2 diabetes mellitus, pathogenesis, insulin resistance, beta cells, experimental animals, streptozotocin.**
ABBREVIATIONS **T2DM – type 2 diabetes mellitus; DM – diabetes mellitus; T1DM – type 1 diabetes mellitus; β-cells – beta cells; STZ – streptozotocin; IR – insulin resistance; Lep – leptin; IAPP – islet amyloid polypeptide.**

INTRODUCTION

For many decades, diabetes mellitus (DM) has been one of the major health challenges in the world due to its associated increased morbidity, disability, and mortality. According to the International Diabetes Federation (IDF), there were 537 million people with DM in 2021; this number could reach 643 million by 2030, while the actual prevalence of DM is several times higher than what is on record [1]. DM is a chronic disease that develops either when the pancreas does not produce enough insulin (the hormone regulating blood sugar level) or when the body cannot effectively use the hormone it produces. A common consequence of uncontrolled DM is hyperglycemia, or elevated blood sugar, eventually leading to severe damage to numerous body systems, especially the nerves and blood vessels [2].

The presented review is a logical follow-up to our work that summarizes data on the pathogenesis of type 1 DM (T1DM) and considers the most commonly used experimental animal models as the most important tool in studying DM. The mechanisms of the most adequate and easily reproducible DM model, namely the streptozotocin-induced model of DM, were analyzed and discussed in [3]. Type 2 diabetes mellitus (T2DM) is the most common endocrine disease; it is diagnosed in more than 90% of all diabetic patients. T2DM symptoms may be similar to those of T1DM, although they are often less severe [2]. This review will focus on the pathogenic mechanisms of T2DM onset and progression, as well as modeling of various disease stages, in rodents for further use in the search for new therapeutic agents and treatments for T2DM.

T1DM and T2DM have numerous clinical, immunological, and genetic differences. T2DM (non-insulin-dependent, or adult-onset diabetes) develops as a result of inefficient use of insulin by the body. The disease is often diagnosed several years after its onset, when complications develop. Until recently, T2DM was observed only in adults; now it is increasingly prevalent in children, since childhood obesity, which

is associated with DM, has become an epidemic [2]. For a long time, there has been an erroneous belief that T2DM is a mild form of the disease, and that it might develop without complications. However, to date, researchers firmly believe that the condition is a severe chronic progressive disease, with more than 50% of patients having late complications by the time of the diagnosis. The high prevalence of T2DM among some ethnic groups and patients' relatives points to the existence of genetic factors that are associated with the disease. In recent years, several genetic polymorphisms associated with DM have been identified; however, no single gene responsible for the most common form of DM, namely non-insulin-dependent DM, has been identified. There are considered to be two subtypes of T2DM: with mutations in individual genes (10–15%) and damage to a set of genes (85–90%) responsible for insulin binding to a cell receptor, internalization of the hormone–receptor complex, autophosphorylation of β receptors, and phosphorylation of other membrane protein components. An example of multiple damage is the insulin resistance (IR) of cells caused by multiple mutations in the insulin receptor gene. Up to 30 different mutations have been identified in this gene [4–9].

T2DM is a multifactorial disease characterized by a large heterogeneity of metabolic defects, the most common of which are insufficient insulin production, IR, and incretin system defects. It is important to understand the multifactorial nature of T2DM, which is determined by the combinatorial effect of genes and the environment. Therefore, there is no simple genetic and epidemiological model that explains the disease inheritance. Hence the need to establish how much of the disease is determined by genes and what is the contribution of environmental factors, the combination of which regulates the threshold/level of tolerance to DM development [6, 7].

Despite the availability of modern treatment strategies, T2DM remains a pressing issue for the healthcare system worldwide. This is mainly due to an increase in the disease incidence associated with factors such as aging and the growth of obesity in the population. The risk of T2DM grows higher with age. Excess weight and obesity contribute to the development of IR and hyperglycemia. The progressive course of T2DM is an indication that lifestyle changes are not enough to achieve and maintain glycemic control; most T2DM patients require drug treatment [4, 5].

T2DM is relatively easy to diagnose when symptoms are present. However, according to the United Kingdom Prospective Diabetes Study (UKPDS), T2DM may remain undiagnosed for many years. It takes from three to six years for T2DM to be diagnosed from the moment of the disease onset. Therefore, early T2DM diagnosis remains relevant, especially in individuals at high risk of developing the disease. More than half of patients already have several complications by the time of their diagnosis. Severe retinopathy is found in 20–40% of patients. The development of diabetic complications, such as retinopathy, nephropathy, and neuropathy, is due to long-term hyperglycemia. This fact points to the necessity and importance of monitoring blood sugar levels [2].

The pathogenesis of T2DM is complex and not yet fully understood. To date, IR, impaired insulin secretion, increased glucose production by the liver, as well as hereditary predisposition, lifestyle, and nutritional habits leading to obesity, are considered to be the key elements of T2DM pathogenesis. Hyperglycemia develops when insulin secretion is no longer able to compensate for IR. Although IR is characteristic of T2DM patients and at-risk individuals, there is evidence of β-cell dysfunction and related disorders of insulin secretion, including the first phase of secretion in response to intravenous glucose infusion, impaired physiological pulsatile secretion of insulin, increased secretion of proinsulin, which indicates impaired insulin processing, and the accumulation of amyloid in pancreatic islets (which is normally secreted together with insulin). The decrease in the β-cell mass and function is of fundamental importance in T2DM pathogenesis. The loss of β-cell mass is poorly understood, although increased β-cell loss is considered to contribute to IR. The proposed mechanisms responsible for the loss of β-cells in T2DM include amyloid formation and endoplasmic reticulum stress; however, their relative contribution remains unknown. The pathology of Langerhans islets in T2DM, which is extremely heterogeneous, is worth attention. For example, many Langerhans islets look completely normal, some islets contain large amyloid deposits, while others do not. The differences in the age of β-cells is believed to be one of the factors underlying their heterogeneity [10, 11]. Amyloid formation in the Langerhans islets has a toxic effect on hormone-producing islet cells, leading to pancreatic damage. As a result, hyperproduction of hormones in T2DM is replaced by their deficiency [12–14]. Hyperglycemia alone can affect insulin secretion, since high glucose levels cause cell desensitization and/or dysfunction (glucose toxicity). These changes in the presence of IR usually develop over many years [10, 11, 15, 16]. An important condition for IR to develop in T2DM is obesity and weight gain. Obesity can be determined by genetic factors. However, di-

etary preferences, exercise intensity, and lifestyle in general also play an important role. The body cannot suppress lipolysis in adipose tissue, so free fatty acids are released from it, and their increased plasma levels can impair insulin-stimulated glucose transport and muscle glycogen synthase activity. Adipose tissue also functions as an endocrine organ, secreting many factors (adipocytokines) to the blood that positively (adiponectin) or negatively (tumor necrosis factor-α (TNF-α), interleukin 6, leptin, and resistin) affect glucose metabolism. Intrauterine growth retardation and low birth weight are also associated with IR development in older age, which may indicate the adverse prenatal effect of environmental factors on glucose metabolism. Currently, IR is mostly associated with impaired insulin action at the post-receptor level; in particular, with a significant decrease in the membrane levels of specific glucose transporters (GLUT-4, GLUT-2, and GLUT-1) [5–7, 17, 18].

According to modern concepts of the cellular and molecular mechanisms of T2DM, IR – or a decreased biological response of cells to one or several effects of normal blood levels of insulin – is the first element in the disease's pathogenesis. IR leads to the inability of insulin-dependent (muscle and adipose) tissues to absorb glucose from plasma and a disruption of glycogen (glucose polymer) synthesis in the liver. The fine mechanisms of IR development in T2DM are not yet fully understood. Although the exact cause of IR has not been elucidated, a number of underlying mechanisms have been suggested: oxidative stress, inflammation, insulin receptor mutations, endoplasmic reticulum stress, and mitochondrial dysfunction [19–24]. IR is known to affect the activity of the enzymes of glycolysis and gluconeogenesis, glycogen synthesis and glycogenolysis, β-oxidation of fatty acids, and lipogenesis. Insulin inhibits the mobilization of fats and intake of free fatty acids circulating in the blood by cells, potentiates protein synthesis in almost all tissues, primarily skeletal muscles, myocardium, and liver, and also affects the capture and transport of amino acids, which comprise all proteins, and major ions. Normally, a two-chain insulin molecule binds to a specific receptor located on the cell membrane carrying a tyrosine kinase fragment with enzymatic activity, which triggers tyrosine autophosphorylation, followed by the activation of the proteins involved in secondary signal transduction (insulin receptor substrate-1 (IRS1), Shc-1, SIRP-α, Gab-1, Cbl-b, etc.). IRS1 proteins activate phosphatidylinositol 3-kinase, which, in turn, triggers the action of protein kinases B. Protein kinases B and C initiate a cascade of enzymes that regulate carbohydrate and fat metabolism and lead to the incorporation of glucose transporters (GLUT-4) into the membranes of insulin-dependent cells (adipocytes and myocytes). This is how glucose molecules are transported from the blood plasma into cells [18, 19, 24, 25]. The mechanisms of nitric oxide synthesis in vascular endothelial cells in muscle tissue, intensive uptake of amino acids and synthesis of cellular proteins, as well as inhibition of apoptotic processes are triggered, together with the activation of glucose intake. Another group of proteins responsible for secondary signal transduction from the insulin receptor (Shc-, Sos-, Ras-, Raf-, and Map-) regulates the mechanisms of mitosis and cell proliferation and activates the synthesis of inflammatory mediators. A detailed study of the pathway of insulin action on intracellular processes allows us to imagine the versatility of the potent factors involved in IR development. Molecular causes behind the loss of the ability to transmit a signal may be the suppression of the activity of IRS1 tyrosine kinase and phosphatidylinositol 3-kinase due to various mutations in the gene encoding the insulin receptor. Impaired glucose entry into the cell can be caused by either a decrease in the efficiency of protein kinases B and C or structural deficiency of the transmembrane glucose transporter (GLUT-4). All of the abovementioned mechanisms of IR development can be congenital, genetically determined; they are described for a series of syndromes. The biological effects of insulin are much more often impaired during life due to the effect of additional factors. A decrease in the tyrosine kinase activity of the insulin receptor is currently considered the key mechanism undergirding the development of acquired IR. Membrane glycoprotein PC-1, which is produced in excess by myocytes and adipocytes, is a known factor involved in the disruption of the tyrosine kinase element in intracellular signal transmission. Inhibitors of tyrosine kinase effects, namely protein kinase C and TNF-α, are also synthesized by adipocytes in large amounts [5, 18, 19].

Another factor involved in IR development is a decrease in the activity of phosphatidylinositol 3-kinase due to either imbalance of its subunits caused by certain hormones (glucocorticoids and sex steroids) or excessive intake of free fatty acids and triglycerides by cells, leading to diacylglycerol accumulation. Adipose tissue plays an important role in the energy homeostasis of the whole organism and regulation of metabolic functions. It serves as a deposit of excess energy, in the form of triglycerides, in adipocytes and regulates lipid mobilization during fasting by releasing free fatty acids [24, 26, 27]. With the discovery of adipocyte-derived factors such as leptin, adiponectin, and resistin, adipose tissue is recognized as a complex endocrine organ. Adipose tissue can attach to

many organs (liver, pancreas, muscles, and the brain) through adipokine signaling and modulate systemic metabolism [27–31]. Thus, adipose tissue dysfunction plays an important role in the pathogenesis of such metabolic disorders as obesity, IR, and DM [32].

In addition to the described general mechanisms of impaired insulin action, the biologically active substances produced by adipocytes, which have a profound effect on systemic metabolism, play the most important role in IR development in the case of excessive growth of adipose tissue. Adipocyte-derived metabolites (adipocytokines) can affect various biochemical processes in many organs and tissues. Currently, more than 100 chemical compounds of similar origin are known, many of which are directly or indirectly associated with IR [27, 33, 34].

The peptide hormone leptin (Lep), one of the first identified adipocytokines, is encoded by the *ob* gene (obesity gene) [35, 28]. In addition to adipocytes, many tissues and organs (liver, muscles, ovaries, etc.) also produce Lep, which indicates the diversity of its biological effects. Lep occupies a central place in the regulation of energy homeostasis and body weight. The most studied mechanism of the hormone's action is the stimulation of the satiety center located in the hypothalamus. Normally, Lep in mammals exerts anorexigenic, catabolic, lipolytic, and hypoglycemic effects, thus triggering a negative feedback mechanism. In obesity, the action of Lep is impaired due to the inhibition of its normal transport through the blood–brain barrier or binding to the receptor form circulating in the blood [36, 37].

The feeling of hunger decreases or completely disappears with an increase in Lep blood levels. However, a log-term and persistent increase in the hormone level causes leptin resistance: the resistance of target cells in the hypothalamus to its effects. Lep resistance leads to excess intake of triglycerides and free fatty acids by the cells of insulin-dependent tissues, leading to IR [38].

Adiponectin is produced exclusively by adipocytes and plays an important role in the regulation of lipid and carbohydrate (glucose) metabolism, increasing the sensitivity of adipose and muscle tissues to insulin. The intracellular effects of adiponectin are achieved through the activation of AMP kinase and phosphatidylinositol 3-kinase, which regulate the oxidation of free fatty acids. Adiponectin decreases the production of inflammatory mediators (interleukin 6, interleukin 8, TNF-α, etc.) and the metalloproteases inhibiting the function of insulin receptor tyrosine kinase (IRS1) [39–41]. A decrease in the adiponectin level with excessive development of adipose tissue via the feedback mechanism (decrease in hormone production upon reaching the required level of its effect: accumulation of energy deposit of cells) is one of the factors behind IR development [42, 43].

The sensitivity of adipose and muscle tissues to insulin is also affected by an adipocytokine with a studied mechanism of action: resistin. Angiotensinogen and a number of other hormone-like substances produced by adipose tissue cells have a similar effect [44, 45].

Loss of tissue sensitivity to insulin leads to compensatory hyperproduction of the hormone by pancreatic β-cells. An increase in the plasma levels of insulin for some time makes it possible to overcome the IR barrier, while maintaining the required level of glucose intake by the cells. However, the storage capacity of the insular apparatus of the pancreas gradually becomes exhausted and leads to decompensation: namely, DM [46].

Much attention is paid to the development of innovative technologies to combat DM. Despite the tremendous progress achieved in molecular genetic research in the field of T2DM [47–52], measures for its prevention and treatment have not been developed at the proper level yet.

It is known that success in theoretical research and the development of methods for disease prevention and treatment cannot be achieved without disease modeling in experimental animals and depends on a correct choice of the model animal. Valuable data that can help understand the mechanism of the antidiabetic action of various agents for their subsequent targeted application can be obtained only with the use of experimental models that are closest to the disease etiology and pathogenesis. An objective analysis of the advantages and disadvantages of each model, depending on the established goal, will go a long way in helping avoid erroneous results [3].

T2DM is considered to be a complex, genetically heterogeneous human disease whose pathogenesis is determined by both inheritance and environmental factors in general. T2DM is studied by disease modeling in mice and rats. Rodents are considered the best choice among animal models, because they are relatively inexpensive to maintain; they reproduce rapidly, allowing genetic effects to be studied in several generations within a reasonable period of time; and, very importantly, because the rodent genome shares a more than 90% similarity with the human genome [53]. Rats are more preferable than mice, since it is easier to perform surgery on rats owing to their larger size; in addition, they are more resistant to various diseases.

In this study, we continue to analyze the existing experimental models in order to identify the most

suitable and available model for studying T2DM. The pathogenesis and laboratory models of T1DM are described in our previous work [3].

Rodent models of T2DM fall into two main categories: genetic (spontaneously induced) and non-genetic (experimentally induced) models. Non-genetic models are known to be more common than the genetic ones due to their lower cost; greater availability; easier DM induction; and, of course, simpler composition [3].

Because T2DM is characterized by IR and the inability of β-cells to adequately compensate for it, animal models of T2DM typically include modeling of IR and/or β-cell deficiency. Many animal models are obese, similar to the human condition in which obesity is strongly associated with T2DM development. Obesity can result from naturally occurring mutations, genetic manipulations, and consumption of high-fat foods.

GENETIC MODELS WITH OBESITY

Monogenic models

The following rodents are the most widely used as monogenic models of obesity to test new methods for treating T2DM: *Zucker* rats with diabetes and obesity (*Zucker diabetic fatty, ZDF*), *Lep ob/ob* and *Lepr db/db* mice with Lep deficiency [36, 37]. Impaired Lep reception is observed in these models in obesity. A homozygous mutation in *LEPR* makes the corresponding receptor non-functional. On the one hand, these animals lack the effect of fat reserves on the amount of food consumed, which leads to rapid development of obesity even in a standard, balanced diet. On the other hand, the disruption of Lep reception and internalization by cells impedes its clearance, leading to a sharp increase in the blood level of the hormone and development of immunotropic effects that are normally absent and caused by partial homology between the structures of Lep and a number of cytokines and chemokines [54, 55]. Expression of a large number of the genes involved in the various metabolic pathways that determine changes in body homeostasis is altered in the organs and tissues of these animals. A metabolic imbalance emerges in the body. Since Lep induces satiety, the lack of the functional hormone causes hyperphagia and subsequent obesity in these animals [56–58]. These changes are largely consistent with those in patients with alimentary obesity.

Lep ob/ob mice derive from animals with a spontaneous mutation found in an outbred colony at Jackson's laboratory in 1949. Mice with this phenotype were crossed with C57BL/6 mice, but it was not until 1994 that the mutant protein was identified as Lep [59]. These mice gain weight and develop hyperinsulinemia by two weeks of age. By week 4, hyperglycemia becomes apparent and the blood level of glucose continues to grow, peaking at 3–5 months of age and then decreasing as the mouse matures. Animals also experience hyperlipidemia, impaired thermoregulation, and decreased physical activity. Pancreatic hypertrophy is observed. Despite impaired insulin clearance, islets maintain secretion, which does not make this model fully representative of T2DM in humans. However, *C57Bl/KS* mice develop much more severe diabetes, with islet atrophy and early mortality. In addition, these mice are sterile [60, 61].

Lepr db/db mice were obtained at the Jackson's laboratory as a result of an autosomal recessive mutation in the Lep receptor. These mice develop hyperinsulinemia at two weeks of age, obesity and hyperphagia at week 3–4 of age, and hyperglycemia at week 4–8. The most commonly used strain is *C57BLKS/J*; these mice develop ketosis at the age of several months and have a relatively short lifespan [62, 63].

Zucker rats offer a classical model to study obesity, T2DM, hypertension, and cardiac dysfunction. These rats were named after Columbia University pathologists Louis and Theodore Zucker, who discovered a gene responsible for obesity in rats in 1961. Zuckers crossed *Merck M* and *Sherman* mice and revealed a spontaneous recessive mutation *fa* (*fatty*) in *Lepr*, the gene encoding the receptor to the satiety hormone Lep. The mutant Lep receptor causes obesity in these rats at week four [64]; the animals also develop hyperinsulinemia, hyperlipidemia, hypertension, and impaired glucose tolerance [63]. Mutation in these rats led to the emergence of a rat substrain with a diabetogenic phenotype: inbred *ZDF* rats, diabetic obese *Zucker* rats. These rats are less obese than *Zucker* rats but have more pronounced IR. It is impossible to compensate for IR in these animals due to the increased apoptosis in their β-cells [65]. Hyperinsulinemia is observed at about eight weeks of age, followed by a decrease in the insulin levels [66]. Diabetes usually develops around week 8–10 in males; females do not develop overt diabetes. These rats also show signs of diabetic complications [63].

Polygenic models

In contrast to the monogenic models described above, polygenic models of obesity can provide a more accurate model of the disease in humans. Numerous polygenic murine models of obesity, glucose intolerance, and diabetes are known, which makes it possible to perform a detailed study of different genotypes and their susceptibility. However, polygenic models (unlike monogenic ones) lack wild-type controls but demonstrate sexual dimorphism, with a preference for males

[67]. Polygenic models, namely *KK* and *KK AY* mice, *OLETF* rats, *NZO* mice, etc., are characterized by obesity-induced hyperglycemia, severe hyperinsulinemia, IR in both muscle and adipose tissue, and pronounced changes in the pancreatic islets: from hypertrophy and degranulation to fibrosis and their replacement by the connective tissue [67–70]. A number of works focused on the elimination of T2DM symptoms, analysis of the relationship between obesity and glucose homeostasis, as well as diabetic complications, have been done using polygenic models [71–86].

Induced obesity models

A high-fat diet leads to obesity. The model for feeding *C57BL/* mice a high-fat diet was first presented in 1988 [87]. It has been shown that mice fed a high-fat diet (about 60% of fats) can weigh more than a control group fed a standard diet after a week. Using this diet for several weeks causes a more pronounced weight gain, associated with IR, while the lack of compensation of β-cells leads to impaired glucose tolerance [88]. The obesity in this model is considered to be caused environmentally, rather than determined genetically; hence, it is more similar to the disease in humans compared to genetic models of obesity-induced diabetes. It has been shown that, in transgenic and knockout models, which may not show an overt diabetic phenotype in normal conditions, a high-fat diet stimulates β-cells and the gene starts to play an important role. The susceptibility to diet-induced metabolic changes depends on the mouse's strain. Thus, the effects may be left unnoticed in case of using a more resistant strain [89–95]. For example, inbred *C57BL/6* mice are characterized by heterogeneity in response to a high-fat diet. However, differential responses to a high-fat diet are not always in place even when using genetically homogenous rats and mice [96].

Rodents defined as **useful models** are used to study T2DM. They include the desert gerbil (*Psammomys obesus*; first discovered in 1960) and the recently described Nile grass rat (*Arvicanthis niloticus*) [97]. Most of these animals when kept in captivity with a normal diet for a year spontaneously develop diabetes that progresses from mild hyperglycemia with hyperinsulinemia to severe hyperglycemia with hypoinsulinemia and ketoacidosis. Progression from one stage to another can be prevented by restricting food intake. However, recovery from the final hyperglycemic/insulinopenic stage is impossible. Although these rodents are not hyperphagic, constant availability of a high-calorie diet results in obesity, dyslipidemia, hyperglycemia, as well as other signs of diabetes and metabolic syndromes, such as decreased β-cell mass, atherosclerosis, and hepatic steatosis, in them. Because of poor adaptation to overnutrition, *P. obesus* may be an ideal model for the thrifty gene effect, due to which the animal often develops IR and the metabolic syndrome after a rapid switch from food deficiency to excess. These animals are a valuable spontaneous model for research aimed at preventing diet-induced diabetes and represent a novel system of the interactions between genes and diet that affect energy use. This model will allow for a better understanding of the approaches to prevent and treat T2DM and the metabolic syndrome [97–101].

Models without obesity

However, not all T2DM patients are obese; thus, T2DM modeling in non-obese animals with β-cell dysfunction is indeed necessary [102]. *Goto-Kakizaki* (*GK*) rats are the most common non-obese models of T2DM [103]. This model was obtained by multiple crossing of *Wistar* rats, which are characterized by the worst glucose tolerance. It is assumed that IR is not the main initiator of hyperglycemia in this model, and impaired glucose metabolism is considered a consequence of reduced β-cell mass [104] and/or their aberrant function [105]. The effect of the morphology of pancreatic Largenhans islets on their metabolism varies in different rat colonies. For example, in some of them (Stockholm and Dallas colonies), the volume and density of β-cells are similar to those of the control; apparently, hyperglycemia is caused by the defects in insulin secretion, while a decrease in the β-cell mass is observed in the Paris colony of *GK* rats [105]. *GK* is one of the best characterized animal models of spontaneous T2DM; it is suitable for studying crucial aspects of the disease. The defective β-cell mass and function in the *GK* model are believed to be a reflection of complex interactions between multiple pathogenic factors. These factors include several independent loci containing the genes responsible for some diabetic features (except for a decrease in β-cell mass), gestational metabolic disorder inducing epigenetic programming of the pancreas (decreased neogenesis and/or β-cell proliferation) that is transferred to the next generation, loss of β-cell differentiation due to chronic exposure to hyperglycemia/hyperlipidemia, inflammatory mediators, oxidative stress, and impaired islet microarchitecture [101]. *GK* rats have been used to study both β-cell dysfunction in T2DM [106–109] and diabetic complications [110, 111].

hIAPP mice. Human T2DM is characterized by amyloid formation in the islet tissue derived from islet amyloid polypeptide (IAPP) [10, 112, 113]. In addition to humans and macaques, pancreatic islets in cats

also produce amyloid, which makes this animal a good model to study islet amyloidosis. This aspect of the disease is not usually modeled in rodents, since rodent IAPP is not amyloidogenic [11, 12, 114, 115]. However, transgenic mice expressing human *IAPP* (*hIAPP*) under the insulin promoter have been developed; these mice can produce amyloid in their islets. Using a large number of hIAPP models, it has been shown that *hIAPP* overexpression increases β-cell toxicity [116]. In addition, replicating β-cells are more susceptible to hIAPP toxicity; therefore, this model limits the adaptation of β-cells to increased insulin requirements [117].

Knockout and transgenic mice are also used to create specific T2DM models. These models have become a powerful tool in elucidating the role of specific genes in the glucose metabolism and disease pathogenesis [63, 118]. The use of knockout and transgenic mice made it possible to identify the transcription factors involved in the pancreas development and insulin signaling pathways. Tissue-specific knockouts turned out to be particularly useful in studying insulin signaling, since mice with global knockout of the insulin receptor are not viable [119–123].

Although T2DM is the most common form of DM, model development is more difficult in the case of T2DM, compared to T1DM. Genetic models such as obese diabetic *Zucker* rats and *db/db* mice are perhaps the closest to the human disease. However, the use of these models is limited because they have some crucial differences, do not accurately reflect T2DM in humans [124], and are also expensive.

STREPTOZOTOCIN MODELS OF T2DM

Streptozotocin models of T2DM (STZ T2DM) are the most commonly used animal models of T2DM. Two potentially useful STZ T2DM models have been developed. The model with simultaneous administration of nicotinamide to rats for partial protection of β-cells against the effects of STZ [125] is based on the fact that nicotinamide prevents the diabetogenic effect of STZ [126, 127]. This combination creates a model of insulin-deficient – but not insulin-resistant – T2DM, characterized by stable, moderate hyperglycemia associated with an approximately 60% loss of β-cell function [125, 128]. The use of this protocol results in moderate, non-fasting hyperglycemia in 75–80% of the animals, while the other animals either develop severe hyperglycemia after 2–3 weeks or remain normoglycemic but with glucose intolerance. The same protocol can be used in mice. It should be taken into account that the STZ dose and the time between administration of nicotinamide and STZ are of crucial importance. For example, if the STZ dose is too high or the time period between nicotinamide and STZ administration is too long, then a more severe insulin deficiency will be observed [129].

Since most T2DM patients have a combination of impaired insulin secretion and IR, another model has been developed to more closely mimic the human condition. To develop IR, animals were kept on a high-fat diet, followed by administration of moderate doses of STZ to cause β-cell dysfunction [130]. This resulted in hyperglycemia associated with hyperinsulinemia and IR [131]. The recommended diet provides 60% of calories from fat; a commercial, balanced diet should be used instead of the standard diet supplemented with fat [132]. The use of a high-fat diet to induce IR, followed by low to moderate doses of STZ to develop mild to moderate insulin deficiency, may currently be the most useful T2DM model. Animals kept on a high-fat diet are generally considered to be the best model for characterizing many complications associated with human DM [133].

An STZ dose should induce stable hyperglycemia in rats fed a high-fat diet for at least 130 days. If the STZ dose is too high, then the model represents T1DM and the mortality of the rats increases [134]. The use of two lower doses of STZ (30 mg/kg, intraperitoneally) administered at weekly intervals causes diabetes in 85% of the animals, with an average fasting blood glucose level of ~14 mmol/L (~252 mg/dL) [134]. Other researchers recommend using an STZ dose of 30 mg/kg intraperitoneally as the optimal dose for 12-week-old *Sprague-Dawley* rats fed a high-fat diet for eight weeks [135].

When STZ enters the bloodstream, it is delivered to pancreatic β-cells by glucose transporter protein 2 (GLUT-2). Inside the β-cells, STZ interrupts a number of important cellular processes and, if there is enough damage, it all culminates in DNA damage and cell death [3, 136, 137]. The final outcome of STZ administration is a decrease in the functional mass of β-cells, which manifests itself in insulin deficiency and further inability to metabolize glucose [137]. The combination of insulin deficiency with a high-fat diet, which requires elevated insulin levels to account for cellular IR [138, 139], leads to the glucose intolerance [140] characteristic of human T2DM. Prolonged mild β-cell damage results in more sustained and consistent fine effects than a single high dose. For example, administration of STZ using osmotic mini-pumps, in contrast to intraperitoneal and intravenous administration, provides significantly greater control over the resulting level of hyperglycemia while preserving the obesity phenotype [141]. The authors concluded that the observed overall increase in effectiveness is most likely due to the long-term effect on β-cells. In

addition, the dose-dependent effect of STZ is due to a reciprocal reduction in the insulin secretory capacity and morphological changes in the pancreas. This model is considered capable of reproducing different stages of T2DM, which are defined by the dose-dependent effect of STZ on glucose intolerance. This method requires fewer animals to observe significant effects than the previously used methods [142, 143], when the animals either do not respond to STZ or die depending on the drug dose [141].

As noted earlier, despite the wide variety of animal models of DM described to date, preference is given to STZ-induced diabetes. The mechanism of STZ action, doses and ways of its administration, as well as species and gender differences in sensitivity to STZ are described in detail in the first part of our study [3]. The advantage of STZ-induced diabetes is the relative ease of reproduction, high selectivity, and the possibility of inducing DM of varying severity and duration, which makes it possible to simulate not only gradually developing β-cell dysfunction, but also impaired glucose tolerance and the disorders associated with it [3].

Thus, it is important to emphasize that the long course of T2DM in humans makes it difficult to model the disease and that additional animal models and techniques are required. It is important to develop animal models that accurately reproduce T2DM pathogenesis in humans, since this will allow to identify preventive and therapeutic strategies against T2DM and the complications associated with it. When studying T2DM, it is important to consider the mechanisms underlying hyperglycemia and their relevance to the study. These mechanisms may include IR and/or β-cell deficiency. Indeed, the conclusion on whether drug intervention can reduce symptoms in any given model may hinge on whether β-cells have failed. Models also vary in their physiological significance, with some being more reminiscent of disease progression than others. Models such as pancreatic regeneration are quite extreme, and it remains to be established whether the mechanisms of β-cell expansion in these models may play a role in DM development in humans.

The choice of the model depends on the study objective. Animal models that are useful for evaluating potential antidiabetic agents and diabetic complications have limited construct validity and are therefore less useful as tools to determine disease etiology [144].

Using rats and mice to model diabetes has clear advantages over other species; these advantages include animal size, short induction period, easy DM induction, and economic efficiency [145]. Mice have made a huge contribution to the understanding of human biology as an experimental animal. Mouse models are widely used to study human diseases because of the genetic homology between them [107]. As for DM, mouse models are invaluable for studying obesity and T2DM, determining the role of inflammation, IR, and potential treatment strategies [146–148]. Rats are often used as a model to study the metabolic profile and pathologies associated with different T2DM stages [149]. Rat as an experimental model of human diseases has great advantages over mice and other rodents [150]. It is easier to study the physiology and accumulate information using rodents [142]. However, in order to gain insight into the diverse manifestations of DM in patients, it is highly advisable to use different models. More than one rodent species or strain should be studied, and the sex of the animal should also be considered, since many of the models described above, for example *Zucker* and *OLETF* rats and *NZO* mice, as well as many knockout and transgenic models of DM, are characterized by sexual dimorphism, which is not observed in humans [151]. It has been suggested that this is due to the action of sex hormones in some cases [152], although the exact mechanism of sexual dimorphism has not been elucidated. Indeed, the effects of sex hormones may vary in different mouse models; for example, gonadectomy in males prevents DM in some models, while being ineffective or even increasing disease incidence in others [151]. Sexual dimorphism may also include differences in mitochondria and stress responses [151]. When using knockout and transgenic mice, the presence of the hypothalamic syndrome and its effect on the phenotype should be excluded and appropriate controls are needed.

Experimental models are widely used to study drugs and the mechanisms underlying metabolic disorders. Since the prevalence and complications associated with DM continue to increase worldwide, DM models play a key role in the study of the disease's pathogenesis and its complications in humans such as retinopathy, nephropathy, cardiomyopathy, and neuropathy. Despite all the advantages offered by these animals in the creation of new drugs, they come with individual restrictions that would limit the development of new agents and therapeutic interventions. Obese and non-obese animals with hyperglycemia, IR, and β-cell resistance are commonly used to study T2DM. Since experimental models differ in their physiological purposes and are used to study various complications of T2DM in humans, selection of a model for a particular study should be considered with great caution. In addition to the models used to elucidate the mechanisms underlying DM, various animal models are currently utilized to develop and

validate new treatment strategies, most of which allow one to study some specific aspects of DM, while being of little use in other studies. All models have their pros and cons, and choosing the right one for a particular case is not always easy, since it affects the study results and their interpretation. When choosing a DM model, it is highly advisable to use a variety of different models to represent the diversity observed in diabetic patients. The number of available models is constantly on the rise, and it is important to consider their potential role in various aspects of the DM study.

Thus, despite the variety of biological models, the issue of a precise correspondence between the majority of experimental models and processes occurring in the human body remains unresolved. It is important that the results obtained during experimental modeling using laboratory animals represent a body of evidence that, with a certain degree of probability, can be extrapolated to humans.

Nevertheless, it is necessary to emphasize that, although the question of the extent to which the results extracted from biological models can be extrapolated to the human body is both the most important and the most difficult, experimental models remain our main tool for studying the pathophysiology and possible approaches to the treatment of DM [153]. ●

This work was supported by the Ministry of Science and Higher Education of the Russian Federation, agreement No. 075-15-2021-1075 dated September 28, 2021.

REFERENCES

1. The IDF Diabetes Atlas 10th Edition.
2. Bulletin of the World Health Organization No. 312, April 2016.
3. Gvazava I.G., Petrakova O.S., Rogovaya O.S., Borisov M.A., Terskih V.V., Vorotelyak E.A., Vasiliev A.V. // Acta Naturae. 2018. V. 10 № 1 (36). P. 25–35.
4. Dedov I.I., Shestakova M.V., Galstyan G.R. // Diabetes Mellitus. 2016. V. 19. № 2. P. 104–112.
5. Dedov I.I., Tkachuk B.A., Gusev N.B., Shirinsky V.P., Vorotnikov A.V., Kocheruga T.N., Mayorov A. U., Shestakova M.V. // Diabetes Mellitus. 2018. V. 21. № 5. P. 364–375.
6. Balabolkin M.I. // Medical Department. 2004. V. 1. № 9. P. 48–57.
7. Zheng, Y., Ley S.H., Hu F.B. // Nat. Rev. Endocrinol. 2018. V. 14. P. 88–98.
8. Permutt M.A., Wasson J., Cox N. // J. Clin. Invest. 2005. V. 115. № 6. P. 1431–1439.
9. De Rosa M.C., Glover H.J., Stratigopoulos G., LeDuc C.A., Su Q., Shen Y., Sleeman M.W., Chung W.K., Leibel R.L., Altarejos J.Y. // JCI Insight. 2021. V. 6. № 16. P. 149137–149155.
10. Weir G.C., Bonner-Weir S. //Ann. N.Y. Acad. Sci. 2013. V. 1281. P. 92–105.
11. Aguayo-Mazzucato C., van Haaren M., Mruk M., Lee Jr.T., Crawford C., Hollister-Lock J., Sullivan B.A., Johnson J.W., Ebrahimi A., Dreyfuss J.M., Deursen J.V., Weir G.C., Bonner-Weir S. // Cell Metab. 2017. V. 25. № 4. P. 898–910.
12. Gudkova A.Y., Antimonova O.I., Shavlovsky M.M. // Med. Acad. J. 2019. V. 19. № 2. P. 27–36.
13. Sevcuka A., White K., Terry C. // Life (Basel). 2022. V. 12. № 4. P. 583–602.
14. Bhowmick D.C., Singh S., Trikha S., Jeremic A.M. // Handb. Exp. Pharmacol. 2018. V. 245. P. 271–312.
15. Mukherjee N., Lin L. Contreras C.J., Templin A.T. // Metabolites. 2021. V. 11. № 11. P 796–825.
16. Hu F., Qiu X., Bu S. // Arch. Physiol. Biochem. 2020. V. 126. № 3. P. 235–241.
17. Tokarz V. L., MacDonald P.E., Klip A. // J. Cell. Biol. 2018. V. 217. № 7. P. 2273–2289.
18. Thurmond D.C., Pessin J.E. // Mol. Membr. Biol. 2001. V. 18. № 4. P. 237–245.
19. Yaribeygi H., Farrokhi F.R., Butler A.E., Sahebkar A. // J. Cell. Physiol. 2019. V. 234. № 6. P. 81528161–81528170.
20. Bitar M.S., Al-Saleh E., Al-Mulla F. // Life Sci. 2005. V. 77. № 20. P. 2552–2573.
21. Sarparanta J., García-Macia M., Singh R. // Curr. Diabetes Rev. 2017. V. 13. № 4. P. 352–369.
22. Latouche C., Natoli A., Reddy-Luthmoodoo M., Heywood S.E., Armitage J.A., Kingwell B.A. // PLoS One. 2016. V. 11. № 5. P. e0155108.
23. Hasnain S.Z., Prins J.B., McGuckin M.A. // J. Mol. Endocrinol. 2016. V. 56. № 2. P. 33–54.
24. Tkachuk V.A., Vorotnikov A.V. // Diabetes mellitus. 2014. V. 2. P. 29–40.
25. Hirabara S.M, Gorjão R., Vinolo M.A., Rodrigues A.C., Nachbar R.T., Curi R. // J. Biomed. Biotechnol. 2012. V. 2012. P. 379024–379040.
26. Rosen E.D., Spiegelman B.M. // Cell. 2014. V. 156. № 1–2. P. 20–44.
27. Luo L., Liu M. // J. Endocrinol. 2016. V. 31. № 3. P. 77–99.
28. Friedman J.M., Halaas J.L. // Nature. 1998. V. 395. № 6704. P. 763–770.
29. Giralt M., Cereijo R., Villarroya F. // Handb. Exp. Pharmacol. 2016. V. 233. P. 265–282.
30. Scherer P.E. // Diabetes. 2006. V. 6. P. 1537–1545.
31. Stern J.H., Rutkowski J.M., Scherer P.E. // Cell Metab. 2016. V. 23. № 5. P. 70–84.
32. Flenkenthaler F., Ländström E., Shashikadze B., Backman M., Blutke A., Philippou-Massier J., Renner S., Hrabe de Angelis M., Wanke R., et al. // Front. Med. 2021. V. 8. P. 751277–751289.
33. Rajala M.W., Lin Y., Ranalletta M., Yang X.M., Qian H., Gingerich R., Barzilai N., Scherer F.E. // Mol. Endocrinol. 2002. V. 16. № 8. P. 1920–1930.
34. Kharitonenkov A., Shiyanova T.L, Koester A., Ford A.M, Micanovic R., Galbreath E.J., Sandusky G.E., Hammond L.J., Moyers J.S., Owens R.A., et al. //J. Clin. Invest. 2005. V. 115. № 6. P. 1627–1635.
35. Zhang Y., Proenca R., Maffei M., Barone M., Leopold L,

Friedman J.M. // Nature. 1994. V. 372. № 6505. P. 425–532.
36. Schaab M., Kratzsch J. // Best Pract. Res. Clin. Endocrinol. Metab. 2015. V. 29. № 5. P. 661–670.
37. Trusov N.V., Apryatin S.A., Gorbachev A.Yu., Naumov V.A., Mzhelskaya K.V., Gmoshinski I.V. // Problems Endocrinol. 2018. V. 64. № 6. P. 371–382.
38. Scherer P.E. // Diabetes. 2016. V. 65. № 6. P. 1452–1461.
39. Chawla A., Nguyen K.D., Goh Y.P. // Nat. Rev. Immunol. 2011. V. 11. P. 738–749.
40. Hotamisligil G.S., Shargill N.S., Spiegelman B.M. // Science. 1993. V. 259. P. 87–91.
41. Cai Z., Huang Y., He B. // Cells. 2022. V. 11. № 9. P. 1424–1437.
42. Turer A.T., Khera A., Ayers C.R., Turer C.B., Grundy S.M., Vega G.L., Scherer P.E. // Diabetologia. 2011. V. 54. № 10. P. 2515–2524.
43. Ahl S., Guenther M., Zhao Sh., James R., Marks J., Szabo A., Kidambi S. // J. Clin. Endocrinol. Metab. 2015. V. 100. № 11. P. 4172–4180.
44. Rajala M.W., Lin Y., Ranalletta M., Yang X.M., Qian H., Gingerich R., Barzilai N., Philipp E., Scherer Ph.E. // Mol. Endocrinol. 2002. V. 16. № 8. P. 1920–1930.
45. Steppan C.M., Bailey S.T., Bhat S., Brown E.J., Banerjee R.R., Wright C.M., Patel H.R., Ahima R.S., Lazar M.A. // Nature. 2001. V. 409. № 6818. P. 307–312.
46. Aguilar-Salinas C.A., García E., Robles L., Riaño D., Ruiz-Gomez D.G., García-Ulloa A.C., Melgarejo M.A., Zamora M., Guillen-Pineda L., Mehta R., et al. // J. Clin. Endocrinol. Metab. 2008. V. 93. № 10. P. 4075–4079.
47. Stefan N. // Lancet Diabetes Endocrinol. 2020. V. 8. № 7. P. 616–627.
48. Schleinitz D., Krause K., Wohland T., Gebhardt C., Linder N., Stumvoll M., Blüher M., Bechmann I., Kovacs P., Gericke M., Tönjes A. // Eur. J. Hum. Genet. 2020. V. 28. № 12. P. 1714–1725.
49. Raajendiran A., Krisp C., De Souza D.P., Ooi G., Burton P., Taylor R.A., Molloy M.P., M.J. // Am. J. Physiol. Endocrinol. Metab. 2021. V. 320. № 6. P. 1068–1084.
50. Gastaldelli A., Gaggini M., DeFronzo R. // Curr. Opin. Clin. Nutr. Metab. Care. 2017. V. 20. № 4. P. 300–309.
51. Guilherme A., Henriques F., Bedard A.H., Czech M.P. // Nat. Rev. Endocrinol. 2019. V. 15. № 4. P. 207–225.
52. Duvnjak L., Duvnjak M. // J. Physiol. Pharmacol. 2009. V. 60. Suppl. 7. P. 19–24.
53. Gibbs R.A., Weinstock G.M., Metzker M.L., Muzny D.M., Sodergren E.J., Scherer S. Scott G., Steffen D., Worley K.C., Burch P.E., et. al. // Nature. 2004. V. 428. P. 493–521.
54. Lopez-Jaramillo P., Gomez-Arbelaez D., Lopez-Lopez J., López-López C., Martínez-Ortega J., Gómez-Rodríguez A., Triana-Cubillos S. // Horm. Mol. Biol. Clin. Investig. 2014. V. 18. № 1. P. 37–45.
55. Perez-Perez A., Vilarino-Garcia T., Fernandez-Riejos P., Martín-González J., Segura-Egea J.J., Sánchez-Margalet V. // Cytokine Growth Factor Rev. 2017. V. 35. P. 71–84.
56. Yoshida S., Tanaka H., Oshima H., Yamazaki T., Yonetoku Y., Ohishi T. // Biochem. Biophys. Res. Commun. 2010. V. 400. № 4. P. 745–751.
57. Gault V.A., Kerr B.D., Harriott P., Flatt P.R. // Clin. Sci. (London). 2011. V. 121. P. 107–117.
58. Park J.S., Rhee S.D., Kang N.S., Jung W.H., Kim H.Y., Kim J.H. // Biochem. Pharmacol. 2011. V. 81. P. 1028–1035.
59. Zhang Y., Proenca R., Maffei M., Barone M., Leopold L., Friedman J.M. // Nature. 1994. V. 372. P. 425–432.
60. Lindstrom P. // Scientificworld Journal. 2007. V. 7. P. 666–685.
61. Fang J.Y., Lin C.H., Huang T.H., Chuang S.Y. // Nutrients. 2019. V. 11. P. 530–573.
62. Chen H., Charlat O., Tartaglia L.A., Woolf E.A., Weng X., Ellis S.J., Lakey N.D., Culpepper J., Moore K.J., Breitbart R.E. // Cell. 1996. V. 84. P. 491–495.
63. King A.J.F. // Br. J. Pharmacol. 2012. V. 166. № 3. P. 877–894.
64. Phillips M.S., Liu Q., Hammond H.A., Dugan V., Hey P.J., Caskey C.J., Hess J.F. // Nat. Genet. 1996. V. 13. P. 18–19.
65. Pick A., Clark J., Kubstrup C., Levisetti M., Pugh W., Bonner-Weir S., Polonsky K.S. // Diabetes. 1998. V. 47. P. 358–364.
66. Shibata T., Takeuchi S., Yokota S., Kakimoto K., Yonemori F., Wakitani K. // Br. J. Pharmacol. 2000. V. 130. P. 495–504.
67. Leiter E.H. // Methods Mol. Biol. 2009. V. 560. P. 1–17.
68. Chakraborty G., Thumpayil S., Lafontant D.E, Woubneh W., Toney J.H. // Lab. Anim. (N.Y.). 2009. V. 38. P. 364–368.
69. Kawano K., Hirashima T., Mori S., Natori T. // Diabetes. Res. Clin. Pract. 1994. V. 24. (Suppl.). P. 317–320.
70. Clee S.M., Attie A.D. // Endocr. Rev. 2007. V. 28. P. 48–83.
71. Chen W., Zhou X.B., Liu H.Y., Xu C., Wang L.L., Li S. // Br. J. Pharmacol. 2009. V. 157. P. 724–735.
72. Fukaya N., Mochizuki K., Tanaka Y., Kumazawa T., Jiuxin Z., Fuchigami M., Toshinao Goda T.// Eur. J. Pharmacol. 2009. V. 624. P. 51–57.
73. Mochizuki K., Fukaya N., Tanaka Y., Fuchigami M., Goda T. // Metabolism. 2011. V. 60. № 11. P. 1560–1565.
74. Guo K., Yu Y.H., Hou J., Zhang Y. // Nutr. Metab. (London). 2010. V. 7. P. 57–68.
75. Jia D., Yamamoto M., Otani M., Otsuki M. // Metabolism. 2004. V. 53. № 4. P. 405–413.
76. Ishiyama S., Kimura M., Nakagawa T., Fujimoto Y., Uchimura K., Kishigami S., Mochizuki K. // Front. Endocrinol. (Lausanne). 2021. V. 1. P. 746838–746845.
77. Kottaisamy C.P.D., Raj D.S., Prasanth Kumar V., Sankaran U. // Lab. Anim. Res. 2021. V. 37. № 1. P. 23–35.
78. Loza-Rodríguez H., Estrada-Soto S., Alarcón-Aguilar F.J., Huang F., Aquino-Jarquín G., Fortis-Barrera Á., Giacoman-Martínez A., Almanza-Pérez J.C. // Eur. J. Pharmacol. 2020. V. 883. P. 173252–173260.
79. Yoshinari O., Igarashi K. // Br. J. Nutr. 2011. V. 106. P. 995–1004.
80. Xu T.Y., Chen R.H., Wang P., Zhang R.Y., Ke S.F., Miao C.Y. // Clin. Exp. Pharmacol. Physiol. 2010. V. 37. № 4. P. 441–446.
81. Itoh T., Kobayashi M., Horio F., Furuichi Y. // Nutrition. 2009. V. 25. № 2. P. 134–141.
82. Kluth O., Mirhashemi F., Scherneck S., Kaiser D., Kluge R., Neschen S., Joost H.G., Schürmann A. // Diabetologia. 2011. V. 54. P. 605–616.
83. Lee M.Y., Shim M.S., Kim B.H., Hong S.W., Choi R., Lee E.Y., Nam S.M., Kim G.W., Shin J.Y., Shin Y.G., et al. // Diabetes. Metab. J. 2011. V. 35. P. 130–137.
84. Choi R., Kim B.H., Naowaboot J., Lee M.Y., Hyun M.R., Cho E.J., Lee E.S., Lee E.Y., Yang Y.C., Chung C.H., et al. // Exp. Mol. Med. 2011. V. 43. № 12. P. 676–683.
85. Fang R.C., Kryger Z.B., Buck D.W., De la Garza M., Galiano R.D., Mustoe T.A. // Wound. Repair. Regen. 2010. V. 18. P. 605–613.
86. Rai V., Moellmer R., Agrawal D.K. // Mol. Cell. Biochem. 2022. V. 477. № 4. P. 1239–1247.
87. Surwit R.S., Kuhn C.M., Cochrane C., McCubbin J.A.,

Feinglos M.N. // Diabetes. 1988. V. 37. P. 1163–1167.
88. Winzell M.S., Ahren B. // Diabetes. 2004. V. 53. Suppl. 3. P. 215–219.
89. Surwit R.S., Feinglos M.N., Rodin J., Sutherland A., Petro A.E., Opara E.C., Kuhn C.M., Rebuffé-Scrive M. // Metabolism. 1995. V. 44. P. 645–651.
90. Bachmanov A.A., Reed D.R., Tordoff M.G., Price R.A., Beauchamp G.K. // Physiol. Behav. 2001. V. 72. P. 603–613.
91. Sclafani A. // Physiol. Behav. 2007. V. 16. № 90 (4). P. 602–611.
92. Almind K., Kahn C.R. // Diabetes. 2004. V. 53. P. 3274–3285.
93. Torre-Villalvazo I., Cervantes-Pérez L.G., Noriega L.G., Jiménez J.V., Uribe N., Chávez-Canales M., Tovar-Palacio C., Marfil-Garza B.A., Torres N., Bobadilla N.A., et al. // Am. J. Physiol. Endocrinol. Metab. 2018. V. 314. № 1. P. 53–65.
94. Lackey D.E., Lazaro R.G., Li P., Johnson A., Hernandez-Carretero A., Weber N., Vorobyova I., Tsukomoto H., Osborn O. // Am. J. Physiol. Endocrinol. Metab. 2016. V. 311. № 6. P. 989–997.
95. Pereira-Silva D.C., Machado-Silva R.P., Castro-Pinheiro C., Fernandes-Santos C. // Int. J. Exp. Pathol. 2019. V. 100. № 3. P. 153–160.
96. Burcelin R., Crivelli V., Dacosta A., Roy-Tirelli A., Thorens B. // Am. J. Physiol. Endocrinol. Metab. 2002. V. 282. P. 834–842.
97. Noda K., Melhorn M.I., Zandi S., Frimmel S., Tayyari F., Hisatomi T., Almulki L., Pronczuk A., Hayes K.C., Hafezi-Moghadam A., et al. // FASEB J. 2010. V. 24. P. 2443–2453.
98. Noda K., Nakao S., Zandi S., Sun D., Hayes K.C., Hafezi-Moghadam A. // FASEB J. 2014. V. 28. № 5. P. 2038–2046.
99. Sinasac D.S., Riordan J.D., Spiezio S.H., Yandell B.S., Croniger C.M., Nadeau J.H. // Int. J. Obes. (London). 2016. V. 40. № 2. P. 346–355.
100. Pirmardan R.E., Barakat A., Zhang Y., Naseri M., Hafezi-Moghadam A. // FASEB J. 2021. V. 35. № 6. P. 21593–21600.
101. Chaabo F., Pronczuk A., Maslova E., Hayes K. // Nutr. Metab. (London). 2010. V. 7. P. 29–35.
102. Weir G.C., Marselli L., Marchetti P., Katsuta H., Jung M.H., Bonner-Weir S. // Diabetes. Obes. Metab. 2009. V. 11. Suppl. 4. P. 82–90.
103. Goto Y., Kakizaki M., Masaki N. // Tohoku J. Exp. Med. 1976. V. 119. P. 85–90.
104. Portha B., Giroix M.H., Serradas P., Gangnerau M.N., Movassat J., Rajas F., Bailbe D., Plachot C., Mithieux G., Marie J.C., et al. // Diabetes. 2001. V. 50. Suppl. 1. P. 89–93.
105. Ostenson C.G., Efendic S. // Diabetes. Obes. Metab. 2007. V. 9. Suppl. 2. P. 180–186.
106. Portha B., Lacraz G., Kergoat M., Homo-Delarche F., Giroix M.H., Bailbe D, Gangnerau M.N., Dolz M., Tourrel-Cuzin C., Movassat J., et al. // Mol. Cell. Endocrinol. 2009. V. 297. P. 73–85.
107. Kottaisamy C.P.D., Raj D.S., Kumar P.V., Sankaran U. // Lab. Anim. Res. 2021. V. 37. № 1. P. 23–29.
108. Zhao J.D., Li Y., Sun M., Yu C.J., Li J.Y., Wang S.H., Yang D., Guo C.L., Du X., Zhang W.J., et al. // World. J. Gastroenterol. 2021. V. 2. № 8. P. 708–724.
109. Szkudelska K., Deniziak M., Sassek M., Szkudelski I., Noskowiak W., Szkudelski T. // Int J. Mol. Sci. 2021. V. 22. № 5. P. 2469–2476.
110. Ehses J.A., Lacraz G., Giroix M.H., Schmidlin F., Coulaud J., Kassis N., Irminger J.C., Kergoat M., Portha B., Homo-Delarche F., et al. // Proc. Natl. Acad. Sci. USA. 2009. V. 106. P. 13998–14003.
111. Okada S., Saito M., Kinoshita Y., Satoh I., Kawaba Y., Hayashi A., Oite T., Satoh K., Kanzaki S. // Biomed. Res. 2010. V. 31. P. 219–230.
112. Burillo J., Marqués P., Jiménez B., González-Blanco C., Benito M., Guillén C. // Cells. 2021. V. 10. № 5. P. 1236–1247.
113. Asiri M.M.H., Engelsman S., Eijkelkamp N., Höppener J.W.M. // Cells. 2020. V. 9. № 6. P. 1553–1563.
114. Hoppener J.W., Oosterwijk C., van Hulst K.L., Verbeek J.S., Capel P.J., de Koning E.J., Clark A., Jansz H.S., Lips C.J. // J. Cell. Biochem. 1994. V. 55. Suppl. P. 39–53.
115. Zhang X.X., Pan Y.H., Huang Y.M., Zhao H.L. // World. J. Diabetes. 2016. V. 7. № 9. P. 189–197.
116. Matveyenko A.V., Butler P.C. // ILAR. J. 2006. V. 47. P. 225–233.
117. Matveyenko A.V., Gurlo T., Daval M., Butler A.E., Butler P.C. // Diabetes. 2009. V. 58. P. 906–916.
118. Hara M., Wang X., Kawamura T., Bindokas V.P., Dizon R.F., Alcoser S.Y., Magnuson M.A., Bell G.I. // Am. J. Physiol. Endocrinol. Metab. 2003. V. 284. P. 177–183.
119. Sanavia T., Huang C., Manduchi E., Xu Y., Dadi P.K., Potter L.A., Jacobson D.A., Di Camillo B., Magnuson M.A., Stoeckert C.J. Jr., Gu G. // Front. Cell. Dev. Biol. 2021. V. 9. P. 648791–64801.
120. Sasaki S., Lee M.Y.Y., Wakabayashi Y., Suzuki L., Winata H., Himuro M., Matsuoka T.A., Shimomura I., Watada H., Lynn F.C., et al. // Diabetologia. 2022. V. 65. № 5. P. 811–828.
121. Habener J.F., Kemp D.M., Thomas M.K. // Endocrinology. 2005. V. 146. P. 1025–1034.
122. Oliver-Krasinski J.M., Kasner M.T., Yang J., Crutchlow M.F., Rustgi A.K., Kaestner K.H., Stoffers D.A. // J. Clin. Invest. 2009. V. 119. № 7. P. 1888–1898.
123. Wang Q., Jin T. // Islets. 2009. V. 1. P. 95–101.
124. Wang B., Chandrasekera P.C., Pippin J.J. // Curr. Diabetes. Rev. 2014. V. 10. № 2. P. 131–145.
125. Masiello P., Broca C., Gross R., Roye M., Manteghetti M., Hillaire-Buys D., Novelli M., Ribes G. // Diabetes. 1998. V. 47. P. 224–229.
126. Junod A., Lambert A.E., Stauffacher W., Renold A.E. // J. Clin. Invest. 1969. V. 48. P. 2129–2139.
127. Schein P.S., Cooney D.A., Vernon M.L. // Cancer Res. 1967. V. 27. P. 2324–2332.
128. Ghasemi A., Khalifi S., Jedi S.S. // Acta. Physiologica Hungarica. 2014. V. 101. P. 408–420.
129. Masiello P. // Int. J. Biochem. Cell. Biol. 2006. V. 38. № 5. P. 873–893.
130. Reed M.J., Meszaros K., Entes L.J., Claypool M.D., Pinkett J.G., Gadbois T.M., Reaven G.M. // Metabolism. 2000. V. 49. P. 1390–1394.
131. Chao P.C., Li Y., Chang C.H., Shieh J.P., Cheng J.T., Cheng K. C. // Biomed. Pharm. 2018. V. 101. P. 155–161.
132. Gheibi S., Kashfi K., Ghasemi A. // Biomed. Pharm. 2017. V. 95. P. 605–613.
133. Furman B.L. // Curr. Protoc. 2021. V. 1. P. 78–99.
134. Zhang M., Lv X.Y., Li J., Xu Z.G., Chen L. // Exp. Diab. Res. 2008. V. 2008. P. 704045–704054.
135. Yorek M.A. // Int. Rev. Neurobiol. 2016. V. 127. P. 89–112.
136. Elsner M., Tiedge M., Guldbakke B., Munday R., Lenzen S. // Diabet. 2002. V. 45. P. 1542–1549.
137. Lenzen S. // Diabetologia. 2008. V. 51. P. 216–226.
138. Olefsky J., Crapo P.A., Ginsberg H., Reaven G.M. // Metabolism. 1975. V. 24. № 4. P. 495–503.
139. Kibenge M.T., Chan C.B. // Metabolism. 2002. V. 51.

№ 6. P. 708–715.
140. Srinivasan K., Viswanad B., Asrat L., Kaul C., Ramarao P. // Pharm. Res. 2005. V. 52. P. 313–320.
141. Premilovac D., Gasperini R.J., Sawyer S., West A., Keske M.A., Taylor B.V., Foa L. // Sci. Rep. 2017. V. 7. № 1. P. 14158–14169.
142. Skovsø S. // J. Diab. Inv. 2014. V. 5. P. 349–358.
143. de la Garza-Rodea A.S., Knaän-Shanzer S., den Hartigh J.D., Verhaegen A.P., van Bekkum D.W. // J. Am. As. Lab. Anim. Science. 2010. V. 49. P. 40–44.
144. Furman B.L., Candasamy M., Bhattamisra S.K., Veettil S.K. // J. Ethnopharmacol. 2020. V. 30. № 247. P. 112264–112274.
145. Wu K.K., Huan Y. // Atherosclerosis. 2007. V. 191. № 2. P. 2419–2426.
146. Heydemann A. // J. Diabetes Res. 2016. V. 2016. P. 2902351–2902360.
147. Islam M.S, du Loots T. // Meth. Find. Exp. Clin. Pharmacol. 2009. V. 31. № 4. P. 249–261.
148. Iannaccone P.M., Jacob H.J. // Dis. Model Mech. 2009. V. 2. № 5–6. P. 206–210.
149. Sharma P., Garg A., Garg S., Singh V. // Asian J. Biomat. Res. 2016. V. 2. P. 99–110.
150. Bryda E.C. // Mol. Med. 2013. V. 110. № 3. P. 207–211.
151. Franconi F., Seghieri G., Canu S., Straface E., Campesi I., Malorni W. // Pharm. Res. 2008. V. 57. № 1. P. 6–18.
152. Arai I., Miyazaki N., Seino Y., Fukatsu A. // Biosci. Biotech. Biochem. 2007. V. 71. P. 1920–1926.
153. Mestas J., Hughes C.C. // J. Immunol. 2004. V. 172. № 5. P. 2731–2738.

Mechanisms of P-Glycoprotein Regulation Under Exogenous and Endogenous Oxidative Stress *In Vitro*

Yu. V. Abalenikhina*, A. V. Shchulkin, P. Yu. Mylnikov, E. D. Rokunov, E. N. Yakusheva
Ryazan State Medical University named after Academician I.P. Pavlov, Ryazan, 390026 Russia
*E-mail: abalenihina88@mail.ru
Received June 26, 2022; in final form, August 11, 2022
DOI: 10.32607/actanaturae.11759

ABSTRACT **We investigated the mechanisms of P-glycoprotein (P-gp) transporter regulation in Caco-2 cells under exogenous and endogenous oxidative stress (OS). Exogenous OS was modeled by exposure of the growth medium to hydrogen peroxide at concentrations of 0.1, 0.5, and 1 μM for 24 h or 10 μM for 72 h. Endogenous OS was modeled by incubating cells with *DL*-buthionine sulfoximine (BSO, gamma-glutamylcysteine synthetase inhibitor) at a concentration of 10, 50, and 100 μM for 24 h. The levels of intracellular reactive oxygen species (ROS) were assessed using MitoTracker Red CM-H_2XRos fluorescent probes. Relative P-gp contents were analyzed using Western blot. Exogenous and endogenous OS was shown to increase relative to P-gp contents. An important role played by the Nrf2-Keap1 signaling pathway in increasing the P-gp contents under H_2O_2-induced exogenous OS was revealed using specific inhibitors. The transcription factor HIF1 is involved in the regulation of the P-gp levels under 24-hour exogenous OS, and the transcription factor CAR is involved in the regulation of transporter levels under 72-hour OS. All tested transcription factors and signaling pathways are involved in P-gp induction under endogenous OS. Most likely, this is associated with the bimodal effect of BSO on Pgp. On the one hand, BSO induces the development of OS; on the other, BSO, as a xenobiotic, is able to stimulate PXR and CAR, which, in turn, increase the P-gp contents.**
KEYWORDS **P-glycoprotein, oxidative stress, Western blot, Nrf2, HIF1α, CAR, PXR, Caco-2 cell line.**
ABBREVIATIONS **ROS – reactive oxygen species; BSO – *DL*-buthionine sulfoximine; OS – oxidative stress; CAR – constitutive androstane receptor; HIF1α – hypoxia-inducible factor 1a; Nrf2 – nuclear factor erythroid 2-related factor 2; PXR – pregnane X receptor; Pgp – P-glycoprotein.**

INTRODUCTION

P-glycoprotein (P-gp, ABCB1), a product of the multidrug resistance gene (*MDR1*), is an ATP-dependent transporter protein localized on the cytoplasmic membranes of intestinal enterocytes, hepatocytes, renal tubule epithelial cells, and blood–tissue barrier endothelial cells [1].

P-gp displays wide substrate specificity and acts as an efflux transporter that controls the cell's uptake of transporter substrates, such as antitumor, antihypertensive, and antihistamine drugs, cardiac glycosides, antiplatelet agents, anticoagulants, steroid and thyroid hormones, antibiotics, HIV proteinase inhibitors, and immunosuppressants. Given these properties, P-gp is believed to play an important role in the protection of tumor cells from cytotoxic agents (development of multidrug tumor resistance), inhibition of substrate transport into fetal tissues and sequestered organs (brain, testicles), and the pharmacokinetics (absorption, distribution, excretion) of drugs [2, 3].

A number of substances and factors can affect P-gp activity and expression. For example, P-gp expression changes occur in the blood-brain barrier in neurological diseases (epilepsy) [4] and in gastric cancer and osteosarcoma cells [5, 6].

Oxidative stress (OS) is a typical pathological process induced by a shift in the balance between oxidants and antioxidants towards oxidants, which leads to redox signaling and control impairment and/or biomacromolecule damage [7]. OS plays an important role in the pathogenesis of many diseas-

es, including those whose character is cardiovascular, oncological, bronchopulmonary, ophthalmic, etc. [8]. Incubation of a rat hepatocyte culture with H_2O_2 (0.5–1 mM, 72 h) was shown to increase the expression of the *P-gp* gene and the level and activity of the transporter protein encoded by this gene [9]. Exposure of a primary rat endothelial cell culture to H_2O_2 at a concentration of up to 500 μM for 48 h was found to increase P-gp expression and, to a lesser extent, affect the activity of the transporter protein [10]. At the same time, treatment of hCMEC/D3 cells (an *in vitro* blood–brain barrier model) with H_2O_2 (0.5–5 mM, 20 min) reduced the transport activity of P-gp in [11]. Exposure of endothelial rat brain cells to H_2O_2 at a concentration of 200 μM was shown to cause the development of OS, increase the expression of mRNAs of the *mdr1a* and *mdr1b* genes encoding P-gp, as well as elevate the synthesis of the P-gp protein. Pretreatment of cells with polyethylene glycol-catalase reversed these changes [12]. Exposure of rat hepatocytes to a catalase inhibitor, 3-amino-1,2,4-triazole (2–4 mM for 72 h or 10 mM for 1 h), led to increased expression of *mdr1b* mRNA and P-gp [9]. On the contrary, antioxidants (1 mM ascorbate, 10 mM mannitol) considerably suppressed *mdr1b* mRNA expression and P-gp overexpression [13, 14]. Caco-2 cells cultured in a medium containing 1 μM/L H_2O_2 increased P-gp expression, while H_2O_2 at a concentration of 10 mM/L decreased the expression of the transporter [15]. P-gp expression in mitochondria of D407 cells (retinal pigment epithelium) was increased by H_2O_2 and suppressed by antioxidants [16].

In our laboratory, studies on Caco-2 cells showed that short-term (3 h) exposure to H_2O_2 at concentrations of 10 and 50 μM decreases P-gp activity and at 100 μM also reduces the levels of the transporter protein. Increasing the exposure duration to 24 and 72 h revealed P-gp induction at low H_2O_2 concentrations (0.1–1 μM, 24 h and 10 μM, 72 h), and increasing the H_2O_2 concentration to 100 μM and higher led to a decrease in the P-gp content and activity [17].

Thus, most studies have demonstrated that pro-oxidants increase P-gp expression and activity, which can be suppressed during the adaptation process failure and decompensated OS development.

A decrease in P-gp levels under OS conditions is believed to be associated with damage to the transporter protein molecule by reactive oxygen species (ROS), but the mechanisms for increasing P-gp expression have not been elucidated. The transcription factors Nrf2 and HIF1 are supposed to be involved in this process [17, 18]. The aim of this study was to explore the mechanisms of P-gp regulation in OS.

EXPERIMENTAL

Cell culture

In this study, we used the human colon adenocarcinoma Caco-2 cell line (Shared Research Facility "Collection of Vertebrate Cell Cultures", Saint-Petersburg, Russia). The cells were cultured at 37°C and 5% CO_2 in a WS-189C incubator (World Science, Korea) in a Dulbecco's modified Eagle's medium (DMEM) supplemented with high glucose (4,500 mg/L), *L*-glutamine (4 mM), 15% fetal bovine serum, 100 U/mL penicillin, and 100 μg/mL streptomycin (all reagents from Sigma-Aldrich, USA). The cells were seeded in six-well plates (Corning, USA); the well surface area was 9.6 cm^2; the number of cells per well was $1.8–2.0 \times 10^6$; the working volume of the growth medium was 1.5 mL. The cells were cultured for 21 days, because such an amount of time was required for their spontaneous differentiation into enterocyte-like cells overexpressing P-gp [19].

In the study, the following experimental groups were formed:

1) Control ($n = 3$): cells incubated in the growth medium supplemented with an equivalent volume of water for injection (solvent of H_2O_2 and BSO);

2) P-gp induction under simulated OS conditions.

Exogenous OS was simulated by adding into the growth medium H_2O_2 at a concentration of 0.1, 0.5, and 1 μM for 24 h ($5–50 \times 10^{-17}$ mol/cell) and 10 μM for 72 h (5×10^{-15} mol/cell).

Endogenous OS was induced using an inhibitor of glutathione synthesis, *DL*-buthionine sulfoximine (BSO, γ-glutamylcysteine synthetase inhibitor) [20] at final concentrations of 10, 50, and 100 μM in the growth medium ($5–50 \times 10^{-15}$ mol/cell).

Pro-oxidant concentrations and exposure duration were chosen in accordance with the results of preliminary experiments on P-gp induction [17, 21].

3) OS inhibition: pro-oxidants and 1 mM glutathione were simultaneously added to the growth medium [22].

4) Evaluation of the role of the Nrf2-mediated mechanism in P-gp induction under OS: an inhibitor, N-(1,3-benzodioxol-5-ylmethyl)-5-(4-fluorophenyl)-thieno[2,3-d]pyrimidin-4-amine (AEM1, Sigma-Aldrich), at a concentration of 5 μM was added to the growth medium with cells 30 min before their exposure to H_2O_2/BSO [23].

5) Evaluation of the role of the HIF1-mediated mechanism in P-gp induction under OS: N,N'-(disulfanediylbis(ethane-2,1-diyl))bis(2,5-dichlorobenzenesulfonamide) (KC7F2, Sigma-Aldrich), at a concentration of 7.5 μM was added to the growth medium

with cells 30 min before their exposure to H_2O_2/BSO [24].

6) Evaluation of the role of the CAR-mediated mechanism in P-gp induction under OS: an inhibitor, ethyl [5-[(diethylamino)acetyl]-10,11-dihydro-5H-dibenz[b,f]azepin-3-yl]carbamate (CINPA1, TOCRIS, UK), at a concentration of 10 μM was added to the growth medium with cells 30 min before their exposure to H_2O_2/BSO [25].

7) Evaluation of the role of the PXR-mediated mechanism in P-gp induction under OS: ketoconazole (Sigma-Aldrich) at a concentration of 10 μM was added to the growth medium with cells 30 min before their exposure to H_2O_2/BSO [26].

Each experiment was performed in triplicate. During 72-hour exposure, the growth medium containing a pro-oxidant and an inhibitor was changed every 24 h.

Pro-oxidant-induced ROS overproduction was confirmed using fluorescent probes

Cells were cultured in 24-well plates. After incubation with H_2O_2 for 3 h and BSO for 24 h at the tested concentrations, the level of intracellular ROS was assessed by staining the cells with MitoTracker Red CM-H_2XRos (Invitrogen, USA). MitoTracker Red probes (non-fluorescent form) contain reduced dihydrorosamine that penetrates into living cells, binds to the thiol groups in mitochondria, and fluoresces upon ROS oxidation.

The cells were visualized using an Olympus CKX53 inverted microscope (Olympus, Japan), then detached from the wells and lysed using 0.2% Triton X-100 (Sigma-Aldrich; https://www.thermofisher.com/order/catalog/product/M7513). The level of free radicals in the cell lysate was evaluated based on the fluorescence intensity (λ_{ex} = 579 nm, λ_{em} = 599 nm) using an RF-6000 spectrofluorometer (Shimadzu, Japan) and converted to the cell number using a Countess 3 Automated Cell Counter (USA).

In the remaining experiments, the cells were cultured in six-well plates.

Preparation of complete cell lysates

After the end of exposure to H_2O_2 and BSO, the cells were detached from the six-well plates using a trypsin–EDTA solution (0.25% trypsin and 0.2% EDTA, Sigma-Aldrich), washed three times with a phosphate buffer solution (BioRad, USA), and lysed in NP40 cell lysis buffer (ThermoFisher Scientific, USA) supplemented with a mixture of proteinase inhibitors (2 mM 4-(2 aminoethyl)benzenesulfonyl fluoride hydrochloride (AEBSF), 0.3 μM aprotinin, 130 μM bestatin, 1 mM EDTA, 14 μM *trans*-epoxysuccinyl-*L*-leucylamido(4-guanidino)butane (E-64), and 1 μM leupeptin, Sigma-Aldrich), 10^7 cells per 100 μL of the buffer, at +4°C and constant stirring for 30 min. The resulting lysate was centrifuged at 5,000 g (CM-50, Eppendorf, Germany). The supernatant was used in the biochemical analyses.

The protein content in the samples was evaluated by the Bradford method using a Pierce Coomassie plus (Bradford) assay kit (ThermoFisher, USA) [27].

Evaluation of the relative P-gp content in Caco-2 cells by Western blot

Supernatant proteins (20 μg) were subjected to electrophoresis using a 7.5% TGX Stain-Free FastCast acrylamide kit (BioRad, USA) in a Laemmli buffer system (BioRad). Samples were mixed with a Laemmli buffer containing 50 mM β-mercaptoethanol (Helicon, USA) at a 1:3 ratio and incubated at 70°C for 10 min. Electrophoresis was performed at 100 V for 90 min.

Proteins were transferred to a nitrocellulose membrane (Trans-Blot Turbo Mini-Size nitrocellulose, BioRad) using a Mini Trans-Blot Cell (BioRad) at 25 V and 1.3 A for 10 min.

The proteins on the membrane were blocked with a 1% casein blocker solution (BioRad) containing 0.1% Tween-20 (Sigma, Germany) at room temperature for 1 h.

The P-gp protein was detected using primary mouse monoclonal antibodies (P-glycoprotein antibody, MA5-13854, Invitrogen) at a dilution of 1:200 in a casein blocker solution (BioRad) at 37°C for 2 h. Primary antibodies were visualized by incubation with rabbit anti-mouse IgG (H + L) secondary antibodies, HRP (Invitrogen) (1:4,000 dilution) at room temperature for 1 h. Chemiluminescence was detected using a ChemiDoc XRS+ system (BioRad). Band intensities were evaluated densitometrically using the ImageLab software (BioRad).

The molecular weight of P-gp was confirmed by comparison with precision plus protein standards, dual color (BioRad).

The P-gp content was normalized to the housekeeping protein GAPDH content (primary antibodies GAPDH Loading Control Monoclonal Antibody (GA1R), DyLight 68 (Invitrogen), 1:1,000 dilution, secondary rabbit antibodies – Rabbit-anti-Mouse IgG (H + L) Secondary Antibody, HRP (Invitrogen, 1:4,000 dilution).

Statistical analysis

Data were analyzed using the GraphPad Prism 8 software. The results are presented as a mean ± standard deviation (M ± SD). The statistical sig-

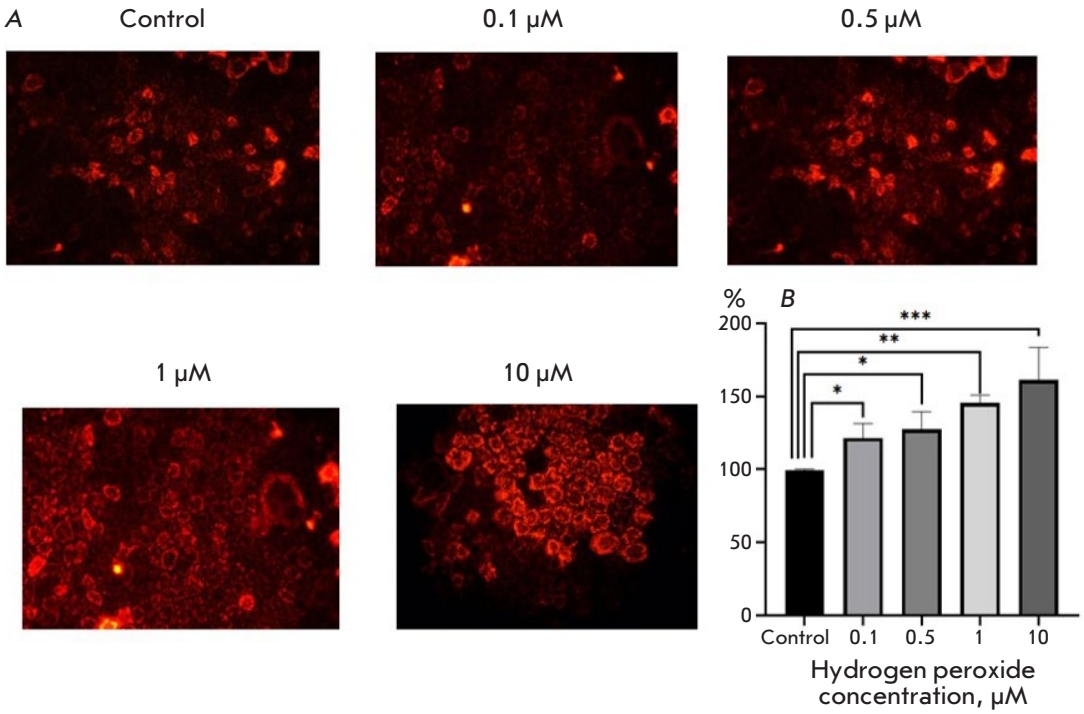

Fig. 1. Hydrogen peroxide (H_2O_2)-induced changes in the ROS level in Caco-2 cells. (*A*) Staining with MitoTracker Red CM-H_2XRos; magnification: 400×. (*B*) Fluorescence intensity in a cell lysate. $^{*}p \leqslant 0.05$; $^{**}p < 0.01$; $^{***}p \leqslant 0.001$ compared with control (Dunnett's test)

nificance of the differences was assessed using an analysis of the variance (ANOVA); pairwise comparisons were performed using a Dunnett's test. Differences were considered statistically significant at $p < 0.05$.

RESULTS

ROS production upon simulated oxidative stress

Exposure of Caco-2 cells to H_2O_2 at a concentration of 0.1, 0.5, 1.0, and 10 μM for 3 h resulted in an increase in the fluorescence intensity of the cells stained with MitoTracker Red CM-H_2XRos by 21.5% ($p = 0.05$), 27.3% ($p = 0.046$), 45.4% ($p = 0.004$), and 61.1% ($p = 0.001$), respectively, compared with that in the control taken as 100% (*Fig. 1*).

Similarly, the fluorescence intensity of Caco-2 cells exposed to BSO at a concentration of 10, 50, and 100 μM for 24 h and stained with MitoTracker Red CM-H_2XRos increased by 38.8% ($p = 0.001$), 46.5% ($p = 0.0004$), and 70.2% ($p = 0.0001$), respectively, compared with that in the control (*Fig. 2*).

These results indicate an increase in ROS production in the used experimental models.

Changes in the relative P-gp content in Caco-2 cells under exogenous and endogenous oxidative stress

Exposure to H_2O_2 (simulation of exogenous OS) at a concentration of 0.1, 0.5, and 1 μM for 24 h caused an increase in the P-gp content by 78.9% ($p = 0.0013$), 67.1% ($p = 0.0019$), and 44.6% ($p = 0.029$), respectively (*Fig. 3A*), compared with that in the control. An increase in the duration of the exposure to 72 h at an H_2O_2 concentration of 10 μM elevated the P-gp level by 68.9% ($p = 0.0033$), compared with that in the control (*Fig. 3A*).

Incubation of Caco-2 cells with BSO (simulation of endogenous stress) at a concentration of 10, 50, and 100 μM for 24 h resulted in an increase in the relative P-gp content by 71.6% ($p < 0.0001$), 51.6% ($p < 0.0001$), and 25.4% ($p = 0.007$), respectively (*Fig. 3B*).

Upon increasing exposure to 72 h, the effect of BSO was eliminated and the P-gp level did not differ significantly from that in the control.

The addition of GSH at a concentration of 1 mM to the growth medium containing H_2O_2 at all concentrations and for all incubation periods prevented any increase in the P-gp content; its level did not differ significantly from that in the control (*Fig. 4A*).

Upon combined use of 1 mM glutathione and 100 μM BSO and incubation for 24 h, the relative P-gp content increased by 19.7% ($p = 0.003$) compared with that in the control; however, this increase was less pronounced than that when the pro-oxidant was used alone. In this case, GSH prevented any increase in the P-gp level caused by exposure to BSO at the lower concentrations of 10 and 50 μM for 24 h (*Fig. 4B*).

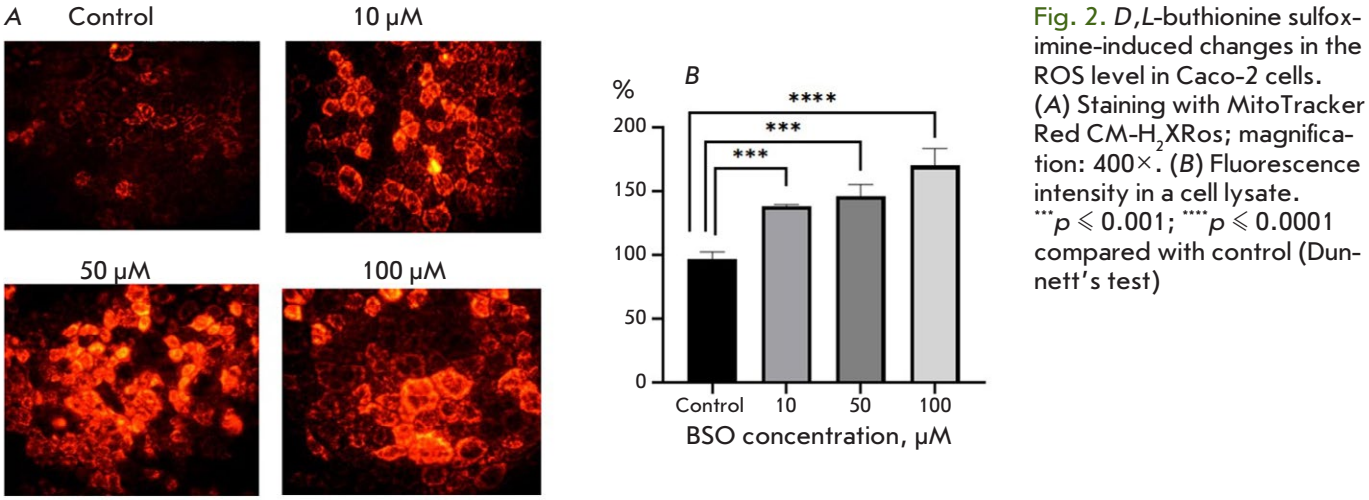

Fig. 2. *D,L*-buthionine sulfoximine-induced changes in the ROS level in Caco-2 cells. (*A*) Staining with MitoTracker Red CM-H_2XRos; magnification: 400×. (*B*) Fluorescence intensity in a cell lysate. $^{***}p \leqslant 0.001$; $^{****}p \leqslant 0.0001$ compared with control (Dunnett's test)

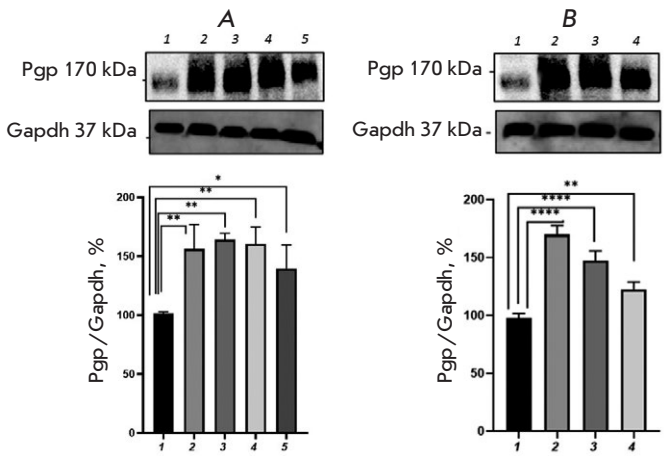

Fig. 3. Relative P-glycoprotein content in Caco-2 cells exposed to H_2O_2 (*A*, exogenous oxidative stress) and *DL*-buthionine sulfoximine (*B*, endogenous oxidative stress). (*A*) 1 – control; 2, 3, 4, 5 – hydrogen peroxide at a concentration of 10 μM (72 h), 0.1, 0.5, and 1 μM (24 h), respectively. (*B*) 1 – control; 2, 3, 4 – *DL*-buthionine sulfoximine at concentrations of 10, 50, and 100 μM (24 h), respectively. $^{*}p < 0.05$; $^{**}p < 0.01$; $^{****}p < 0.0001$, statistically significant differences from the control (Dunnett's test)

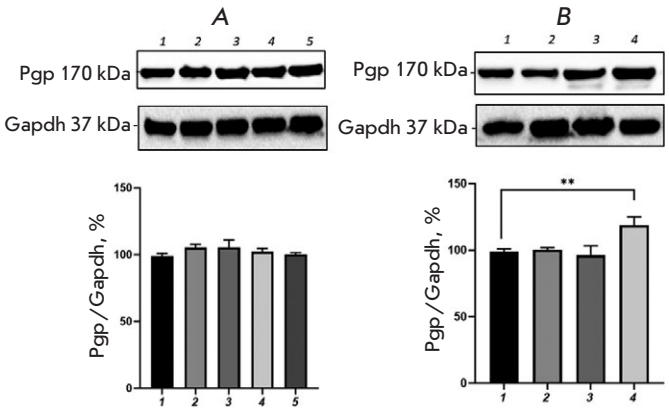

Fig. 4. Relative P-glycoprotein content in Caco-2 cells exposed to H_2O_2 (*A*, exogenous oxidative stress) and *DL*-buthionine sulfoximine (*B*, endogenous oxidative stress) in combination with glutathione (1 mM). (*A*) 1 – control; 2, 3, 4, 5 – hydrogen peroxide at a concentration of 10 μM (72 h), 0.1, 0.5, and 1 μM (24 h), respectively. (*B*) 1 – control; 2, 3, 4 – *DL*-buthionine sulfoximine at concentrations of 10, 50, and 100 μM (24 h), respectively. $^{**}p < 0.01$, statistically significant differences from the control (Dunnett's test)

Therefore, exposure of Caco-2 cells to H_2O_2 and BSO (simulation of exogenous and endogenous OS) leads to an increase in the P-gp level, and the use of the endogenous antioxidant glutathione eliminates this induction, except for the exposure to BSO (100 μM) for 24 h.

Investigation of the mechanisms increasing the P-gp level in the presence of hydrogen peroxide and *DL*-buthionine sulfoximine

The mechanisms associated with an increased P-gp level under exogenous and endogenous OS were studied using the transcription factor inhibitors AEM1

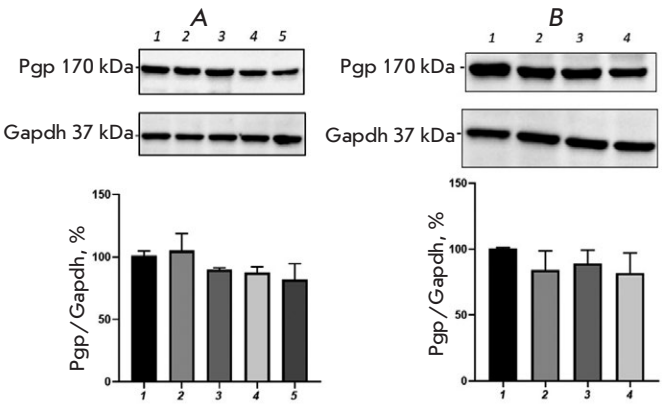

Fig. 5. Relative P-glycoprotein content in Caco-2 cells exposed simultaneously to an Nrf2 inhibitor (AEM1, 5 μM) and H_2O_2 (*A*) or *DL*-buthionine sulfoximine (*B*). (*A*) 1 – control; 2, 3, 4, 5 – hydrogen peroxide at a concentration of 10 μM (72 h), 0.1, 0.5, and 1 μM (24 h), respectively. (*B*) 1 – control; 2, 3, 4 – *DL*-buthionine sulfoximine at concentrations of 10, 50, and 100 μM (24 h), respectively

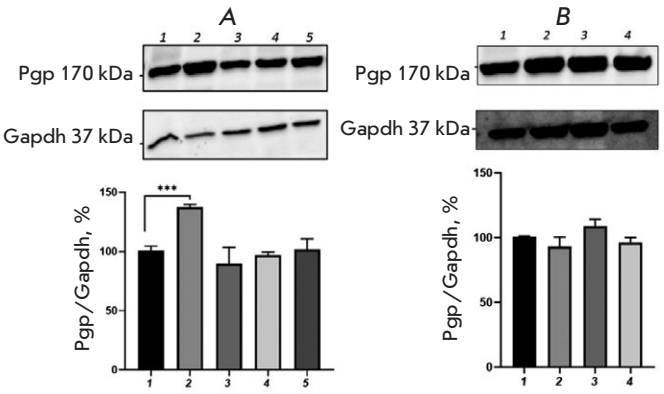

Fig. 6. Relative P-glycoprotein content in Caco-2 cells exposed simultaneously to an HIF1α inhibitor (KC7F2, 7.5 μM) and H_2O_2 (*A*) or *DL*-buthionine sulfoximine (*B*). (*A*) 1 – control; 2, 3, 4, 5 – hydrogen peroxide at a concentration of 10 μM (72 h), 0.1, 0.5, and 1 μM (24 h), respectively. (*B*) 1 – control; 2, 3, 4 – *DL*-buthionine sulfoximine at concentrations of 10, 50, and 100 μM (24 h), respectively. $^{***}p < 0.001$, statistically significant differences from control (Dunnett's test)

(Nrf2), KC7F2 (HIF1α), CINPA1 (CAR), and ketoconazole (PXR), which stimulate the expression of the *MDR1* gene encoding P-gp.

Co-incubation of the Nrf2 inhibitor AEM1 (5 μM) with H_2O_2 (all concentrations and exposure times) prevented any increase in the relative P-gp content; its level did not differ significantly from that in the control (*Fig. 5A*).

The addition of AEM1, in combination with BSO (10, 50, and 100 μM), and incubation for 24 h also prevented any increase in the relative P-gp content; the transporter protein level did not differ from that in the control) (*Fig. 5B*).

The HIF1α inhibitor KC7F2 (7.5 μM) prevented any increase in the transporter level in the presence of H_2O_2 (24 h, all concentrations); the relative P-gp content did not differ significantly from that in the control. Incubation with KC7F2 for 72 h did not significantly affect the relative P-gp content; its content increased by 37% relative to that in the control ($p = 0.0004$) (*Fig. 6A*).

The addition of KC7F2 to cells incubated with BSO (10, 50, and 100 μM) also led to a normalization of the relative P-gp content; its level did not differ significantly from that in the control (*Fig. 6B*).

The addition of the CAR inhibitor CINPA1 (5 μM) to the cells incubated with 0.1, 0.5, and 1 μM H_2O_2 for 24 h did not suppress the pro-oxidant effect; the relative P-gp content increased by 51.5% ($p = 0.0008$), 46.5% ($p = 0.0019$), and 31.3% ($p = 0.02$), respectively, compared with that in the control (*Fig. 7A*).

However, prolonged incubation (72 h) with CINPA1 prevented any increase in the P-gp content under the action of 10 μM H_2O_2 (*Fig. 6A*).

CINPA1 combined with BSO (10, 50, and 100 μM) prevented any increase in the relative P-gp content; the transporter protein level did not differ significantly from that in control (*Fig. 7B*).

The PXR inhibitor ketoconazole (10 μM) with H_2O_2 did not suppress the effect of the oxidative stress inducer. The relative P-gp content increased by 64.6, 53.5, and 36.4% upon exposure to H_2O_2 (0.1, 0.5, and 1 μM, 24 h) and by 62.6% upon exposure to H_2O_2 (10 μM, 72 h), $p < 0.0001$ in each series of experiments, *Fig. 8A*.

At the same time, ketoconazole prevented any increase in the P-gp content under the action of BSO at a concentration of 100 μM and did not affect the effect of the pro-oxidant at a concentration of 10 and 50 μM; the P-gp level increased by 18.8% ($p = 0.0027$) and 14.1% ($p = 0.015$), respectively, compared with that in the control (*Fig. 8B*).

Therefore, P-gp is regulated mainly through the Nrf2-Keap1 signaling pathway under exogenous OS (H_2O_2), while all of the studied transcription factors are involved in the regulation of P-gp under endogenous OS (BSO).

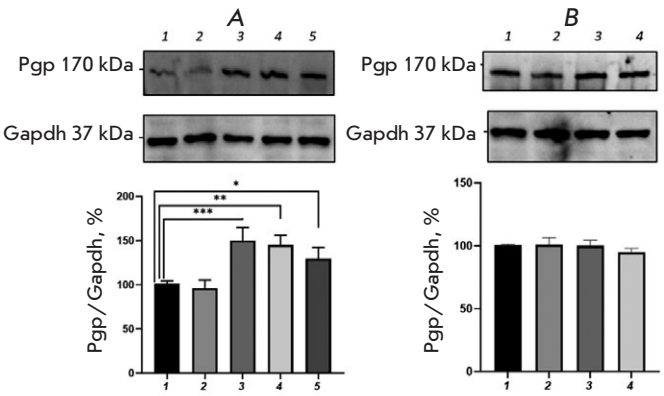

Fig. 7. Relative P-glycoprotein content in Caco-2 cells exposed simultaneously to a CAR inhibitor (CINPA1, 5 μM) and H_2O_2 (*A*) or *DL*-buthionine sulfoximine (*B*). (*A*) 1 – control; 2, 3, 4, 5 – hydrogen peroxide at a concentration of 10 μM (72 h), 0.1, 0.5, and 1 μM (24 h), respectively. (*B*) 1 – control; 2, 3, 4 – *DL*-buthionine sulfoximine at concentrations of 10, 50, and 100 μM (24 h), respectively. $^{*}p < 0.05$; $^{**}p < 0.01$; $^{***}p < 0.001$, statistically significant differences from the control (Dunnett's test)

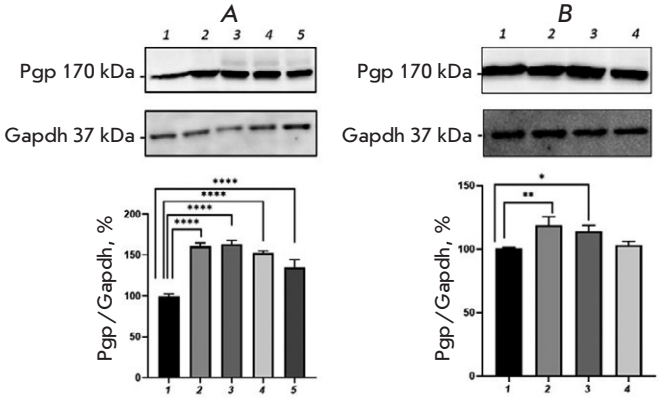

Fig. 8. Relative P-glycoprotein content in Caco-2 cells exposed simultaneously to a PXR inhibitor (ketoconazole, 10 μM) and H_2O_2 (*A*) or *DL*-buthionine sulfoximine (*B*). (*A*) 1 – control; 2, 3, 4, 5 – hydrogen peroxide at a concentration of 10 μM (72 h), 0.1, 0.5, and 1 μM (24 h), respectively. (*B*) 1 – control; 2, 3, 4 – *DL*-buthionine sulfoximine at concentrations of 10, 50, and 100 μM (24 h), respectively. $^{*}p < 0.05$; $^{**}p < 0.01$; $^{****}p < 0.0001$, statistically significant differences from the control (Dunnett's test)

DISCUSSION

Oxidative stress is a redox-dependent process associated with many pathologies of various origins. The cause of OS can be exogenous (exposure to a pro-oxidant) and/or endogenous (suppression of the intracellular antioxidant defense) [28].

In the present study, exogenous OS was modeled by exposure of Caco-2 cells to hydrogen peroxide. H_2O_2 is able to penetrate through cell membranes. In cells, H_2O_2 interacts with metals of variable valency (Fe^{2+} or Cu^{+}) in the Fenton and Haber–Weiss reactions to form highly toxic, oxygen-containing free radicals (hydroxyl radical $^{\cdot}OH$ and superoxide anion $O_2^{\cdot -}$), which can cause oxidative damage to cell biomacromolecules [29]. Given the micromolar range of the H_2O_2 concentrations used in the study and the rapid elimination of H_2O_2 by the cells [30], the revealed changes in the P-gp content are most likely due to the signal cascades triggered by the pro-oxidant.

Endogenous OS was induced by incubation of the cells with BSO that inhibits the γ-glutamylcysteine synthetase (γ-GCS) enzyme that plays a key role in the synthesis and maintenance of the cellular glutathione level. Glutathione (GSH) is a thiol-containing tripeptide that exhibits antioxidant activity and is necessary for the functioning of antioxidant enzymes (glutathione peroxidase, glutathione S-transferase). A decrease in the level of endogenous glutathione reduces the endogenous antioxidant system capacity, which provokes OS development [31].

The dynamics of OS development was confirmed in this study by ROS detection based on the fluorescence intensity of MitoTracker Red CM-H_2XRos. Exposure to H_2O_2 caused an increase in ROS in 3 h, while exposure to BSO increased the concentration of ROS in 24 h, after the endogenous glutathione pool had been depleted.

The development of both exogenous and endogenous OS led to an increase in the relative P-gp content. However, addition of the antioxidant glutathione and used pro-oxidants to the cells prevented P-gp induction by H_2O_2 and reduced (100 μM) or suppressed (10 and 50 μM) P-gp induction by BSO.

Partial suppression of P-gp induction by glutathione may be associated with the fact that BSO, being a xenobiotic, can increase the P-gp content via stimulation of the *MDR1* gene expression.

Currently, several mechanisms of P-gp regulation are known, the main one being alteration of the expression of the *MDR1* gene that encodes the transporter protein [31].

In this study, we evaluated the role of the Nrf2, HIF1a, CAR, and PXR transcription factors, which are activated under oxidative stress [17, 33–35] and may hypothetically elevate P-gp expression.

The Nrf2 signaling pathway is considered to be the main mechanism that regulates the antioxidant defense of cells in OS. Under physiological conditions, the nuclear transcription factor Nrf2 is involved in the Keap1-Nrf2-Cullin-3 complex, which ensures that it remains in the cytosol and blocks its specific activity. Nrf2 is a redox-sensitive transcription factor; oxidation of the SH-groups in Keap1 leads to the activation of the factor, its translocation to the nucleus, and alteration of biological effects – induction of antioxidant enzymes [36].

The hypoxia-inducible factor (HIF1) is a transcription factor that plays a key role in a cell's adaptation to decreasing oxygen levels in tissues [37]. HIF1 is a heterodimer composed of two protein subunits, HIF1α and HIF1β. The functional status of HIF1 is controlled by the expression and activity of its α-subunit that is regulated on several levels: transcription, translation, post-translational changes, and translocation to the nucleus [38]. Under normoxic conditions, oxygen-dependent proline hydroxylases modify proline in HIF1α. Under OS, proline hydroxylases are inactive; in these conditions, the α- and β-subunits are able to bind to each other, penetrate into the nucleus, and activate the expression of the target genes.

The constitutive androstane receptor (CAR; nuclear receptor subfamily 1 group I member 3, NR1I3) and pregnane X receptor (PXR; steroid and xenobiotic receptor SXR; nuclear receptor subfamily 1 group I member 2, NR112) are members of the nuclear receptor superfamily that is comprised mainly of transcription factors [39].

These receptors are localized mainly in the liver and intestines, where they regulate the expression of phase I biotransformation enzymes, such as cytochrome P450 isoenzymes CYP3A and CYP2B, and transporter proteins: in particular P-gp.

The relative contents of CAR and PXR increase under OS conditions in response to the accumulation of peroxidation products [34, 35].

The role of Nrf2 in P-gp regulation was assessed using AEM1 (ARE expression modulator 1) that blocks the interaction between Nfr2 and ARE (antioxidant respons(iv)e element HIF t) and suppresses the expression of the genes controlled by this transcription factor. AEM1 was found to block the ability of H_2O_2 and BSO (at all applied concentrations and exposure times) to induce P-gp.

Therefore, Nrf2 is involved in P-gp regulation under both exogenous and endogenous OS.

The HIF1α inhibitor KC7F2 (controls the biological activity of HIF1α) is a symmetrical compound that selectively inhibits the cellular synthesis of HIF1α, but not HIF1β, without affecting HIF1α mRNA transcription or HIF1α protein stability. In cells exposed to H_2O_2 and BSO for 24 h, KC7F2 normalized the P-gp level (prevented pro-oxidant-mediated induction); during exposure, in combination with H_2O_2 for 72 h, KC7F2 had no significant effect (the relative P-gp content increased under exposure to hydrogen peroxide).

Thus, there are two transcription factors, Nrf2 and HIF1, which are involved in P-gp regulation under both endogenous and exogenous OS. Both factors may be capable of binding to the promoter of the *MDR1* gene, which encodes P-gp, and increasing its expression. We have previously shown that Nrf2 causes an increase in HIF1α expression during OS [33]; i.e., Nrf2 can act through HIF1α. Because Nrf2 inhibition, in contrast to HIF1α, prevented P-gp induction in all during incubation for 24 and 72 h under exogenous and endogenous OS, the two described mechanisms apparently function in tandem in the cell.

In the present study, we used CINPA1 (CAR inhibitor, not PXR activator 1) as a CAR inhibitor; CINPA1 interacts with and blocks the CAR ligand-binding domain and inhibits its binding to co-activators [40]. For PXR inhibition, we used an antifungal agent from the azole group, ketoconazole, which binds to the AF-2 (activation function) region of the N-terminal ligand-binding domain of PXR and, thus, suppresses its activation [41].

CINPA1 did not suppress P-gp induction by H_2O_2 upon 24-hour incubation, and it prevented any increase in the P-gp level upon 72-hour exposure. H_2O_2 was shown to induce CAR [34] that, in turn, apparently increases P-gp expression upon 72-hour exposure.

The combined use of BSO and CINPA1 prevented an increase in the relative P-gp content; the transporter protein level did not differ significantly from that in the control.

The PXR inhibitor ketoconazole, applied together with H_2O_2, did not suppress the effect of the OS inducer. However, ketoconazole completely prevented an increase in the P-gp level under the action of BSO at a concentration of 100 μM and, partially, at concentrations of 10 and 50 μM. CAR and PXR are the main intracellular xenosensory receptors; i.e., they interact with xenobiotics and trigger an intracellular response to neutralize and eliminate the xenobiotics.

BSO, being a xenobiotic, may be suggested to independently activate CAR and PXR, and they, in turn, increase P-gp expression. The persistence of an ele-

vated P-gp level during the combined use of BSO and glutathione, which was revealed in the present study, supports this suggestion.

It is interesting to note that upon simulation of both exogenous and endogenous oxidative stress, despite the simultaneous involvement of different transcription factors in P-gp induction, inhibition of only one of them led to the suppression of any increase in the P-gp content, which indicates that several mechanisms should act simultaneously to induce P-gp in certain situations.

CONCLUSION

In conclusion, an increase in the P-gp content under exogenous OS induced by the incubation of Caco-2 cells with H_2O_2 is primarily mediated by the Nrf2-Keap1 signaling pathway that is involved in the regulation of the transporter protein at exposure durations of 24 and 72 h. The transcription factors HIF and CAR are involved in the P-gp regulation upon 24-hour and 72-hour exposure to H_2O_2, respectively. Apparently, PXR does not significantly affect the regulation of the transporter protein in this OS model.

Simulation of endogenous OS in Caco-2 cells using the glutathione synthesis inhibitor BSO revealed that all tested transcription factors and signaling pathways are involved in the P-gp induction. Most likely, this is due to the bimodal effect of BSO on P-gp. On the one hand, BSO induces OS; on the other, being a xenobiotic, BSO is able to stimulate PXR and CAR. ●

REFERENCES

1. Yakusheva E.N., Titov D.S. // Biochemistry (Moscow). 2018. V. 83. № 8. P. 907–929.
2. Han L.W., Gao C., Mao Q. // Expert Opinion on Drug Metabolism & Toxicology. 2018. V. 14. № 8. P. 817–829.
3. Chai A.B., Leung G.K.F., Callaghan R., Gelissen I.C. // FEBS J. 2020. V. 287. № 4. P. 612–625.
4. Wang G.X., Wang D.W., Liu Y., Ma Y.H. // Int. J. Neurosci. 2016. V. 126. № 5. P. 385–392.
5. Xu H.W., Xu L., Hao J.H., Qin C.Y., Liu H. // J. Int. Med. Res. 2010. V. 38. № 1. P. 34–42.
6. Gao Y., Liao Y., Shen J.K., Feng Y., Choy E., Cote G., Harmon D., Mankin H.J., Hornicek F.J., Duan Z. // J. Orthop. Res. 2016. V. 34. № 9. P. 1606–1612.
7. Sies H, Jones D.P. Oxidative stress. In Encyclopedia of stress. Amsterdam: Elsevier, 2007. P. 45–48.
8. Cabello-Verrugio C., Simon F., Trollet C., Santibañez J.F. // Oxid. Med. Cell. Longev. 2017. 4310469.
9. Ziemann C., Bürkle A., Kahl G.F., Hirsch-Ernst K.I. // Carcinogenesis. 1999. V. 20. № 3. P. 407–414.
10. Felix R.A., Barrand M.A. // J. Neurochem. 2002. V. 80. № 1. P. 64–72.
11. Hoshi Y., Uchida Y., Tachikawa M., Ohtsuki S., Couraud P., Suzuki T., Terasaki T. // J. Cerebral Blood Flow Metabolism. 2019. V. 40. № 2. P. 420–436.
12. Robertson S.J., Kania K.D., Hladky S.B., Barrand M.A. // J. Neurochem. 2009. V. 111. № 1. P. 132–141.
13. Hirsch-Ernst K.I., Ziemann C., Foth H., Kozian D., Schmitz-Salue C., Kahl G.F. // J. Cell Physiol. 1998. V. 176. № 3. P. 506–515.
14. Miyata Y., Asano Y., Muto S. // Am. J. Physiol. Renal Physiol. 2002. V. 282. № 4. P. 718–729.
15. Terada Yu., Ogura J., Tsujimoto T., Kuwayama K., Koizumi T., Sasaki Sh., Maruyama H., Kobayashi M., Yamaguchi H., Iseki K. // J. Pharm. Pharm. Sci. 2014. V. 17. № 2. P. 266–276.
16. Zhang Yu., Li Ju., Yang W., Xian Zh., Feng Q., Ruan X. // Int. J. Ophthalmol. 2017. V. 10. № 7. P. 1055–1063.
17. Shchulkin A.V., Abalenikhina Y.V., Erokhina P.D., Chernykh I.V., Yakusheva E.N. // Biochemistry (Moscow). 2021. V. 86. № 2. P. 197–206.
18. Seebacher N.A., Richardson D.R., Jansson P.J. // Br. J. Pharmacol. 2015. V. 172. № 10. P. 2557–2572.
19. Hilgers A.R., Conradi R.A., Burton P.S. // Pharmac. Res. 1990. V. 7. № 9. P. 902–910.
20. Haddad J.J. // Eur. Cytokine Netw. 2001. V. 12. № 4. P. 614–624.
21. Abalenikhina Yu.V., Erokhina P.D., Mylnikov P.Yu., Shchulkin A.V., Yakusheva E.N. // Appl. Biochem. Microbiol. 2022. V. 58. № 3. P. 232–242.
22. Rao R.K., Li L., Baker R.D., Baker S.S., Gupta A. // Am. J. Physiol. Gastrointest. Liver Physiol. 2000. V. 279. № 2. P. 332–340.
23. Bollong M.J., Yun H., Sherwood L., Woods A.K., Lairson L.L., Schultz P.G. // ACS Chem. Biol. 2015. V. 10. P. 2193–2198.
24. Ke Q., Costa M. // Mol. Pharmacol. 2006. V. 70. № 5. P. 1469–1480.
25. Cherian M.T., Lin W., Wu J., Chen T. // Mol. Pharmacol. 2015. V. 87. № 5. P. 878–889.
26. Kota B.P., Tran V.H., Allen J., Bebawy M., Roufogalis B.D. // Pharmacol. Res. 2010. V. 62. № 5. P. 426–431.
27. Bradford M.M. // Anal. Biochem. 1976. V. 7. № 72. P. 248–254.
28. Liguori I., Russo G., Curcio F., Bulli G., Aran L., Della-Morte D., Gargiulo G., Testa G., Cacciatore F., et al. // Clin. Interv. Aging. 2018. V. 26. № 13. P. 757–772.
29. Sies H. // Redox Biol. 2017. V. 11. P. 613–619.
30. Wagner B.A., Witmer J.R., van't Erve T.J., Buettner G.R. // Redox Biol. 2013. V. 1. № 1. P. 210–217.
31. Adeoye O., Olawumi J., Opeyemi A., Christiania O. // JBRA Assist. Reprod. 2018. V. 1. № 22. P. 61–66.
32. Li S., Yang Y., Ding X., Yang M., She S., Peng H., Xu X., Ran X., Li S., Hu P., et al. // Oncotarget. 2017. V. 17. № 8 (3). P. 4549–4562.
33. Abalenikhina Yu.V., Mylnikov P.Yu., Shchulkin A.V., Chernykh I.V., Yakusheva E.N. // Bull. Exp. Biol. Med. 2022. V. 173. № 3. P. 301–306.
34. Shchul'kin A.V., Abalenikhina Y.V., Seidkulieva A.A., Ryabkov A.N., Yakusheva E.N. // Bull. Exp. Biol. Med. 2021. V. 171. № 5. P. 615–618.
35. Abalenikhina Y.V., Sudakova E.A., Slepnev A.A., Seidkulieva A.A., Erokhina P.D., Shchulkin A.V., Yakusheva E.N. // Biochemistry (Moscow), Suppl. Ser. A: Membrane

Cell Biol. 2022. V. 16. № 1. P. 21–28.
36. Bellezza I., Giambanco I., Minelli A., Donato R. // Biochim. Biophys. Acta Mol. Cell. Res. 2018. V. 1865. № 5. P. 721–733.
37. Schofield C.J., Ratcliffe P.J. // Biochem. Biophys. Res. Commun. 2005. V. 338. № 1. P. 617–626.
38. Ke Q., Costa M. // Mol. Pharmacol. 2006. V. 70. № 5. P. 1469–1480.
39. di Masi A., De Marinis E., Ascenzi P., Marino M. //Mol. Aspects Med. 2009. V. 30. № 5. P. 297–343.
40. Cherian M.T., Lin W., Wu J., Chen T. // Mol. Pharmacol. 2015. V. 87. № 5. P. 878–889.
41. Wang H., Huang H., Li H., Teotico D.G., Sinz M., Baker S.D., Staudinger J., Kalpana G., Redinbo M.R., Mani S. // Clin. Cancer Res. 2007. V. 13. № 8. P. 2488–2495.

MicroRNA Expression Profile Changes in the Leukocytes of Parkinson's Disease Patients

N. S. Ardashirova*, N. Yu. Abramycheva, E. Yu. Fedotova, S. N. Illarioshkin
Research Center of Neurology, Moscow, 125367 Russia
*E-mail: ardashirova.n@yandex.ru
Received May 16, 2022; in final form, July 04, 2022
DOI: 10.32607/actanaturae.11729

ABSTRACT **Parkinson's disease (PD) is one of the most common movement disorders. It is primarily diagnosed clinically. A correct diagnosis of PD in its early stages is important for the development of a pathogenic treatment, which necessitates a search for potential biomarkers of the disease. We evaluated the diagnostic value of several microRNAs and their relationship with the clinical characteristics of PD. The study included 70 PD patients and 40 healthy volunteers. We analyzed the expression of 15 microRNAs in blood leukocytes, which were selected based on literature data and modern concepts of molecular PD pathogenesis. All patients were evaluated using the Hoehn and Yahr scale, UPDRS, NMSQ, and PDQ-39. The data analysis revealed a statistically significant increase in the expression of miR-7-5p, miR-29c-3p, and miR-185-5p and a statistically significant decrease in the expression of miR-29a-3p and miR-30c-1-5p in leukocytes in PD. However, the altered microRNA profile was shown to have a moderate diagnostic value for PD diagnosis. MicroRNA expression changes were associated with the motor and non-motor phenotypic features of PD and administration of anti-Parkinson's drugs. Also, a relationship between some of the microRNAs studied and the duration and severity of PD was found, which may potentially be used to monitor disease progression.**
KEYWORDS **Parkinson's disease, microRNA, biomarkers.**
ABBREVIATIONS **PD – Parkinson's disease; REM-sleep – rapid eye movement sleep; RNA – ribonucleic acid; UPDRS – unified Parkinson's disease rating scale; NMSQ – non-motor symptoms questionnaire; HADS – hospital anxiety and depression scale; MoCA – Montreal cognitive assessment; PDQ-39 – Parkinson's disease questionnaire.**

INTRODUCTION

Parkinson's disease (PD) is one of the most common movement disorders and a serious medical and social problem. According to modern concepts, PD belongs to the synucleinopathies, a group of disorders characterized by the formation of pathological alpha-synuclein aggregates in the central and peripheral nervous system [1], also including dementia with Lewy bodies, multiple system atrophy, and isolated autonomic failure. An important predictor of synucleinopathies is a REM sleep behavior disorder [1].

Currently, PD is primarily diagnosed clinically. In this case, even movement disorder experts are able to make a correct clinical diagnosis of PD using pathologic findings in just approximately 80% of the cases [2]. Contemporary methods of radionuclide neuroimaging (positron emission and single photon emission-computed tomography) can be used to accurately assess dopaminergic pathways and, thereby, significantly improve the accuracy of the PD diagnosis [3]. However, these are expensive procedures that are associated with radiation exposure and they cannot be used to differentiate PD from atypical parkinsonian syndromes [4]. The insufficient accuracy that characterizes a life-time diagnosis, especially in the early stages of PD, is considered one of the important causes behind the failure of the drug trials utilized in the pathogenic treatment of PD [5]. Therefore, the development of informative and accessible diagnostic biomarkers of PD is critical.

The molecular pathogenesis of PD is complex. One of its components is presumably an impaired epigenetic regulation of gene expression, which involves microRNAs [6]. To date, more than 5,000 different microRNAs have been identified in the human genome (http://www.mirbase.org). The studied mechanism of microRNA action involves the implementation of RNA silencing. In the RNA-induced silencing complex

(RISC), microRNA binds to the 3'-end of a complementary mRNA, leading to mRNA degradation and the prevention of protein translation [7]. There are other mechanisms of expression regulation which involve microRNAs [8]. Importantly, a single microRNA can bind to more than 200 different mRNAs, thus inducing shifts in the regulation of protein cascades [9]. These changes may be the basis for various pathological processes, including those leading to neurodegeneration.

In PD, shifts in blood microRNA levels may reflect, for the most part, the involvement of numerous organs and systems in the pathological process. It is the multiple organs pathology that is believed to cause the development of the non-motor (gastrointestinal, cardiac, etc.) manifestations that are so characteristic of PD. Therefore, better understanding of the features of blood microRNA levels could help us develop a new informative PD biomarker for an early and differential diagnosis of the disease, prediction of its course, a more accurate assessment of the motor and non-motor manifestation ratio, etc.

The possibility of using certain microRNAs in the diagnosis of PD has already been considered [10–12]. Some studies have tested panels of several microRNAs as a PD biomarker [13–16]. However, it should be taken into account that the microRNA profile is quite dynamic and is affected by various factors. For example, the microRNA profile has been shown to be influenced by ongoing anti-Parkinson's therapy [17–20] and deep brain stimulation [21]. Based on the analysis of published data, we selected 15 microRNAs whose expression in the blood and brain of PD patients differed significantly from that of the controls in at least two studies.

In this study, we evaluated the significance of the selected microRNAs for a PD diagnosis and their correlation with the clinical characteristics of this disease.

EXPERIMENTAL

The study included 70 PD patients and 40 healthy volunteers. The PD group comprised 35 males and 35 females (mean age, 60.5 ± 11.8 years). Study and control group patients were comparable in gender and age. The study was approved by the local ethical committee of the Research Center of Neurology. All participants signed an informed consent.

The diagnosis of PD was made according to the International Parkinson and Movement Disorder Society (MDS) criteria [22]. The age of onset was 53 ± 13 years, with a disease duration of 6.4 ± 7.0 years. The mixed form of PD was diagnosed in 52 (74.3%) patients, and the akinetic-rigid form of PD was present in 18 (25.7%) patients. The mean score of clinical symptom severity on the Unified Parkinson's Disease Rating Scale (UPDRS) was 65.6 ± 27.1, and the mean Hoehn and Yahr stage of PD was 2.4 ± 0.9.

All patients completed the Non-Motor Symptoms Questionnaire (NMSQ), with the mean score of 9.0 ± 5.2. The patients underwent testing using the Hospital Anxiety and Depression Scale (HADS) (mean scores of 6.4 ± 4.0 and 7.0 ± 4.6 for anxiety and depression, respectively) and the Montreal Cognitive Assessment scale (MoCA) (mean score of 23.1 ± 4.2). The patients assessed their quality of life using the Parkinson's Disease Questionnaire (PDQ-39) (mean score of 44 ± 30).

Most of the PD patients received anti-Parkinson's drugs, including levodopa (41 patients, 58.6%), dopamine receptor agonists (30 patients, 42.6%), and amantadine drugs (20 patients, 28.6%). Twenty-three patients (32.9%) did not receive any therapy at the time of enrollment.

We studied the following 15 microRNAs: miR-7-1-5p, miR-24-1-3p, miR-29a-3p, miR-29c-3p, miR-30c-1-5p, miR-106a-5p, miR -126-3p, miR-129-1-5p, miR-132-3p, miR-135b-5p, miR-146a-5p, miR-185-5p, miR-214-3p, miR-221-3p, and miR -520d-5p.

The leukocyte fraction was isolated from the venous blood of all subjects. Then, total RNA was isolated using a RNeasy mini kit (Qiagen) according to the manufacturer's standard protocol. After RNA isolation, reverse transcription specific to each microRNA was performed using stem-loop primers and a reverse transcription kit (Syntol). The relative concentration of each RNA was determined during a real-time polymerase chain reaction using the appropriate kit (Syntol); miR-191-5p was used as a reference RNA. The RNA concentration was calculated using the $2(-\Delta\Delta C(T))$ method.

Statistical processing was performed using the SPSS and Statistica 10.0 software. The Shapiro–Wilk test was used to check if the variable followed a normal distribution. Due to the distribution of microRNA values not being normal, the nonparametric Mann–Whitney, Kruskal–Wallis, and Spearman correlation coefficient tests were used. We also used a logistic regression analysis and ROC analysis. The statistical significance level was set to 0.05.

RESULTS

A statistically significant increase in the expression level of three microRNAs – miR-7-1-5p, miR-29c-3p, and miR-185-5p – and a statistically significant decrease in the expression level of two microRNAs – miR-29a-3p and miR-30c-1-5p – were revealed in the

Table 1. MicroRNA expression in PD patients and healthy volunteers

microRNA	Parkinson's disease	Control group	*p* (U)
miR-7-1-5p	**0.68 [0.19; 1.7]**	**0.2 [0.04; 1.5]**	**0.024***
miR-24-1-3p	455.72 [0.43; 654.6]	480.88 [0.83; 602.4]	0.684
miR-29a-3p	**0.63 [0.41; 1.01]**	**0.97 [0.66; 1.4]**	**0.003****
miR-29c-3p	**1.76 [0.93; 3.58]**	**0.77 [0.59; 1.98]**	**0.003****
miR-30c-1-5p	**0.53 [0.34; 1.43]**	**1.03 [0.46; 1.77]**	**0.043***
miR-106a-5p	1.41 [0.43; 3.5]	1.39 [0.76; 2.8]	0.691
miR-126-3p	0.23 [0.15; 0.44]	0.4 [0.11; 0.8]	0.194
miR-129-1-5p	0.47 [0.2; 2.21]	0.4 [0.23; 0.71]	0.403
miR-132-3p	1.01 [0.4; 2.01]	0.87 [0.37; 1.39]	0.209
miR-135b-5p	54.5 [4.02; 2479.78]	284.29 [1.02; 149791.83]	0.946
miR-146a-5p	0.11 [0.03; 1.37]	0.07 [0.03; 0.34]	0.337
miR-185-5p	**13631.02 [380.56; 21875.07]**	**863.02 [0.17; 14684.43]**	**0.017***
miR-214-3p	15.23 [6.97; 22.65]	15.75 [6.01; 27.3]	0.709
miR-221-3p	0.63 [0.42; 1.04]	0.72 [0.49; 0.99]	0.443
miR-520d-5p	0.27 [0.05; 1.02]	0.52 [0.04; 1.77]	0.374

*$p < 0.05$; **$p < 0.01$. All cases where $p < 0.05$ are shown in bold.

PD group compared to the control group (*Table 1*). However, despite the statistical significance of the differences detected, there was a significant overlap in the relative expression levels in these groups.

Next, we assessed the possibility of using individual microRNAs as PD biomarkers. The ROC analysis revealed that some microRNAs could be used to differentiate PD from the controls: miR-7-1-5p (AUC = 0.63, $p = 0.024$; 95% CI 0.517–0.742), miR-185-5p (AUC = 0.638; $p = 0.016$; 95% CI 0.53–0.744), miR-29c-3p (AUC = 0.673; $p = 0.003$; 95% CI 0.56–0.778). However, the sensitivity and specificity of these biomarkers are obviously insufficient for a PD diagnosis. A logistic regression analysis using the backward Wald method was employed to search for the most optimal microRNA combination that could possess the highest informative value as a biomarker. The combination of miR-29c-3p and miR-185-5p proved to be the most informative. During the subsequent ROC analysis, the area under the curve was 0.715 (*Fig. 1*). Thus, this two-microRNA model allows a 71.5% probability of differentiating PD patients from healthy individuals.

We studied the relationship between microRNA expression and the clinical characteristics of PD. No significant correlations between the microRNA levels and the age of onset were found, besides one weak correlation ($R < |0.3|$) between the age at study entry and miR-135b-5p. The analysis of any correlations between microRNA levels and disease duration revealed six weak but significant correlations (miR-132-3p, miR-146a-5p, miR-106a-5p, miR-24-1-3p, miR-29a-3p, miR-30c -1-5p) and two moderate correlations (miR-126-3p, $R = 0.316$; $p = 0.07$ and miR-129-1-5p, $R = 0.385$; $p = 0.001$). These microRNAs may serve as markers of disease progression.

The analysis of the microRNA expression in different PD forms showed that the miR-29a-3p level in the akinetic-rigid form was significantly higher than that in the mixed form, 1.06 [0.6; 1.59] and 0.6 [0.43; 0.85] ($p = 0.018$), respectively. A negative correlation was found between the miR-30c-1-5p level and the Hoehn and Yahr disease stage ($R = -0.303$; $p = 0.19$). At the same time, a differential expression of these two microRNAs (*Table 1*) was detected in PD and the control groups. No correlation was found

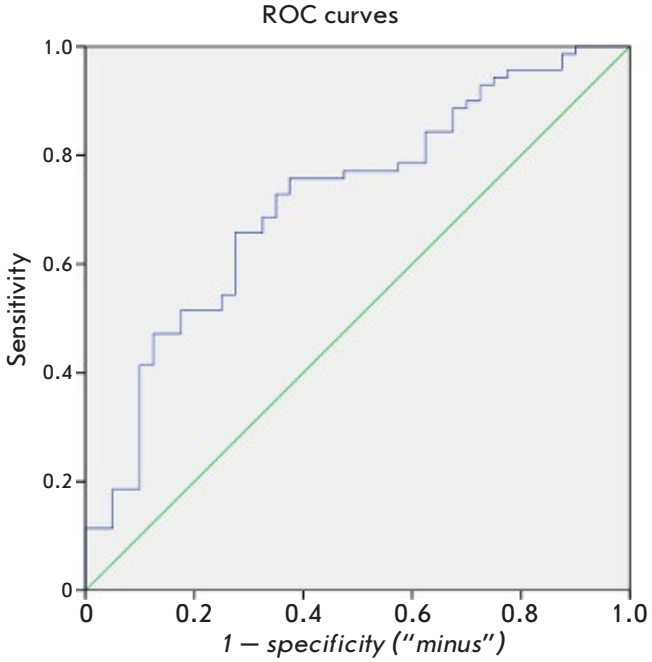

Fig. 1. ROC analysis of a logistic regression model with miR-29c-3p and miR-185-5p for the diagnosis of Parkinson's disease

between microRNA levels and the total UPDRS (including subscales) score. A negative correlation was revealed between the miR-106a-5p level and the total NMSQ score ($R = -0.358$, $p = 0.011$). No correlations were found with HADS scores. Also, there were no correlations with the cognitive impairment severity (MoCA scale).

The miR-29a-3p expression ($p = 0.045$) was statistically significantly reduced in patients treated with levodopa. The patients receiving both dopamine receptor agonists and amantadine demonstrated a decrease in miR-7-1-5p in ($p = 0.0048$ and $p = 0.037$, respectively). Interestingly, the expression of both miR-7-1-5p and miR-29a-3p was different in PD patients and the controls (*Table 1*).

DISCUSSION

To date, a significant number of studies on the biomarker potential of microRNAs in PD have been performed. However, the results remain mostly contradictory, due to the variety of the blood components (plasma, leukocytes, serum, vesicles) being studied and the wide range of microRNAs analyzed, not to mention the different methods used to detect them [23].

In this study, we used 15 microRNAs that had been shown in previous studies to exhibit significant expression differences between PD and the controls. According to our data, the combination of two microRNAs – miR-29c-3p and miR-185-5p – has the greatest diagnostic value in PD. A significant increase in the miR-7-1-5p level and a significant decrease in miR-29a-3p in PD were also observed, with these levels being significantly affected by antiparkinsonian therapy, as shown in our work. In addition, a significant decrease in miR-30c-1 in PD was revealed. The level of this microRNA steadily decreased as the disease progressed, and its severity increased according to the Hoehn–Yahr functional scale, suggesting that it can be used as a marker of disease progression (i.e., a marker of advanced PD stages).

However, a number of other microRNAs, with levels similar to those of the controls, appeared to be associated with non-motor manifestations of PD (miR-106a-5p) and disease duration (miR-126-3p, miR-129-1-5p). Thus, while not being direct biomarkers of the disease, these microRNAs may be valuable in more accurately identifying non-motor phenotypes of PD and more objectively monitoring the course of the disease.

The role of miR-185 in PD was analyzed in several studies. A decrease in the miR-185 level was observed in MPTP-treated SH-SY5Y dopaminergic neuroblastoma cells, while increased miR-185 expression reduced MPTP-induced apoptosis and autophagy [24]. A study by Rahimmi et al. in SH-SY5Y cells and Wistar rats with rotenone-induced parkinsonism revealed that inhibition of miR-185 expression with a specific small interfering RNA leads to a significant increase in the *LRRK2* gene expression. This gene plays an important role in the pathogenesis of PD, with its mutations leading to the development of hereditary forms of PD [25]. A decrease in miR-185 and an increased *LRRK2* expression were demonstrated in the substantia nigra and striatum of animal models. A study by Briggs et al. also reported miR-185 expression changes in the substantia nigra, but in the opposite direction [26]. The use of miR-185 as a biomarker was evaluated in several studies, and two of them revealed a decreased expression level of this microRNA in PD, compared with that in the control group [15, 27]. In contrast, our study has shown an increased expression of this potential marker. Thus, the data on the miR-185 expression level in PD remain inconclusive.

The miR-29 family includes three microRNAs: miR-29a, miR-29b, and miR-29c. The studies on the use of these microRNAs as biomarkers have repeatedly demonstrated decreased miR-29a and miR-29c expressions in the blood of PD patients, with the miR-29a and miR-29c expressions tending to de-

crease with the disease severity (Hoehn and Yahr scale) [28]. A prospective study of patients at risk of synucleinopathies revealed decreased miR-29a and miR-29c levels in patients with REM sleep behavior disorders who were subsequently diagnosed with synucleinopathy [29]. Several studies investigated miR-29a alone and demonstrated a decrease in its level, which is consistent with our results [14, 30, 31]. Serafin et al. reported an increased miR-29a expression only in levodopa-treated patients and did not find changes in untreated patients [19]. Our study has also revealed decreased miR-29a levels upon levodopa therapy.

The increased miR-29c expression found in PD patients in the Turkish population [32] is consistent with our results, but it contradicts most of the available data [12, 14, 31]. The targets of this highly pathogenetically promising family of microRNAs include mRNAs of the *PARK-7* (*DJ-1*) gene, whose mutations can lead to PD, GPR37 mRNA, with its substrate being the parkin protein associated with the development of early PD, and various regulators of apoptosis processes (*Puma*, *Bim*, *Bak*, *Bcl2*, *IGF1*, *AKT1*). The targets of individual microRNAs from the miR-29 family can significantly overlap, but their role in the pathogenesis of various PD forms is beyond doubt.

MiR-7 was reported to reduce the expression of alpha-synuclein [33, 34], the impaired processing of which is considered one of the key components of PD pathogenesis. One study demonstrated a decreased miR-7 expression in the brain of PD patients, probably resulting in the increased expression of alpha-synuclein [6]. In addition, a decreased miR-7 expression was shown to increase the risk of apoptosis and inhibit the growth of dopaminergic neurons in culture [35]. In our study, on the contrary, the expression level of miR-7 in the PD group was significantly higher than that in the control group. Alieva et al. also indicated a many-fold increase in the miR-7 expression in a subgroup of PD patients receiving anti-Parkinson's drugs [18]. Our study did not find any effect of the levodopa therapy on the miR-7 level, while administration of dopamine receptor agonists and amantadines was associated with a decreased miR-7 expression. Conflicting results on the miR-7 level in PD and the effect of anti-Parkinson's therapy on it require further clarification.

The decrease in the miR-30c-1 level in PD reported in the studies by Vallelunga et al. and Martins et al. is consistent with our results [31, 36]. No direct effect of miR-30c-1 on the expression of the genes responsible for the development of PD was found. However, according to various databases, the putative targets of this microRNA (*Notch1*, *HDAC4*, *BECN1*, *UBE2I*, *HSPA4*, and *DNMT1*) were shown to play a role in regulating the autophagy and apoptosis of dopaminergic cells [37].

CONCLUSION

To summarize, we have shown that the combination of two microRNAs (miR-29c-3p and miR-185-5p) can be considered a potential PD biomarker, with moderate diagnostic significance. The expression level of several microRNAs has been found to reflect the clinical characteristics of PD, to depend on the disease duration and stage and ongoing therapy, serve as a marker of the disease form, and be associated with the severity of non-motor manifestations and the quality of life of PD patients. According to published data, some of the diagnostic microRNAs are associated with certain components of PD pathogenesis. Our results are preliminary and require further research. ●

REFERENCES

1. Coon E.A., Singer W. // CONTINUUM: Lifelong Learning in Neurology. 2020. V. 26. № 1. P. 72–92.
2. Rizzo G., Copetti M., Arcuti S., Martino D., Fontana A., Logroscino G. // Neurology. 2016. V. 86. № 6. P. 566–576.
3. Gerasimou G., Costa D.C., Papanastasiou E., Bostanjiopoulou S., Arnaoutoglou M., Moralidis E., Aggelopoulou T. Gotzamani-Psarrakou A. // Ann. Nucl. Med. Japan. 2012. V. 26. № 4. P. 337–344.
4. Arena J.E., Stoessl A.J. // Parkinsonism and Related Disorders. 2016. V. 22. P. S47–S51.
5. Lang A.E., Espay A.J. // Movement Disorders. 2018. V. 33. № 5. P. 660–677.
6. Tatura R., Kraus T., Giese A., Arzberger T., Bucholz M., Höglinger G., Muller U. // Parkinsonism and Related Disorders. 2016. V. 33. P. 115–121.
7. Wahid F., Shehzad A., Khan T., Kim Y.Y. // Biochim. Biophys. Acta – Mol. Cell Res. 2010. V. 1803. № 11. P. 1231–1243.
8. Mathonnet G., Fabian M.R., Svitkin Y.V., Parsyan A., Huck L., Murata T., Biffo S., Merrick W., Darzynkiewicz E., Pillai R.S., et al. // Science. 2007. V. 317. № 5845. P. 1764–1767.
9. Leggio L., Vivareli S., L'Episcopo F., Tirolo C., Caniglia S., Testa N., Barchetti B., Iraci N. // Int. J. Mol. Sci. 2017. V. 18. P. 2698.
10. Ma F., Zhang X., Yin K.-J. // Exp. Neurol. 2020. V. 323. P. 113094.
11. Cao X., Lu J.-M., Zhao Z.-Q., Li M.-C., Lu T., An X.-S., Xue L.-J. // Neurosci. Lett. 2017. V. 644. P. 94–99.
12. Ma W., Li Y., Wang C., Xu F., Wang M., Liu Y. // Cell. Biochem. Funct. 2016. V. 34. P. 511–515.
13. Kean S., Petillo D., Kang U.J., Resau J.H., Berryhill B., Linder J., Forsgren L., Neuman L.A., Tan A.C. // J. Parkinson's Dis. 2012. V. 2. P. 321–331.
14. Botta-orfila T., Morato X., Compta Y., Lozano J.J., Falgas N., Valldeoriola F., Pont-Sunyer C., Vilas D., Mengual L., Fernandez M., et al. // J. Neurosci. Res. 2014. V. 92. № 8. P. 1–7.

15. Ding H., Huang Z., Chen M., Wang C., Chen X., Chen J., Zhang J.// Parkinsonism Related Disorders J. 2016. V. 22. P. 68–73.
16. Dong H., Wang C., Lu S., Yu C., Huang L., Feng W., Xu H., Chen X., Zen K., Yan Q., et al. // Biomarkers. 2016. V. 21. № 2. P. 129–137.
17. Margis R.R., Margis R.R., Rieder C.R.M. // J. Biotechnol. 2011. V. 152. № 3. P. 96–101.
18. Alieva A., Filatova E.V., Karabanov A.V., Illarioshkin S.N., Limborska S.A., Shadrina M.I., Slominsky P.A. // Parkinsonism Related Disorders J. 2014. V. 21. № 1. P. 14–16.
19. Serafin A.., Foco L., Zanigni S., Blankenburg H., Picard A., Zanon A., Gianni G., Pichler I., Maurizio F.F., Cortell P., Pramstaller P.P., Hicks A.A., Domingues F.S., Schwienbacher C. // Neurology. 2015. V. 84. P. 1–9.
20. Caggiu E., Paulus K., Mameli G., Arru G., Sechi G. P., Sechi L.A. // eNeurologicalSci. 2018. V. 13. P. 1–4.
21. Soreq L., Salomonis N., Bronstein M., Greenberg D.S., Israel Z., Bergman H., Soreg H.// Front. Mol. Neurosci. 2013. V. 6. P. 1–20.
22. Postuma R., Berg D., Stern M., Poewe W., Olanow C.W., Oertel W., Obeso J., Marek K., Litvan I., Lang A., et al. // Mov. Disord: Official J. Mov. Disord. Soc. 2015. V. 30. № 12. P. 1591–1601.
23. Nies Y.H., Mohamad Najib N.H., Lim W.L., Kamaruzzaman M.A., Yahaya M.F., Teoh S.L.// Front. Neurosci. 2021. V. 15. P. 660379.
24. Wen Z., Zhang J., Tang P., Tu N., Wang K., Wu G. // Mol. Med. Rep. 2018. V. 17. № 1. P. 131–137.
25. Rahimmi A., Peluso I., Rajabi A., Hassanzadeh K. // Oxid. Med. Cell. Longev. Hindawi. 2019. V. 2019. P. 5019815.
26. Briggs C.E., Wang Y., Kong B., Woo T.U., Iyer L.K., Sonntag K.C. // Brain Res. 2015. V. 1618. P. 111–121.
27. Chen L., Yu Z. // Brain Behav. 2018. V. 8. № 4. P. e00941.
28. Bai X., Tang Y., Yu M., Wu L., Liu F., Ni J., Wang Z., Wang J., Fei J., Wang W., et al.// Sci. Rep. 2017. V. 7. № 1. P. 5411.
29. Fernández-Santiago R., Iranzo A., Gaig C., Serradell M., Fernández M., Tolosa E., Santamaría J., Ezquerra M. // Ann Neurol. 2015. V. 77. № 5. P. 895–901.
30. Barbagallo C., Mostile G., Baglieri G., Giunta F., Luca A., Raciti L., Zappia M., Purrello M., Ragusa M., Nicoletti A. // Cell. Mol. Neurobiol. 2020. V. 40. № 4. P. 531–546.
31. Martins M., Rosa A., Guedes L.C., Fonseca B.V., Gotovac K., Violante S., Mestre T., Coelho M., Rosa M.M., Martin E.R., et al. // PLoS One. 2011. V. 6. № 10. P. e25443.
32. Ozdilek B., Demircan B. // Int. J. Neurosci. 2020. V. 131. № 12. P. 1181–1189.
33. Doxakis E. // J. Biol. Chem. 2010. V. 285. № 17. P. 12726–12734.
34. Junn E., Lee K.W., Jeong B.S., Chan T.W., Im J.Y., Mouradian M.M. // Proc. Natl. Acad. Sci. USA. 2009. V. 106. № 31. P. 13052.
35. Li S. Lv X., Zhai K., Xu R., Zhang Y., Zhao S., Qin X., Yin L., Lou J.// Am. J. Transl. Res. 2016. V. 8. № 2. P. 993–1004.
36. Vallelunga A., Ragusa M., Di Mauro S., Iannitti T., Pilleri M., Biundo R., Weis L., Di Pietro C., De Iuliis A., Nicoletti A., et al. // Front. Cell. Neurosci. 2014. V. 8. P. 1–10.
37. Vallelunga A., Iannitti T., Dati G., Capece S., Maugeri M., Tocci E., Picillo M., Volpe G., Cozzolino A., Squillante M., et al. // Mol. Biol. Rept. 2019. V. 46. № 2. P. 1661–1666.

Suppression of the Testis-Specific Transcription of the *ZBTB32* and *ZNF473* Genes in Germ Cell Tumors

S. S. Bulanenkova, O. B. Filyukova, E. V. Snezhkov, S. B. Akopov*, L. G. Nikolaev
Shemyakin-Ovchinnikov Institute of Bioorganic Chemistry, Russian Academy of Sciences, Moscow, 117997 Russia
*E-mail: sergeyakopov@mail.ru
Received October 28, 2021; in final form, August 22, 2022
DOI: 10.32607/actanaturae.11620

ABSTRACT **The family of genes containing C2H2 zinc finger domains, which has more than 700 members, is one of the largest in the genome. Of particular interest are C2H2 genes with potential tissue-specific transcription, which determine the functional properties of individual cell types, including those associated with pathological processes. The aim of this work was to identify C2H2 family genes with tissue-specific transcription and analyze changes in their activity during tumor progression. To search for these genes, we used four databases containing data on gene transcription in human tissues obtained by RNA-Seq analysis. The analysis showed that, although the major part of the C2H2 family genes is transcribed in virtually all tissues, a group of genes has tissue-specific transcription, with most of the transcripts being found in the testis. After having compared all four databases, we identified nine such genes. The testis-specific transcription was confirmed for two of them, namely *ZBTB32* and *ZNF473*, using quantitative PCR of cDNA samples from different organs. A decrease in *ZBTB32* and *ZNF473* transcription levels was demonstrated in germ cell tumors. The studied genes can serve as candidate markers in germ cell tumors.**
KEYWORDS **zinc-finger proteins, testis, germ cell tumors, transcription.**

INTRODUCTION

The family of genes containing zinc-finger domains of the C2H2 type includes more than 700 members and is one of the most numerous [1, 2]. One of the main functions of the zinc finger structure is DNA binding; therefore, many proteins of this family have the properties of transcription factors [1]. Apart from zinc fingers, different family members may contain additional N-terminal domains, such as KRAB, SCAN, and BTB/POZ, which determine the regulatory functions of proteins [3]. Despite the evolutionary prevalence of this family in mammals [4], its significance for cell activity is still not entirely clear to us. In general, studies are focused on a detailed analysis of the structure and function of individual family members such as CTCF [5, 6]. Some genes are associated with a series of diseases [7]. Considering the large number of family members, attempts are being made to define more general and universal functions for its members. For instance, their involvement in the organization of the chromatin structure is considered [8]. In particular, their ability to ensure the proximity of distant genomic regions through zinc fingers binding to DNA and protein–protein contacts is assumed [5]. One of the functions of the protein family containing the KRAB repressor domain is to suppress the activity of retroelements, whose large number explains the wide distribution of the C2H2 family in the human genome [9, 10]. An additional difficulty in the study of this family is introduced by the fact that the properties of zinc fingers are not limited to DNA binding; a number of these domains also interact with RNA and proteins [7, 11, 12]. Thus, the study of this family seems to be a massive and multi-stage endeavor aimed at finding out whether different family members are related to each other through a common functional unity and whether they perform narrow specific functions or act as multifunctional proteins.

Taking into account the diversity of the members of the family, it is sensible to assume their involvement in the regulation of various biological processes, both those common to all cells and those specific to individual cell types. A natural question arises about the activity of the C2H2 family members in various pathologies, including malignant cell transformation. Taking into account the fact that the number

of tissue-specific genes is an order of magnitude lower than that of ubiquitously expressed genes and that most of them are expressed in the testes [13, 14], it is safe to assume that this pattern is also preserved among C2H2 family genes.

In this work, we analyzed several databases containing information on gene transcription in different human body tissues and identified several testis-specific genes of the C2H2 family. We experimentally confirmed the highly specific transcription of two of these genes in the testes compared to other tissues. Analysis of tumor and normal testicular tissues showed suppressed gene transcription in germ cell tumors.

The study of testis-specific genes might eventually help us to better understand the processes of tumorigenesis and their possible practical application in predicting, diagnosing, and treating cancer.

EXPERIMENTAL

Data sources

Averaged data on gene transcription levels in different tissues presented in TPM (Transcripts Per Million, [15]) were obtained from https://proteinatlas.org (Human Protein Atlas, HPA), https://gtexportal.org/home/ (The Genotype-Tissue Expression, GTEX, version GTEx_Analysis_2017-06-05_v8_RNASeQCv1.1.9_gene_median_tpm.gct.gz, without transformed lymphocytes), https://www.ebi.ac.uk/ (using data from E-MTAB-513 (Illumina Body Map), E-MTAB-4344 (ENCODE project), E-MTAB-2836 (HPA), and E-MTAB-5214 (GTEx)). Complete data on gene transcription in all tissue samples presented in TPM were obtained from the GTEx website (https://gtexportal.org/home/), version GTEx_Analysis_2017-06-05_v8_RNASeQCv1.1.9_gene_tpm.gct.gz.

Tissue-specific genes were selected for each database as described below. First, all genes with an expression level of at least 5 TPM were selected from each tissue. Further analysis was carried out for each selected gene. The gene expression level in a particular tissue was compared with that in other tissues. The ratio of the gene expression level in TPM to its expression levels in other tissues was calculated for each tissue. Next, the minimum value was chosen from the set of values obtained for each tissue. If this value was at least 3, the gene was assumed to possess tissue-specific expression.

Tissue samples

Lung, kidney, large and small intestine, skeletal muscle, lymph node, spleen, and anterior cerebral cortex samples were obtained from healthy adult patients who had died from injuries incompatible with life. Testicular tumor samples (31) were obtained by orchiectomy; they included 27 samples of germ cell origin and 11 samples of adjacent normal tissues, with 7 germ cell samples (testicular parenchyma) among them. A total of 18 samples were paired (6 pairs of germ cell origin and three pairs of non-germ cell origin). Two samples of normal testicular tissue, obtained during surgical castration of patients with prostate cancer, were further used as controls (see supplementary *Table_S1* for details; available upon request). All representative samples were immediately frozen in liquid nitrogen. The samples were collected according to Federal Law No. 180 "On Biomedical Cell Products" (Order of the Ministry of Health of the Russian Federation No. 517n dated August 11, 2017; Appendix 2, see http://publication.pravo.gov.ru/Document/View/0001201709290030) and approved by the ethical committees of the Institute of Bioorganic Chemistry n.a. M.M. Shemyakin and Yu.A. Ovchinnikov of the Russian Academy of Sciences and N.N. Blokhin National Medical Research Center of Oncology of the Ministry of Health of the Russian Federation.

RNA isolation

Total RNA was isolated using guanidine isothiocyanate according to [16]. All RNA preparations were treated with DNase I (Promega, USA) according to the manufacturer's recommendations. Final samples were purified using the RNeasy MINI RNA kit (Qiagen, USA). The quality and purity of the RNA samples were determined by electrophoresis in 1% agarose gel. RNA concentrations were determined by spectrophotometry.

Quantitative PCR of cDNA (RT-PCR)

The first strands were synthesized using a random hexanucleotide primer (Promega) and PowerScript reverse transcriptase (Clontech, USA) according to the manufacturer's instructions. The cDNA template amount in each PCR reaction was equivalent to 10 ng of total RNA. The sequences of the primers used in the study are presented in *Table 1*. Primers were selected using the Primer–Blast software (https://www.ncbi.nlm.nih.gov/tools/primer-blast/index.cgi), with primer location in different exons being one of the criteria. The reaction was performed in the qPCR-HS SYBR buffer system (Evrogen, Russia) on a LightCycler 480 PCR platform (Roche, USA) using the following temperature program: 95°C for 3 min, followed by 40 cycles at 95°C for 20 s, 65°C for 20 s, and 72°C for 40 s. The transcription level was assessed relative to the geometric mean abundance of the 18S rRNA and *GAPDH* transcripts. All experiments were performed in three technical replicates.

Table 1. Sequences of primers for quantitative PCR

Gene	Forward	Reverse	Product length, bp
18S	TGAGAAACGGCTACCACATC	GCTATTGGAGCTGGAATTACC	203
GAPDH	ACTCCTCCACCTTTGACGCT	TCTTCCTCTTGTGCTCTTGCT	179
ZBTB32	GCCCTATGCGTGCTCTGTCT	GGTCATGGCCGAGAAGTCC	139
ZNF473	GGAAGCCCAGAAGCAACAAG	TTCTGGATCGCCTAGCAAACT	189
ZNF446	AATAGAGGGGTCTGTCCAGC	CCGTACTTCTCCAGCATCGC	231

Statistical analysis of experimental data

Comparison of two data groups was performed using the Mann–Whitney test for independent samples and the Wilcoxon test for paired samples. In order to analyze the transcription consistency, the Spearman correlation coefficient was calculated. The significance level was set at 0.05. All database calculations were performed using Excel2010, the R software environment [17], and the stats and openxlsx (https://github.com/ycphs/openxlsx) packages. To determine the tissue specificity of gene transcription, the ratio of the transcription level for each gene expressed in TPM in all tissues, except for the studied one, to the gene transcription in the studied tissue was calculated; this made it possible to avoid division-by-zero errors in the absence of transcription in other organs. The highest ratio was determined for each gene; if it did not exceed 0.3, then the gene was selected for further analysis.

Correlation matrices were constructed using the stats, cluster (https://CRAN.R-project.org/package=cluster), and corrplot (https://github.com/taiyun/corrplot) packages. For cluster analysis, dendrogram construction, and calculation of the optimal number of clusters, we used the stats, cluster, dendextend [18], NbClust [19], and clValid [20] packages. A value equal to 1 - Spearman's rank correlation coefficient modulus was used as a measure of the distance between genes. Clusters were defined using the hierarchical classification algorithm and the complete linkage method. Scripts are available upon request.

Additional Online Resources

Generation of Venn diagrams: http://bioinformatics.psb.ugent.be/webtools/Venn/;

GePIA (Gene Expression Profiling Interactive Analysis, http://gepia.cancer-pku.cn/) [21]: comparison of gene transcription levels in normal and tumor samples based on GTEx (https://gtexportal.org/home/) and TCGA (The Cancer Genome Atlas Program, https://portal.gdc.cancer.gov/) data;

HGNC (HUGO Gene Nomenclature Committee): https://www.genenames.org/;

Ensembl: https://www.ensembl.org/index.html;

Online Gene ID to Gene Symbol Converter: https://www.biotools.fr/;

Human genome browser [22]: https://genome.ucsc.edu/

RESULTS

Nine genes of the C2H2 family have testis-specific transcription

Large-scale RNA sequencing data provided by the Illumina Body Map, Encyclopedia of DNA Elements (ENCODE) [23], Genotype-Tissue Expression (GTEx) [24], and Human Protein Atlas (HPA) [25] projects were used for the analysis. The presented data sources differ in the number of tissues and samples per tissue (ranging from one to several hundreds) and the method of biomaterial sampling used (collection during either surgery or autopsy). A more detailed description of databases is presented in [13].

We analyzed the transcription levels averaged over several samples and presented in TPM. C2H2 family genes were selected from each data set; the selection was based on the fact of belonging to group 28 in the HGNC database [26], using Ensembl identification numbers. The number of tissues and genes of the C2H2 family, presented in different databases, is shown in *Table 2*.

Next, we estimated the total number of genes of this family transcribed in different tissues at a level of at least 3 TPM. Except for a few tissues where

Table 2. Representation of tissues and genes in databases

Database	Tissues, number	C2H2 gene, number
Illumina Body Map	16	717
ENCODE	13	718
GTEx	53	718
HPA	43	709

the number of genes transcribed at this level is in the range of 200–300 (e.g., liver and skeletal muscle), most tissues contain more than 450 such genes, with the largest number of genes (over 600) transcribed at this level in the testes. Thus, we can conclude that most of the genes of this family are active in almost all the presented tissues (see supplementary *Table_S2*; available upon request).

Next, we searched for the C2H2 family genes specific to each tissue. First, we selected genes with a transcription level of at least 5 TPM in a specific tissue. A gene was considered active predominantly in a given tissue if its transcription level was at least three times higher than that in any other tissue or organ.

The results of the analysis of the tissue-specific transcription of the genes presented in each of the databases are shown in supplementary *Table_S3* (available upon request). We would like to note that all four databases provide data only for tissues of the adrenal glands, testicles, ovaries, liver, and lung. In all cases, the largest number of genes with tissue-specific transcription ($\geqslant$ 16) was found in the testes. C2H2 genes with tissue-specific transcription ($\leqslant$ 10) were also found in ovaries, brain, spleen, cerebral cortex, bone marrow, and prostate. However, unlike in the case of testes, the comparison of the results presented in different databases revealed almost no common genes. This observation is consistent with the results of [14], which revealed 35 genes with tissue-specific transcription, while the number of testis-specific genes of the C2H2 family in other organs and tissues did not exceed six. Thus, while a major portion of C2H2 family genes are non-specifically transcribed in most tissues, the largest tissue-specific fraction of the genes is transcribed in the testes.

Further, we focused on this gene fraction. A total of 52 such genes were found in all the databases. It should be noted that the number and set of genes vary slightly between different database versions. This is due to the fact that, when new data are added to the databases, the average transcription level changes and the genes at the boundaries of the conditions set may end up on either side. It is also worth mentioning that databases such as Illumina and Encode include a small number of tissues (and the smallest number of samples per tissue: from one to three) compared to HPA and GTEx, which increases the probability of a false identification of a gene as testis-specific, due to the lack of information on its transcription in tissues not present in the database. Therefore, we further analyzed 25 genes whose transcription levels in the testes exceeded the maximum level in other organs by more than 1.5-fold in all considered databases. Of these, 13 genes coincided with the data from [14] on 35 testis-specific genes. The discrepancies can be explained by the use of different databases (GTEx and HPA in this study and TiGER in [14]) and the different algorithms used to search for tissue-specific genes. Thus, it can be seen that gene selection depends on the search algorithm and the database version. All of this points to the great importance of directly confirming the analyzed data experimentally.

We selected the genes common to all databases from the sets of genes isolated from each database (*Fig. 1*). A total of nine genes were selected: *ZBTB32*, *CTCFL*, *ZNF560*, *ZNF541*, *ZNF473*, *ZNF165*, *PRDM9*, *ZSCAN5A*, and *ZNF487*. All these genes, with the exception of *PRDM9*, *ZSCAN5A*, and *ZNF487*, are defined as testis-specific by using various database versions and are also present in the group of testis-specific genes [14]. Data on the transcription of nine genes in the testes according to the four analyzed databases, as well as the median and maximum values of gene transcription in tissues other than the testes, are presented in *Table 3*; the structural characteristics of the genes are shown in *Table 4* (similar data for all 52 genes are provided in supplementary *Table_S4*; available upon request).

Table 3. Transcription of selected genes in testes according to four databases (in TPM)*

Gene	HPA	ENCODE	GTEx	Illumina
ZNF473	76.4 (11.1/4.25)	79 (8/2.5)	49.1 (8.3/3.25)	46 (8/4)
ZBTB32	43.3 (7.5/0.15)	84 (4/0)	109.3 (6.5/0.3)	32 (5/0.4)
ZNF541	19.2 (1.7/0.1)	40 (1/0.3)	45.7 (2.7/0.3)	18 (2/0.3)
ZSCAN5A	34.6 (11.3/3.4)	12 (2/0.95)	14.4 (2.3/1.2)	12 (3/1)
ZNF487	51.4 (9.9/2.95)	28 (7/2)	23.2 (4.4/2.1)	21 (5/2)
PRDM9	7 (1.7/0)	9 (0/0)	6.9 (0/0)	6 (0/0)
ZNF560	11.9 (1.2/0)	15 (0.2/0)	15.5 (0.6/0)	12 (0.3/0)
CTCFL	20.4 (0.8/0.3)	14 (0.2/0)	7.5 (0.1/0)	17 (0.5/0,2)
ZNF165	35.8 (7.4/1.55)	46 (15/2)	45.6 (7.6/1.35)	49 (9/2)

*Maximum and median transcription values for selected genes in other tissues (in TPM) are presented according to the same database and indicated in brackets with a slash.

Table 4. Data on protein domains and gene location

Gene	C2H2 number	Other domains	Location
CTCFL	11	–	20q13.31
PRDM9	14	SET, KRAB	5p14.2
ZBTB32	3	BTB/POZ	19q13.12
ZNF165	6	SCAN	6p22.1
ZNF473	20	KRAB	19q13.33
ZNF541	5	ELM2, SANT	19q13.33
ZNF560	15	KRAB+KRAB	19p13.2
ZSCAN5A	5	SCAN	19q13.43
ZNF487	3	KRAB	10q11.21

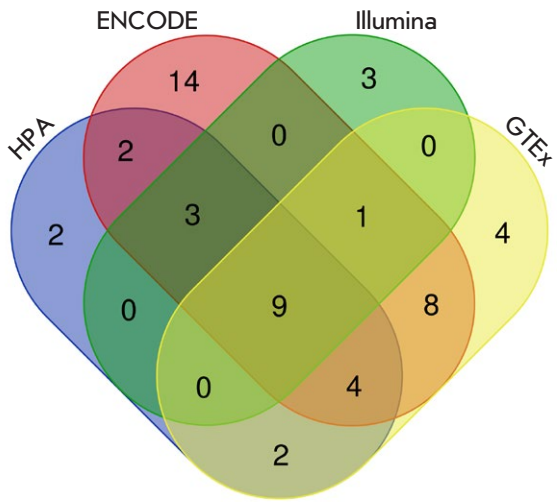

Fig. 1. Venn diagram showing preselected genes common to the four databases: Human Protein Atlas, ENCODE, Illumina BodyMap, and GTEx. The diagram was generated using the online program (http://bioinformatics.psb.ugent.be/webtools/Venn/)

At the same time, there are differences in the transcription profiles of the selected genes. *CTCFL*, *PRDM9*, and *ZNF560* are highly testis-specific genes; their transcription levels in other tissues do not exceed 0.6 TPM. Furthermore, the transcription level of these genes in the testes is approximately 2–3 times lower than that of the *ZBTB32*, *ZNF165*, *ZNF473*, and *ZNF541* genes. The levels of *ZBTB32*, and *ZNF541* are almost undetectable in most tissues (the median varies in the range of 0–0.6 TPM). However, *ZBTB32* transcription can reach 7.5 TPM in a number of organs and cells, such as B cells, lymph node, appendix, spleen, tonsils, and Peyer's patches, while the *ZNF541* gene level in the adrenal glands reaches 2–3 TPM. *ZNF165*, *ZSCAN5A*, *ZNF487*, and *ZNF473* are transcribed at a low level in almost all the tissues, and their level is at least three times higher in the testes than in any other tissue.

For further analysis, we selected two genes, *ZNF473* and *ZBTB32*, which are important for determining the tissue identity of the testes [27].

Transcription of *ZBTB32* and *ZNF473* is suppressed in testicular germ cell tumors

We experimentally determined the levels of the *ZBTB32* and *ZNF473* transcripts in samples of human testes, lung, kidney, large and small intestine, skeletal muscle, lymph node, spleen, and anterior cerebral cortex. The transcription level was assessed by real-time PCR using a cDNA template and geometric mean levels of *GAPDH* and 18S rRNA transcripts for normalization. The results are presented in *Fig. 2A,B*. As it can be seen from the figure, the *ZNF473* and *ZBTB32* levels in the testes exceed those in other organs by at least five- and four-fold, respectively. Low but detectable levels of *ZNF473* and *ZBTB32* were observed in lymphoid tissues (spleen and lymph nodes), while being insignificant in the other tested tissues, which is consistent with the results of the database analysis discussed above.

In order to compare the transcription profiles of the two studied genes and confirm their independence from the aspects of sample preparation, reaction conditions, etc., we performed a parallel transcriptional analysis of a randomly selected gene, *ZNF446*, which also belongs to the C2H2 family. This gene was not selected from the databases according to the abovementioned criteria; it transcribed in testes and other tissues at a low level (1–10 TPM), without a pronounced tissue specificity. Our results confirm the absence of a tissue-specific transcription of *ZNF446* (*Fig. 2C*).

We determined the transcription levels of the same genes using a cDNA panel obtained from tumor and normal testicular tissues. Transcription levels were assessed as described above. The results are shown in *Fig. 3*. The panel is represented by parenchyma samples from healthy testes (control samples 17N and 19N), tumors, and normal tissues adjacent to them. A number of samples are represented by tumor/adjacent conditionally normal tissue (normal) pairs obtained from one patient. Tumors (and adjacent norms) are represented by both samples of germ cell origin

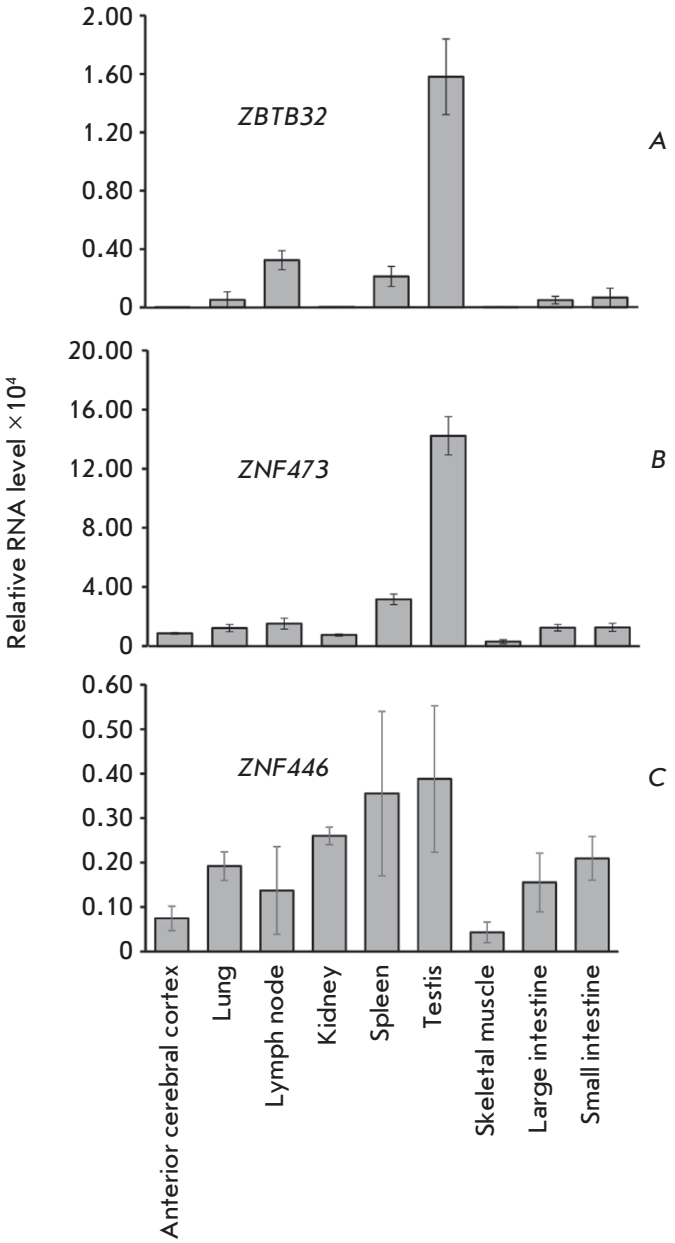

Fig. 2. Relative content of *ZBTB32* (*A*), *ZNF473* (*B*), and *ZNF446* (*C*) transcripts in various tissues. The RNA level was normalized to the geometric mean levels of the housekeeping 18S rRNA and *GAPDH* gene transcripts

(seminoma, teratoma, yolk sac tumor, embryonic cancer, and mixed tumors) and non-germ cell samples, represented by the stromal and paratesticular tumors (Leydig cell tumor, rhabdomyosarcoma, and leiomyosarcoma).

In germ-cell tumors, *ZBTB32* transcription is suppressed to an almost undetectable level (*Fig. 3A*), while *ZNF473* transcription is decreased to the values characteristic of other tissues (*Fig. 3B*). No clear patterns of changes in the *ZNF446* transcription were found during tumor formation (*Fig. 3C*).

The samples of normal tissues adjacent to germ cell tumors are characterized by a large spread in the *ZBTB32* and *ZNF473* transcription levels from values close to those in the control samples (samples 5N, 8N, and 14N) to ones characteristic of tumors (samples 7N and 21N). In paired samples with a high level of normal transcription (pairs No. 8, 14, and 32), *ZBTB32* and *ZNF473* transcription in the tumor is downregulated at least eight and three times, respectively. It should be noted that *ZNF446* transcription can be either down- or upregulated in these samples. One of the reasons for the spread in the *ZBTB32* and *ZNF473* transcription levels in the samples adjacent to a germ cell tumor may be the onset of malignant cell transformation in tissues that are morphologically defined as normal. In addition, an effect of certain tumor cell types on neighboring tissues cannot be excluded. For example, transcription of testis-specific genes of the *PIWI* family in tumor-adjacent tissue was shown to be associated with the tumor type [28]. However, no patterns were noted between the tumor type and gene transcription level in the adjacent normal tissue in the studied samples. The study of the effect of different tumors on the properties of adjacent tissues may be a promising task for future research.

There is a spread in the expression levels of *ZNF473*, *ZBTB32,* and *ZNF446* in non-germ cell tissues. Comparison of the transcript levels of these genes in non-germ tumors (samples 10T, 12T, 20T, and 33T) and adjacent normal tissues (samples 10N, 12N, 13N, and 33N) reveals multidirectional changes in the expression of all three genes during the formation of non-germ tumors and no clear patterns of changes in the transcription levels of all three genes.

In general, a significant decrease in the *ZNF473* and *ZBTB32* transcription levels is observed in tumor as compared to healthy tissue (the Mann–Whitney p-value is <0.02 in both cases and >0.4 in *ZNF446*). These genes can act as markers for germ cell-derived tumors.

To confirm these data, we compared the transcription levels of 25 previously identified genes in normal and tumor testis samples (*Table 5*) using the online resource GePIA [21]. The transcription level of most of the genes (with the exception of *ZNF728, ZNF560,* and *ZFP42*) in the tumor is reduced by more than three-fold, to values comparable to those in other tissues. The transcription level of *ZNF728* in the tumor decreases by less than two-fold, the level of *ZNF560*

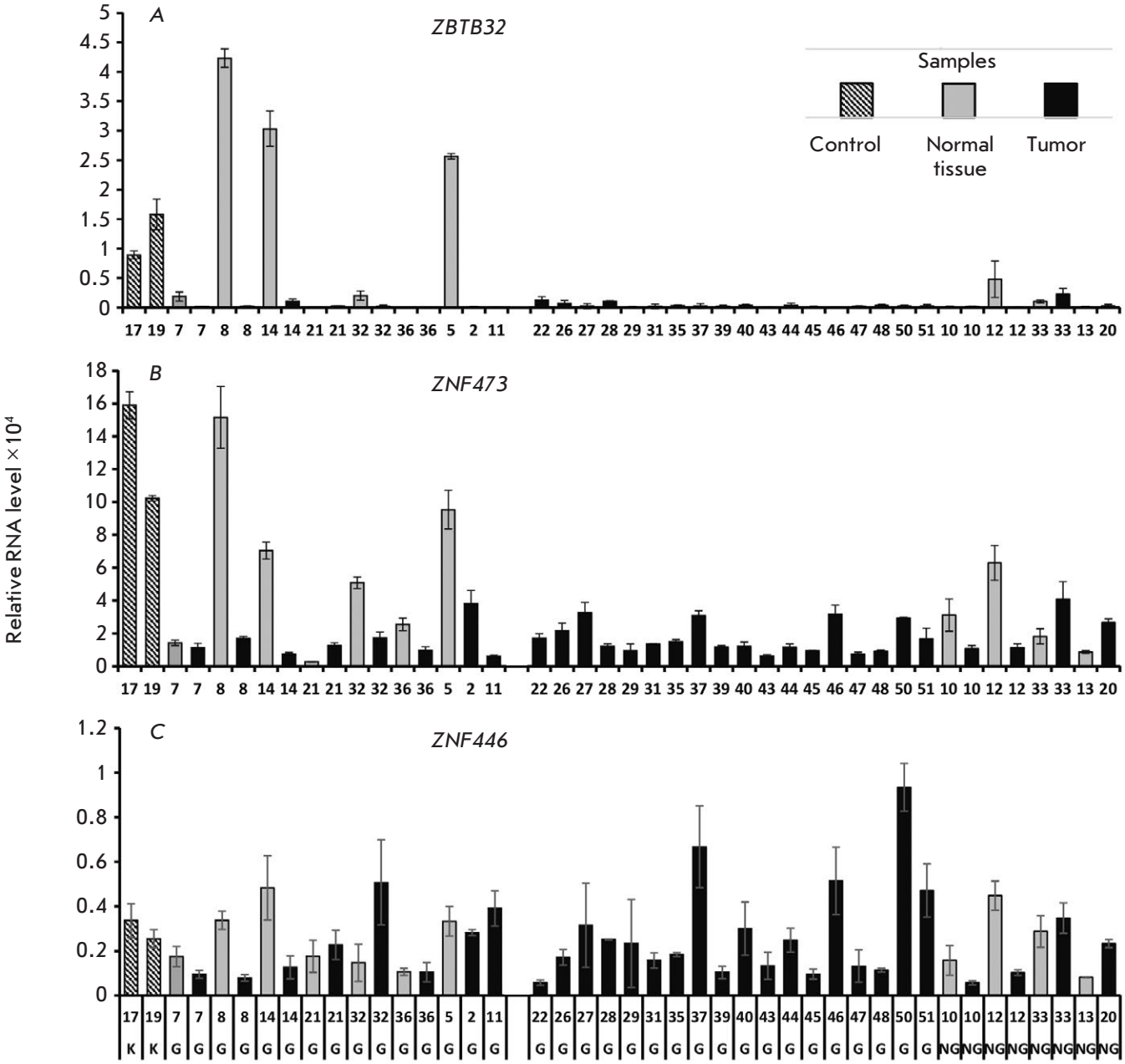

Fig. 3. Relative levels of *ZBTB32* (*A*), *ZNF473* (*B*), and *ZNF446* (*C*) transcripts in testicular tumor germ and non-germ cell samples. Control samples (healthy testicular parenchyma) are indicated by the dashed line, samples from healthy tissue adjacent to the tumor are highlighted in gray, and tumor tissue samples are marked in black. Healthy and tumor tissue samples sharing the same number belong to the same patient. The letters at the bottom stand for: K – control samples; G – germ cell tumor samples; NG – tumor samples that do not contain germ cells. The RNA level was normalized to the geometric mean levels of 18S rRNA and *GAPDH*

remains almost unchanged, while the level of *ZFP42*, on the contrary, increases by 17 times.

The results we obtained for the *ZBTB32* and *ZNF473* genes are consistent with the GePIA data. This allows us to consider other genes with similar behavior as potential markers of tumor formation in the testes, according to the GePIA. One can assume that most of the studied genes are part of the net-

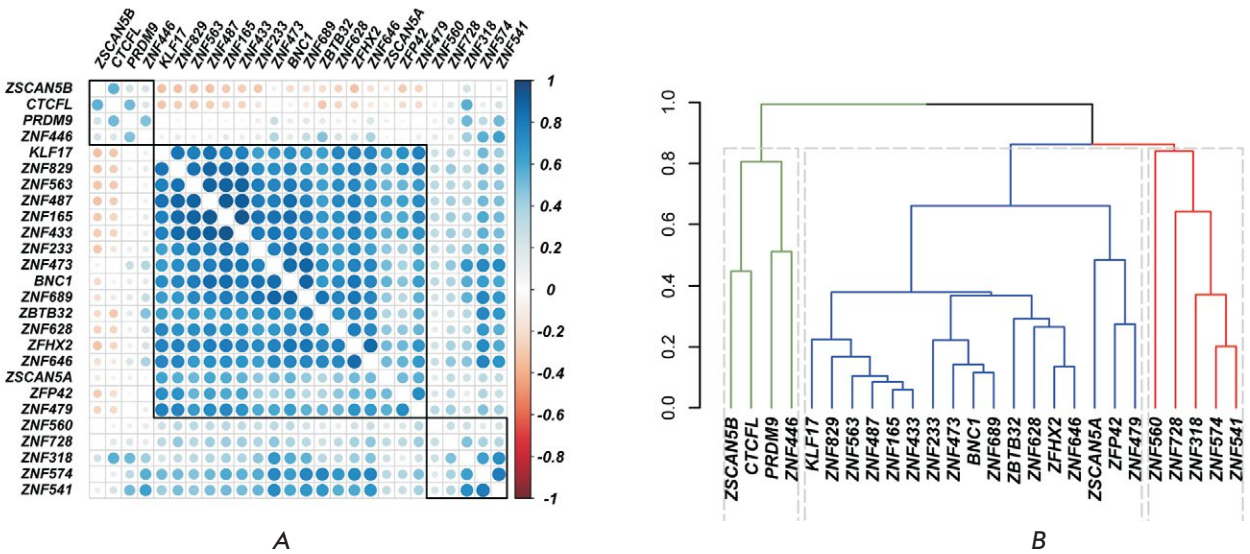

Fig. 4. Correlation matrix of the transcription levels of 25 genes selected based on their testis-specific expression and the control gene *ZNF446* in 361 testis samples from the GTEx collection (*A*). The genes are arranged according to hierarchical clustering using the complete linkage method. Cluster boundaries are outlined in black. Spearman's correlation coefficients are presented; their values are indicated by color. Dendrogram shows the consistency of gene expression (*B*). As a measure of the difference, a value equal to 1 - the Spearman correlation coefficient modulus was used. Three clusters are outlined; they are indicated by different colors; the dotted gray line indicates cluster boundaries

works of intergenic interactions responsible for the main cellular processes determining testis functions; these processes are suppressed in tumorigenesis.

In this regard, the similarity of the transcription profiles for *ZBTB32* and *ZNF473* in germline samples between normal and tumor tissue is important; it suggests the consistency of their transcription. We analyzed the transcriptional consistency of 25 selected testis-specific genes using the GTEx database containing data of large-scale RNA sequencing in 361 normal testis samples and generated a correlation matrix for them and the control *ZNF446* gene (*Fig. 4A*).

Using correlation coefficients as a measure of the distance between the genes according to the formula (1 - the correlation coefficient modulus), we created a hierarchical tree using the hierarchical classification algorithm (*Fig. 4B*). It should be noted that, when using this approach, the most "closely located" genes are the ones with an increased correlation coefficient, regardless of its sign. The optimal number of clusters is within the range of 2–3, as determined by different algorithms. There is a good correlation between different methods of hierarchical classification (correlation coefficients for cophenetic analysis exceed 0.51). When clustered by different methods, most of the genes, including *ZNF473* and *ZBTB32*, fall into one cluster, while only four genes, namely *CTCFL*, *ZSCAN5B*, *PRDM9*, and the control gene *ZNF446* falls into another cluster. Thus, most of the selected genes are consistently transcribed in the testes. The transcription levels of the genes within the same cluster are positively correlated with each other. The genes included in different clusters can be part of different branches of the gene network specific to testes and, consequently, be involved in different biological processes in testes. Establishing the position of the studied genes in the hierarchy of intergenic interactions and their relationship with intracellular processes in the testis is a massive, but promising, undertaking for future research.

DISCUSSION

The study of gene expression is of particular interest in the case of pathological processes, including malignant cell transformation. An important step is the search for genes that can be further used as diagnostic markers or objects for targeted gene therapy. Of particular interest are genes with pronounced tissue-specific expression, since they provide a specific cellular response to external and internal stimuli. In this work, we chose the family of genes encoding C2H2 zinc finger domains as the study object. This family is of particular interest, because, firstly, most of its members, due to the presence of a DNA-

Table 5. Transcription levels of testis-specific C2H2 genes in normal and tumor testis samples according to GePIA*

Gene	Normal, TPM	Tumor, TPM	Normal/ tumor ratio, times	*p*-value
ZBTB32	93.0	0.93	100.0	1.78e–77
PRDM9	4.52	0.05	90.4	7.58e–78
ZNF541	27.4	0.36	76.2	1.19e–99
KLF17	15.8	0.31	51.0	5.38e–24
CTCFL	9.11	0.20	45.6	1.60e–77
ZNF479	3.34	0,13	25.7	6.61e–39
ZFHX2	17.7	1.09	16.2	4.19e–56
ZNF487	33.0	2.48	13.3	4.01e–63
ZNF433	32.9	2.61	12.6	1.77e–75
ZSCAN5B	2.25	0.18	12.5	7.78e–45
ZNF165	21.3	2.20	9.68	2.25e–44
ZNF563	15.3	1.98	7.71	2.93e–70
ZNF473	39.1	6.37	6.14	3.95e–47
ZSCAN5A	34.6	5.94	5.83	1.09e–59
ZNF628	31.7	5.45	5.82	7.35e–45
ZNF233	9.55	1.68	5.68	1.84e–32
ZNF829	12.6	3.28	3.85	5.86e–20
ZNF646	32.7	8.83	3.70	3.21e–38
ZNF689	22.4	6.40	3.50	1.54e–33
ZNF318	46.8	14.3	3.27	7.26e–34
BNC1	19.6	6.45	3.04	3.99e–9
ZNF574	37.0	15.7	2.36	2.47e–22
ZNF728	5.86	3.44	1.70	1.94e–7
ZNF560	8.89	7.53	1.18	4.09e–2
ZFP42	2.54	43.0	0.06	2.86e–34

*Transcription medians are shown in TPM. Genes are arranged in decreasing order of the ratio of their transcription levels in normal tissue and tumor. Nine genes selected simultaneously from four databases are highlighted in bold.

binding domain, belong to transcription factors: i.e., regulatory genes, and, secondly, the large size of the family makes it likely to identify a number of peculiar patterns in their gene expression.

To date, several large databases on gene expression in various tissues and organs have been created thanks to developments in large-scale sequencing technology. It is possible to select candidate genes using user-defined algorithms to search for genes with tissue-specific expression. Databases differ in the number of and method used to obtain samples; therefore, it is important to correctly compare the obtained results when searching for and analyzing candidate genes. In this work, we performed a simultaneous analysis of four databases based on the average level of gene expression in a tissue/organ in each database. As a result, nine genes of the C2H2 family with potential testis-specific transcription were selected. Two genes, *ZBTB32* and *ZNF473*, were chosen for further analysis; their tissue-specific transcription in testicular parenchyma cells has been confirmed experimentally.

Important parameters of gene expression include its change during malignant transformation of cells. The online resource GePIA (Gene Expression Profiling Interactive Analysis) is dedicated to this type of data. The resource is based on an algorithm that allows one to compare large-scale sequencing data obtained from two sources: the GTEx collection of normal tissues and the TCGA collection of tumor tissues. According to the latter resource, transcription of *ZBTB32*, *ZNF473*, *PRDM9*, *CTCFL*, *ZNF165*, *ZNF541*, as well as a number of other genes, is downregulated in testicular germ cell tumors. Therefore, these genes can be considered as potential markers of malignant transformation of germ cells. We have experimentally confirmed a decrease in the transcription level of two selected genes (*ZBTB32* and *ZNF473*) in germ cell tumors. No clear patterns in the expression of these genes in non-germ cell tumors and adjacent normal tissues were found. The expression of these genes in normal non-germ cell tissues is initially low, and it remains at this level in non-germ cell tumors. A decrease in the transcription of these genes in germ cells can serve as a risk marker for the development of germ cell tumors. The absence of *ZBTB32* transcription can also serve as evidence of a lack of contamination of adjacent normal tissues when obtaining a tumor sample in experiments in which the purity of the tumor sample is important. However, in the latter case, additional markers are necessary to distinguish germ cell tumors from non-germ cells.

Thus, the data on gene expression accumulated in databases is of great help in the search for candidate genes that could be involved in pathological processes. Further analysis in the form of experimental confirmation of the patterns revealed *in silico*, the identification of gene functions, and position in the hierarchy of gene networks is an interesting but massive task for future research. ●

The authors are grateful to M.V. Zinovieva for the provided cDNA samples.

REFERENCES
1. Alba M.M. // Genome Biol. 2017. V. 18. P. 168.
2. Tupler R., Perini G., Green M.R. // Nature. 2001. V. 409. P. 832–833.
3. Collins T., Stone J.R., Williams A.J. // Mol. Cell. Biol. 2001. V. 21. P. 3609–3615.
4. Tadepally H.D., Burger G., Aubry M. // BMC Evol. Biol. 2008. V. 8. P. 176.
5. Kotova E.S., Akopov S.B., Sverdlov E.D., Nikolaev L.G. // Biopol. Cell. 2014. V. 30. P. 260–272.
6. Kim S., Yu N.K., Kaang B.K. // Exp. Mol. Med. 2015. V. 47. P. e166.
7. Cassandri M., Smirnov A., Novelli F., Pitolli C., Agostini M., Malewicz M., Melino G., Raschella G. // Cell Death Discov. 2017. V. 3. P. 17071.
8. Fedotova A.A., Bonchuk A.N., Mogila V.A., Georgiev P.G. // Acta Naturae. 2017. V. 9. P. 47–58.
9. Lukic S., Nicolas J.C., Levine A.J. // Cell Death Differ. 2014. V. 21. P. 381–387.
10. Najafabadi H.S., Mnaimneh S., Schmitges F.W., Garton M., Lam K.N., Yang A., Albu M., Weirauch M.T., Radovani E., Kim P.M., et al. // Nat. Biotechnol. 2015. V. 33. P. 555–562.
11. Brayer K.J., Segal D.J. // Cell. Biochem. Biophys. 2008. V. 50. P. 111–131.
12. Burdach J., O'Connell M.R., Mackay J.P., Crossley M. // Trends Biochem. Sci. 2012. V. 37. P. 199–205.
13. Aguet F., Ardlie K.G. // Curr. Genet. Med. Repts. 2016. V. 4. P. 163–169.
14. Kim P., Park A., Han G., Sun H., Jia P., Zhao Z. // Nucl. Acids Res. 2018. V. 46. P. D1031–D1038.
15. Wagner G.P., Kin K., Lynch V.J. // Theory Biosci. 2012. V. 131. P. 281–285.
16. Sambrook J., Maniatis T., Fritsch E.F. Molecular Cloning: A Laboratory Manual. Cold Spring Harbor, N.Y.: Cold Spring Harbor Lab. Press, 1987.
17. R CoreTeam. R: A language and environment for statistical computing. Vienna, Austria: R. Fdn for Statistical Computing, 2014.
18. Galili T. // Bioinformatics. 2015. V. 31. P. 3718–3720.
19. Charrad M., Ghazzali N., Boiteau V., Niknafs A. // J. Stat. Softw. 2014. V. 61. P. 1–36.
20. Brock G., Pihur V., Datta S., Datta S. // J. Stat. Softw. 2008. V. 25. P. 1–22.
21. Tang Z., Li C., Kang B., Gao G., Zhang Z. // Nucl. Acids Res. 2017. V. 45. P. W98–W102.
22. Kent W.J., Sugnet C.W., Furey T.S., Roskin K.M., Pringle T.H., Zahler A.M., Haussler D. // Genome Res. 2002. V. 12. P. 996–1006.
23. ENCODE Project Consortium // Nature. 2012. V. 489. P. 57–74.
24. GTEx Consortium // Science. 2015. V. 348. P. 648–660.
25. Uhlen M., Hallstrom B.M., Lindskog C., Mardinoglu A., Ponten F., Nielsen J. // Mol. Syst. Biol. 2016. V. 12. P. 862.
26. Gray K.A., Yates B., Seal R.L., Wright M.W., Bruford E.A. // Nucl. Acids Res. 2015. V. 43. P. D1079–D1085.
27. Pierson E., Koller D., Battle A., Mostafavi S., Ardlie K.G., Getz G., Wright F.A., Kellis M., Volpi S., Dermitzakis E.T. // PLoS Comput Biol. 2015. V. 11. P. e1004220.
28. Gainetdinov I.V., Kondratieva S.A., Skvortsova Y.V., Zinovyeva M.V., Stukacheva E.A., Klimov A., Tryakin A.A., Azhikina T.L. // Oncotarget. 2016. V. 7. P. 22439–22447.

Extracellular Vesicles Derived from Metastatic Melanoma Cells Transfer α7-nAChR mRNA, Thus Increasing the Surface Expression of the Receptor and Stimulating the Growth of Normal Keratinocytes

M. L. Bychkov[1], A. V. Kirichenko[1,2], I. N. Mikhaylova[3], A. S. Paramonov[1], M. P. Kirpichnikov[1,4], M. A. Shulepko[1], E. N. Lyukmanova[1,4*]

[1]Shemyakin-Ovchinnikov Institute of Bioorganic Chemistry, Russian Academy of Sciences, Moscow, 117997 Russia

[2]Moscow Institute of Physics and Technology, State University, Dolgoprudny, Moscow region, 141701 Russia

[3]Federal State Budgetary Institution named N.N. Blokhin National Medical Research Center of Oncology of the Ministry of Healthcare of the Russian Federation, Russia, Moscow, 115548 Russia

[4]Interdisciplinary Scientific and Educational School of Moscow University "Molecular Technologies of the Living Systems and Synthetic Biology", Faculty of Biology, Lomonosov Moscow State University, Moscow, 119234 Russia

*E-mail: ekaterina-lyukmanova@yandex.ru

Received April 29, 2022; in final form, July 27, 2022

DOI: 10.32607/actanaturae.11734

ABSTRACT **We have previously shown that extracellular vesicles secreted by metastatic melanoma cells stimulate the growth, migration, and stemness of normal keratinocytes. This study showed for the first time that extracellular vesicles secreted by the metastatic melanoma cell lines mel H, mel Kor, and mel P contain, both at the mRNA and protein levels, the α7-type nicotinic acetylcholine receptor (α7-nAChR), which is involved in the regulation of the oncogenic signaling pathways in epithelial cells. Incubation with the vesicles secreted by mel H cells and containing the highest amount of mRNA coding α7-nAChR increased the surface expression of α7-nAChR in normal Het-1A keratinocytes and stimulated their growth. Meanwhile, both of these effects disappeared in the presence of α-bungarotoxin, an α7-nAChR inhibitor. A bioinformatic analysis revealed a correlation between the increased expression of the *CHRNA7* gene coding α7-nAChR in patients with metastatic melanoma and a poor survival prognosis. Therefore, extracellular vesicles derived from metastatic melanoma cells can transfer mRNA coding α7-nAChR, thus enhancing the surface expression of this receptor and stimulating the growth of normal keratinocytes. Targeting of α7-nAChR may become a new strategy for controlling the malignant transformation of keratinocytes.**

KEYWORDS **α7-nAChR, vesicles, metastatic melanoma, keratinocytes, oncotherapy, cancer.**

ABBREVIATIONS **α7-nAChR – α7 nicotinic acetylcholine receptor; BEBM – bronchial epithelial cell growth basal medium; α-Bgtx – α-bungarotoxin; HRP – horseradish peroxidase; WST-1 – water-soluble tetrazolium salt 1.**

INTRODUCTION

Melanoma is an aggressive tumor that is formed by transformed melanocytes [1]. Melanoma progression is mediated by the secretion of extracellular vesicles (membrane-enveloped structures loaded with various proteins and nucleic acids) by tumors cells. Extracellular vesicles are involved in the transduction of oncogenic signals between tumor cells, as well as between the tumor and the surrounding tissues [2, 3]. Fibroblasts, immune cells, and keratinocytes regulate melanocyte physiology and control melanoma proliferation, invasion, and angiogenesis by the secretion of paracrine growth factors and intercellular communication [4, 5]. However, keratinocytes

can secrete mitogenic and pro-inflammatory factors under stress conditions (e.g., under photo-induced damage) [6].

We have shown previously that extracellular vesicles secreted by metastatic melanoma cells stimulate the growth, migration, and stemness of normal keratinocytes [7]. The α7 nicotinic acetylcholine receptor (α7-nAChR) is involved in the regulation of the differentiation and growth of normal keratinocytes [8]. Its activation by nicotine or nicotine derivatives contained in tobacco (nitrosamines) promotes malignant transformation of keratinocytes [9]. However, the potential involvement of α7-nAChR in the stimulation of the keratinocyte growth induced by extracellular vesicles derived from melanoma cells has not been studied yet.

Here, we demonstrated for the first time that extracellular vesicles secreted by metastatic melanoma cells contain α7-nAChR at the mRNA and protein levels. Incubation in the presence of vesicles derived from the mel H cells increased the surface expression of α7-nAChR in normal keratinocytes and stimulated their growth; these effects were not observed in the presence of α-bungarotoxin (α-Bgtx), an α7-nAChR inhibitor. These findings provide a new insight into the role of extracellular vesicles secreted by metastatic melanoma and α7-nAChR in the malignant transformation of keratinocytes.

EXPERIMENTAL

The metastatic melanoma cell lines mel H, mel Kor, and mel P were collected from patients at the N.N. Blokhin National Medical Research Center of Oncology, Ministry of Healthcare of the Russian Federation (Moscow, Russia), and characterized earlier [10]. The cells were grown in the RPMI-1640 medium (PanEco, Russia) supplemented with 10% fetal bovine serum (Cytiva, UK) and 1% penicillin/streptomycin (PanEco). To remove endogenous exosomes, fetal bovine serum was centrifuged (70 min, 120,000 *g*), filtered, and mixed with cell media. Human keratinocytes Het-1A (ATCC, USA) were cultured in the BEB medium (Lonza, Switzerland) according to the procedure described earlier [7]. Extracellular vesicles were isolated from metastatic melanoma cells using the procedure described in [7]: the cells were cultured in an exosome-depleted medium; the growth medium was centrifuged sequentially at 10,000 *g* (15 min, 4°C) and 120,000 *g* (70 min, 4°C). Protein complexes were removed by gel filtration using the Superdex G-250 resin (GE Healthcare, USA). Vesicle size was estimated by the dynamic light scattering (DLS) method using the DynaPro Titan instrument (Wyatt Technology, USA). Expression of the exosomal marker TSG101 in the vesicles was confirmed by Western blotting.

The nAChR subunit mRNA expression was analyzed by real-time PCR according to the procedure described earlier in [7]. Expression of the *CHRNA3, CHRNA4, CHRNA5, CHRNA7, CHRNA9, CHRNB2*, and *CHRNB4* genes (primers are listed in *Table 1*) was analyzed using a Roche LightCycler 96 amplificator (Roche, Switzerland). The mRNA level was normalized to the expression of S18 ribosomal RNA.

The presence of α7-nAChR in the extracellular vesicles at the protein level was analyzed by Western blotting [7]. After the gel electrophoresis and transfer of vesicle lysates, nitrocellulose membranes were blocked with 5% milk and incubated with primary anti-TSG101 (1 : 1000, ABIN2780037, Antibodies-Online, Germany) or anti-α7-nAChR rabbit antibodies (1 : 1000, ABIN5611363, Antibodies-Online) at 4°C overnight, washed, and incubated with HRP-conjugated anti-rabbit antibodies (1 : 5000, 111-035-003, Jackson Immunoresearch, USA) for 1 h at 20°C. The membranes were then washed, and the HRP signal was registered using the ECL substrate (Bio-Rad, USA) and an ImageQuant LAS 500 camera system (GE Healthcare, USA).

To study the effect of extracellular vesicles on keratinocyte proliferation, the cells were seeded in

Table 1. The primers used in this study

Gene	Primer		Amplicon size, bp
	Forward	Reverse	
S18 SSU RNA	CTC AAC ACG GGA AAC CTC AC	CGC TCC ACC AAC TAA GAA CG	110
CHRNA3	TGT CCC TCT CTG CTT TGT CAC	CCC AGG TTC TTG ATC GGA TGT T	169
CHRNA4	TCG TCC TCT ACA ACA AGT GAG	GGT CCA GGA GCC GAA TTT CA	199
CHRNA5	CGT CTG GTT GAA ACA GGA ATG G	ACA GTG CCA TTG TAC CTG ATG A	185
CHRNA7	TTT ACA GTG GAA TGT GTC AGA	TGT GGA ATG TGG CGT CAA G	88
CHRNA9	GGA GGC CAG ACA TCG TCT TA	CAC TGC TGG TTG TCA AAA GGG	168
CHRNB2	ATC TCC TGG ATC CTT CCC GC	AGA AGG ACA CCT CGT ACA TGC C	290
CHRNB4	CGC CTT CCC TGG TCC TTT TC	TGT TCA CAC CCT CGT AGC GG	381

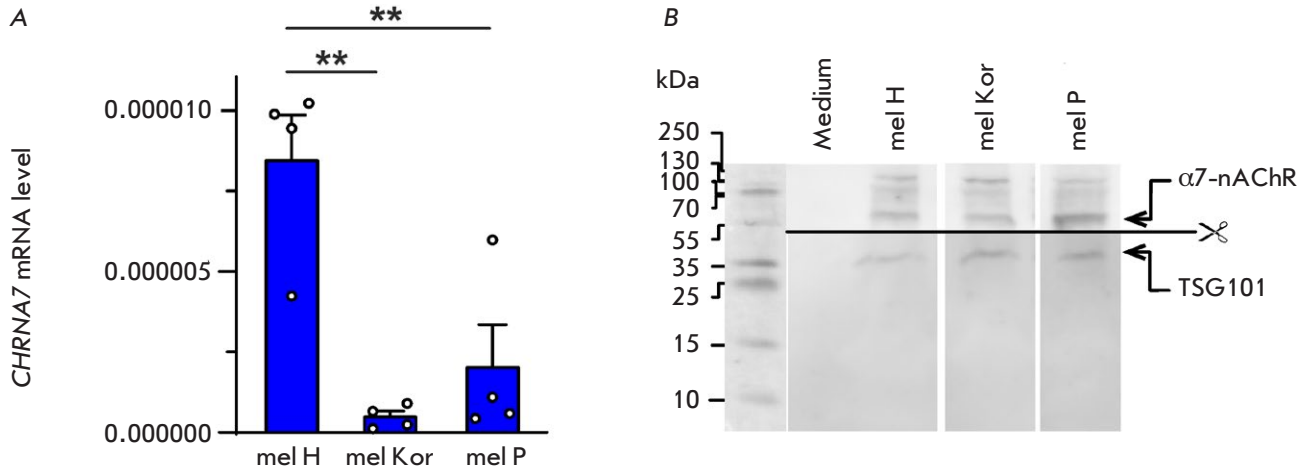

Fig. 1. Analysis of the α7-nAChR expression in extracellular vesicles derived from metastatic melanoma cells. (*A*) – Analysis of the *CHRNA7* expression in extracellular vesicles derived from mel H, mel Kor, and mel P cells. Expression of mRNA was assayed by real-time PCR and normalized to the S18 ribosomal RNA. The data are presented as the mean mRNA level ± SEM (n = 4). ** ($p < 0.01$) indicates a significant difference between the data groups according to one-way ANOVA, followed by the Tukey's post hoc test. (*B*) – Analysis of α7-nAChR protein expression in extracellular vesicles derived from mel H, mel Kor, and mel P cells by Western blotting. TSG101 was used as an exosomal marker

96-well plates (5 × 10^3 cells/well); after 24 h, they were supplemented with vesicles (total protein concentration 50 μg/ml) and/or 10 μM α-bungarotoxin (α-Bgtx, an α7-nAChR inhibitor, Tocris, UK) and additionally incubated for 72 h without media replacement. The concentration of the total vesicular protein corresponded to that in the plasma of the cancer patients (20–100 μg/mL) [7]. Cell viability was analyzed using a WST-1 colorimetric assay (Santa Cruz, USA) [11]. The data were normalized to averaged data in the control wells containing untreated cells.

The effect of the vesicles and α-Bgtx on α7-nAChR expression in keratinocytes was studied after staining the cells with TRITC-labeled α-Bgtx (Sigma-Aldrich, USA) using an Attune NxT flow cytometer (Life Technologies, USA) and the procedure described earlier [11]. The median fluorescence was normalized to the autofluorescence of unstained cells.

The correlation between the *CHRNA7* expression level in patients with metastatic melanoma from the TCGA database (the SKCM study) and the prognosis of their survival was analyzed using the Xena software [12].

RESULTS AND DISCUSSION

Extracellular vesicles secreted by melanoma cells contain microRNA, mRNA, and proteins that stimulate the proliferation, migration, and stemness of normal keratinocytes [7]. However, the recruitment of nAChRs, which regulate many oncogenic processes in epithelial cells, into these effects of extracellular vesicles has not been studied previously.

We have demonstrated by real-time PCR for the first time that extracellular vesicles secreted by patient-derived metastatic melanoma cells mel H, mel Kor, and mel P contain *CHRNA7* mRNA encoding the α7-nAChR subunit of the homopentameric receptor (*Fig. 1A*). The highest *CHRNA7* expression level was observed for vesicles secreted by mel H cells. Meanwhile, no mRNA encoding the α3, α4, α5, α9, β2, and β4 subunits of nAChR were detected. Western blotting proved that the vesicles derived from all the studied melanoma cell lines contained the α7-nAChR protein (*Fig. 1B*). Interestingly, the previous analysis of the protein composition of extracellular vesicles secreted by primary melanomas had detected no α7-nAChR [3]. Expression of this receptor can possibly be a specific feature of extracellular vesicles derived from metastatic melanoma.

We have shown earlier that extracellular vesicles secreted by metastatic melanoma mel P contain mRNA encoding the epidermal growth factor receptor (EGFR), and that incubation of normal keratinocytes in the presence of these vesicles leads to upregulated EGFR expression on the keratinocyte surface and stimulates their proliferation [7]. Here, we studied the effect of extracellular vesicles derived from metastatic melanoma mel H, mel Kor, and mel P cells on the α7-nAChR expression in normal keratinocytes. Flow cytometry revealed that only incubation in the presence of extracellular vesicles derived from mel H cells causes a statistically significant upregulation of the α7-nAChR expression on the surface of normal keratinocytes. Treatment of keratinocytes with vesicles

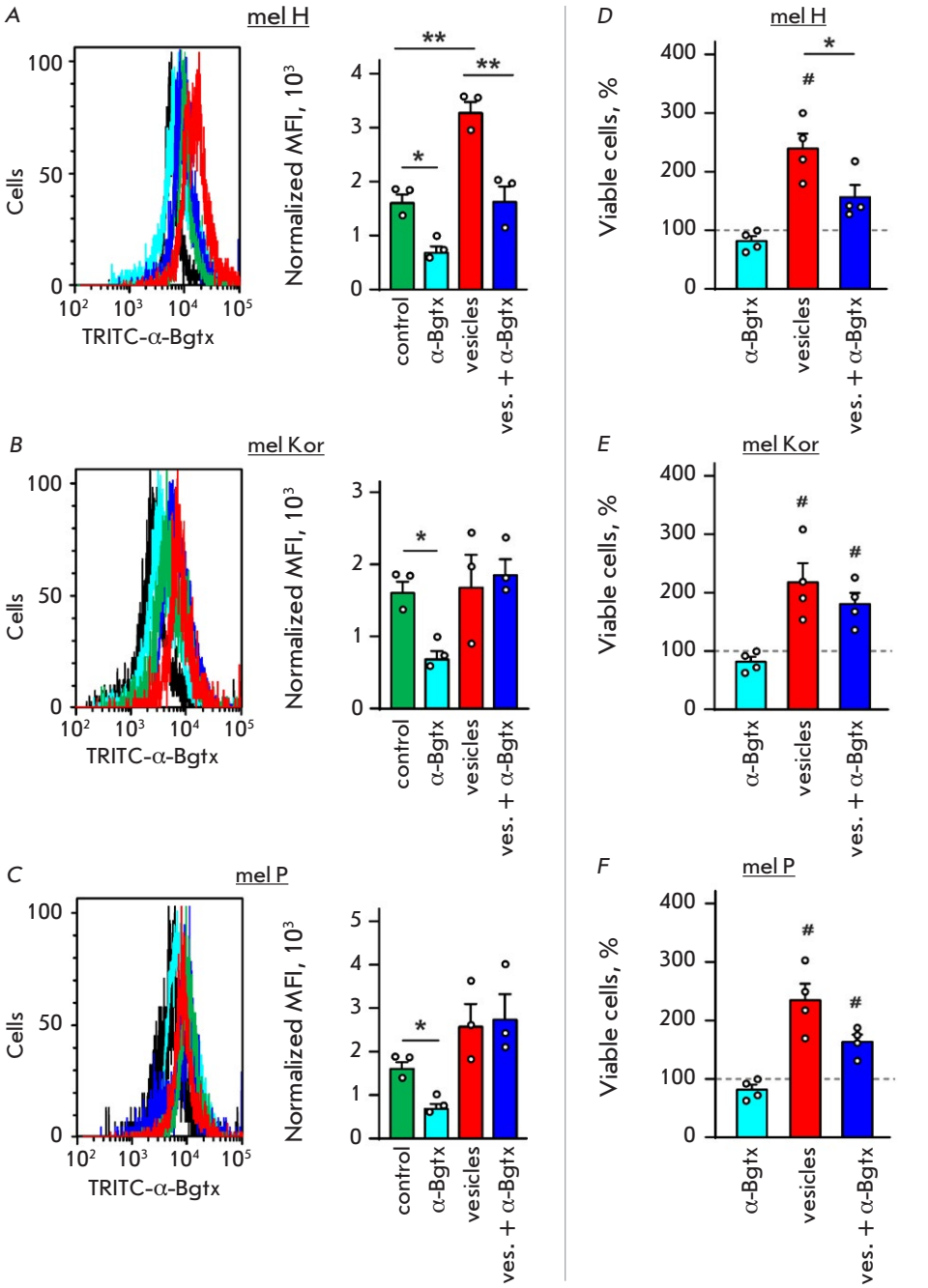

Fig. 2. Analysis of the effects of extracellular vesicles secreted by metastatic melanoma cells and α-Bgtx on the α7-nAChR expression and keratinocyte proliferation. *A–C* – Expression of α7-nAChR on the surface of normal keratinocytes incubated in the presence of extracellular vesicles derived from mel H (*A*), mel Kor (*B*), and mel P (*C*) cells and/or α-Bgtx. The data are presented as normalized median fluorescence (MFI) ± SEM (n = 3). * ($p < 0.05$) and ** ($p < 0.01$) indicate a significant difference between the data groups according to one-way ANOVA, followed by the Tukey's post hoc test. *D–F* – The effects of extracellular vesicles derived from mel H (*D*), mel Kor (*E*), and mel P (*F*) cells and/or α-Bgtx on the proliferation of normal keratinocytes. The data are % of untreated cells ± SEM (n = 4). # ($p < 0.05$) indicates a significant difference from the untreated cells according to the one-sample t-test. * ($p < 0.05$) indicates a significant difference between the data groups according to one-way ANOVA, followed by the Tukey post hoc test

derived from mel Kor and mel P had no effect on the expression level of the receptor (*Fig. 2A–C*). The results are consistent with the PCR data showing that the highest *CHRNA7* expression level is actually observed in vesicles derived from mel H cells (*Fig. 1A*). It is plausible that vesicles derived from metastatic melanoma cells mel H transfer mRNA encoding α7-nAChR to keratinocytes, thus increasing the expression of this receptor in normal cells. Interestingly, incubation in the presence of α-Bgtx, an inhibitor of α7-nAChR, reduced the expression of this receptor on the keratinocyte surface (*Fig. 2A–C*) both in the presence and absence of vesicles derived from mel H cells, pointing to some positive feedback between the receptor activity and its expression.

In all the cases, incubation with vesicles derived from the mel H, mel Kor, and mel P cells significantly increased the number of viable keratinocytes (*Fig. 2D–F*). However, α-Bgtx cancelled the mitogenic effect induced only by mel H-derived vesicles and this correlates with the fact that incubation of keratinocytes with vesicles from mel Kor and mel P caused no changes in the α7-nAChR expression in keratinocytes (*Fig. 2B,C*). It is noteworthy that incubation

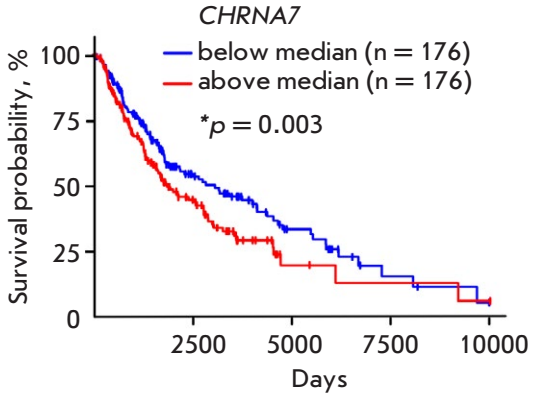

Fig. 3. Bioinformatic analysis of the correlation between the survival of patients with metastatic melanoma and the *CHRNA7* expression level. Patients were divided into two groups with the gene expression levels above and below the median value. Statistical analysis of patient survival was performed by the Kaplan–Meier method using the log-rank test

with α-Bgtx in the absence of vesicles did not significantly reduce the number of viable keratinocytes (*Fig. 2D–F*), although the toxin significantly reduced the expression of the receptor (*Fig. 2A–C*). This indicates that keratinocyte growth is independent of the α7-nAChR regulation under normal conditions, but transfer of the *CHRNA7* gene by the vesicles from mel H cells significantly increases the receptor expression in keratinocytes, thus additionally stimulating their proliferation. It seems that, although expression of the α7 receptor is comparable in all the analyzed types of vesicles (*Fig. 1B*), *CHRNA7* mRNA is the principal transferred component that stimulates keratinocyte growth in the presence of vesicles. Other factors unrelated to α7-nAChR (e.g., EGFR mRNA) are probably responsible for the increased keratinocyte proliferation observed upon incubation with vesicles from the mel Kor and mel P cells [7].

In order to understand how the *CHRNA7* expression level can affect the development of oncogenic processes and, particularly, correlate with cell malignancy, we performed a bioinformatic analysis of the expression of this receptor in biopsy specimens taken from patients with metastatic melanoma. A Kaplan–Meier analysis showed that the upregulated *CHRNA7* expression icorrelates with an unfavorable survival prognosis in patients with metastatic melanoma (*Fig. 3*). Our findings indicate that α7-nAChR is potentially involved in the pathogenesis of metastatic melanoma, and that transfer of mRNA encoding this receptor within extracellular components can be a mechanism responsible for the stimulation of tumor progression.

CONCLUSIONS

Expression of α7-nAChR, both at the mRNA and protein levels, was detected for the first time in extracellular vesicles secreted by different lines of metastatic melanoma cells. Extracellular vesicles derived from the mel H cells demonstrating the highest *CHRNA7* expression were shown to transfer receptor mRNA to normal keratinocytes, thus increasing the α7-nAChR expression on their surface and stimulating their growth. Since no such effect of vesicles derived from the mel H cells was observed in the presence of α-Bgtx, it is a promising strategy to target α7-nAChR to control the malignant transformation of normal keratinocytes. ●

This work was supported by the Russian Science Foundation (project No. 17-74-20161).

REFERENCES

1. Dratkiewicz E., Simiczyjew A., Mazurkiewicz J., Ziętek M., Matkowski R., Nowak D. // Cells. 2021. V. 10. № 4. P. 862.
2. Tucci M., Mannavola F., Passarelli A., Stucci L.S., Cives M., Silvestris F. // Oncotarget. 2018. V. 9. № 29. P. 20826–20837.
3. Boussadia Z., Lamberti J., Mattei F., Pizzi E., Puglisi R., Zanetti C., Pasquini L., Fratini F., Fantozzi L., Felicetti F., et al. // J. Exp. Clin. Cancer Res. 2018. V. 37. № 1. P. 245.
4. Falcone I., Conciatori F., Bazzichetto C., Ferretti G., Cognetti F., Ciuffreda L., Milella M. // Cancers (Basel). 2020. V. 12. № 10. P. 2870.
5. Villanueva J., Herlyn M. // Curr. Oncol. Rep. 2008. V. 10. № 5. P. 439–446.
6. Hachiya A., Kobayashi A., Yoshida Y., Kitahara T., Takema Y., Imokawa G. // Am. J. Pathol. 2004. V. 165. № 6. P. 2099–2109.
7. Bychkov M.L., Kirichenko A.V., Mikhaylova I.N., Paramonov A.S., Yastremsky E.V., Kirpichnikov M.P., Shulepko M.A., Lyukmanova E.N. // Biomedicines. 2022. V. 10. № 3. P. 660.
8. Shulepko M., Bychkov M., Kulbatskii D., Lyukmanova E. // Rus. J. Bioorg. Chem. 2019. V. 45. № 2. P. 66–75.
9. Arredondo J., Chernyavsky A.I., Grando S.A. // Life Sci. 2007. V. 80. № 24–25. P. 2243–2247.
10. Mikhaîlova I.N., Lukashina M.I., Baryshnikov A.I., Morozova L.F., Burova O.S., Palkina T.N., Kozlov A.M., Golubeva V.A., Cheremushkin E.A., Doroshenko M.B., et al. // Vestn. Ross. Akad. Med. Nauk. 2005. № 7. P. 37–40.
11. Lyukmanova E., Bychkov M., Sharonov G., Efremenko A., Shulepko M., Kulbatskii D., Shenkarev Z., Feofanov A., Dolgikh D., Kirpichnikov M. // Br. J. Pharmacol. 2018. V. 175. № 11. P. 1973–1986.
12. Goldman M.J., Craft B., Hastie M., Repečka K., McDade F., Kamath A., Banerjee A., Luo Y., Rogers D., Brooks A.N., et al. // Nat. Biotechnol. 2020. V. 38. № 6. P. 675–678.

Morphological Characterization of Astrocytes in a Xenograft of Human iPSC-Derived Neural Precursor Cells

D. N. Voronkov[1*], A. V. Stavrovskaya[1], A. S. Guschina[1], A. S. Olshansky[1], O. S. Lebedeva[2], A. V. Eremeev[2], M. A. Lagarkova[2]

[1]Research Center of Neurology, Moscow, 125367 Russia

[2]Federal Research and Clinical Center of Physical Chemical Medicine of the Federal Medical and Biological Agency of the Russian Federation, Moscow, 119435 Russia

[*]E-mail: voronkov@neurology.ru

Received March 28, 2022; in final form, August 22, 2022

DOI: 10.32607/actanaturae.11710

ABSTRACT **Transplantation of a mixed astrocyte and neuron culture is of interest in the development of cell therapies for neurodegenerative diseases. In this case, an assessment of engraftment requires a detailed morphological characterization, in particular an analysis of the neuronal and glial populations. In the experiment performed, human iPSC-derived neural progenitors transplanted into a rat striatum produced a mixed neuron and astrocyte population *in vivo* by the sixth month after transplantation. The morphological characteristics and neurochemical profile of the xenografted astrocytes were similar to those of mature human astroglia. Unlike neurons, astrocytes migrated to the surrounding structures and the density and pattern of their distribution in the striatum and cerebral cortex differed, which indicates that the microenvironment affects human glia integration. The graft was characterized by the zonal features of glial cell morphology, which was a reflection of cell maturation in the central area, glial shaft formation around the transplanted neurons, and migration to the surrounding structures.**

KEYWORDS **iPSC, neural precursors, transplantation, striatum, astrocytes.**

ABBREVIATIONS **iPSCs – induced pluripotent stem cells; PBS – phosphate buffered saline; 6-OHDA – 6-hydroxydopamine.**

INTRODUCTION

Transplantation of human iPSC-derived neurons and astrocytes to experimental animals is used not only to develop cell therapies, but also to actively study the pathogenesis of neurodegenerative diseases and various aspects of cell-to-cell interactions [1, 2].

There are a large number of protocols with varying degrees of efficiency for the targeted differentiation of human iPSC-derived neural stem cells into neurons with a specific phenotype, in particular midbrain dopaminergic neurons [3–8]. Variations in exposure time, various combinations, and factor ratios significantly affect the differentiation efficiency and percentage of formed dopamine neurons [8, 9]. In this case, only neural precursors can be effectively transplanted into the brain of laboratory animals, because mature neurons are easily damaged. However, early neural progenitors are not yet committed to a specific neuronal fate, their differentiation is poorly predictable, and uncontrolled graft proliferation is also possible. In addition, differentiation of even homogeneous clones in the transplantation area depends on the host microenvironment [10]. All this necessitates control over iPSC-derived neuron differentiation and a morphological analysis of the proliferation and migration of graft cells.

Transplantation of a mixed astrocyte and neuron culture (co-grafting) is of considerable interest, because several studies have shown that the approach is associated with better graft survival and an increased therapeutic effect [11, 12]. Astrocytes are required for the formation of the environment (scaffold) of transplanted cells, to promote growth of their neurites, and participate in the synaptogenesis of and energy supply to the graft [13]. In addition, there are data on a positive effect of astrocyte monoculture transplantation on models of neurodegenerative diseases, which is apparently due to the

action of the growth factors produced by astroglia [13–16].

In this study, we used neural progenitor cultures produced at the Laboratory of Cell Biology of the Federal Research and Clinical Center of Physical–Chemical Medicine of the Federal Medical and Biological Agency. Transplantation to animals was performed in a series of experiments on the transplantation of neural progenitors committed to dopaminergic neurons for Parkinson's disease simulation.

The aim of this study was to characterize morphologically and evaluate the migration of the glial cells present in a culture of human iPSC-derived neural progenitors 6 months after their transplantation into the brain of rats.

EXPERIMENTAL

Generation of cell cultures

The neuron culture for transplantation was differentiated from the iPSCs of a healthy donor (without neurological pathologies), which were derived from the skin fibroblasts of a male donor (age, 60 years) who had signed an informed consent. The used IPSRG4S iPSC line had a normal karyotype and had been previously characterized according to generally accepted standards [17].

Differentiation of the iPSCs

The iPSCs were detached from the substrate using a trypsin solution and seeded at a density of 40,000 cells/cm^2 in a mTeSR1 medium supplied with a 5 μM ROCK inhibitor. Upon reaching a density of about 80–90%, the mTeSR1 medium was replaced with a neuronal differentiation medium (14 days, medium change every other day). The produced neural progenitors were detached from the substrate with a Versen solution via incubation of the cells in a CO_2 incubator at 37°C for 10 min and centrifuged at 240 *g* for 5 min. The cells were plated (at a density of 4 × 10^5 cells/cm^2) onto Matrigel-coated Petri dishes and cultured in a neural progenitor culture medium for 10 days (medium change every other day). After 10 days, the cells were passaged (4 × 10^5 cells/cm^2) and cultured in the same medium. At the second passage, the cells were detached from the substrate using a 0.01% trypsin solution which was inactivated with a DMEM medium containing 10% fetal bovine serum. The cells in suspension were counted, washed with physiological saline (centrifuged at 240 *g* for 5 min), re-suspended in saline to a concentration of 3.5 × 10^5 cells per 10 μL, and used for the transplantation. The cell dose chosen for the transplantation into the rat striatum was consistent with that reported earlier [3]. iPSC neural differentiation medium: DMEM/F12, 2% serum replacement, 1% N2 supplement, 21 mM glutamine, 50 U/mL penicillin/streptomycin, 10 μM SB431542, 2 μM dorsomorphin, and 0.5 μM LDN-193189. Neural progenitor culture medium: DMEM/F12 1 : 1 Neurobasal, 2% B27 supplement, 2 mM glutamine, 50 U/mL penicillin/streptomycin, 100 ng/mL Shh, 100 ng/mL FGF8, and 2 μM purmorphamine.

Animals and stereotaxic procedures

Zoletil-100 at a dose of 30 mg/kg of body weight and xylanite at a dose of 3 mg/kg intramuscularly were used for anesthesia; atropine at a dose of 0.04 mg/kg subcutaneously was used for premedication, 10–15 min before administration of xylanite. We used 6 male Wistar rats (age, 3.5 months; body weight, 300–350 g) provided by the Stolbovaya nursery. Before administration of a cell suspension, the rats received unilateral stereotaxic intranigral injections of 12 μg of 6-OHDA in 3 μL of a 0.05% ascorbic acid solution at the Paxinos rat brain atlas coordinates (AP = –4.8; L = 2.2; V = 8.0) to simulate the parkinsonian syndrome. Twenty-one days after 6-OHDA administration, a suspension of 3.5 × 10^5 cells in 10 μL of physiological saline was injected into the striatum (AP = –0.9; L = 2.5; V = 5.5) on the side of the damaged dopaminergic terminals. The suspension was loaded into a 10 μL Hamilton microsyringe equipped with a ga26S/51mm needle and injected at a constant rate for 7 min (about 1.5 μL/min). After the injection, the needle was left at the injection site for 1 min and then slowly removed. The same volume of saline was injected into the contralateral caudate nucleus. One day before cell transplantation and then daily throughout the experiment, the animals received cyclosporine at a dose of 15 mg/kg.

Immunohistochemistry

For a immunomorphological assessment of the graft, the animals were withdrawn from the experiment 6 months after cell grafting. The brain was removed and fixed in 10% formalin for 24 h. Samples were soaked in sucrose and frozen in OCT. Frontal sections (10 μm thick) were prepared using a Tissue Tek Sakura cryostat. Before applying antibodies, the sections were heated in a double boiler (15 min, citrate buffer, pH 6.0). The cooled sections were washed with buffer (PBS, 0.01 M, pH 7.2) and incubated with primary antibodies in a humid chamber at room temperature for 18 h (*Table 1*).

To confirm the differentiation of neurons in the graft, we also used anti-human neuron-specific enolase (NSE, Leica) and anti-tyrosine hydroxylase (TH,

Table 1. The antibodies used in the study

Abbreviation	Protein, name, synonyms	Specificity*	Localization
GFAP	Glial fibrillary acidic protein	Hm, Rt	Astrocytes
AQP4	Aquaporin-4	Hm, Rt	Astrocyte end-feet
ALDH1L1	10-formyl tetrahydrofolate dehydrogenase	Hm, Rt	Astrocytes
Vim	Vimentin	Hm, Rt	Immature astrocytes, activated astroglia
PGP 9.5	Ubiquitin carboxy-terminal hydrolase 1	Hm, Rt	Neurons
IBA1	Allograft inflammatory factor 1 (AIF1)	Hm, Rt	Microglia
C3	Complement component C3	Hm, Rt	Glia, neurons
ki67	Proliferation marker (Ki-67)	Hm, Rt	Dividing cells
GS-r	Glutamine synthetase	Rt	Astrocytes, oligodendroglia
MHC-I	Major histocompatibility complex class I	Hm	Human cells
MTC-h	80 kDa mitochondrial outer membrane marker, MTCO2	Hm	Human cells
HNA	Human nuclear antigen	Hm	Human cells

*Hm – human; Rt – rat.

Sigma, USA, T8700) antibodies. The cell culture was stained for beta-3-tubulin (anti-TUJ1 antibodies, Nordic Biosite, Sweden) to detect neural progenitors.

Antibody specificity and midbrain astrocyte morphology were evaluated in midbrain autopsy samples derived from patients (n = 4; age, 52 to 82 years) without a history of neurological pathology, which were received from the archives of the Laboratory of Neuromorphology of the Research Center of Neurology.

Sections were analyzed for antibody binding using fluorescent and peroxidase techniques. In the immunofluorescent technique, anti-rabbit or mouse immunoglobulin goat or donkey antibodies labeled with Atto 488 or Atto 555 fluorochromes (Invitrogen, USA) were used. The sections were embedded in a Fluoroshield medium containing DAPI. An anti-mouse HRP detection system (Nordic Biosite) kit was used in the immunoperoxidase technique.

Morphometry

For this study, a Nikon Eclipse Ni-u or Nikon SMZ-18 fluorescent microscope with an appropriate set of filters was used. Morphometry was performed using the ImageJ software. We used 6–12 serial sections of the graft area from each animal, which were made at an interval of 70–100 μm. At least 5 fields of view per section in the area of interest were used for cell counting. At least 50 cells from each sample were used to assess the size of astrocytes. To evaluate the density of the astrocytes, the cells were manually selected in the image, and their number was counted in the microscope field of view (48,000 μm^2). For the distribution analysis, all glial cells were marked in section images and mean values for six animals were determined. The spatial distribution diagram was plotted using the Python Plotly library. The area occupied by astrocytic processes was defined as a convex polygon connecting the tips of the distal processes (convex hull area). The spatial distribution of astroglia was evaluated using the Clark–Evans (CE) aggregation index [18], which is based on the nearest neighbor cell distance; in this case, CE = 1 is for a random distribution, CE < 1 is for the clustering of objects, and CE > 1 is for a uniform distribution. The aggregation index was calculated using the R programming language and spatstat library.

Statistical analysis

The data from each animal were averaged. Groups were compared using repeated measures ANOVA with a Tukey's post-hoc test; differences were considered statistically significant at $p < 0.05$. Statistical processing was performed using the Statistica 7.0 and GraphPad Prism software. Data are presented as a mean ± standard deviation (SD).

Bioethics

The experiments were performed in accordance with international rules on the use of laboratory animals, in compliance with bioethical standards, and a possible reduction in the number of used animals. Permission of the ethics committee for the research: Protocol No. 10-7/20 of November 27, 2020.

RESULTS

Both beta-3-tubulin-positive and beta-3-tubulin-negative cells were found in the culture (*Fig. 1A*). The presence of mature neurons containing human NSE and neurons containing tyrosine hydroxylase was confirmed in grafts in all cases (*Fig. 1B,C*), which indicates the differentiation of transplanted neural progenitors into midbrain neurons.

Double staining of sections with species-specific antibodies to the mitochondrial protein MTCO2(hm) revealed both bodies and processes of non-neuronal cells in the grafts. In addition, antibodies to human nuclear antigen (HNA) and species-specific antibodies to glutamine synthetase (GS-r) binding to the rat protein were used to distinguish between human and rat cells.

Transplanted human neurons (expressing PGP 9.5, NSE, and TH mature neuronal markers and having HNA-positive nuclei) were detected along the entire needle track in the cerebral cortex, striatum, and corpus callosum. In this case, bulky clusters of neurons were found in the corpus callosum area and at the border of structures (*Fig. 1B*), which is probably associated with "spreading" of an introduced cell suspension along the gray and white matter boundaries due to their different densities. Three zones were identified in the graft area (*Fig. 2A,B*): 1) the central area containing densely packed human neurons directing their processes mainly along the needle track or nerve fibers in the corpus callosum; 2) the glial shaft area formed by rare neurons, densely packed astrocytes, and the entanglement of their numerous processes; and 3) the lateral area where human neurons were not detected.

Both human and rat astrocytes were found in the central graft area and its astrocytic shaft (*Fig. 2C*), with the proportion of human astrocytes (GFAP-positive, GS-r-negative) accounting for 58.7 ± 9.9% of their total number in the field of view. In addition, vimentin-positive astrocytes, with their processes directed mainly along the needle track, were found in the central area (*Fig. 2D*). Because these cells were not found at the graft periphery, we suggest that their presence indicates continued differentiation of transplanted cells even by the sixth month after transplantation. In the central area, both a moderate amount of activated microglia with thickened processes and single macrophages were found (*Fig. 2D*).

Outside the central graft area, the identified human cells (HNA- and MTC-h-positive) expressed mature astrocyte markers such as GFAP, ALDH1L1, and AQP4 (*Fig. 3A,B,C*).

An analysis of the proliferative activity did not reveal Ki67-positive GFAP-containing cells (*Fig. 3D*). Single (per section) Ki67-positive human cells (containing MTC-h) were found in the central and lat-

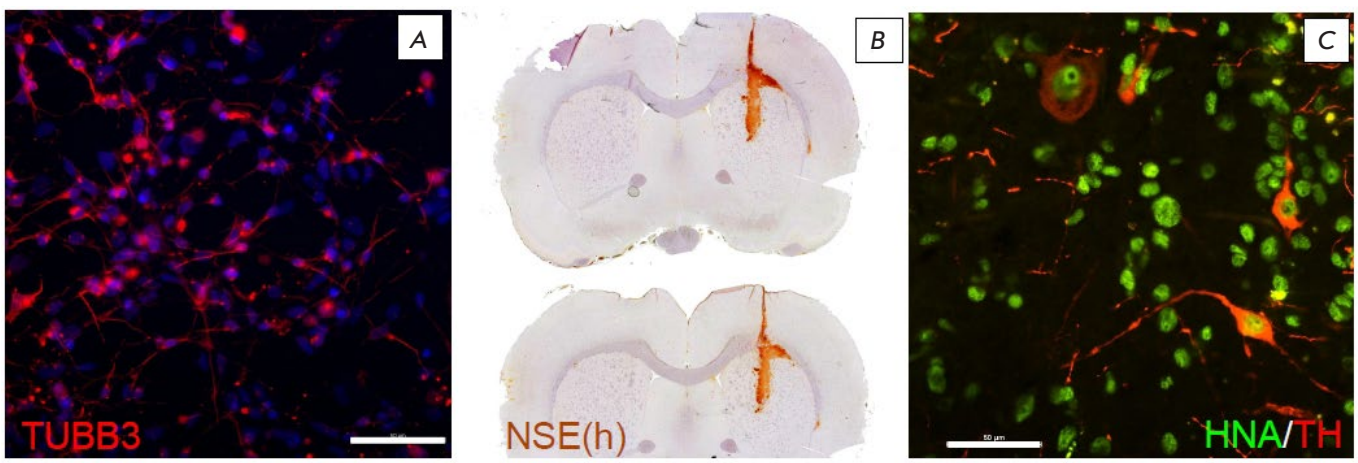

Fig. 1. Neural markers in the IPSC culture and in the graft. (*A*) Beta-3-tubilin in culture (TUBB3, red). (*B*) Human neuron-specific enolase (NSE) in the graft area (immunoperoxidase staining). (*C*) Human tyrosine hydroxylase-positive neurons in the graft (HNA, green; TH, red). Scale bar: (*A*), (*C*), 50 μm

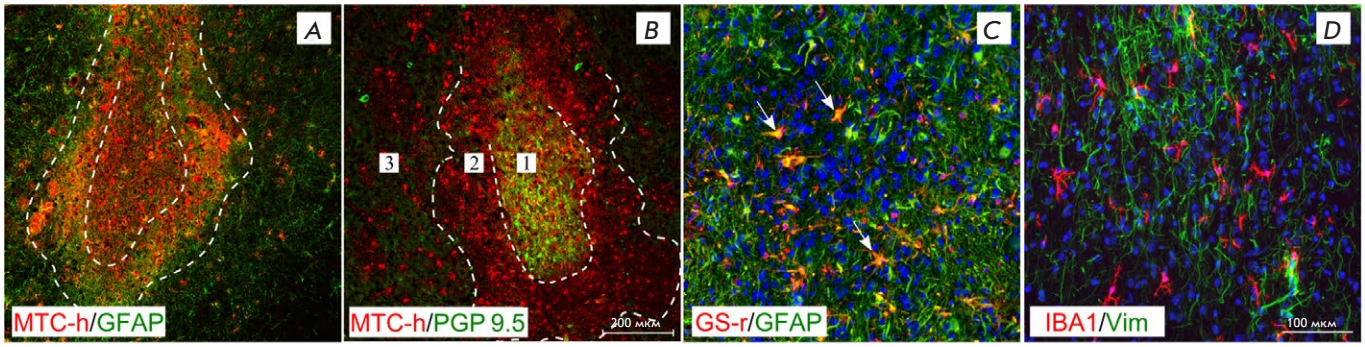

Fig. 2. Glial-neural organization of the graft 6 months after transplantation. (*A*) Human cell graft area in the striatum; GFAP staining (green) and MTC-h staining (red). (*B*) Human cell graft area in the striatum, PGP 9.5 staining (green) and MTC-h staining (red). (*C*) Human (green, GFAP) and rat (orange, GFAP/GS-positive cells, indicated by arrows) astrocytes in the graft area. (*D*) Vimentin-positive astrocytes (green) and microglia (red) in the graft area. The boundaries of the selected areas in (*A*) and (*B*) are denoted with a dashed line: *1* – central area; *2* – glial scar area; *3* – lateral area. Scale bar: (*A*), (*B*), 200 μm; (*C*), (*D*), 100 μm

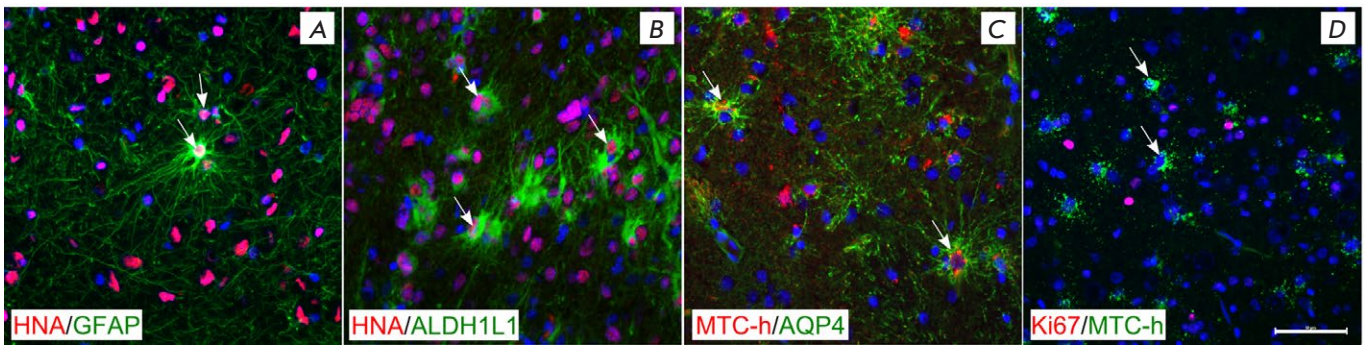

Fig. 3. Expression of glial markers in the transplanted cells. (*A*) GFAP-containing astrocyte in the central graft area. (*B*) ALDH1L1-containing astrocytes in the central graft area. (*C*) AQP4 localization on the human astrocytic processes in the lateral area. (*D*) Lack of Ki-67-positive human cells in the lateral graft area. Human astrocytes are indicated by arrows. Scale bar: (*A*), (*B*), (*C*), (*D*), 100 μm

eral graft areas. In general, both the neurochemical profile and the morphology of the identified human astrocytes were similar to those of mature functional astrocytes.

Human astrocytes were morphologically different from rat astrocytes: they had more thin processes without marked polarization (*Fig. 4A,B,C*). Their endfeet often wrapped around the vessels. The morphology of the transplanted astrocytes was similar to that of human midbrain astrocytes (*Fig. 4D*). The area occupied by the processes of transplanted human astrocytes (convex) was significantly larger than that of the rat astrocytes and was close in value to that of midbrain astrocytes (in the substantia nigra area) in an autopsy of a human brain (*Fig. 4 A,B,C*).

To assess the severity of the reactive changes, we performed staining for complement component C3, which revealed that rat astrocytes in the scar region (on the contralateral side of the transplantation area) had high expression of C3, which was localized in thickened deformed processes. In addition, the bodies of human astrocytes were often hypertrophied in the glial shaft area and the processes were thickened, which indicates reactive changes. However, at a distance from the glial shaft, most astrocytes had smaller sized bodies and thin processes. Some astrocytes were intensively stained for human MHC-I in the glial shaft area (*Fig. 5C*), which indicates their reactive changes. The transplanted astrocytes in the glial shaft area often contained C3, but it was localized mainly

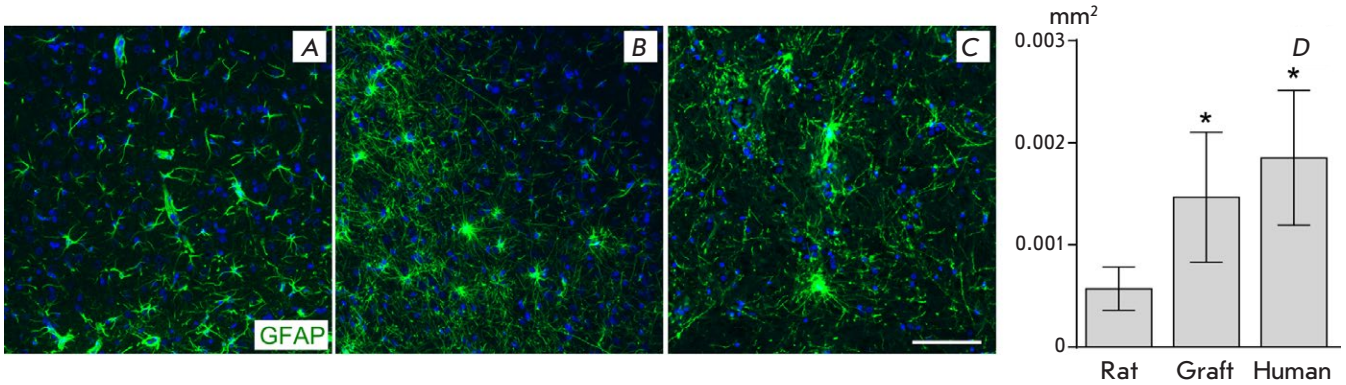

Fig. 4. Size and morphology of GFAP-containing rat astrocytes (*A*), transplanted human astrocytes (*B*), and human midbrain astrocytes (*C*). Evaluation of the area occupied by astrocyte processes (*D*). Scale bar: (*A*), (*B*), (*C*), (*D*), 100 μm. *ANOVA, a post-hoc Tukey's test, $p < 0.05$ compared with rat astrocytes

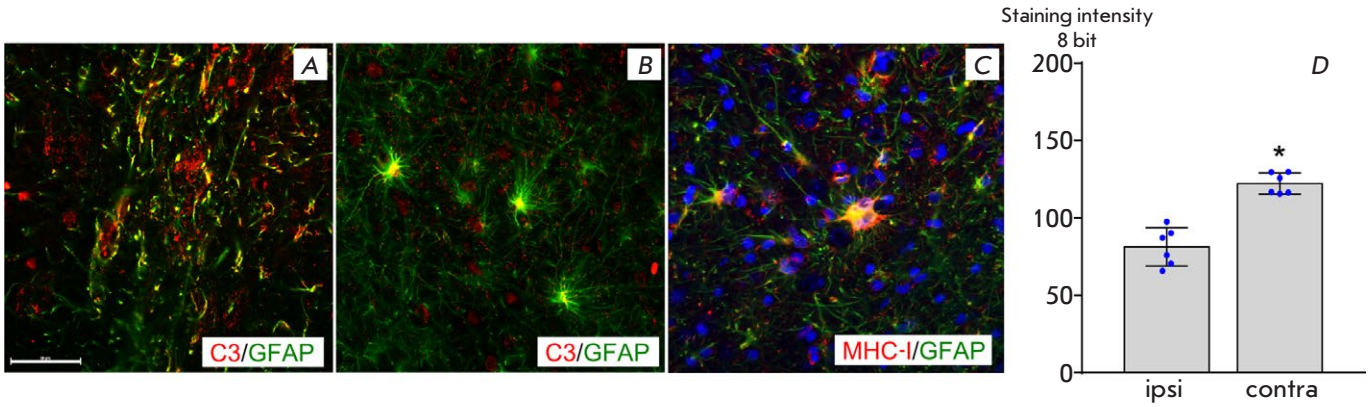

Fig. 5. Neuroinflammatory marker expression in the astrocytes. (*A*) Localization of complement component C3 in the processes of reactive rat astrocytes in the saline injection area (contralateral hemisphere), GFAP (green), C3 (red). (*B*) Localization of complement component C3 in the bodies of the transplanted human astrocytes. (*C*) Staining of the transplanted astrocytes for human MHC-I. (*D*) The staining intensity for complement component C3 is significantly lower in the area of a glial scar surrounding the graft (ipsi-) compared with that of the reactive rat astrocytes in the saline injection site on the controlateral side (contra-). * $p < 0.05$, Student's *t*-test. Scale bar: (*A*), (*B*), (*C*), 100 μm

in their bodies (*Fig. 5A,B*). An analysis of the fluorescence intensity showed that the intensity of staining for C3 in the rat astrocytes (on the side of the striatal saline injection) in the reactive gliosis area was significantly higher ($p < 0.05$, Student's test) compared with staining for C3 in the glial shaft area surrounding the graft. In addition to the expression of neuroinflammatory markers by astrocytes in the glial shaft area, it should be noted that AQP4 was distributed over the entire surface of the processes, and not only in the area of contact between the end-feet and the vessels.

An analysis of the distribution of MTC-h-positive human astrocytes outside the glial shaft showed that the highest astrocyte density was in the lateral corpus callosum (*Fig. 6B*).

Human astrocytes were found up to cortical layer V and in the striatum, mainly in its dorsolateral part. Mapping of the distribution of human astrocytes revealed different directions of migration, depending on the microenvironment. For example, there were two main pathways for the spread of transplanted astroglia: one front moved laterally along the corpus callosum and radially into the lower cortical layers, and the second spread from the graft area to the striatum (*Fig. 6A*). The distribution pattern of the transplanted astroglia in the rat brain was assessed using the Clark–Evans index, which significantly differed in the striatum and the cortex (*Fig. 6C*) and revealed a uniform distribution of astrocytes, without clustering, in the caudate nucleus and a random distribution in the

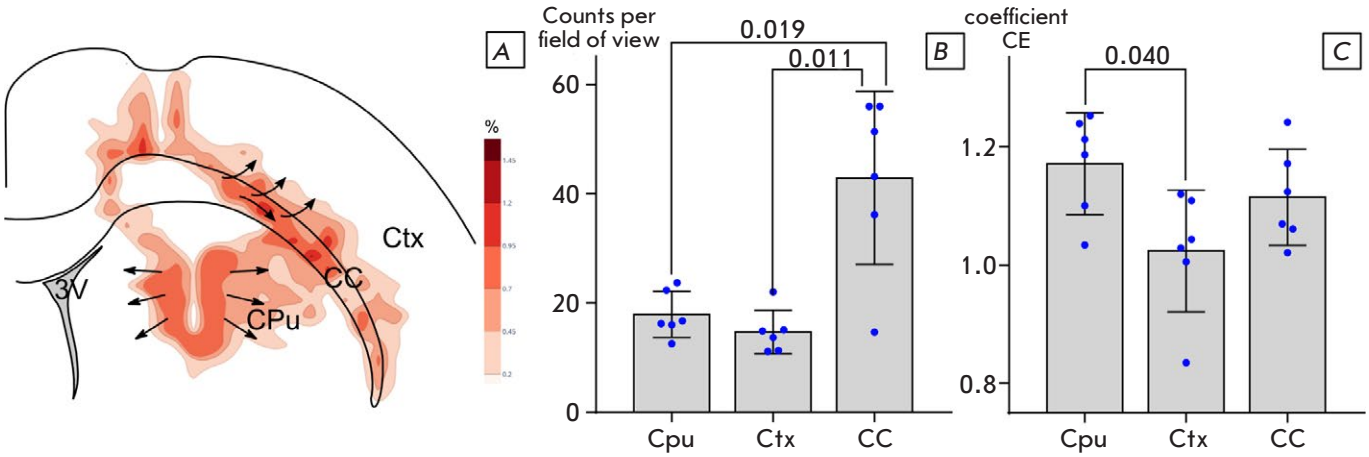

Fig. 6. Distribution of xenografted human astroglia in the rat brain structures. (*A*) Astroglia density distribution map (the darker the shading, the higher the density). (*B*) Mean density (cell number per field of view) of a human astrocyte distribution in the striatum (Cpu), cerebral cortex (Ctx), and corpus callosum (CC). (*C*) The changes in the Clark–Evans aggregation index (CE). The *p*-Values of RM ANOVA are indicatted in plots; a post-hoc Tukey's test

cortex. This indicates that the transplanted cells do not tend to form clusters (groups), which is apparently due to the lack of proliferation or its low frequency at a distance from the graft.

Therefore, in our experiment, transplanted cells derived from human iPSCs yielded a mixed neuron and astrocyte population *in vivo* by the sixth month after transplantation. The size and expressed proteins (ALDH1L1, GFAP, AQP4) of the xenografted astrocytes were similar to those of mature astroglia, except for the vimentin-positive cells present in the central area, which indicates continued astroglia maturation by the sixth month. The glial wall around the graft was formed by both rat and human astrocytes. Unlike neurons, the human astrocytes migrated to the surrounding structures, and their density and distribution pattern in the striatum and cerebral cortex differed significantly, which indicates the influence of the microenvironment on human glia integration.

DISCUSSION

After the transplantation of human glial progenitors and neural stem cells into the mouse spinal cord, the human astrocytes have been shown to migrate along myelinated tracts, partially replace host astrocytes, form functional connections with each other, and come into contact with vessels [19, 20]. The high level of AQP4 expression, which we found in the transplanted human astrocytes, is apparently associated with their migration, tissue remodeling, and the structural plasticity of glia. Increased expression of AQP4 and loss of its localization in the astrocyte end-feet are associated with cell motility; in particular, during a pathology and tumor growth [21, 22].

Early studies on fetal midbrain tissue transplantation into the striatum revealed that graft astrocytes were involved in axon guidance and the formation of neural connections with graft neurons [23]. In addition, astroglia affects, through paracrine mechanisms, neuronal growth and differentiation and synaptic contact formation. For example, co-culturing and co-transplantation of embryonic ventral midbrain-derived astrocytes and neural progenitors into animals increased the number of dopamine neurons in the graft and enhanced their chances of survival and synaptic integration [12]. Human astrocytes are characterized by a greater phenotypic diversity than rat astrocytes and a more developed tree of processes and are able to propagate calcium waves more efficiently [24], which was shown to increase the efficiency of synaptic transmission in the hippocampus in an experiment involving the transplantation of human astrocytes into a mouse brain [25].

In terms of safety in cell product transplantation, the degree of graft cell maturity and risk of teratoma formation should be assessed. An evaluation of the proliferation index alone does not allow one to differentiate tumor growth from the normal development of transplanted cells [26]. In the present study, the histological graft features meet the criteria proposed by Sugai [26] for differentiated nervous tissue, which include limited growth, cell distribution pattern, and zonal structure reflecting glial cell maturation, gli-

al shaft formation around transplanted neurons, and glial cell migration outside the graft. Our findings are consistent with data indicating migration of transplanted astrocytes to a mature brain. For example, migration of graft astrocytes occurred upon xenografting of human fetal striatal tissue into a rat brain; in this case, the proliferation index, high in the early stages, decreased by the sixth month [27]. Later, the possibility of massive migration of astrocytes upon xenografting of glial progenitors, including those derived from iPSCs, was demonstrated, which may be used to generate chimeric model animals with highly compact human astroglia [25, 28–30] for studying various aspects of neurodegenerative disease pathogenesis.

In addition to positive effects, xenografted astrocytes apparently may also have a negative influence, provoking neuroinflammation and exerting a toxic effect. The present study revealed a hypertrophy of astrocytes in the glial shaft area and the expression of complement component C3 by transplanted reactive astrocytes, and intense staining of some cells for MHC-I, which all indicate pro-inflammatory changes in glia. C3 expression is considered as a feature of neurotoxic astrocytes [31, 32]; however, the idea of a binary division of reactive astroglia into neurotoxic and neuroprotective has recently attracted criticism [33]. Different phenotypes of activated glia are distinguishable, which necessitates a more detailed functional evaluation of transplanted astrocytes. Although the reactive changes in astrocytes and glial scar formation can slow down axonal growth, astrocyte activation is associated with remodeling of the surrounding tissue and graft integration. For example, according to Tomov, a glial reaction surrounding the graft differs from the formation of a typical glial scar and is associated with the formation of the environment (glial scaffold) around the transplanted cells, in particular with graft revascularization [13].

CONCLUSION

This study has shown that the morphological features and distribution of transplanted astrocytes reflect their complex interactions with host cells and transplanted neurons. In addition to the migration and integration of transplanted astrocytes to brain structures, transplantation is accompanied by glial shaft formation and reactive changes in astroglia. The distribution features of xenografted astrocytes should be considered upon planning experiments, and control of the glial component is required in assessing the graft condition. ●

REFERENCES

1. Doss M.X., Sachinidis A. // Cells. 2019. V. 8. № 5. P. 403.
2. Bigarreau J., Rouach N., Perrier A.L., Mouthon F., Charvériat M. // Int. J. Mol. Sci. 2022. V. 23. № 3. P. 1684.
3. Kriks S., Shim J.-W., Piao J., Ganat Y.M., Wakeman D.R., Xie Z., Carrillo-Reid L., Auyeung G., Antonacci C., Buch A., et al. // Nature. 2011. V. 480. № 7378. P. 547–551.
4. Antonov S.A., Novosadova E.V. // Int. J. Mol. Sci. 2021. V. 22. № 7. P. 3381.
5. Bianchi F., Malboubi M., Li Y., George J.H., Jerusalem A., Szele F., Thompson M.S., Ye H. // Stem Cell Res. 2018. V. 32. P. 126–134.
6. Muñoz S.S., Engel M., Balez R., Do-Ha D., Cabral-da-Silva M.C., Hernández D., Berg T., Fifita J.A., Grima N., Yang S., et al. // Cells. 2020. V. 9. № 9. P. 2018.
7. Liu Y., Liu H., Sauvey C., Yao L., Zarnowska E.D., Zhang S.-C. // Nat. Protoc. 2013. V. 8. № 9. P. 1670–1679.
8. Arenas E., Denham M., Villaescusa J.C. // Development. 2015. V. 142. № 11. P. 1918–1936.
9. Engel M., Do-Ha D., Muñoz S.S., Ooi L. // Cell. Mol. Life Sci. 2016. V. 73. № 19. P. 3693–3709.
10. Tanimoto Y., Yamasaki T., Nagoshi N., Nishiyama Y., Nori S., Nishimura S., Iida T., Ozaki M., Tsuji O., Ji B., et al. // Stem Cells Transl. Med. 2020. V. 9. № 4. P. 465–477.
11. Kondo T., Funayama M., Tsukita K., Hotta A., Yasuda A., Nori S., Kaneko S., Nakamura M., Takahashi R., Okano H., et al. // Stem Cell Repts. 2014. V. 3. № 2. P. 242–249.
12. Song J.-J., Oh S.-M., Kwon O.-C., Wulansari N., Lee H.-S., Chang M.-Y., Lee E., Sun W., Lee S.-E., Chang S., et al. // J. Clin. Invest. 2017. V. 128. № 1. P. 463–482.
13. Tomov N. // Neural Regen. Res. 2020. V. 15. № 7. P. 1173–1178.
14. Proschel C., Stripay J.L., Shih C., Munger J.C., Noble M.D. // EMBO Mol. Med. 2014. V. 6. № 4. P. 504–518.
15. Nicaise C. // World J. Stem Cells. 2015. V. 7. № 2. P. 380–398.
16. Izrael M., Slutsky S.G., Admoni T., Cohen L., Granit A., Hasson A., Itskovitz-Eldor J., Krush Paker L., Kuperstein G., Lavon N., et al. // Stem Cell Res. Ther. 2018. V. 9. № 1. P. 152.
17. Holmqvist S., Lehtonen Š., Chumarina M., Puttonen K.A., Azevedo C., Lebedeva O., Ruponen M., Oksanen M., Djelloul M., Collin A., et al. // NPJ Park. Dis. 2016. V. 2. № 1. P. 16009.
18. Kendall T.J., Duff C.M., Thomson A.M., Iredale J.P. // Sci. Rep. 2020. V. 10. № 1. P. 17572.
19. Lu P., Ceto S., Wang Y., Graham L., Wu D., Kumamaru H., Staufenberg E., Tuszynski M.H. // J. Clin. Invest. 2017. V. 127. № 9. P. 3287–3299.
20. Chen H., Qian K., Chen W., Hu B., Blackbourn L.W., Du Z., Ma L., Liu H., Knobel K.M., Ayala M., et al. // J. Clin. Invest. 2015. V. 125. № 3. P. 1033–1042.
21. Smith A.J., Duan T., Verkman A.S. // Acta Neuropathol. Commun. 2019. V. 7. № 1. P. 74.
22. Vandebroek A., Yasui M. // Int. J. Mol. Sci. 2020. V. 21. № 5. P. 1603.

23. Petit A., Pierret P., Vallée A., Doucet G. // J. Neurosci. 2001. V. 21. № 18. P. 7182–7193.
24. Sosunov A.A., Wu X., Tsankova N.M., Guilfoyle E., McKhann G.M., Goldman J.E. // J. Neurosci. 2014. V. 34. № 6. P. 2285–2298.
25. Han X., Chen M., Wang F., Windrem M., Wang S., Shanz S., Xu Q., Oberheim N.A., Bekar L., Betstadt S., et al. // Cell Stem Cell. 2013. V. 12. № 3. P. 342–353.
26. Sugai K., Fukuzawa R., Shofuda T., Fukusumi H., Kawabata S., Nishiyama Y., Higuchi Y., Kawai K., Isoda M., Kanematsu D., et al. // Mol. Brain. 2016. V. 9. № 1. P. 85.
27. Hurelbrink C.B., Armstrong R.J.E., Dunnett S.B., Rosser A.E., Barker R.A. // Eur. J. Neurosci. 2002. V. 15. № 7. P. 1255–1266.
28. Windrem M.S., Schanz S.J., Morrow C., Munir J., Chandler-Militello D., Wang S., Goldman S.A. // J. Neurosci. 2014. V. 34. № 48. P. 16153–16161.
29. Benraiss A., Wang S., Herrlinger S., Li X., Chandler-Militello D., Mauceri J., Burm H.B., Toner M., Osipovitch M., Jim Xu Q., et al. // Nat. Commun. 2016. V. 7. № 1. P. 11758.
30. Preman P., Tcw J., Calafate S., Snellinx A., Alfonso-Triguero M., Corthout N., Munck S., Thal D.R., Goate A.M., De Strooper B., et al. // Mol. Neurodegener. 2021. V. 16. № 1. P. 68.
31. Liddelow S.A., Guttenplan K.A., Clarke L.E., Bennett F.C., Bohlen C.J., Schirmer L., Bennett M.L., Münch A.E., Chung W.-S., Peterson T.C., et al. // Nature. 2017. V. 541. № 7638. P. 481–487.
32. Bombeiro A.L., Hell R.C.R., Simões G.F., de Castro M.V., de Oliveira A.L.R. // Neurosci. Lett. 2017. V. 647. P. 97–103.
33. Escartin C., Galea E., Lakatos A., O'Callaghan J.P., Petzold G.C., Serrano-Pozo A., Steinhäuser C., Volterra A., Carmignoto G., Agarwal A., et al. // Nat. Neurosci. 2021. V. 24. № 3. P. 312–325.

An ELISA Platform for the Quantitative Analysis of SARS-CoV-2 RBD-neutralizing Antibodies As an Alternative to Monitoring of the Virus-Neutralizing Activity

N. N. Kostin[1], T. V. Bobik[1], G. A. Skryabin[1], M. A. Simonova[1], V. D. Knorre[1], V. A. Abrikosova[1], Y. A. Mokrushina[1], I. V. Smirnov[1], N. L. Aleshenko[2], N. A. Kruglova[3], D. V. Mazurov[3], A. E. Nikitin[2], A. G. Gabibov[1*]

[1]Shemyakin-Ovchinnikov Institute of Bioorganic Chemistry of the Russian Academy of Sciences, Moscow, 117997 Russia

[2]Central Clinical Hospital of the Russian Academy of Sciences, Moscow, 117593 Russia

[3]Institute of Gene Biology Russian Academy of Sciences, Moscow, 119334 Russia

*E-mail: gabibov@mx.ibch.ru

Received July 25, 2022; in final form, August 22, 2022

DOI: 10.32607/actanaturae.11776

ABSTRACT **Monitoring of the level of the virus-neutralizing activity of serum immunoglobulins ensures that one can reliably assess the effectiveness of any protection against the SARS-CoV-2 infection. For SARS-CoV-2, the RBD-ACE2 neutralizing activity of sera is almost equivalent to the virus-neutralizing activity of their antibodies and can be used to assess the level of SARS-CoV-2 neutralizing antibodies. We are proposing an ELISA platform for performing a quantitative analysis of SARS-CoV-2 RBD-neutralizing antibodies, as an alternative to the monitoring of the virus-neutralizing activity using pseudovirus or "live" virus assays. The advantage of the developed platform is that it can be adapted to newly emerging virus variants in a very short time (1–2 weeks) and, thereby, provide quantitative data on the activity of SARS-CoV-2 RBD-neutralizing antibodies. The developed platform can be used to (1) study herd immunity to SARS-CoV-2, (2) monitor the effectiveness of the vaccination drive (revaccination) in a population, and (3) select potential donors of immune plasma. The protective properties of the humoral immune response in hospitalized patients and outpatients, as well as after prophylaxis with the two most popular SARS-CoV-2 vaccines in Russia, were studied in detail using this platform. The highest RBD-neutralizing activity was observed in the group of hospitalized patients. The protective effect in the group of individuals vaccinated with Gam-COVID-Vac vaccine was 25% higher than that in outpatients and almost four times higher than that in individuals vaccinated with the CoviVac vaccine.**

KEYWORDS **Gam-COVID-Vac, Sputnik V, CoviVac, virus-neutralizing activity, antibodies, SARS-CoV-2, COVID-19.**

INTRODUCTION

As of July 2022, more than 564 million people have been infected by the SARS-CoV-2 coronavirus and more than 6.3 million people have died from the COVID-19 infection all over the world [1]. Since the start of the pandemic, several dozen vaccines approved by the WHO [2, 3] and therapeutic antibodies [4–6] have been developed. The vaccines were engineered on the basis of various platforms: protein subunits, viral vectors, RNA, DNA, inactivated viruses, etc. Unfortunately, the evaluation of the efficacy of the developed vaccines was impeded by the differences in the platforms, antigens, as well as immunologic assays and parameters used to assess the immune response. In late 2020, the WHO, the National Institute for Biological Standards and Control (NIBSC), and the Coalition for Epidemic Preparedness Innovations (CEPI) elaborated and distributed the International Standard for human anti-SARS-CoV-2 immunoglobulin (the NIBSC code: 20/136) [7]. The standard is a

freeze-dried pool of plasma from 11 donors with a previous history of COVID-19; the pool has a neutralizing antibody activity of 1,000 international units per milliliter (IU/ml) and contains 1,000 binding antibody units per milliliter (BAU/ml). The elaboration of this standard has reduced the interlaboratory variability and provided a common language for data presentation, which is important for developing diagnostics, vaccines, and therapeutic antibodies, as well as for donor selection [8]. The level of virus-neutralizing activity of serum immunoglobulins ensures reliable assessment of the level of protection one enjoys against the SARS-CoV-2 infection. Considerable time and financial resources are necessary in studies that use the live virus to obtain quality data. The efforts of many researchers have recently focused on the development of quantitative procedures that are alternative to the existing platforms, where samples of the live SARS-CoV-2 virus are used [9–13].

In this work, we have studied the humoral response in individuals who received the most popular prophylactic vaccines in the Russian Federation – Gam-COVID-Vac (rAd26/rAd5, brand name Sputnik V) [14] and CoviVac (the inactivated virus) [15] – compared it to the antibody response in patients who had had mild and severe COVID-19, and analyzed the correlation between RBD and virus neutralization. As a result, we have proposed a platform for the quantitative analysis of SARS-CoV-2 RBD-neutralizing antibodies, as an alternative to monitoring the virus-neutralizing activity.

EXPERIMENTAL

Quantitative determination of RBD-specific IgG and identification of their isotypes by ELISA

To perform a quantitative determination of RBD-specific IgG, 100 μl of a PBS solution of recombinant RBD (amino acid residues 320–537) produced in CHO cells (1 μg/ml) were added to the wells of MaxiSorp 96-well plates (Nunc, Denmark) and the plate was incubated overnight at 2–8°C. The unoccupied binding sites were then blocked by adding 150 μl of blocking buffer (PBS, 0.05% Tween-20, 0.1% sodium caseinate) into each well and incubating the plate at room temperature for 1 h. Serum samples in the blocking buffer were prepared in three dilutions (1 : 10, 1 : 50, 1 : 250) and three replicates in a separate 96-well plate with low sorption capacity. WHO primary standard solutions (NIBSC code: 20/136) and solutions of the secondary standard (obtained in the laboratory from a pool of serum samples collected from individuals who had had COVID-19 and characterized with respect to the primary standard) were prepared in the same plate in a blocking buffer in seven sequential threefold serial dilutions. Next, the serum samples and standards (100 μl/well) were added to the wells containing adsorbed RBD and incubated for 30 min in a thermo-shaker at 37°C, 700 rpm. After the incubation, the plate was washed five times by adding 350 μl of PBST (PBS, 0.05% Tween-20) to each well and 100 μl of horseradish peroxidase-conjugated anti-human IgG antibodies (Biosan, Novosibirsk, Russia, Cat. # I-3021) diluted 1 : 10 000 in a blocking buffer were then added to each well. After 30-min incubation (37°C, 700 rpm) and washing, 100 μl of the substrate TMB solution was added to each well and the plate was incubated for 15 min in the dark. The enzymatic reaction was stopped by adding 10% of the solution of orthophosphoric acid, and optical density (OD) in the wells at a wavelength of 450 nm (OD_{450}) was measured on a plate spectrophotometer. The curves showing the mean OD value as a function of the concentration of RBD-specific IgG in the standards (BAU/ml) were plotted using the GraphPad Prism 8 software (USA). These curves were used to calculate the concentrations of RBD-specific IgG in the serum samples: the dilution of the sample whose mean OD_{450} lay in the OD_{450} range of the curve of the standard solution was chosen, and the resulting value (in BAU/ml) was multiplied by the respective dilution. The subclasses of RBD-specific IgG were analyzed according to the protocol described above, even though the calibration curves were not plotted, and the horseradish peroxidase conjugates of the following antibodies were used: anti-human IgG1 antibodies (HyTest, Finland, Cat. # 1G2cc), anti-human IgG2 antibodies (HyTest, Finland, Cat. # 1G5), anti-human IgG3 antibodies (HyTest, Finland, Cat. # 1G3cc), and anti-human IgG4 antibodies (HyTest, Finland, Cat. # 1G4cc). ELISA of IgG against nucleocapsid and linear antigens was carried out according to the procedure reported in [16]. The detection limit in the quantitative and qualitative assays of RBD-specific IgG was determined as follows: the mean OD_{450} value in the negative samples plus three standard deviations from the mean value in the negative samples.

Determining the neutralizing activity for the live virus

The neutralizing activity of the blood serum samples was determined in a neutralization reaction (NR) in which the formation of negative colonies produced by the SARS-CoV-2 virus in a 24-h-old monolayer of Vero C1008 cells under agar coating was inhibited. Serum dilutions were prepared in normal saline supplemented with antibiotics (streptomycin sulfate and benzylpenicillin G sodium salt), 100 U/ml

each. The working dilution of the virus-containing suspension based on the SARS-CoV-2 virus was prepared in a Hanks' balanced salt solution supplemented with 2% fetal bovine serum (FBS) and antibiotics. Concentration of SARS-CoV-2 in the prepared dilution was 100–150 PFU/ml (40–60 plaques per flask). A one-day-old monolayer of Vero C1008 cells in T25 flasks was used in the experiment. A mixture of equal volumes of the serum and SARS-CoV-2 virus culture was incubated at 37°C for 1 h. At least four flasks were used for each serum dilution. A mixture of the serum and virus culture (0.5 ml of each component) was placed in each flask, and the inoculum was uniformly distributed over the entire monolayer. The flasks were placed horizontally and left at 37°C. After adsorption of the antibodies–virus complex on the cells for 1 h, the inoculum was decanted, the primary agar coating designed for the SARS-CoV-2 virus was applied (10.0 ml per flask), and the monolayer was incubated at 37°C for two days. After the two days, a secondary agar coating containing a 0.1% Neutral Red solution was applied onto the infected monolayer for staining the cells and 24-hr incubation was performed at room temperature in the dark. Next, the negative colonies in the flasks were counted. The most dilute serum sample in which the formation of negative colonies by the SARS-CoV-2 virus was inhibited by at least 50% compared to the negative control (FBS containing no antibodies specific to the SARS-CoV-2 virus) was assumed to be the antibody titer in the analyzed serum sample.

Determining the neutralizing activity in the pseudovirus system

Testing with pVNT was performed using recombinant lentiviruses carrying the SARS-CoV-2 S protein and encoding firefly luciferase (Luc) [17]. To obtain pseudovirus particles, HEK293T cells were cultured in T75 flasks to a 50–70% confluence level and transfected with a mixture of plasmids (15 μg of pLuc, 15 μg of pGAG, 5 μg of pRev, and 2 μg of SARS-CoV-2 S protein per flask) using PEI (75 μg per flask) as a transfection agent. The cells were then incubated at 37°C, 5% CO_2 for 72 h in the DMEM supplemented with 10% FBS. After the 72 h, the cell culture supernatant was centrifuged first at 150 *g* and then at 3,900 *g*, followed by filtration through a filter with a pore size of 0.20 μm. The resulting aliquots of the supernatant were stored at –80°C. The HEK293T-ACE2 cells were inoculated into 96-well plates at a density of 2×10^4 cells/well and incubated overnight. Serial dilutions of serum samples in the DMEM medium supplemented with 10% FBS were prepared. The diluted serum samples (5 μl) were then mixed with the pseudovirus-containing medium (50 μl) in 96-well plates and incubated at 37°C, 5% CO_2 for 1 h. Next, 50 μl of the medium was removed from the wells of the plates containing HEK293T-ACE2 cells and the cells were infected with virus–serum mixtures (50 μl/well). The inoculated HEK293T-ACE2 cells were then incubated at 37°C, 5% CO_2 for 48 h. The controls were tested in three replicates; the analyzed samples were tested once. After the 48-h incubation, the medium was collected from the wells containing the cells; 100 μl of a lysing buffer (25 mM Tris-phosphate, pH 7.8, 1% Triton X-100, 10% glycerol, 2 mM DTT) was added into each well, and the plate was incubated for 5 min at room temperature. Next, 20 μl of the Bright-Glo™ Luciferase Assay Substrate reagent (Promega, USA) was added to the white 96-well plates containing 80 μl of the cell lysate, and the luminescence intensities were measured. The curves showing the luminescence intensity as a function of serum dilution were plotted using the GraphPad Prism 8 software, and serum titers ensuring 50% pseudovirus neutralization were calculated.

Quantitative determination of RBD-specific neutralizing antibodies by competitive ELISA

A PBS solution of recombinant RBD produced by expression of RBD (amino acid residues 320–537) in CHO cells was added into the wells of MaxiSorp 96-well plate (Nunc, Denmark) (100 μl) at a concentration of 1 μg/ml, and the plate was incubated overnight at 2–8°C. Next, the unoccupied binding sites were blocked by adding 150 μl of a blocking solution (PBS, 0.05% Tween-20, 0.1% BSA) into each well and incubating the plate at room temperature for 1 h. Serum samples in the blocking buffer were prepared in three dilutions (1 : 10, 1 : 50, and 1 : 250) and three replicates in a separate 96-well plate with a low sorption capacity. Solutions of the primary WHO standard and the secondary standard (obtained in the laboratory from the pool of serum samples collected from individuals who had had COVID-19 and characterized with respect to the primary standard) in the blocking buffer at final concentrations of 10, 20, and 40 IU/ml were prepared in the same plate. The analyzed serum samples and standards were then added into the wells of the plate containing the adsorbed RBD (100 μl/well) and incubated for 30 min in a thermo-shaker at 37°C, 700 rpm. After the incubation, the plate was washed five times by placing 350 μl of PBST (PBS, 0.05% Tween-20) into each well; 100 μl of the solution of recombinant hACE2-3×FLAG (0.2 μg/ml) in the blocking buffer was added into the wells. After 30-min incubation at 37°C, 700 rpm and washing, 100 μl of anti-FLAG antibodies conjugated

to horseradish peroxidase (Sigma Aldrich, USA, Cat. # A8592) at a 1 : 10 000 dilution in the blocking buffer were added into each well and the plate was incubated for an additional 30 min using the procedure described above. After the plate had been washed, 100 μl of the TMB substrate solution was added into each well and the plate was incubated in the dark for 15 min. The enzymatic reaction was stopped by adding a 10% orthophosphoric acid solution, and the OD_{450} values in the wells were measured on a spectrophotometer plate reader. The curves showing OD_{450} as a function of the concentration of RBD-specific neutralizing antibodies in IU standards (IU/ml) were plotted using the GraphPad Prism 8 software. These curves were used to calculate the concentrations of RBD-specific neutralizing antibodies in the serum samples; for this purpose, a dilution of the sample that laid in the range of OD_{450} values of the standard curve was selected and the obtained value in IU/ml was multiplied by the respective dilution. The detection limit was determined as follows: the mean OD_{450} value in the negative samples minus three standard deviations from the mean in the negative samples.

RESULTS

Developing the ELISA kit for a quantitative determination of the SARS-CoV-2 S1 RBD-neutralizing activity in human sera

There are several methods for a quantitative determination of the virus-neutralizing activity of serum samples: the standard assay with live viruses (cVNT), the assay with pseudoviruses (pVNT), and the competitive ELISA assay, which is based on immunochemical methods (sVNT). The standard "live" virus assays (in the case of SARS-CoV-2) need to be performed indoors, in facilities with a biosafety level no lower than BSL-3. Assays involving pseudoviruses (PV) are labor-intensive and time-consuming. Competitive ELISA assays are convenient for routine serodiagnosis and take comparatively less time. However, they need to be validated with respect to other types of assays.

We have developed an ELISA kit for a quantitative determination of the activity of SARS-CoV-2 RBD-specific neutralizing antibodies in serum or plasma [18]. The method is based on a competitive enzyme-linked immunosorbent assay (sVNT) for measuring the interaction between the recombinant receptor-binding domain (RBD) of the surface glycoprotein (S protein) of the SARS-CoV-2 coronavirus and the recombinant human ACE2 receptor (ACE2), in the presence of the analyzed sample. During the first stage, SARS-CoV-2 RBD-neutralizing antibodies (if present in the analyzed samples) interact with RBD adsorbed on the surface of the wells of a dismountable polystyrene plate. During the second stage, the RBD interacts with the human recombinant ACE2 receptor. If the analyzed sample contains no RBD-neutralizing antibodies, the RBD–ACE2 complex appears. If the sample contains RBD-neutralizing antibodies, the RBD–ACE2 complex is formed either partially or not at all. The resulting RBD–ACE2 complex is detected using an immunoenzyme conjugate at the third stage (*Fig. 1*).

The total time needed to perform the assay is 2–2.5 h. The international WHO standard is used for detection; the detection limit is 4 IU/ml.

The RBD-neutralizing activity of serum samples measured by competitive ELISA assay strongly correlates with virus neutralization

We have performed a successful validation of the designed competitive ELISA kit by comparing the RBD-neutralizing activity data to the virus neutralization data obtained using both standard testing with "live" viruses (cVNT) and testing with pseudoviruses (pVNT). The fidelity parameters of linear approximation (r^2) were 0.97 and 0.90, respectively (*Fig. 2*).

Characterizing the groups of serum samples and analyzing their protective properties

We analyzed 134 serum samples obtained from four groups of individuals (*Table 1*): patients who had suffered severe COVID-19 (*Hospitalized patients*); patients who had had mild COVID-19 (*Outpatients*); individuals who had not previously had COVID-19 and had been vaccinated with two doses of Gam-COVID-Vac (*Vaccinated with Gam-COVID-Vac*); and individuals who had not previously had COVID-19 and had been vaccinated with two doses of CoviVac (*Vaccinated with CoviVac*).

All the serum samples were analyzed using both the developed sVNT method, which determines the SARS-CoV-2 RBD-neutralizing antibodies (RBD-nAb) activity – the ability of sera to inhibit (neutralize) RBD–ACE2 binding – and our in-house quantitative ELISA kit, which determines the total concentration of SARS-CoV-2 RBD-specific immunoglobulins G (IgG). In the latter case, quantification is also performed with respect to the international WHO standard; the detection limit is 1 BAU/ml.

The frequency of occurrence of IgG-positive sera samples among the groups *Hospitalized patients*, *Outpatients*, and *Vaccinated with Gam-COVID-Vac* varied from 85 to 93%. In the group *Vaccinated with CoviVac*, the frequency of occurrence was as low as 26% (*Fig. 3A*). Among these IgG-seropositive

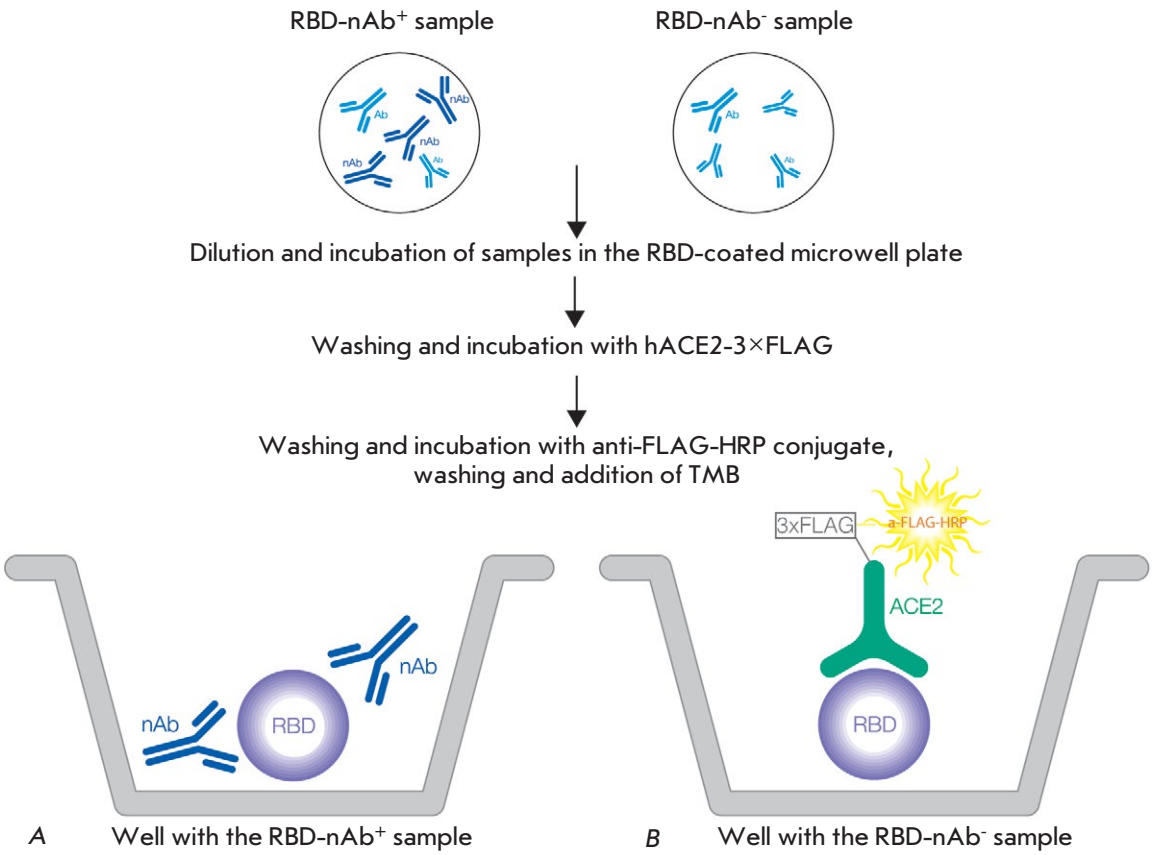

Fig. 1. Scheme of the quantitative determination of the activity of SARS-CoV-2 RBD-specific neutralizing antibodies in serum or plasma (sVNT). Antibodies in the serum sample interact with the recombinant RBD adsorbed in the wells. If the sample contains RBD-neutralizing antibodies (*A*), they block the binding of RBD to ACE2. If the sample does not contain neutralizing antibodies (*B*), the RBD adsorbed on the plate binds to recombinant ACE2. This binding is detected by peroxidase-labeled antibodies against the 3×FLAG sequence (3×FLAG) contained in recombinant ACE2. Therefore, the colorimetric signal recorded in the assay is inversely proportional to the concentration of the neutralizing antibodies in the sample. Designations: Ab – antibodies without neutralizing activity; ACE2 – recombinant human ACE2 receptor; HRP – antibodies to the FLAG epitope labeled with horseradish peroxidase; nAB – antibodies with RBD-neutralizing activity; RBD – the recombinant receptor-binding domain of the coronavirus SARS-CoV-2 S protein

sera samples, the frequency of occurrence of RBD-nAb-positive serum samples varied from 67 to 95% (*Fig. 3B*). The frequency of occurrence of RBD-nAb-positive serum samples in the group (showing the protective properties of the serum samples in the group) varied from 22 to 81% (*Fig. 3C*).

The concentrations of SARS-CoV-2 RBD-specific IgG in the seropositive samples in different groups varied insignificantly (*Fig. 4A*). However, although the concentrations of RBD-specific IgG in the seropositive samples were almost identical for all the groups, the activity of RBD-specific virus-neutralizing antibodies was substantially higher in the group *Hospitalized patients* compared to those in the other groups (*Fig. 4B*).

In order to further elucidate the nature of the humoral response, the double-positive (RBD-IgG$^+$ and RBD-nAb$^+$) samples were tested using subtype-specific conjugates. An analysis of IgG subclasses revealed an increased production of IgG3 antibodies in the group of individuals vaccinated with Gam-COVID-Vac, along with a switch to the IgG1 subclass in all the groups (*Fig. 5*).

The relationship between the activity of RBD-neutralizing antibodies and concentration of anti-RBD IgG

In order to characterize the relationship between the activity of SARS-CoV-2 RBD-specific nAb and the concentration of SARS-CoV-2 RBD-specific IgG, we conducted a linear regression analysis of each group of serum samples. Differences in RBD-nAb activity (normalized with respect to the concentration of RBD-

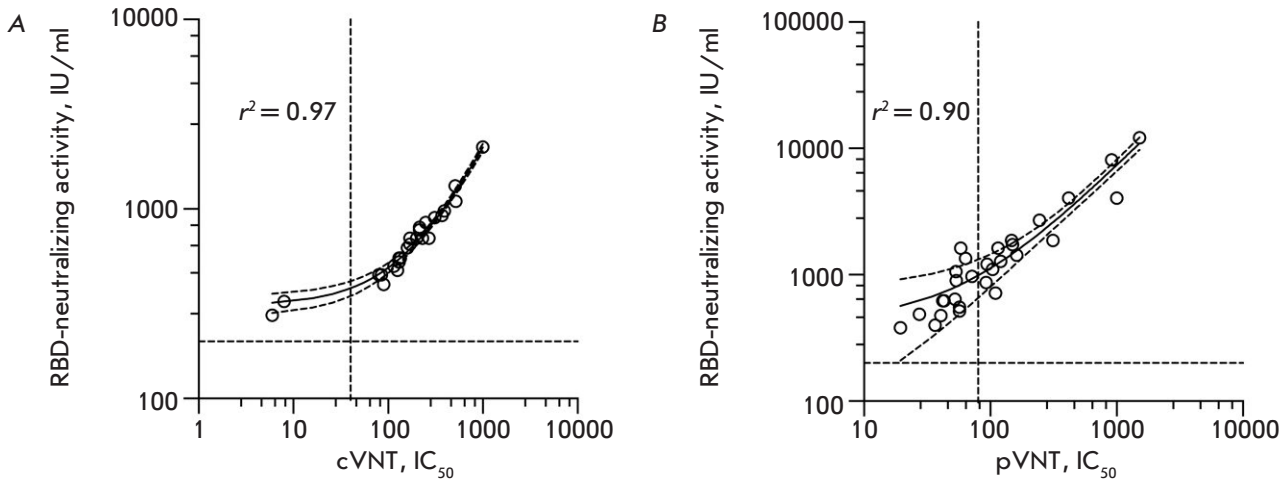

Fig. 2. Validation of the RBD neutralization test by comparison with the conventional and pseudovirus neutralization assays. (*A*) Plot showing the activity of SARS-CoV-2 RBD-specific neutralizing antibodies in sera obtained by sVNT against serum titers that yield 50% virus neutralization (IC_{50}) using the cVNT test (26 samples). (*B*) Plot showing the activity of SARS-CoV-2 RBD-specific neutralizing antibodies in sera obtained by sVNT against sera titers at which pseudovirus neutralization of 50% (IC_{50}) was achieved (pVNT test) (29 samples). r^2 is the coefficient of determination. In all the serum samples where no anti-RBD neutralizing antibodies were detected (25 samples), neutralization of the SARS-CoV-2 infection was not detected in all the tests

Table 1. The analyzed serum sample groups

Group	Number	Sex, males/females	Age, median (minimum, maximum)	Time (days) after the symptom onset or injection of the second vaccine dose, median (minimum, maximum)
Hospitalized patients	27	15/12	57 (37, 69)	23 (19, 47)
Outpatients	41	21/20	39 (27, 61)	25 (17, 44)
Vaccinated with Gam-COVID-Vac	43	20/23	41 (25, 62)	21 (14, 28)
Vaccinated with CoviVac	23	11/12	36 (28, 58)	20 (14, 30)

specific IgG) were revealed in the analyzed samples from different groups. The activity of RBD-nAb can be expressed as a slope of the regression line (*Fig. 6*). The activity of RBD-nAb was significantly higher in the serum samples of the group *Hospitalized patients* compared to the other groups.

The RBD-neutralizing properties of serum samples collected from individuals in different groups

To perform an adequate assessment of the RBD-neutralizing activity of the humoral immunity (the protectivity index), one needs to take into account, along with the activity of RBD-neutralizing antibodies, the frequency of immune response formation in the analyzed group. Therefore, the protectivity index of sera in the different groups was calculated as the slope of the regression line (K) in the group (*Fig. 6*) normalized to the frequency of occurrence of SARS-CoV-2 RBD-specific nAb-positive serum samples in the group (*Fig. 3C*). The resulting data are shown in *Fig. 7*.

DISCUSSION

Emergence, development, and persistence of humoral immunity to the SARS-CoV-2 coronavirus in patients who have recovered after COVID-19 and/or had been vaccinated are extremely important and largely inform the measures taken by the state in combatting the coronavirus infection. Neutralizing antibodies play a significant role in protecting the or-

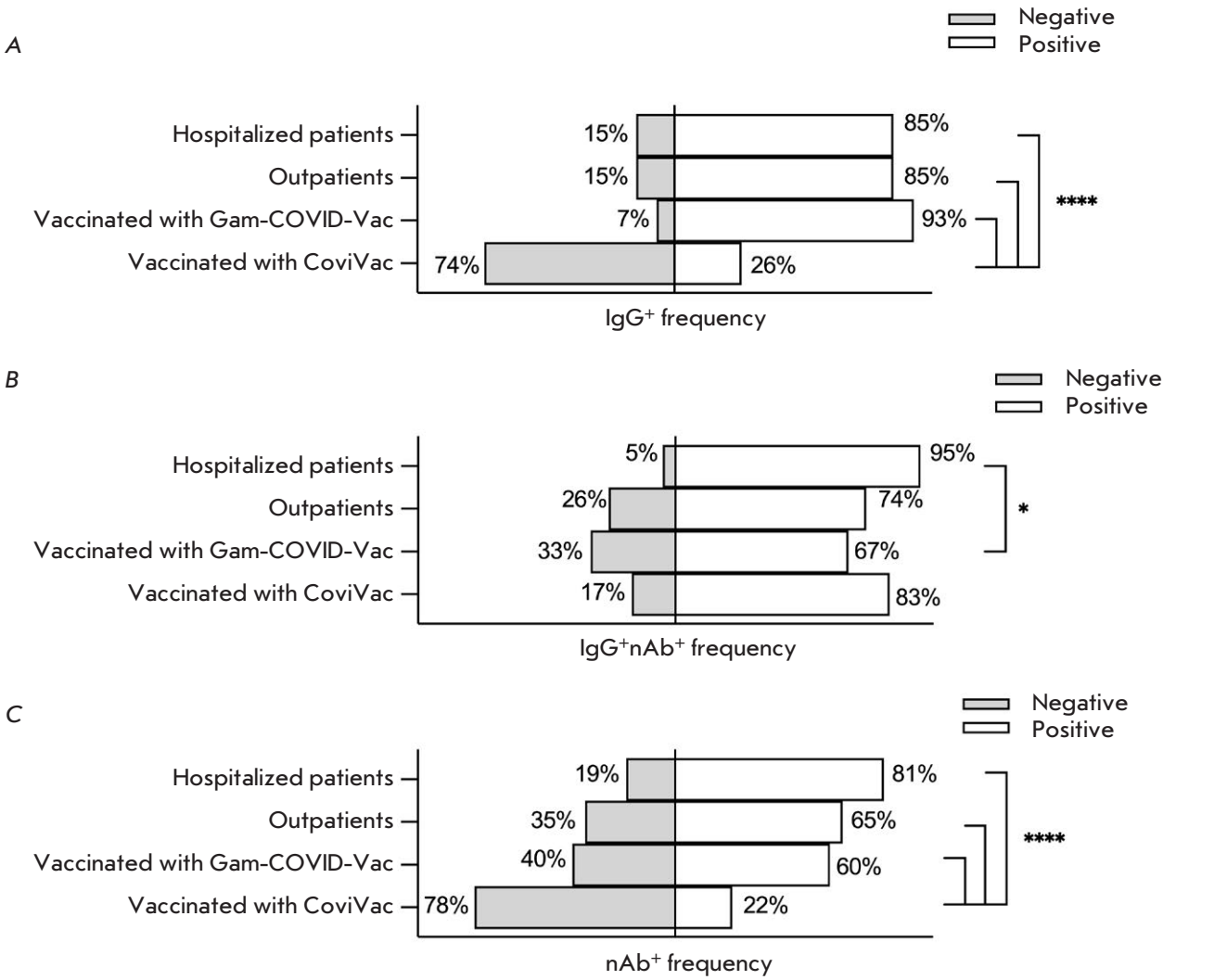

Fig. 3. Frequency of seropositive serum samples in the analyzed groups. (*A*) Frequency of anti-RBD IgG positive serum samples per group. (*B*) Frequency of RBD-nAb seropositive serum samples among RBD-IgG-positive samples. (*C*) Frequencies of occurrence of RBD-nAb-positive samples in the groups. Statistical significance of the intergroup differences was determined using the Fisher's exact test ($^{*}p < 0.05$; $^{****}p < 0.0001$)

ganism against the virus. The mechanisms of action of virus-neutralizing antibodies are rather diverse and involve the inhibition of virion binding to cellular receptors, inhibition of penetration of the viral genomes into the cytoplasm, blocking of the penetration of the viral genomes from the endosome into the cytoplasm, and, finally, simple aggregation of viral particles. The main type of neutralizing antibodies in patients with the SARS-CoV-2 infection are those preventing the interaction between the receptor-binding domain of the virus S protein to the ACE2 cell receptor. A large number of studies showing a correlation between the protection level and the presence of SARS-CoV-2 anti-RBD immunoglobulins G in human serum have been conducted [19–22].

A particular pool of studies has focused on adaptive immunotherapy of COVID-19; namely, on designing recombinant therapeutic virus-neutralizing antibodies against SARS-CoV-2 [23–25]. In this case, the potential protection against new virus variants is of particular interest and there is also much tension around the issue of assaying virus neutralization. For SARS-CoV-2, to some extent, it is fair to say that the RBD-ACE2-neutralizing activity of sera is almost

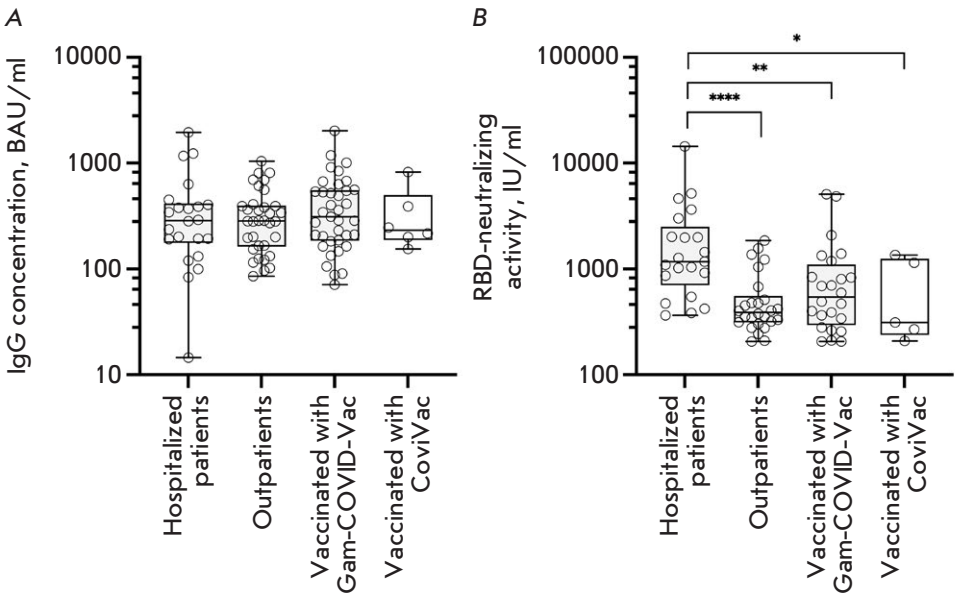

Fig. 4. Concentration of SARS-CoV-2 RBD-specific IgG and the activity of RBD-ACE2 neutralizing antibodies in seropositive serum samples measured by sVNT. (*A*) Concentration of SARS-CoV-2 RBD-specific IgG in seropositive serum samples. (*B*) Neutralizing activity of RBD-specific antibodies (RBD-nAb) in seropositive serum samples. The statistical significance of intergroup differences was determined using the Kruskal–Wallis test ($^{*}p < 0.05$; $^{**}p < 0.01$; $^{****}p < 0.0001$)

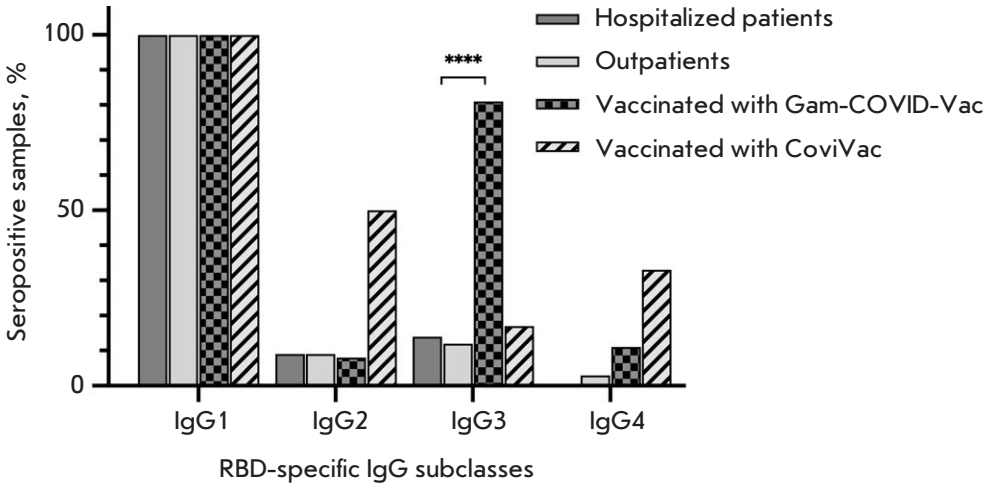

Fig. 5. The frequency of occurrence of SARS-CoV-2 RBD-specific immunoglobulin class G subclasses among RBD-nAb^{+} samples. Statistical significance of intergroup differences was determined using the Fisher's exact test ($^{*}p < 0.05$; $^{****}p < 0.0001$)

equivalent to the virus-neutralizing activity of antibodies and can be used as an analog to assay neutralizing antibodies against SARS-CoV-2.

The objective of this study was to thoroughly investigate the protective properties of the humoral immune response in hospitalized patients and outpatients, as well as individuals who have received prophylaxis with the two vaccines against SARS-CoV-2 which are the most popular in the Russian Federation.

To study the humoral immunity against SARS-CoV-2, we have designed two simple, quick and convenient-to-use ELISA kits: for a quantitative determination of the SARS-CoV-2 anti-RBD-IgG concentration and for a quantitative determination of the SARS-CoV-2 S1 RBD-ACE2-neutralizing activity of antibodies (RBD-nAb). These kits form a platform, that, owing to their modular structure, within a short period of time (up to 1–2 weeks) can be adapted to new strains (by replacing the RBD of the protein) or even to new viruses (by replacing the ACE2 receptor).

We used these kits to determine the following parameters of the blood serum samples for the analyzed groups of patients: the frequency of occurrence of SARS-CoV-2 anti-RBD-IgG positive sera, IgG concentration in serum samples, the frequency of occurrence of SARS-CoV-2 RBD-nAb-positive sera, and the level of neutralizing activity of RBD-nAb in serum samples.

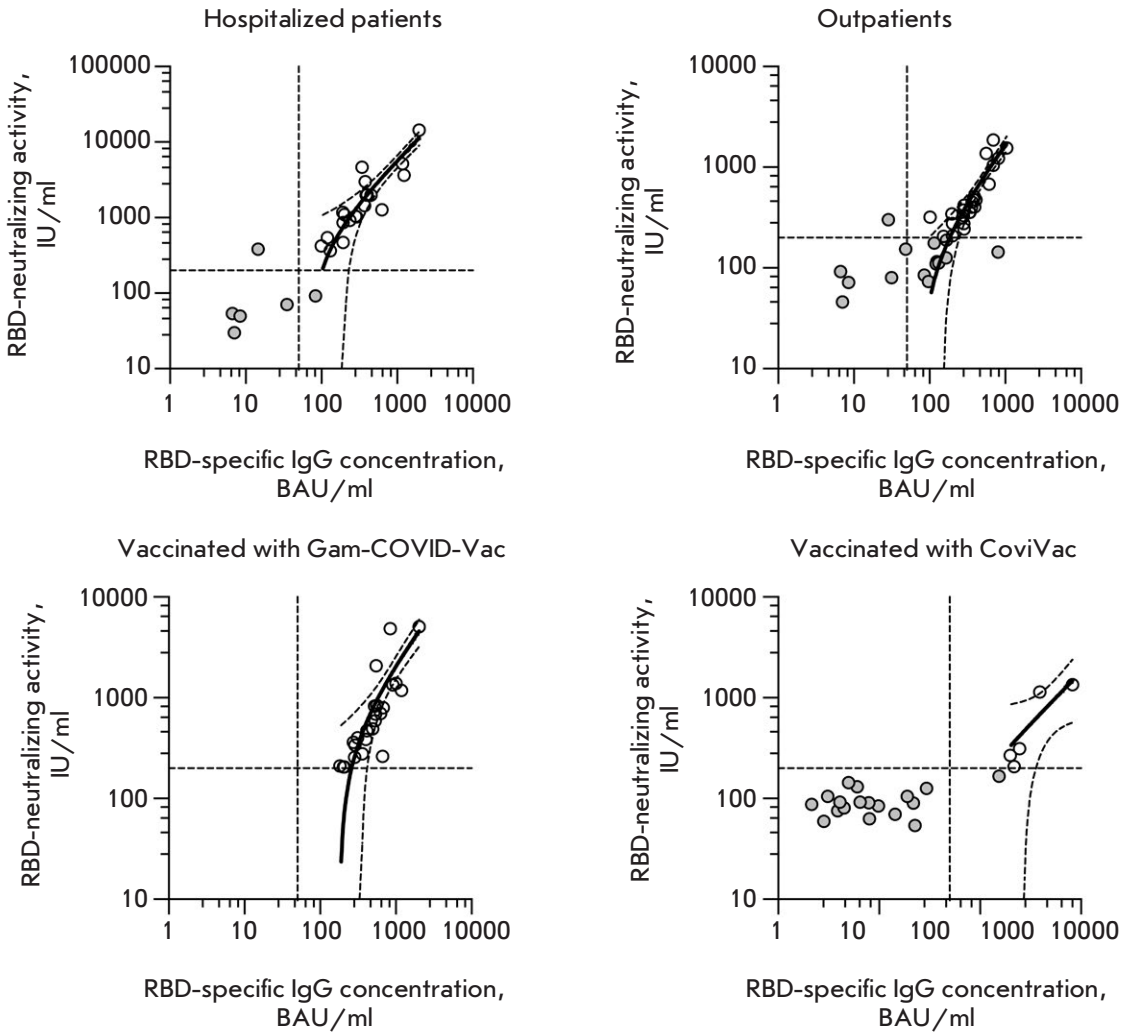

Group	R (CI)	K (CI)
Hospitalized Patients	0.89 (0.74-0.96)	6.0 (4.5-7.5)
Outpatients	0.88 (0.74-0.94)	1.8 (1.4-2.2)
Gam-COVID-Vac vaccinated	0.77 (0.53-0.89)	2.5 (1.6-3.4)
CoviVac vaccinated	0.88 (-0.002-0.99)	1.8 (0.03-3.6)

Fig. 6. Linear regression analysis of the serum antibody RBD-ACE2 neutralizing activity and RBD-specific IgG concentration. Double seropositive (RBD-IgG$^+$ and RBD-nAb$^+$) serum samples are shown as white circles; negative samples are shown as gray circles. The 95% confidence intervals and activity and concentration thresholds are shown with dotted lines. **R** is the Pearson correlation coefficient; **K** is the slope of the regression line; **CI** is the 95% confidence interval

The concentrations of SARS-CoV-2 anti-RBD-IgG antibodies were almost identical for all the seropositive serum samples; however, the frequency of occurrence of IgG-positive sera in the group of individuals vaccinated with CoviVac based on the inactivated virus was more than threefold lower compared to the remaining groups. Earlier, we have demonstrated that most SARS-CoV-2 anti-RBD antibodies in patients who had had COVID-19 were conformationally dependent [16, 26]. CoviVac apparently has an appreciably low immunogenicity, which is probably caused by partial disruption of the structure of the S-protein epitopes during virus inactivation or storage. The frequency of occurrence of RBD-nAb-positive sera, as well as their activity, was highest in the group *Hospitalized patients*.

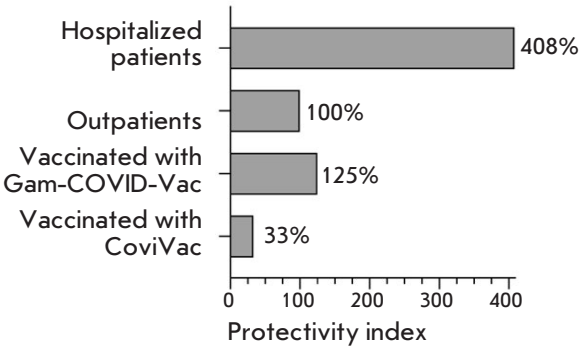

Fig. 7. The virus-neutralizing activity of the humoral immunity in the study groups. The protectivity index of the group *Outpatients* was taken as 100%

We also studied the profile of formation of IgG-antibody subclasses in different groups. IgG1 antibodies were detected in serum samples in all the groups. Notably, the group *Vaccinated with Gam-COVID-Vac* contained also antibodies of the IgG3 subclass. Switching to the production of IgG1 and IgG3 subclasses antibodies seems to be induced by IL-21 [27]. IgG3 antibodies are formed at the early stages of the immune response and are characterized by a high ability to activate complement and high affinity to Fcγ cellular receptors. In addition to the RBD-neutralizing activity, all the aforelisted properties of antibodies of this subclass trigger the activation of antibody-dependent cellular phagocytosis and antibody-dependent cytotoxicity [28–30]. The switching to the production of antibodies of the IgG1 and IgG3 subclasses in the group *Vaccinated with Gam-COVID-Vac* can be explained by the nature of the adenoviral vector used in the Gam-COVID-Vac vaccine.

We have also calculated the RBD-neutralizing activity of the humoral immunity in the analyzed groups. The protectivity index in the group *Vaccinated with Gam-COVID-Vac* was higher than that in the group *Outpatients* by 25% and higher than that in the group *Vaccinated with CoviVac* almost fourfold. The highest RBD-neutralizing activity was observed in the group *Hospitalized patients* (fourfold higher compared to the group *Outpatients*), being indicative of the presence of high-affinity and high-specificity antibodies, along with a high frequency of development of humoral immunity. This fact can be attributed to the long-term viral load in hospitalized patients, which leads to the development of virus-neutralizing antibodies with a high affinity to the viral epitopes [16, 31–33].

CONCLUSIONS

A relevant platform for the quantitative analysis of RBD-neutralizing antibodies against SARS-CoV-2 has been designed as an alternative to monitoring the virus-neutralizing activity, making it possible to quantify the concentrations of SARS-CoV-2 anti-RBD IgG antibodies, as well as the SARS-CoV-2 RBD-ACE2-neutralizing activity of the antibodies.

A comparative study of 134 serum samples collected from patients who had suffered severe and mild COVID-19 and individuals vaccinated with Gam-COVID-Vac and CoviVac was performed.

The highest protectivity index was observed in the group *Hospitalized patients*.

The protective properties of humoral immunity after vaccination with Gam-COVID-Vac was fourfold stronger than that after vaccination with CoviVac.

The advantage of the developed platform is that it allows one to adapt the method to newly emerging virus variants in the shortest possible period of time (1–2 weeks) and, thereby, collect quantitative data on the protection level afforded individuals vaccinated with earlier types of vaccines. ●

This work was supported by the Ministry of Science and Higher Education of the Russian Federation (project No. 075-15-2021-1049).

REFERENCES

1. WHO Coronavirus (COVID-19) Dashboard https://covid19.who.int
2. Calina D., Docea A.O., Petrakis D., Egorov A.M., Ishmukhametov A.A., Gabibov A.G., Shtilman M.I., Kostoff R., Carvalho F., Vinceti M., et al. // Int. J. Mol. Med. 2020. V. 46. P. 3–16.
3. WHO COVID-19 vaccine tracker and landscape https://www.who.int/publications/m/item/draft-landscape-of-covid-19-candidate-vaccines
4. Shang J., Ye G., Shi K., Wan Y., Luo C., Aihara H., Geng Q., Auerbach A., Li F. // Nature. 2020. V. 581. P. 221–224.
5. Guo Y., Huang L., Zhang G., Yao Y., Zhou H., Shen S., Shen B., Li B., Li X., Zhang Q., et al. // Nat. Commun. 2021. V. 12. P. 2623.
6. Zhou X., Wang H., Ji Q., Du M., Liang Y., Li H., Li F., Shang H., Zhu X., Wang W., et al. // Protein & Cell. 2021. V. 12. № 10. P. 818–823.
7. WHO/BS.2020.2403 Establishment of the WHO International Standard and Reference Panel for anti-SARS-CoV-2 antibody https://www.who.int/publications/m/item/WHO-BS-2020.2403
8. Kristiansen P.A., Page M., Bernasconi V., Mattiuzzo G., Dull P., Makar K., Plotkin S., Knezevic I. // Lancet. 2021. V. 397. P. 1347–1348.
9. Cantoni D., Mayora-Neto M., Temperton N. // Oxf. Open

Immunol. 2021. V. 2. № 1. iqab005.
10. Ferrara F., Temperton N. // Methods Protoc. 2018. V. 1. № 1. P. 8.
11. Muruato A.E., Fontes-Garfias C.R., Ren, P., Garcia-Blanco M., Menachery V., Xie X., Shi. P. // Nat. Commun. 2020. V. 11. № 1. P. 4059.
12. Tan C.W., Chia W.N., Qin X., Liu P., Chen M.I., Tiu C., Hu Z., Chen V.C., Young B.E., Sia W.R., et al. // Nat. Biotechnol. 2020. V. 38. № 9. P. 1073–1078.
13. Byrnes J.R., Zhou X.X., Lui I., Elledge S.K., Glasgow J.E., Lim S.A., Loudermilk R.P., Chiu C.Y., Wang T.T., Wilson M.R., et al. // mSphere. 2020. V. 5. № 5. P. e00802–20.
14. Logunov D.Y., Dolzhikova I.V., Zubkova O.V., Tukhvatulin A.I., Shcheblyakov D.V., Dzharullaeva A.S., Grousova D.M., Erokhova A.S., Kovyrshina A.V., Botikov A.G., et al. // Lancet. 2020. V. 396. P. 887–897.
15. Kozlovskaya L.I., Piniaeva A.N., Ignatyev G.M., Gordeychuk I.V., Volok V.P., Rogova Y.V., Shishova A.A., Kovpak A.A., Ivin Y.Y., Antonova L.P., et al. // Emerging Microbes & Infections. 2021. V. 10. № 1. P. 1790–1806.
16. Bobik T.V., Kostin N.N., Skryabin G.A., Tsabai P.N., Simonova M.A., Knorre V.D., Stratienko O.N., Aleshenko N.L., Vorobiev I.I., Khurs E.N., et al. // Acta Naturae. 2021. V. 13. P. 102–115.
17. Kruglova N., Siniavin A., Gushchin V., Mazurov D. // Viruses. 2021. V. 13. P. 1133.
18. Kostin N.N., Bobik T.V., Skryabin G.A., Simonova M.A., Mokrushina Y.A., Smirnov I.V., Balmasova I.P., Aleshenko N.L., Nikitin A.E., Chekhonin V.P., Gabibov A.G. Russian Federation patent application No. 2021140129 “Method for determining the activity of SARS-CoV-2 neutralizing antibodies in the serum or plasma of people who have had COVID-19 or are vaccinated with vaccines for the prevention of a new coronavirus infection COVID-19, using a set of reagents for enzyme immunoassay containing a recombinant receptor-binding domain (RBD) of SARS-CoV-2 surface glycoprotein S of the SARS-CoV-2 coronavirus and a recombinant human ACE2 receptor” (invention priority dated 12/31/21).
19. Lumley S.F., O’Donnell D., Stoesser N.E., Matthews P.C., Howarth A., Hatch S.B., Marsden B.D., Cox S., James T., Warren F., et al. // N. Engl. J. Med. 2021. V. 384(6). P. 533–540.
20. Williams D.E. // Sci. Rep. 2022. V. 12. № 1. P. 9379.
21. Murugesan M., Mathews P., Paul H., Karthik R., Mammen J.J., Rupali P. // PLoS One. 2022. V. 17. № 5. P. e0268797.
22. Tomic A., Skelly D.T., Ogbe A., O’Connor D., Pace M., Adland E., Alexander F., Ali M., Allott K., Azim Ansari M., et al. // Nat. Commun. 2022. V. 13. № 1. P. 1251.
23. Guo Y., Huang L., Zhang G., Yao Y., Zhou H., Shen S., Shen B., Li B., Li X., Zhang Q. et al. // Nat. Commun. 2021. V. 12. № 1. P. 2623.
24. Zhou X., Wang H., Ji Q., Du M., Liang Y., Li H., Li F., Shang H., Zhu X., Wang W., et al. // Protein Cell. 2021. V. 12. № 10. P. 818–823.
25. Chen D., Zhao Y., Li M., Shang H., Li N., Li F., Wang W., Wang Y., Jin R., Liu S., et al. // Theranostics. 2021. V. 11. № 4. P. 1901–1917.
26. Bobik T.V., Kostin N.N., Skryabin G.A., Tsabai P.N., Simonova M.A., Knorre V.D., Mokrushina Y.A., Smirnov I.V., Kosolapova J.A., Vtorushina V.V., et al. // Pathogens. 2021. V. 10. P. 705.
27. Avery D.T., Bryant V.L., Ma C.S., de Waal Malefyt R., Tangye S.G. // J. Immunol. 2008. V. 181. № 3. P. 1767–1779.
28. Damelang T., Rogerson S.J., Kent S.J., Chung A.W. // Trends Immunol. 2019. V. 40. P. 197–211.
29. Collins A.M., Jackson K.J.L. // Front. Immunol. 2013. V. 4. P. 235.
30. Chu T.H., Patz E.F., Ackerman M.E. // MAbs. 2021. V. 13. P. 1882028.
31. Bošnjak B., Stein S.C., Willenzon S., Cordes A.K., Puppe W., Bernhardt G., Ravens I., Ritter C., Schultze-Florey C.R., Gödecke N., et al. // Cell. Mol. Immunol. 2021. V. 18. № 4. P. 936–944.
32. Chia W.N., Zhu F., Ong S.W.X., Young B.E., Fong S.-W., Le Bert N., Tan C.W., Tiu C., Zhang J., Tan S.Y., et al. // Lancet Microbe. 2021. V. 2. P. e240–e249.
33. Moriyama S., Adachi Y., Sato T., Tonouchi K., Sun L., Fukushi S., Yamada S., Kinoshita H., Nojima K., Kanno T., et al. // Immunity. 2021. V. 54. P. 1841–1852.

GENERAL RULES

Acta Naturae publishes experimental articles and reviews, as well as articles on topical issues, short reviews, and reports on the subjects of basic and applied life sciences and biotechnology.

The journal *Acta Naturae* is on the list of the leading periodicals of the Higher Attestation Commission of the Russian Ministry of Education and Science. The journal Acta Naturae is indexed in PubMed, Web of Science, Scopus and RCSI databases.

The editors of *Acta Naturae* ask of the authors that they follow certain guidelines listed below. Articles which fail to conform to these guidelines will be rejected without review. The editors will not consider articles whose results have already been published or are being considered by other publications.

The maximum length of a review, together with tables and references, cannot exceed 50,000 characters with spaces (approximately 30 pages, A4 format, 1.5 spacing, Times New Roman font, size 12) and cannot contain more than 16 figures.

Experimental articles should not exceed 30,000 symbols (approximately 15 pages in A4 format, including tables and references). They should contain no more than ten figures.

A short report must include the study's rationale, experimental material, and conclusions. A short report should not exceed 12,000 symbols (5–6 pages in A4 format including no more than 12 references). It should contain no more than three figures.

The manuscript and all necessary files should be uploaded to www.actanaturae.ru:

1) text in Word 2003 for Windows format;
2) the figures in TIFF format;
3) the text of the article and figures in one pdf file;
4) the article's title, the names and initials of the authors, the full name of the organizations, the abstract, keywords, abbreviations, figure captions, and Russian references should be translated to English;
5) the cover letter stating that the submitted manuscript has not been published elsewhere and is not under consideration for publication;
6) the license agreement (the agreement form can be downloaded from the website www.actanaturae.ru).

MANUSCRIPT FORMATTING

The manuscript should be formatted in the following manner:

- Article title. Bold font. The title should not be too long or too short and must be informative. The title should not exceed 100 characters. It should reflect the major result, the essence, and uniqueness of the work, names and initials of the authors.
- The corresponding author, who will also be working with the proofs, should be marked with a footnote *.
- Full name of the scientific organization and its departmental affiliation. If there are two or more scientific organizations involved, they should be linked by digital superscripts with the authors' names. Abstract. The structure of the abstract should be very clear and must reflect the following: it should introduce the reader to the main issue and describe the experimental approach, the possibility of practical use, and the possibility of further research in the field. The average length of an abstract is 20 lines (1,500 characters).
- Keywords (3 – 6). These should include the field of research, methods, experimental subject, and the specifics of the work. List of abbreviations.
- INTRODUCTION
- EXPERIMENTAL PROCEDURES
- RESULTS AND DISCUSSION
- CONCLUSION

  The organizations that funded the work should be listed at the end of this section with grant numbers in parenthesis.
- REFERENCES

  The in-text references should be in brackets, such as [1].

RECOMMENDATIONS ON THE TYPING AND FORMATTING OF THE TEXT

- We recommend the use of Microsoft Word 2003 for Windows text editing software.
- The Times New Roman font should be used. Standard font size is 12.
- The space between the lines is 1.5.
- Using more than one whole space between words is not recommended.
- We do not accept articles with automatic referencing; automatic word hyphenation; or automatic prohibition of hyphenation, listing, automatic indentation, etc.
- We recommend that tables be created using Word software options (Table → Insert Table) or MS Excel. Tables that were created manually (using lots of spaces without boxes) cannot be accepted.
- Initials and last names should always be separated by a whole space; for example, A. A. Ivanov.
- Throughout the text, all dates should appear in the "day.month.year" format, for example 02.05.1991, 26.12.1874, etc.
- There should be no periods after the title of the article, the authors' names, headings and subheadings, figure captions, units (s – second, g – gram, min – minute, h – hour, d – day, deg – degree).
- Periods should be used after footnotes (including those in tables), table comments, abstracts, and abbreviations (mon. – months, y. – years, m. temp. – melting temperature); however, they should not be used in subscripted indexes (T_m – melting temperature; $T_{p.t}$ – temperature of phase transition). One exception is mln – million, which should be used without a period.
- Decimal numbers should always contain a period and not a comma (0.25 and not 0,25).
- The hyphen ("-") is surrounded by two whole spaces, while the "minus," "interval," or "chemical bond" symbols do not require a space.
- The only symbol used for multiplication is "×"; the "×" symbol can only be used if it has a number to its

right. The "·" symbol is used for denoting complex compounds in chemical formulas and also noncovalent complexes (such as DNA·RNA, etc.).
- Formulas must use the letter of the Latin and Greek alphabets.
- Latin genera and species' names should be in italics, while the taxa of higher orders should be in regular font.
- Gene names (except for yeast genes) should be italicized, while names of proteins should be in regular font.
- Names of nucleotides (A, T, G, C, U), amino acids (Arg, Ile, Val, etc.), and phosphonucleotides (ATP, AMP, etc.) should be written with Latin letters in regular font.
- Numeration of bases in nucleic acids and amino acid residues should not be hyphenated (T34, Ala89).
- When choosing units of measurement, SI units are to be used.
- Molecular mass should be in Daltons (Da, KDa, MDa).
- The number of nucleotide pairs should be abbreviated (bp, kbp).
- The number of amino acids should be abbreviated to aa.
- Biochemical terms, such as the names of enzymes, should conform to IUPAC standards.
- The number of term and name abbreviations in the text should be kept to a minimum.
- Repeating the same data in the text, tables, and graphs is not allowed.

GUIDENESS FOR ILLUSTRATIONS

- Figures should be supplied in separate files. Only TIFF is accepted.
- Figures should have a resolution of no less than 300 dpi for color and half-tone images and no less than 600 dpi.
- Files should not have any additional layers.

REVIEW AND PREPARATION OF THE MANUSCRIPT FOR PRINT AND PUBLICATION

Articles are published on a first-come, first-served basis. The members of the editorial board have the right to recommend the expedited publishing of articles which are deemed to be a priority and have received good reviews.

Articles which have been received by the editorial board are assessed by the board members and then sent for external review, if needed. The choice of reviewers is up to the editorial board. The manuscript is sent on to reviewers who are experts in this field of research, and the editorial board makes its decisions based on the reviews of these experts. The article may be accepted as is, sent back for improvements, or rejected.

The editorial board can decide to reject an article if it does not conform to the guidelines set above.

The return of an article to the authors for improvement does not mean that the article has been accepted for publication. After the revised text has been received, a decision is made by the editorial board. The author must return the improved text, together with the responses to all comments. The date of acceptance is the day on which the final version of the article was received by the publisher.

A revised manuscript must be sent back to the publisher a week after the authors have received the comments; if not, the article is considered a resubmission.

E-mail is used at all the stages of communication between the author, editors, publishers, and reviewers, so it is of vital importance that the authors monitor the address that they list in the article and inform the publisher of any changes in due time.

After the layout for the relevant issue of the journal is ready, the publisher sends out PDF files to the authors for a final review.

Changes other than simple corrections in the text, figures, or tables are not allowed at the final review stage. If this is necessary, the issue is resolved by the editorial board.

FORMAT OF REFERENCES

The journal uses a numeric reference system, which means that references are denoted as numbers in the text (in brackets) which refer to the number in the reference list.

For books: the last name and initials of the author, full title of the book, location of publisher, publisher, year in which the work was published, and the volume or issue and the number of pages in the book.

For periodicals: the last name and initials of the author, title of the journal, year in which the work was published, volume, issue, first and last page of the article. Must specify the name of the first 10 authors. Ross M.T., Grafham D.V., Coffey A.J., Scherer S., McLay K., Muzny D., Platzer M., Howell G.R., Burrows C., Bird C.P., et al. // Nature. 2005. V. 434. № 7031. P. 325–337.

References to books which have Russian translations should be accompanied with references to the original material listing the required data.

References to doctoral thesis abstracts must include the last name and initials of the author, the title of the thesis, the location in which the work was performed, and the year of completion.

References to patents must include the last names and initials of the authors, the type of the patent document (the author's rights or patent), the patent number, the name of the country that issued the document, the international invention classification index, and the year of patent issue.

The list of references should be on a separate page. The tables should be on a separate page, and figure captions should also be on a separate page.

The following e-mail addresses can be used to contact the editorial staff: actanaturae@gmail.com, tel.: (495) 727-38-60.

ActaNaturae

Acta Naturae journal places a special focus on interdisciplinary research lying at the interface of various biological disciplines: molecular biology, biochemistry, molecular genetics, and biomedicine.

Acta Naturae is published in Russian and English languages. It has been included in the List of the leading peer-reviewed journals of the Higher Attestation Commission of the Ministry of Science and Education of the Russian Federation and is indexed in the RSCI, PubMed, Web of Science, and Scopus databases.

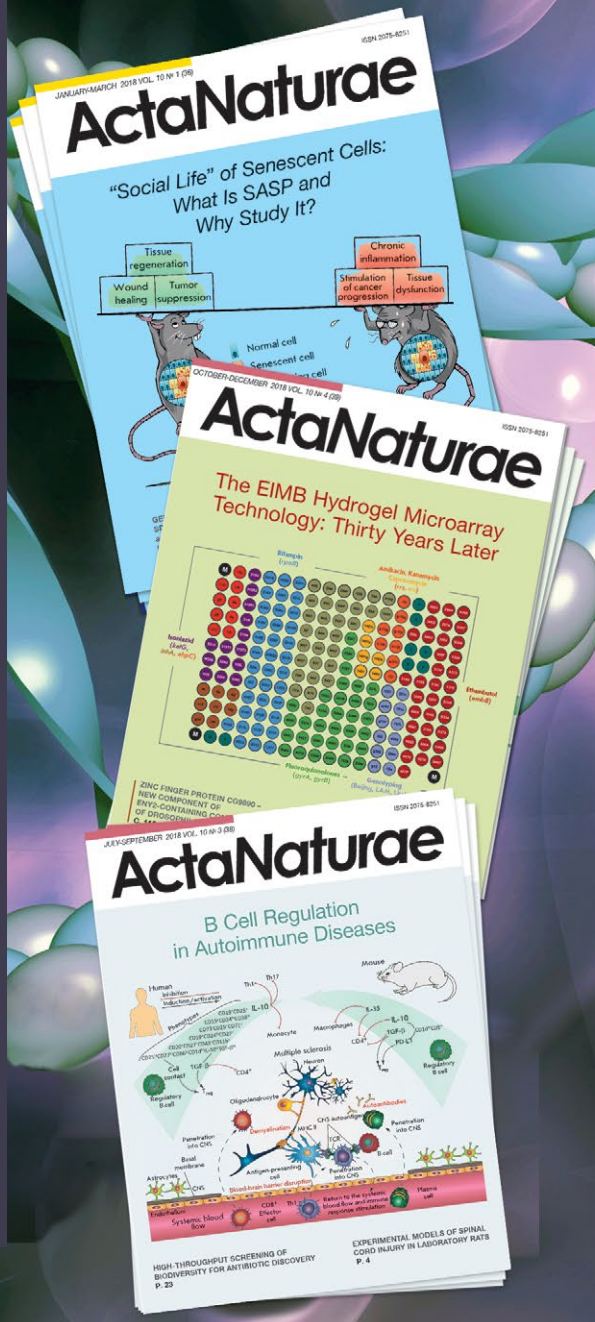

INFORMATION FOR AUTHORS

You can contact the Editorial Board via e-mail actanaturae@gmail.com and telephone +7 (495) 727-38-60.

The manuscript and supplementary files can be uploaded on the website www.actanaturae.ru.